Disorder and additive control of solid form and morphology in continuous crystallisation

Klapwijk, Anneke

Award date:
2017

Awarding institution:
University of Bath

Disorder and additive control of solid form and morphology in continuous crystallisation

Anneke Rachel Klapwijk

A thesis submitted for the degree of Doctor of Philosophy

University of Bath
Department of Chemistry

September 2016

Abstract

Crystallisation is an important unit operation in the processing of pharmaceuticals and other fine chemicals. This thesis presents research in the area of crystallisation and solid-state chemistry and investigates methods towards optimising the physical and particle properties of organic solid forms. The work was carried out in the context of the EPSRC Centre for Innovative Manufacturing in Continuous Manufacturing and Crystallisation (CMAC). CMAC aims to accelerate the adoption of continuous manufacturing processes for the production of higher quality chemical products at lower cost and more sustainably. Chapters 1-3 present an introduction to the research area in crystallisation tackled, along with background theory and experimental methods employed.

Crystal morphology is important for the ease of downstream processing in the production of pharmaceuticals and fine chemicals due to its impact on the bulk properties of a substance. Impurities can play a significant role in the final crystal morphology produced from crystallisation and can therefore be added intentionally (known as additives) to tune the morphology of a substance to a more desirable shape. Chapter 4 presents the discovery of a polymer-additive mediated effect on the crystal morphology of succinic acid; the effect of the additive is dependent on both the concentration of succinic acid and the polymer additive and a thorough investigation of these parameters at different scales is presented. A possible mechanism for the interaction of the polymer with the crystal surface is also described. Chapter 5 reports the transfer of the crystallisation of succinic acid carried out in Chapter 4 into the continuous environment using two different platforms. The system is used to characterise the design of a mesoscale segmented flow crystalliser as well as transferred to a well-established oscillatory flow platform. In the latter platform the additive effect of the polymer on the crystal morphology of succinic acid is successfully reproduced in the continuous environment. Chapter 6 explores the effect of a range of structurally similar additive candidates on the crystallisation of the Active Pharmaceutical Ingredient (API), isoniazid. As employed in Chapter 4, face indexing and analysis of the crystal structure are used to rationalise the effect of the additives.

Chapter 7 and 8 detail small-scale molecular crystallisation studies in attempts to induce disordered or layered solid forms and understand orientational disorder. In Chapter 7 the production of a range of multi-component molecular complexes of the API piroxicam are reported. This includes a solvated system which shows interesting structural and thermal properties which have been studied in detail. Chapter 8 is concerned with studies of orientational disorder in 5-chlorouracil.

This thesis is dedicated to Dr Teunis Klapwijk (1933 – 2015), my wonderful grandfather, who inspired me to study chemistry to PhD level.

Acknowledgements

First and foremost, I would like to thank Professor Chick Wilson for offering me a PhD position in the group and for his endless support and enthusiasm during my PhD; it has been a great experience and I have really enjoyed working in the group and all of the opportunities that have come with it. Thank you to all of my CMAC colleagues for an enjoyable four years in the Centre and for hosting me in the lab at Strathclyde on several occasions. Dr Elena Simone and Professor Zoltan Nagy, thank you for making me feel welcome in the lab at Loughborough University and for all of the knowledge I gained from the collaborative work we carried out together.

Thank you to everyone at Bayer; Dr Wolfgang Beckmann, Dr Michal Sowa and Dr Guillaume Levilian in Leverkusen and Dr Britta Olenik and her team in Wuppertal, for giving me the fantastic opportunity to work with you and for organising a great placement for me in Germany. Thank you to my other industrial mentors: Dr Amy Robertson, Dr Helen Wheatcroft and Dr Chris Price for all of your invaluable advice and guidance during my PhD studies.

I owe a huge thank you to many other people I've worked with during my PhD; Dr Dyanne Cruickshank for your patience and ongoing support, despite sometimes being thousands of miles away! Dr Karen Robertson, thank you for all of your help with flow crystallisation and reading my thesis chapters. Dr Lauren Hatcher, thank you for always being happy to help me with the diffractometers, answer my crystallography questions and for collecting data at the synchrotron for me with Dr Helena Shepard and Lucy Saunders. Thank you also to Professor Karen Edler for her advice on the polymer additives, Professor Colin Pulham for collection of VT-PXRD data at the synchrotron and the Johnson group at Bath for use of their TGA instrument.

To past and present members of the Wilson group, thank you for your friendship, useful discussions and help along the way. It's been great to work with such supportive and friendly people and I've really enjoyed sharing an office with you all. Ruth, thank you for being a fantastic project student and for all of your hard work during your project. And to Lauren, thank you for your assistance with the COBC experiments, for reading my thesis and for being a great roommate on trips away; I definitely owe you a lot of cups of tea!

Finally, thank you to Chris and my family for all of your support and encouragement during my studies.

Table of Contents

List of figures

List of tables

List of abbreviations

24DNBA..... 2,4-dinitrobenzoic acid
25DNSA..... 2,5-dinitrosalicylic acid
26DHBA..... 2,6-dihydroxybenzoic acid
34DHBA..... 3,4-dihydroxybenzoic acid
35DHBA..... 3,5-dihydroxybenzoic acid
35DNBA..... 3,5-dinitrobenzoic acid
44BP ..... 4,4’-bipyridyl
4HBA ..... 4-hydroxybenzoic acid
5CL 5-chlorouracil
API ..... Active pharmaceutical ingredient
ACN ..... Acetonitrile
ACT..... Acetone
BFDH ..... Bravais, Friedel, Donnay and Harker
CCD ..... Charge coupled device
CNT..... Classical nucleation theory
COBC..... Continuous oscillatory baffled crystalliser
CSD..... Cambridge Structural Database
CSTR ..... Continuous stirred tank reactor
DCM..... Dichloromethane
DNC ..... Direct nucleation control
DSC..... Differential Scanning Calorimetry
FBRM..... Focused beam reflectance measurement
FEP ..... Fluorinated ethylene propylene
FTIR ..... Fourier Transform Infra-red
GOOF..... Goodness of fit
GRAS..... Generally recognised as safe
HSM ..... Hot stage microscopy
IZN ..... Isoniazid
KRAIC..... Kinetically regulated automated input crystalliser
LAG..... Liquid assisted grinding
MALDI-TOF..... Matrix-assisted laser desorption/ionisation time of flight
MSMPR..... Mixed suspension mixed product removal
MSZ..... Metastable zone
MSZW ..... Metastable zone width
NMR..... Nuclear magnetic resonance

OA..... Oxalic acid
PAT ..... Process analytical technologies
PEG1000..... Polyethylene glycol 1000
PF127..... Pluronic F127
PP123..... Pluronic P123
PPG4000..... Polypropylene glycol 4000
PVM..... Particle vision and measurement
PX ..... Piroxicam
PXN..... Piroxicam (non-ionised tautomer)
PXZ ..... Piroxicam (zwitterionic tautomer)
PXRD ..... Powder X-ray diffraction
RES..... Resorcinol
RT ..... Residence time
SA ..... Succinic acid
scXRD..... Single crystal X-ray diffraction
SEM..... Scanning Electron Microscopy
SOP..... Site occupancy factor
STR ..... Stirred tank reactor
TA ..... Trimesic acid
TGA..... Thermogravimetric analysis
VT-PXRD..... Variable temperature powder X-ray diffraction

Chapter 1

Introduction

1.1 Context of research

Crystallisation is a vital step in the manufacture of many pharmaceuticals and fine chemicals, of which a high proportion are produced as crystalline solids. Control over the crystallisation process is important for the structural and particle attributes of a substance, enabling optimised function and physical properties to be achieved. Lack of understanding of the solid state behaviour of a substance can lead to unexpected phase transitions and result in altered properties such as stability and solubility: consequently, a material may not perform in the way anticipated. As well as the structural properties, optimisation of particle attributes such as particle size distribution and crystal morphology is important for the efficiency and ease of downstream manufacturing processes such as filtration and drying.

The work presented in this thesis was carried out as part of the Doctoral Training Centre programme within the EPSRC Centre for Innovative Manufacturing in Continuous Manufacturing and Crystallisation (CMAC; see Section 1.3).

1.2 Crystallisation

A crystalline solid consists of molecules arranged in a regular array exhibiting long range order (see Chapter 2). Crystallisation methodology is key to the production of crystals with desired properties, and plays a role both in controlling the crystalline structure (often termed solid form control) and the macroscopic characteristics of the crystalline particle (particle attribute control). Although there are many crystallisation methods adopted, the work here concentrates on crystallisation from solution, the primary method currently adopted for the production of crystalline particles of pharmaceuticals and fine chemicals

in a batch environment. Crystallisation methods can be of significant sophistication, but the basic process of crystallisation from solution can be described by three stages: generation of supersaturation, nucleation and crystal growth.

1.2.1 Supersaturation

Figure 1.1 shows a typical solubility curve as a function of temperature whereby an increase in solubility is observed as the temperature rises. At any given temperature on the curve the solution is saturated. A solution which lies below the equilibrium solubility line is termed undersaturated (existing crystals will dissolve) and a solution which lies above the equilibrium solubility line is supersaturated. A supersaturated solution therefore contains a greater concentration of dissolved solid than can ordinarily be accommodated at that temperature (i.e. greater solution concentration than the equilibrium saturation concentration).[1] For crystallisation from solution to occur supersaturation needs to be generated (methods for generating supersaturation are outlined in Section 1.2.5); supersaturation is therefore considered the driving force for crystallisation.

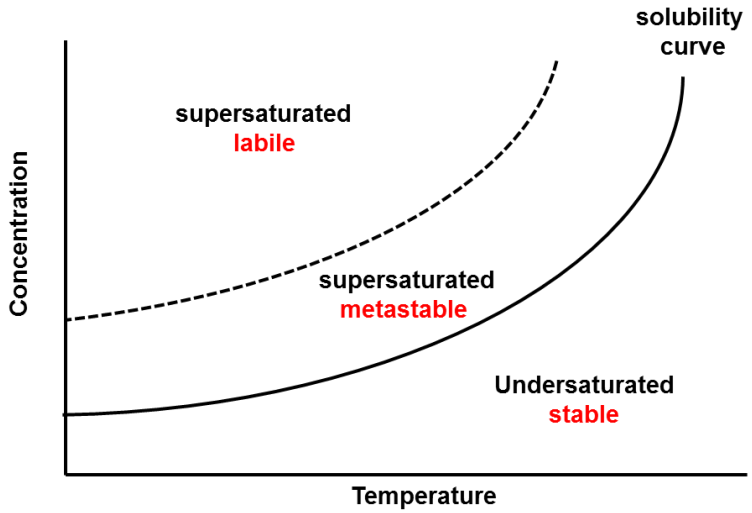

Figure 1.1 - The solubility of a compound as a function of temperature showing the metastable zone width (MSZW).[2]

Above the solubility curve exists a metastable region in which the solution is supersaturated but within which it does not respond with spontaneous nucleation and only existing crystals will grow.[3] The temperature at which spontaneous nucleation occurs for a given saturation concentration can be determined; this marks the limit of the metastable region (dotted black line on Figure 1.1), and is sometimes termed the metastable limit curve. The metastable zone width (MSZW) between these two curves is not always well defined and can vary depending on a number of conditions such as scale,

the cooling rate or the presence of impurities.[4,5] A supersaturated solution whose composition lies beyond the metastable zone is termed labile and within this region spontaneous, uncontrolled nucleation is likely to occur.[2]

A number of equations can be used to describe the supersaturation of a solution. By calculating the difference between the concentration of the solution (c) and the concentration of the solution at equilibrium saturation at the same temperature (c*) the concentration driving force can be determined[2] (Equation 1.1). This value is used to describe supersaturation in this work. Supersaturation can also be described by the supersaturation ratio (S) of the two concentration values (Equation 1.2) or the relative supersaturation (Equation 1.3).[6,7]

$$\Delta c = c - c^* \qquad \text{Equation 1.1}$$

$$S = \frac{c}{c^*} \qquad \text{Equation 1.2}$$

$$\sigma = \frac{c - c^*}{c^*} = S - 1 \qquad \text{Equation 1.3}$$

Thermodynamically, supersaturation can be described as the difference in chemical potential (μ) between a molecule in its equilibrium and supersaturated states ($\Delta\mu = \mu_{ss} - \mu_{eq}$).[7]

1.2.2 Nucleation

Nucleation is defined as "the process of creating a new solid phase from a supersaturated homogeneous mother phase"[2] and plays a decisive role in determining the molecular packing of a crystalline material.[8] There are two types of nucleation: primary and secondary, outlined in Figure 1.2.

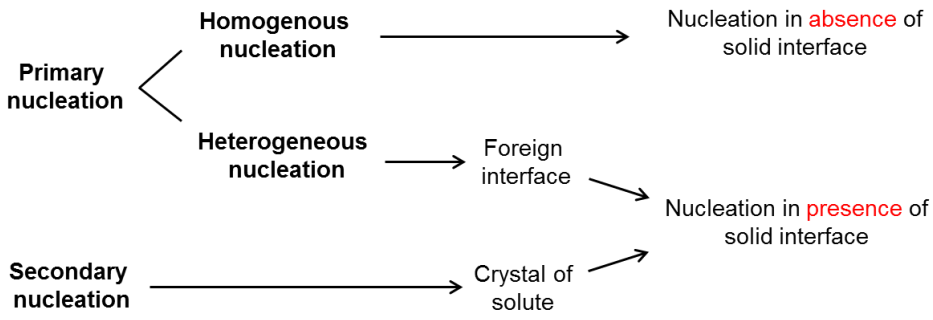

Figure 1.2 - Schematic showing the types of nucleation differentiated by the absence or presence of a solid interface.[3]

1.2.2.1 Primary nucleation

Primary nucleation can be described as homogeneous or heterogeneous, distinguished based on the presence or absence of a solid interface. Homogenous nucleation is the spontaneous nucleation of a solid phase as a result of supersaturation alone (in the absence of any solid interface).[3,9] While the mechanism behind nucleation is not fully understood, in current nucleation research two theories have been accepted for crystal nucleation from supersaturated solutions (Figure 1.3).[10]

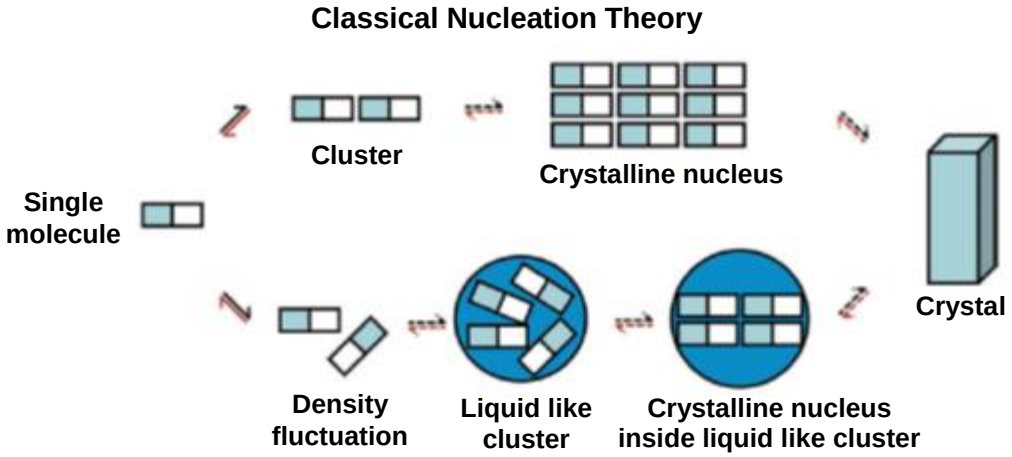

Figure 1.3 - The two alternative pathways for nucleation: (top) classical nucleation theory and (bottom) two-step nucleation theory.[10]

First, classical nucleation theory (CNT) considers the addition of molecules to clusters until a critical size is reached to be able to sustain growth from solution. Clusters of this size are known as critical nuclei and their formation depends on overcoming the free energy barrier for the system[11] (Figure 1.4). The maximum in the curve, at critical size z_c, represents the size at which further growth of the cluster will lead to a decrease in free energy. Any cluster less than this size would only achieve a decrease in free energy by dissolution. The height of the free energy barrier depends on the level of supersaturation of the solution. As supersaturation increases, the height of the barrier and the value of the critical size decrease. Consequently, spontaneous nucleation is possible with increasing levels of supersaturation.[2]

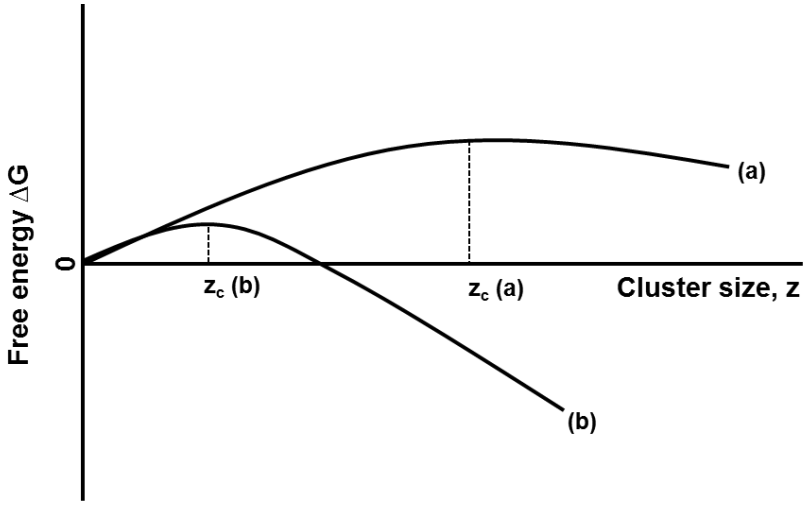

Figure 1.4 - The free energy change as a function of cluster size (z), where z_c represents the critical cluster size at two supersaturation levels: (a) curve at low supersaturation, (b) curve at high supersaturation.[2]

Alternative theories termed non-classical nucleation theories have also been explored.[12,13] In the two-step mechanism,[12] a highly disordered, liquid-like cluster is produced and once the nucleus reaches a certain critical size, crystalline order appears inside the liquid-like clusters.[8]

In practice, homogenous nucleation is uncommon and primary nucleation more often occurs through heterogeneous nucleation.[14] Heterogeneous nucleation is the spontaneous nucleation of a solid phase in the presence of a foreign surface such as dust, other impurities or the wall of the crystallisation vessel.[15] This lowers the free energy barrier of nucleation by providing a surface on which material can be adsorbed. The presence of foreign surfaces can therefore induce nucleation at lower levels of supersaturation than for homogeneous nucleation.[2,4]

1.2.2.2 Secondary nucleation

Secondary nucleation describes the generation of new particles induced by the presence of suspended crystals of the solute.[9] This mechanism usually occurs at lower supersaturations than for both types of primary nucleation.[2,4] Secondary nuclei are formed in a number of different ways, most commonly through collision nucleation in which nuclei are formed by the collision of larger crystals with other crystals, the walls of the crystalliser or the impeller, resulting in smaller particles.[2,3] The shear forces inflicted on a crystal by the solution flowing past can also be sufficient to produce secondary nuclei; this is known as shear nucleation.[2]

1.2.3 Crystal growth

Upon reaching the critical size, addition of solute molecules from the supersaturated solution allows the crystal surface to undergo growth. The conditions and rate of crystal growth are important for the final product purity and crystal morphology.[4] As in nucleation theory, there are several theoretical pathways by which a solute molecule adsorbs onto a crystal face from a supersaturated solution. The growth of crystal faces through the integration of growth units into the crystal lattice is dependent upon the strength and number of interactions likely to form between the crystal face and the growth unit.[2] Crystal faces can be classified into three types depending on the number of interactions they can form with a growth unit, as proposed by Hartman and Perdok.[16-18] There are three bonds possible at a kinked face, two bonds possible at a stepped face and one bond possible on a flat face (Figure 1.5). Crystal growth at a kinked face is the most energetically favourable type of bond, forming three interactions to an existing step rather than forming a new step.

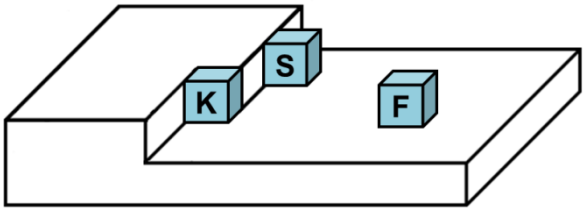

Figure 1.5 - A crystal surface showing growth units docking on a flat site (F), a step site (S) and a kink sites (K).

Early crystal growth mechanisms considered the presence of an adsorbed layer of solute molecules on a crystal face. The Gibbs-Volmer theory postulates that growth units first adsorb onto the crystal surface, followed by diffusion on the surface to a step or kink site for incorporation. Thus, it is thought that crystals grow in a layer by layer fashion.[4,7] This process can be described in terms of overcoming free energy barriers (Figure 1.6).

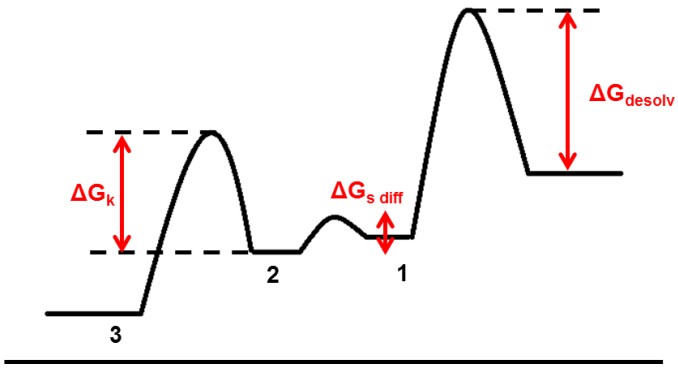

Figure 1.6 - Free energy barriers to overcome during crystal growth.[2]

In order to overcome ΔG_{desolv} the solute molecules must lose some of their solvent molecules to adsorb to the crystal surface, losing one degree of freedom (1). The growth unit then enters the adsorption layer where it overcomes the $\Delta G_{s,diff}$ to migrate across the surface to a step position (2). Further desolvation then occurs to adsorb on a kink site (ΔG_k) (or, less favourably, on a step site) (3).[2,7]

When crystalline materials contain sufficient kink and step sites on the surface, all approaching growth units will find a growth site. In this case, the growth rate is linearly proportional to supersaturation and this mechanism is known as continuous growth. When the crystal surface does not have enough step and kink sites to facilitate continuous growth steps must be created to accept the incoming growth units. One mechanism for step creation is described by two-dimensional nucleation at the surface. Growth units will form clusters on the flat surface which must reach critical size for growth of the layer to be completed.[2,11] There are several models that describe the process of completing the layer.

The mononuclear model assumes that following formation of the surface nucleus, it spreads across the surface at infinite velocity where the growth rate of each face is proportional to its area. This contrasts from the observed behaviour in which the largest faces are the slowest growing, eliminating the model as a possibility. In the polynuclear model, the spreading velocity is zero and the mechanism assumes that the nucleus does not spread, but the combination of several two-dimensional nuclei of critical size would eventually combine and cover the layer. The third model is known as the birth and spread model. This model allows a finite spreading rate independent of size and assumes nucleation occurs at any location on the surface and that there is no intergrowth between layers.[4,11] In both of the latter models it can be seen that the rate-determining step in the two-dimensional nucleation mechanism is the surface nucleation rate; crystal growth is thus a discontinuous process.[4,9]

In contrast, the Burton-Cabrera-Frank (BCF) model of crystal growth proposes that steps are self-generating as a result of screw dislocations in the crystal.[4,11] The screw dislocation acts as a kink in the crystal and the new step grows over only a part of the surface, enabling the growth to wind up into a spiral towards self-perpetuating growth (Figure 1.7). This avoids the need for nucleation on the surface as an available adsorption site has been created spontaneously. This type of growth can result in growth rate dispersion in which different crystals and crystal surfaces have different growth rates due to the mechanism responding to specific dislocations on each crystal.[2,11] As the

morphology of the crystal is dictated by the relative growth rates of the individual faces, this may result in differences in crystal morphology.

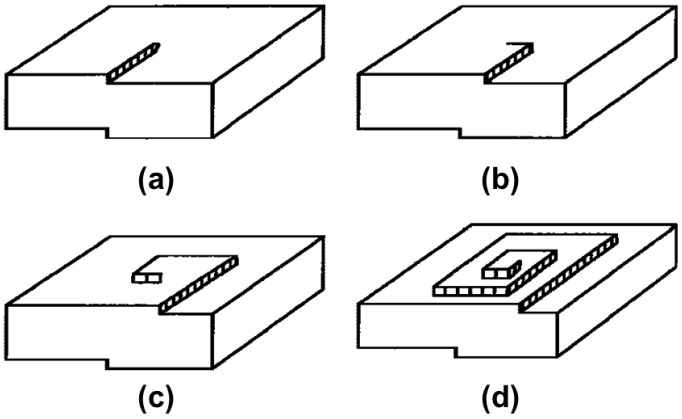

Figure 1.7 - Spiral crystal growth through the presence of screw dislocations.[19]

The features of a growing crystal face such as the surface roughness (quantified by the α-factor) can be used to predict the growth mechanism adopted by the surface. Growth of a rough surface proceeds through continuous growth ($\alpha < 2$) whereas growth of a smooth surface proceeds through a BCF mechanism ($\alpha > 5$). Growth of a face of intermediate roughness may proceed through the birth and spread mechanism.[7] Measurement of the growth rate of a face with respect to supersaturation can also give an indication of the growth mechanism, since the relationship predicted by each mechanism differs. A crystal face growing continuously will give a linear relationship between growth rate and supersaturation.[2] A smooth crystal face growing at low supersaturation may undergo surface roughening at high supersaturation and/or temperature which can be related to a change in the growth mechanism of the face.[20,21] This results in lost molecular selectivity and observation of rounded edges between different crystal faces (non-faceted growth).[22,23] To maximise purity, supersaturation should be limited to maintain faceted growth. In non-faceted growth, the surface is less discriminating and may be more likely to accept impurities.

1.2.4 Crystal morphology

Crystal morphology represents the characteristic external shape of a crystal and is important for the function and physical properties of a material as well as the ease of downstream processing steps such as washing, filtration and compaction.[4] For example, plate shaped crystals may be undesirable due to their tendency to pack as an impermeable layer on filter media resulting in poor efficiency in filtration and washing,

whereas block shaped crystals may filter more readily (Figure 1.8);[2,24] block-like crystals are therefore generally more desirable for large scale processing. Specifically for pharmaceutical materials, crystal shape and size uniformity may also affect the dissolution properties of a drug and thus its bioavailability.

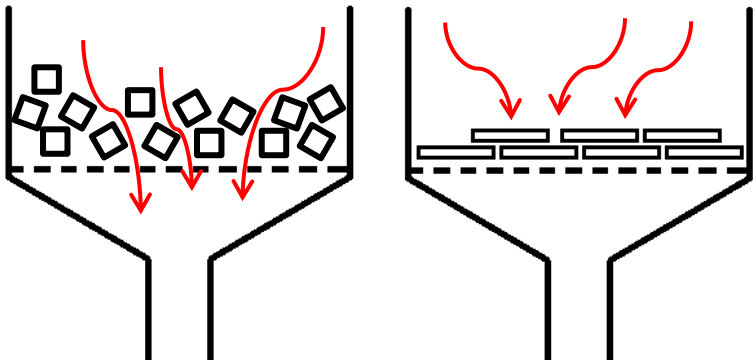

Figure 1.8 - Diagram showing the effect of crystal morphology on filtration: block-like crystals filter well (left) whereas plate-shaped crystals filter less efficiently, packing as an impermeable layer (right). Adapted from [2].

The shape (morphology) of a crystal is governed by the relative growth rates of its individual faces. The growth of a face can be described as the rate of crystal growth along the direction perpendicular to the face – the (100) face thus "grows along" the *a*-direction, for example. A fast growing face will thus have a smaller area in comparison to a face that grows more slowly. Therefore, the morphology of a crystal is defined by its slowest growing faces. Large differences in the growth rates of individual faces will result in plate or needle-like crystals. The growth rate of each crystal face is affected by the internal molecular and crystal structure of the material as well as by external factors such as the choice of solvent, mixing conditions, degree of supersaturation, seeding and the presence of impurities such as structurally similar by-products.[2] The crystallisation conditions can therefore sometimes be altered to optimise the crystal morphology.

1.2.4.1 Prediction of crystal morphology

The morphology of a crystal can be described as either the equilibrium or the growth morphology. The equilibrium shape is produced when the surface free energies of the crystal faces are minimised and is adopted when the crystal equilibrates with its surroundings. It is uncommon for crystals observed experimentally to adopt this shape and the growth morphology is often observed, which is affected by the crystal growth kinetics.[2,4,25]

The relationship between crystal morphology and crystal packing can enable prediction of a theoretical growth morphology. As stated above, the relative growth rates of the individual crystal faces govern the shape of the crystal. Early morphology prediction models related knowledge of the crystal packing or the energy of the crystal faces to the growth rates of individual crystal faces in order to construct a prediction of the crystal morphology.[25]

The BFDH approach (used in this work) is based on the Bravais, Friedel, Donnay and Harker rule which assumes that the rate of crystal growth is inversely proportional to the interplanar spacing of a face (based on the underlying premise that molecules that are closer together as a result of this will have larger interaction energies).[2] The BFDH model extends the prior work of Bravais and Friedel by adding the influence of space group symmetry elements such as screw axes and glide planes.[26,27] However, this approach relies exclusively on knowledge of the crystal structure and therefore does not take into account the effect of the growth environment. The attachment energy model from Hartman and Perdok,[16-18] later extended by Hartman and Bennema,[28] states that the growth on the crystal surface proceeds by the addition of a layer containing the same crystal structure as the rest of the crystal and that the rate of growth perpendicular to a crystal face is proportional to its attachment energy. The attachment energy is defined as the energy released when one growth unit is attached to the surface of the crystal face.[2,25] Crystal faces with a higher attachment energy have a faster growth rate and are therefore of lower morphological importance.

Each of the BFDH and attachment energy models can be used to predict the crystal morphology of vapour-grown crystals, however, they cannot account for the effect of the growth environment in solution crystallisation, as they take no account of, for example, solvent interactions which can sometimes act to inhibit growth on crystal faces (Sections 1.2.4.2 and 1.2.4.3).[4,19] New models for crystal morphology prediction are continuing to be developed that take into account the effects of the growth environment; these may enable more accurate predictions of morphology.[19,29-31]

1.2.4.2 Effect of solvent choice on crystal morphology

The importance of incorporating solvent effects in morphology prediction models is emphasised by the fact that often in crystallisation different morphologies are produced from different solvents. Favourable interactions between solvent molecules and functional groups exposed on the surface of specific faces of the crystals may result in disruption of the growth rates of individual faces. Davey *et al.* studied the effect of solvent choice on

the crystal morphology of β-succinic acid whereby a plate-like morphology was produced from water and a needle-like morphology was produced from isopropanol. Examination of the crystal structure allowed functional groups to be identified at the slow growing faces. In crystallisation from water the slowest growing face features polar functional groups that would interact favourably with polar solvent molecules and thus result in slower growth rates of the face.[2,32] Eddleston *et al.* recently reported the occurrence of triangular plate-like crystals of theophylline form II from hydrophobic solvents containing hydrogen bond acceptor groups but no donor groups (hydrogen bonds are discussed in Section 1.5.1).[33] In contrast, crystallisation from solvents containing both hydrogen bond donor and acceptor groups produced lath-shaped crystals. The formation of triangular crystals was rationalised by considering the packing of the molecules in the crystal structure and the interaction of the solvent molecules with specific crystal faces.

However, solvent-surface interactions must have enough stability to compete with the addition of solute molecules. In the case of sulfathiazole, its polymorphs show different morphologies, but each polymorph showed a similar morphology from all solvents studied.[34] This suggested that morphology changes in that case are a result of different packing arrangements and any solvent-surface interactions did not inhibit the addition of sulfathiazole molecules to the fast growing faces. In contrast, the morphology of 2,6-dihydroxybenzoic acid form I grown from toluene solution and chloroform solution is shown to differ significantly; rectangular plate-like crystals are produced from toluene whereas diamond shaped plates are produced from chloroform (Figure 1.9). Indexing of the crystal faces of 2,6-dihydroxybenzoic acid showed that the (310) face is prominent in the crystals produced from chloroform and absent in those produced in toluene. Analysis of the crystal packing showed that the surface of the (310) face exposes carbonyl and hydroxyl functionalities with which the chloroform solvent molecule can interact.[35]

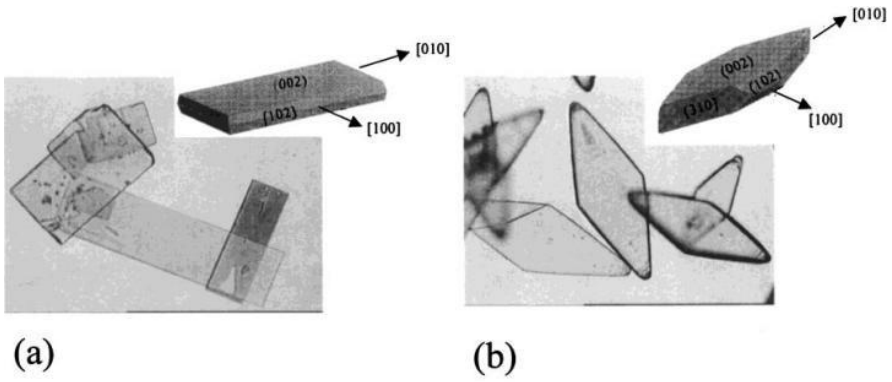

Figure 1.9 - Morphologies from 2,6-dihydroxybenzoic acid form I crystals grown from (a) toluene and (b) chloroform.[35]

Similar studies were recently reported on the crystal morphologies of the α and β polymorphs of *p*-aminobenzoic acid where experimental morphologies from a range of solvents were compared with calculated morphologies.[36]

1.2.4.3 Effect of impurities on crystal morphology

The presence of impurities can also have a major effect on crystal growth. As with solvent molecules, impurities can compete with solute molecules by occupying adsorption sites on the crystal surface. This may cause defects,[11] or inhibit or slow down growth on specific crystal faces by interacting preferentially with functional groups present on the surface of the face. A well-known example of this phenomenon is the case of the crystallisation of urea from water in the presence of biuret, a side-product in the synthesis of urea, with which it is structurally similar. In the absence of the impurity, urea crystallises in a needle-like morphology, but in the presence of biuret growth of the fast growing face is reduced, producing crystals with smaller aspect ratio.[37,38] This disruption of growth is explained by the structural similarity of the biuret molecules, which facilitates competition for surface adsorption on the fast growing (001) face with the urea molecules. This inhibits hydrogen bonding of further urea molecules at such sites and slows down the overall growth rate of the face.[38,39]

Another example of the impurity effect is that of benzoic acid on the growth of benzamide crystals from ethanol. In the absence of the impurity, plate-like crystals are produced. In the crystal structure of benzamide, a hydrogen bonded ribbon of benzamide molecules forms along the crystallographic *b* axis. The structural similarity of benzoic acid to benzamide and the presence of favourable hydrogen bond donor and acceptor groups allows it to occupy a site normally occupied by a benzamide molecule. This also prevents addition of further benzamide molecules in the chain (Figure 1.10).

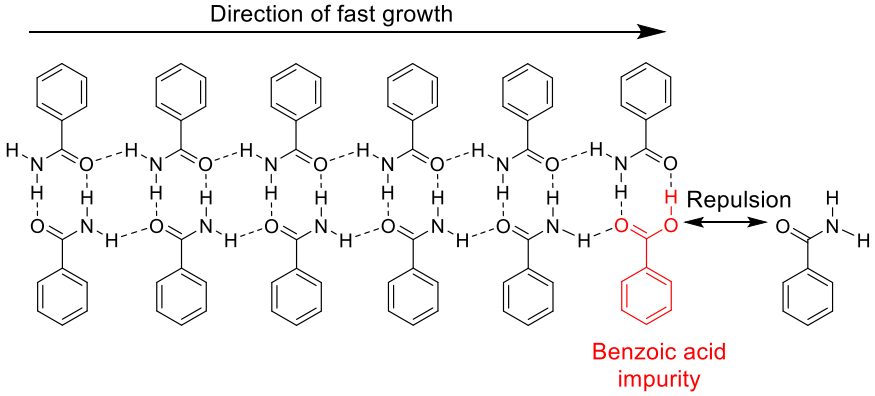

Figure 1.10 – A hydrogen bonded ribbon of benzamide molecules interrupted by a benzoic acid impurity preventing the addition of further benzamide molecules. Adapted from [40].

This inhibits overall growth along the *b* axis resulting in production of needles rather than plate-like crystals.[40,41] The presence of impurities can also influence the crystallisation in a range of other ways such as delaying nucleation,[42-44] slowing down overall growth rates[45] and affecting polymorphic form.[46-50]

In some cases impurities are deliberately added to a crystallisation to engineer the growth of crystals with a desired morphology (by inhibiting growth of selected faces); these are known as additives. There is a broad array of examples in the literature of the effect of structurally similar additives, or size-matched additives with relevant functional groups, on crystal morphology[24,51-54] and crystal size.[43,55] However, significant quantities of these impurities may be required to yield the desired effect, and additives that show structural similarity to the target compound can be susceptible to inclusion into the crystal lattice.[54,56,57] This is undesirable, especially if the additive compound is non-benign – in pharmaceuticals, for example, such additives may not be Generally Recognized As Safe (GRAS)[58] and their incorporation into a resulting solid form would prohibit its potential use in any product.

Control over crystal morphology can also be exerted by introducing impurities that are not structurally similar or size-matched to the target molecule, for example through use of polymer additives. Unlike the structurally similar case, polymer additives are unlikely to be incorporated into the final product due to their dissimilarity to the target material and their large size. The use of polymers in this context is also favoured by the fact that they are commonly used as excipients in drug formulations, and are thus a frequent component in pharmaceutical processing. There are a number of examples in which polymer additives have been shown to affect the crystallisation process: anti-solvent crystallisation of salbutamol sulfate in the presence of small quantities of a polyvinylpyrrolidone (PVP K25) was found to modify the crystal morphology from needle-like crystals to block-like crystals with a lower aspect ratio,[59] while Vetter *et al.* reported the effect of Pluronic F127 on the crystal growth rates of Ibuprofen.[45] A study into the effect of hydroxypropyl methylcellulose (HPMC) on the crystallisation of hydrocortisone acetate showed that, in the presence of the polymer, nucleation was delayed and habit modification to a wing-shaped morphology was observed. The mechanism for inhibition of nucleation was described in terms of prevention of nucleation through the formation of drug-polymer interactions in solution. Mechanisms for the growth inhibition and resultant habit modification were also discussed. Growth is inhibited by adsorption of polymer molecules on the crystal surface through face-specific hydrogen bond interactions. In addition, accumulation of non-adsorbed polymer molecules at the boundary region may provide

resistance for the drug growth units to diffuse through the barrier and incorporate into the growth site.[60] The influence of HPMC and other polymeric additives on the crystallisation of Ritonavir, Flutamide and Felodipine was also recently studied.[61-65]

Several factors may be considered when selecting an additive for crystal growth inhibition such as structural similarity and the presence of functional groups which may interact favourably with the target compound. However, the design of such growth modifiers sometimes lacks such rationale and often relies on trial and error.[39]

1.2.5 Crystallisation methods

As noted above, in order for crystallisation from solution to occur, supersaturation must be generated and there are a number of techniques that can be used such as evaporation, cooling and the addition of an anti-solvent. Grinding (mechanochemical) and solution mediated (slurrying) methods can also be used to facilitate multi-component crystallisation.

1.2.5.1 Evaporative crystallisation

In evaporative crystallisation supersaturation is generated by removal of the solvent by evaporation at a fixed temperature. As the solvent evaporates the solution becomes more concentrated and passes through the metastable zone into the supersaturated region where nucleation and crystal growth occurs (Figure 1.11). Upon crystallisation, the solute concentration decreases, however as a result of the continual evaporation of the solvent, the concentration will increase back into the supersaturated region.

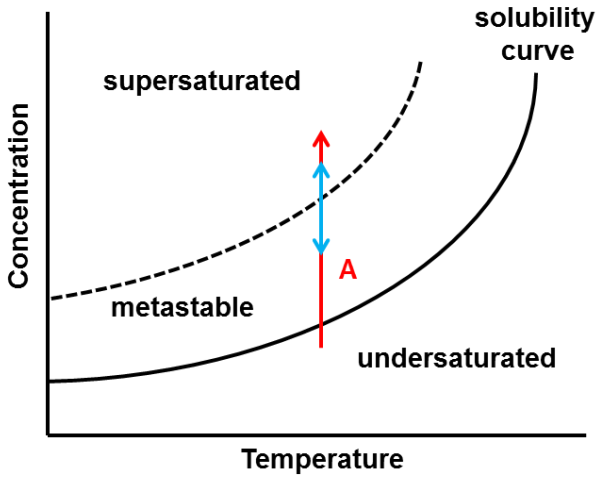

Figure 1.11 - Generation of supersaturation by evaporation (arrow A) with the variation in solute concentration between the metastable and supersaturated regions depicted by the blue doubled headed arrow shown on the solubility diagram.

Evaporative crystallisation is often used as a screening method in materials discovery at small scales by altering variables such as the temperature and choice of solvent. Such variables affect the rate of crystallisation which can impact crystal size and shape. Often slow evaporation at controlled temperatures provides a good environment for single crystal growth.

1.2.5.2 Cooling crystallisation

In cooling crystallisation (without seeding) supersaturation is generated by cooling a saturated solution which reduces the solubility of the solute, driving the solution into the supersaturated region and resulting in nucleation and crystal growth (Figure 1.12).

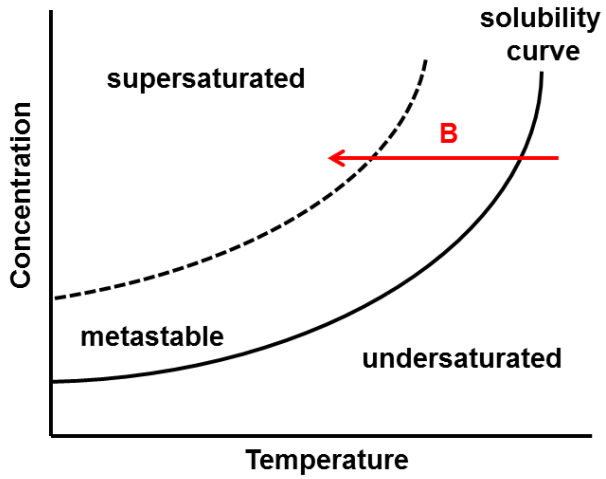

Figure 1.12 - Generation of supersaturation by cooling without seeding (arrow B) shown on a solubility diagram.

Nucleation generates a drop in the solute concentration and if there is knowledge of the MSZW, the cooling profile can be controlled such that following nucleation, cooling continues within the MSZ where only growth is achieved. This strategy limits further primary nucleation leading to improved particle attributes. Cooling crystallisation is more commonly used in large scale pharmaceutical crystallisations. However, it requires there to be a significant solubility decrease with decreasing temperature in order to achieve a good yield.

1.2.5.3 Anti-solvent crystallisation

Another technique used to induce supersaturation is the addition of an anti-solvent. In this type of crystallisation, the solubility of the target compound decreases with the addition of a solvent in which the compound to be crystallised is insoluble / poorly soluble (the anti-solvent). This drives the solution into the supersaturated region where crystallisation

occurs (Figure 1.13). Anti-solvent crystallisation is often used for substances which show little change in the solubility with temperature and can sometimes be used in combination with cooling to improve yield.[66] It may also be used in order to avoid thermal degradation by avoiding the need for heating to elevated temperatures.

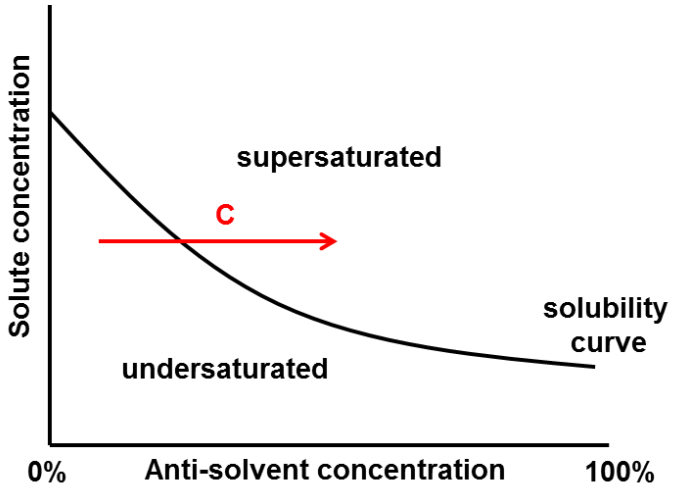

Figure 1.13 - Generation of supersaturation *via* anti-solvent crystallisation (arrow C).

1.2.5.4 Seeding

Seeding is often implemented to improve the resulting particle size distribution and gain more control over the crystalline product such as the polymorphic form. Seeds of the substance are added to a solution in the metastable zone to result only in growth of the seed particles and suppression of spontaneous nucleation, inherently producing a narrow particle size distribution. The temperature at which the seeds are added is also important: addition of seeds in the undersaturated region will result in dissolution of the seeds (Figure 1.14, Point A) whereas addition of the seeds in the labile supersaturated region will cause secondary nucleation, with primary nucleation also occurring resulting in a broad particle size distribution (Figure 1.14, Point D). Addition of the seeds within the MSZ and close to the solubility curve (Figure 1.14, Point B) results in the situation where supersaturation is low and there is little secondary nucleation. This results in slow crystal growth and the production of larger crystals. Seeding close to the metastable limit (Point C, Figure 1.14) is at high supersaturation and induces secondary nucleation. Seed addition at this point results in rapid crystal growth and the formation of many small crystals.[6]

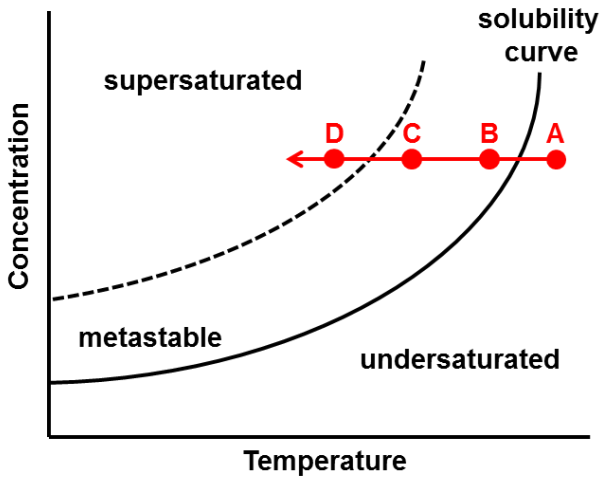

Figure 1.14 - Solubility diagram showing the importance of the seed addition temperature: in the undersaturated region (A), close to the solubility line (B), close to the metastable limit (C) and in the supersaturated region (D). Seed addition at position B would result in the narrowest particle size distribution.

1.2.5.5 Ostwald ripening

Ostwald ripening describes the growth of large particles at the expense of smaller particles. Large particles have a lower solubility than smaller particles which results in dissolution of the small crystals and their mass depositing on the larger particles. This increases the particle size of the larger crystals, decreasing the surface area : volume ratio thus minimising the Gibbs free energy.[2,4] As the driving force for Ostwald ripening is the difference in solubility between the small and the large particles, the process can be accelerated by applying temperature fluctuations known as temperature cycling. This is sometimes utilised in crystallisation in order to obtain a more monodisperse particle size distribution.[7]

1.2.5.6 Other methods for the preparation of multi-component crystalline complexes

Synthesis of multi-component solid forms (discussed in Section 1.4) can sometimes be facilitated using mechanochemical methods.[67,68] Dry or liquid-assisted grinding (LAG) methods are carried out manually using a mortar and pestle or using a mechanical ball mill. This avoids the need to identify a suitable solvent system and is often the first step carried out for co-crystal screening. The product of a mechanochemical experiment will usually be in polycrystalline form, and characterised using powder X-ray diffraction (PXRD). If PXRD indicates the production of new crystalline materials of interest, steps can be taken to grow single crystals of the system for full structural characterisation,

usually involving solution-based methods. Methods such as extrusion have been shown to be effective in the scale-up of mechanochemical synthesis of co-crystals.[69,70]

Another method shown to be effective in producing multi-component materials is carried out by suspending the starting materials in a chosen solvent and stirring the slurry for a specific period of time.[71-73] Upon suspension of starting materials in a solvent, they will each dissolve until reaching their individual solubility in the solvent system. Favourable interactions between the two components may result in the formation of a complex; nucleation and crystal growth of the complex will occur, depleting the solution concentration of the two individual components. Further dissolution of the starting materials will then occur due to the solution being undersaturated with respect to each component. Using the solution as a medium and when provided sufficient time and mobility, the remainder of the starting materials will convert to the complex.[73]

1.3 Industrial Crystallisation

Crystallisation is an essential unit operation in the manufacture of materials produced in solid form which makes up a large part of the pharmaceutical and fine chemicals industry. The equipment used in industrial crystallisation is vast in scope, from multi-purpose batch vessels to highly specialised and process-specific equipment.[74]

1.3.1 Batch crystallisation

The main platform currently employed for both production and purification of solids in the pharmaceutical, agrichemical and fine chemicals industries is the stirred tank reactor (STR). A STR is a jacketed batch vessel in which mixing is facilitated with a motor-induced impeller. Although STRs are a well-established technology and offer the benefit of flexibility to different processes, there can be significant challenges in achieving homogenous processing conditions at large scales. In a STR, as scale increases, uniformity of mass and heat transfer in the vessel decreases, resulting in longer reaction times. Optimisation of mixing inside the vessel upon scale-up is therefore critical.[66] Varying conditions inside the vessel can sometimes result in inconsistent product attributes such as size distribution, polymorphic form and morphology which can have a direct impact on downstream processes such as filtration, drying and formulation as well as on the desired function of the material.[5,75] STRs also occupy significant volumes of space and cleaning of the vessel between batches is a requirement, increasing reactor downtime and solvent use.

1.3.2 Continuous crystallisation

There is significant interest in the application of continuous methods of crystallisation in the pharmaceutical and fine chemical industries in which feed solution is continually added to a crystalliser whilst continually removing product, minimising reactor downtime. Continuous crystallisation is of interest since it may overcome the difficulties that batch production brings. Improved heat and mass transfer can be accessed through use of continuous methods of crystallisation which may enable better control over particle attributes.[11,76] Gaining control of these specific attributes will enable elimination of downstream corrective processes such as milling and granulation used to achieve uniform particle size in preparation for formulation.[75] Continuous processes are also readily scaled-up simply through increasing the throughput and running the system for a longer period of time.[77] Furthermore, a continuous mode of operation offers minimised reactor downtime and reduced environmental footprint through more efficient use of solvents, energy and space.[5] Table 1.1 outlines the key differences between batch and continuous methods of operation.

Table 1.1 - Table outlining the differences between batch and continuous methods.

Batch	Continuous
Multi-purpose equipment that can be used for different processes	Equipment is system dependent
Significant process knowledge	New technology – less process experience
Non-uniform mixing	Uniform mixing – improved heat and mass transfer
Non-linear scale-up	Linear scale-up
Extended processing times	Lower reaction time due to better temperature control
Large footprint – high costs and large volumes of solvent used	Reduced footprint – lower costs and lower volumes of solvent used

There are various platforms designed to facilitate continuous crystallisation. A STR can be adapted to a single-stage mixed-suspension, mixed-product removal (MSMPR) crystalliser in which a feed solution or suspension is continuously fed into the vessel at the same rate at which the product suspension is withdrawn. The suspension of solids inside the vessel is well-mixed such that the composition is the same throughout. Therefore, product suspension has the same attributes as the suspension inside the volume of the crystalliser at the time of withdrawal, which can be described as unclassified withdrawal.[9] MSMPR crystallisers can also be operated periodically which involves periodic solution addition and withdrawal of product slurry rather than continuous withdrawal.[78,79] This allows for an equilibrium period in which no addition or withdrawal of

solution or slurry occurs and the suspension remains in the agitated vessel for a specific residence time. Additional vessels can also be included in the set-up and assembled in series (multi-stage MSMPR) in order to increase residence time (total time spent within the crystalliser) within the system. However, use of additional vessels increases inventory and running costs.[5]

Continuous crystallisation can also be achieved using tubular flow platforms. One example is the continuous oscillatory baffled crystalliser (COBC) developed by NiTech Solutions.[80] The COBC (Figure 1.15) is a jacketed tubular crystalliser containing equally spaced baffled cells in which oscillatory motion is superimposed on the net flow.[5]

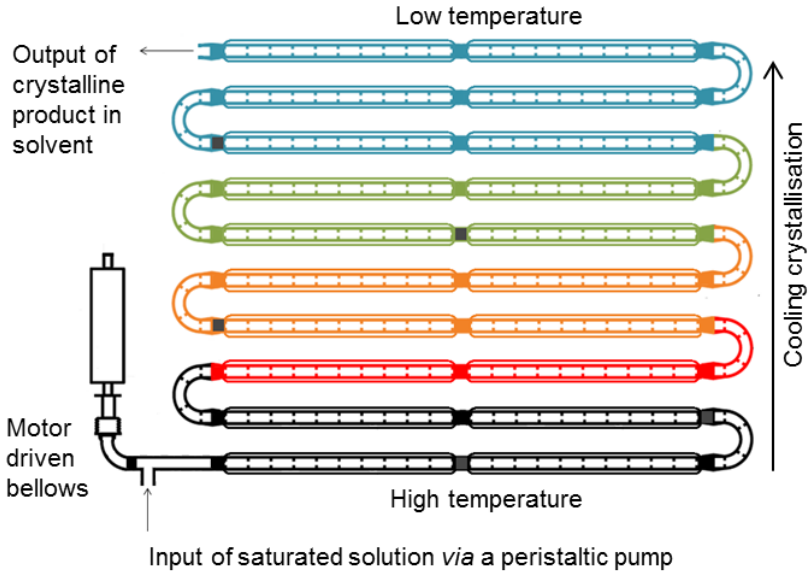

Figure 1.15 - Schematic of the COBC platform in the Wilson group laboratory at the University of Bath.

A saturated solution is pumped into the system and supersaturation is generated by cooling through a temperature gradient along the length of the crystalliser. The tubing jackets allow for improved heat transfer and temperature control within the system compared to the MSMPR platform. Mixing is facilitated through the generation of eddies which result from the interaction of the flow with the baffles inside the crystalliser tubing. This results in uniform mixing within each cell and under optimised conditions, operation at plug flow at flows that would normally result in laminar flow in the absence of restrictions.[5] In plug flow, the velocity of all the components in the tube is equal to the incoming flow ensuring uniform mixing in the radial direction and equal residence time for all components[81] (Figure 1.16). Operation close to plug flow offers the benefit of uniform mixing and a highly reliable environment for the formation of crystals with consistent

properties. There is also potential for real-time monitoring of the crystallisation in the COBC, *via* ports that allow for in-line measurements using process analytical technologies (PAT). The COBC is described in more detail in Chapter 5.

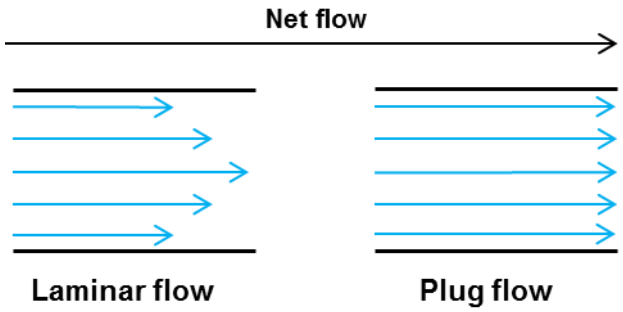

Figure 1.16 - Diagram showing the difference between laminar and plug flow; blue arrows indicate net movement of components within a tubular flow crystalliser.

Other smaller scale tubular platforms are also being explored such as micro and mesoscale reactors. Microfluidic reactors offer the benefit of excellent heat and mass transfer due to their small internal diameters. However, one of the drawbacks of operating at this scale is the risk of sedimentation and blockages of the micrometre-sized channels.[82] Mesoscale flow reactors operate at slightly larger internal diameters; some of which exploit segmented flow which creates individual segments of solution separated by air or a carrier fluid. This allows for each segment to act like a micro-batch reactor for crystallisation to occur under good mixing conditions through the generation of an internal fluid vortex within each segment. One example of a mesoscale platform is the KRAIC (Kinetically Regulated Automated Input Crystalliser) developed at the University of Bath which uses segmented flow to facilitate near plug flow conditions. A more detailed description of the KRAIC platform is presented in Chapter 5.

Despite the benefits of a continuous mode of operation, uptake in the pharmaceutical industry has been slow.[75] There are several challenges related to this inertia to change. Batch methods of operation have been used for many years and there is less process understanding regarding the use of continuous crystallisation methods; development of a process would therefore take more time and it would be perceived as higher risk. Furthermore, there is significant batch capability worldwide as well as a need to get new products to market as quickly as possible, while in some well-established processes there would be limited benefit from transfer to continuous modes of operation. However, as pharmaceutical companies are seeing low approval rates for new molecular entities,[83] there is increased focus on maximising revenue from existing portfolios of APIs, by

reducing manufacturing inefficiencies whilst maintaining high product quality.[84] Additionally, continuous manufacturing processes are well suited to facilitating the concept of personalised medicines.

The pharmaceutical industry is strictly regulated and evidence is required for traceability of materials in continuous processes whereby in a batch operation, the existence of a batch simplifies quality control.[11] However, the use of process analytical technologies (PAT) and employing the methodologies of Quality by Design, where quality is monitored on a continuous basis rather than on a post-production batch basis, are also key drivers in overcoming some of these barriers and decreasing the possibility of batch recalls.[85]

The balance between nucleation and growth is critical in the design of a crystallisation process and has significant implications for e.g. the residence time of the crystallising system within a continuous crystallisation reactor. It is important to note that the crystallisation platform is selected based on the process required. This may depend on factors such as the nature of the substance and the quantity required as well as its crystallisation kinetics. In some cases, continuous modes of operation are not always suitable and crystallisation processes may be better suited to a batch mode of operation.

The aim of research in the Centre for Innovative Manufacturing in Continuous Manufacturing and Crystallisation (CMAC) is to explore to what extent continuous technologies in crystallisation can give precise control over production of a specific solid form and to do so consistently and at the required scale for a manufacturing process.

1.4 Crystal engineering

The design of organic solids is known as crystal engineering, and represents a relatively new area in chemistry. Desiraju defines crystal engineering as *"the understanding of intermolecular interactions in the context of crystal packing and in the utilisation of such understanding in the design of new solids with desired physical and chemical properties".*[86] Crystal engineering relies on knowledge of the intermolecular interactions holding crystalline solids together (see Section 1.5, below).

Unlike synthetic chemistry involving making and breaking covalent bonds, when studying crystal engineering, the nature of non-covalent interactions holding molecules together in the solid state are considered. Hydrogen bonding is frequently exploited in crystal engineering due to its strong, directional and, to some extent, predictable nature.

Hydrogen bonds also have the ability to act cooperatively, forming multiple bonds simultaneously.[87] However, in crystal engineering, there are challenges in predicting where hydrogen bonds will form when a system contains multiple hydrogen bond donor and acceptor sites.[88] Repetitive molecular recognition patterns adopted by certain functional groups, or supramolecular synthons,[89] can be identified and those robust enough to make predictions about the self-assembly of molecules in the solid state are desirable.[90] A method of describing such motifs named graph set notation was devised by Etter and co-workers[88] (Figure 1.17) where G is a letter describing the type of hydrogen bonding pattern such as chains (C), non-cyclic dimers (D), rings (R) or intramolecular bonds (S). For example, a particularly abundant motif adopted in crystal structures is the hydrogen bonded carboxylic acid dimer (Figure 1.17). The cooperative nature of the hydrogen bonds and the stability of the interaction being insensitive to the nature of the rest of the molecule makes this motif (with graph set notation $R_2^2(8)$) highly favourable in crystal structures of molecules containing this moiety.[86]

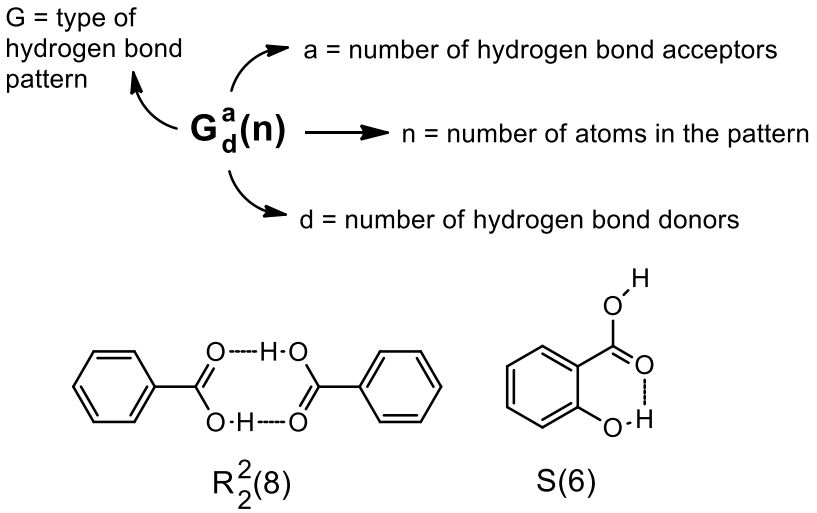

Figure 1.17 - Diagram describing graph set notation and two examples of its application, (left) a carboxylic acid dimer and (right) an intramolecular hydrogen bond.

By studying the complementarities between functional groups in a competitive environment, crystal engineering aims to encourage, by choice of an appropriate co-former molecule, the self-assembly of the desired solid form with specific interactions to yield specific properties.

1.5 Intermolecular interactions

Crystalline materials are held together by non-covalent interactions of varying strengths. A detailed understanding of hydrogen bonding and other intermolecular interactions is required in order to apply crystal engineering principles to the design of new solid forms.[10,90]

1.5.1 Hydrogen bonding

Hydrogen bonding is the dominant intermolecular interaction in many molecular systems and has been studied for over 100 years.[91] In his book, *The nature of the chemical bond*, Pauling stated that "*under certain conditions an atom of hydrogen is attracted by rather strong forces to two atoms, instead of only one, so that it may be considered to be acting as a bond between them*".[92] He later deduced that the interaction had to be electrostatic in nature since "*the hydrogen atom, with only one stable orbital, cannot form more than one pure covalent bond*". Pauling made the assumption that only if X and A are very electronegative, in an X-H···A interaction, would the partial positive charge on hydrogen, and the electrostatic attraction between H and A, be high enough to term the interaction a hydrogen bond. This suggested that hydrogen bonds are formed only between the most electronegative atoms such as N, O and F.[93]

In contrast, Pimentel and McClellan (1960) stated that "*a hydrogen bond exists between the functional group, X-H, and an atom or a group of atoms, A, in the same or different molecules when (a) there is evidence of bond formation, (b) there is evidence that this new bond linking X-H and A specifically involves a hydrogen atom already bonded to X*"[94] This definition makes no assumption about the nature of A and X and allows consideration of the hydrogen bonding potential of other groups. For example, C-H, where X (equal to C in this case) is less electronegative than N, O and F but still remains more electronegative than hydrogen.[93]

More recently, IUPAC defined a hydrogen bond as "*an attractive interaction between a hydrogen atom from a molecule or a molecular fragment X–H in which X is more electronegative than H, and an atom or a group of atoms in the same or a different molecule, in which there is evidence of bond formation".*[95] Other than electronegativity, this definition puts no restriction on X or A since there is evidence for many different types of acceptor and donor groups.

Hydrogen bonds can vary in strength and can be classified in terms of the bond distance between donor and acceptor atoms as outlined by Jeffrey[87] (Table 1.2).

Table 1.2 - Properties of strong, moderate and weak hydrogen bonds.

	Strong	**Moderate**	**Weak**
A-H···B interaction	Mostly covalent	Mostly electrostatic	Electrostatic
Bond lengths	A-H ≈ H···B	A-H < H···B	A-H << H···B
H···B (Å)	~1.2 - 2.5	~1.5 - 2.2	2.2 - 3.2
A···B (Å)	2.2 - 2.5	2.5 - 3.2	3.2 - 4.0
Bond angles (°)	175 - 180	130 – 180	90 - 150
Bond energy (kcal mol^{-1})	14 - 40	4 – 15	<4

As well as forming interactions between molecules, intramolecular hydrogen bonds can also form between donor and acceptor groups of the same molecule depending on their geometry in relation to one another.[93] This can alter the conformation of the molecule and thus affect its molecular packing. While hydrogen bonds commonly feature a single donor atom and acceptor atom, termed two-centre interactions, it is also possible for hydrogen bonds to arrange themselves in bifurcated or three-centred hydrogen bonds. These interactions involve one donor atom and two acceptor atoms or two donor atoms and one acceptor atom (Figure 1.18).[87,93]

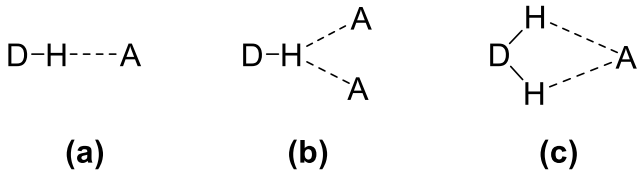

Figure 1.18 - (a) a two-centre hydrogen bond, (b) a bifurcated hydrogen bond with one donor atom and two acceptor atoms and (c) a bifurcated hydrogen bond with two donor atoms and one acceptor atom, where D is donor and A is acceptor.

1.5.2 π-π interactions

Structures that contain two or more aromatic rings that lie adjacent to one another often form interactions known as π-π interactions or π-stacking.[96] These interactions occur when attractive interactions between π-electrons and the σ-framework are more favourable than repulsions between π-electrons. One example of their existence is in the stacking of hydrogen bonded base pairs in DNA.[97] Neighbouring aromatic rings can arrange themselves in different geometries (Figure 1.19), each of which can lead to significant π-stacking interactions. The geometry of the interactions can be influenced by the substituents on the aromatic ring which alter the polarisation of the electron cloud. For example, the presence of an electron donating substituent on one of the rings will increase the π-electron density of the ring, resulting in increased repulsion.[98]

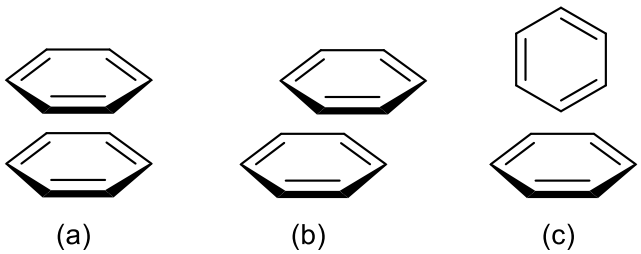

Figure 1.19 - (a) face-to-face π-stacking, (b) offset π-stacking, (c) edge -on or T-shaped π-stacking.

1.5.3 Weak interactions

IUPAC defines van der Waals interactions as "*the attractive or repulsive forces between molecular entities (or between groups within the same molecular entity) other than those due to bond formation or to the electrostatic interaction of ions with one another or with neutral molecules*".[99] Van der Waals forces are relatively weak interactions in comparison to hydrogen bonds. The term broadly describes several types of weak interaction differing in the polarisability of the interacting entities. These include Keesom interactions, dipole-induced-dipole interactions and dispersion interactions.

Keesom or dipole-dipole interactions represent the interaction between two polar molecules and are reliant upon the orientation and distance of the two molecular entities. A polar molecule can also induce a dipole in a neighbouring non-polar molecule in a dipole-induced-dipole interaction. The presence of a nearby molecule with a permanent dipole induces polarity of the electron cloud of the non-polar molecule.[97] In dispersion or London interactions, neighbouring non-polar molecules may attract one another as a result of small transient dipoles induced in each other.[100] Although neither of the molecules possess a permanent dipole moment, variations in the instantaneous positions of their electrons results in attractive interactions between the two dipoles and a lowering of the potential energy of the pair.[97]

Knowledge of these intermolecular interactions allows approaches such as crystal engineering to be used as a means of potentially predicting the ways in which molecules will link together in forming crystalline solids. The principles of crystal engineering, and the harnessing of intermolecular interactions such as the hydrogen bond, are used implicitly throughout this work in producing various crystalline multi-component molecular complexes.

1.6 Types of crystalline solids

Crystalline solids can exist in several different forms as outlined in Figure 1.20.

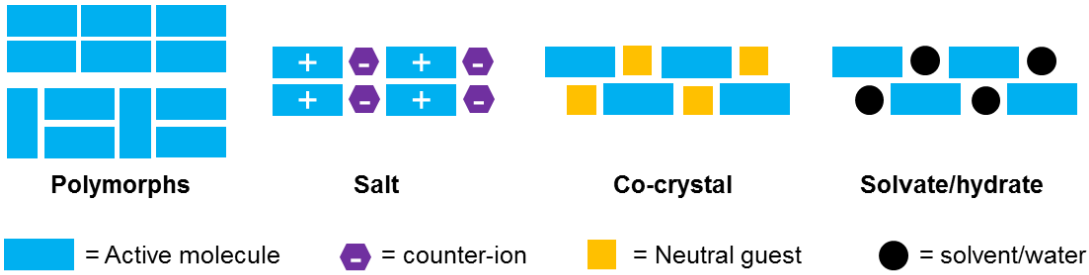

Figure 1.20 - Illustration of possible crystalline solid forms: polymorphs, salt, co-crystal, solvate/hydrate.

1.6.1 Polymorphism

It is common for crystalline solids to exhibit polymorphism, in which the same component can adopt different packing arrangements forming different crystalline forms. McCrone defines a polymorph as "*a solid crystalline phase of a given compound resulting from the possibility of at least two different arrangements of the molecules of that compound in the solid state*".[101,102] As a result of the variation in the structural arrangement of molecules owing to the different intermolecular interactions present, polymorphs may possess different physical properties such as melting point, solubility and hardness.[96]

A well-known example of polymorphism in a pharmaceutical material is that of paracetamol which exists in at least three polymorphic forms, of which two are the most common (Figure 1.21).

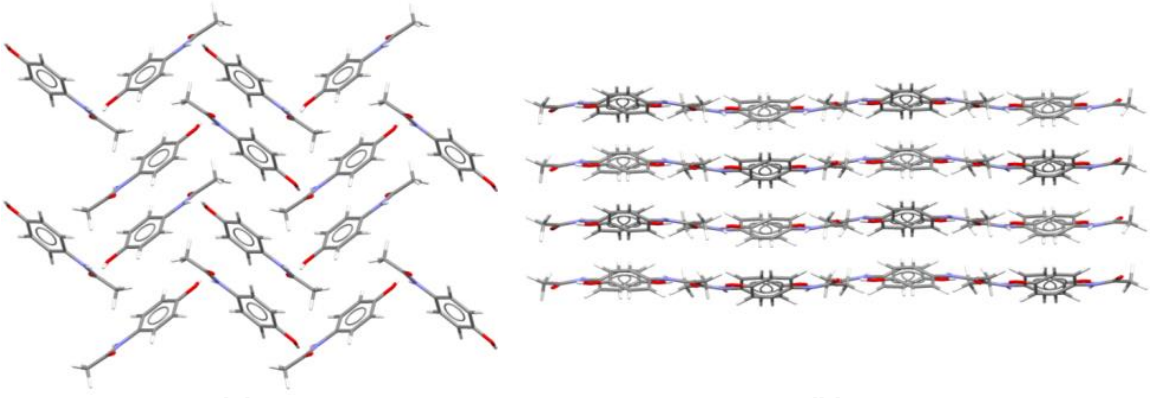

Figure 1.21 - Crystal packing in two polymorphs of paracetamol: (a) herringbone form I viewed down the crystallographic *a* axis, (b) layered form II viewed down the crystallographic *b* axis.

In form I the molecules pack in a herringbone arrangement whereas in form II the molecules pack in slipped layers; paracetamol is therefore an example of packing polymorphism. The ability of the molecules in the metastable form II to pack in layers allows this form to be more easily compressed into tablets than form I,[103] while also being more soluble.[46]

In the pharmaceutical industry, understanding polymorphism is essential when developing a new compound and high throughput polymorph screening is usually carried out utilising a range of crystallisation methods. Identification of the most stable form is important in order to avoid unexpected phase transitions during production or storage. One of the most well-known examples of the unexpected emergence of a new form is the case of the anti-retroviral compound, Ritonavir demonstrating the importance of solid form selection. Only one crystal form was initially identified and semi-solid capsules of the drug were produced and sold as Norvir, an effective treatment for HIV sufferers. However, two years later a new polymorph, form II, emerged following dissolution testing. As a result of its increased thermodynamic stability, form II had greatly reduced solubility compared to form I, with its enhanced stability causing difficulties in reproducing the more soluble metastable form I polymorph in production processes. Consequently, the drug was withdrawn from the market and it was necessary to reformulate Norvir. These factors resulted in huge losses of profit as well as threatening the supply of the treatment to the patients.[104] This case is an example of conformational polymorphism in which compounds with conformationally flexible groups crystallise as distinct polymorphs. Conformational polymorphism can also be observed in the fenamic acid family of non-steroidal anti-inflammatory drugs.[105-107]

1.6.1.1 Thermodynamics of polymorphism

The relative stability of a substance is governed by its free energy whereby the more stable substance has a lower free energy. In the case of polymorphism, the polymorph with the lowest free energy under defined conditions is the most thermodynamically stable form and other forms are known as metastable forms.[108,109] Ostwald's Law of Stages states that the least stable polymorph will nucleate first. Although kinetic factors may delay or prevent the transformation, less stable forms will be thermodynamically driven to transform into the most stable form.[108] In some cases, solution-mediated phase transitions mean that the unstable phase may have converted to a more stable form prior to sampling and characterisation.[3] Such transformation can sometimes be observed using *in situ* process analytical technologies (PAT) such as Raman Spectroscopy.

The thermodynamic behaviour of polymorphs can be described as enantiotropic or monotropic and these can be explained using energy-temperature diagrams as shown in Figure 1.22.[14]

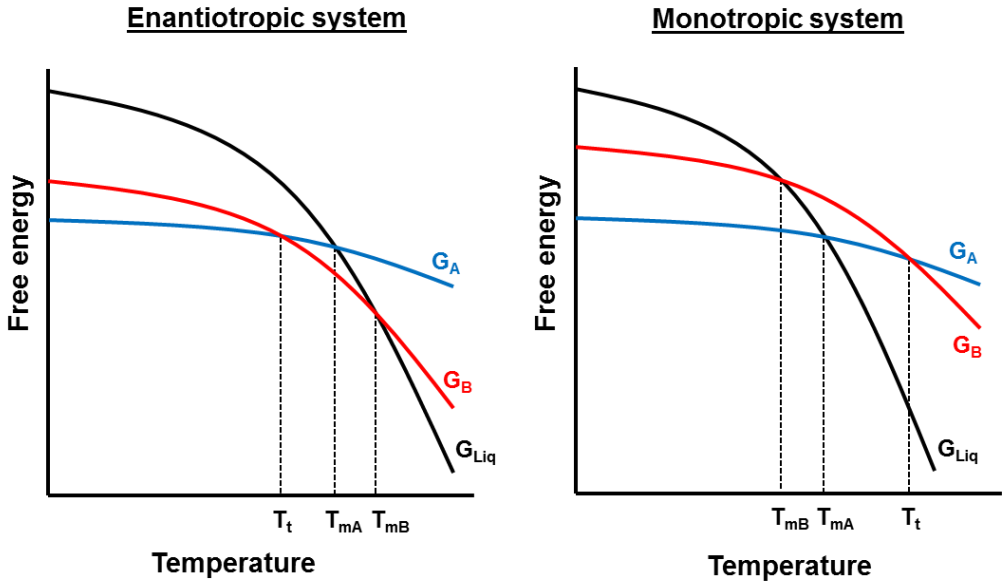

Figure 1.22 - Energy-temperature plots for enantiotropic and monotropic systems, where G is the free energy, T is the temperature, A, B and Liq refer to polymorphs A, B and the liquid phase and T_m and T_t refer to melting and transition point, respectively.

Polymorphs are described as enantiotropic if the isobars of the two forms cross before crossing the isobar of the liquid phase. This results in a transition point where the polymorphs can undergo a reversible solid-state transition. At this transition point the free energies of the polymorphs are equal. Beyond the temperature of the transition point the isobar of the more stable polymorph B crosses the free energy isobar of the liquid and melting is observed. In the case of a monotropic relationship between polymorphs, polymorph A is more stable below the melting point of both polymorphs and so in this case the liquid isobar crosses the isobars of the solid forms before they cross each other. This means that the forms melt before they interconvert. It is important to identify whether a system displays enantiotropic or monotropic behaviour since it will affect processing decisions. If a polymorph is known to convert to a more stable form at low temperatures, this may affect the design of the crystallisation.[14,109]

Enantiotropism and monotropism can also be related to the solubility of polymorphs; the solubility curves of the two solid forms cross in an enantiotropic system while they do not in a monotropic system (Figure 1.23). The temperature at which the solubility curves cross represents the temperature at which the phase transition occurs. In the monotropic

case the solubility curves do not cross and polymorph A is metastable with respect to polymorph B as shown in Figure 1.23. As a result polymorph A is more soluble than polymorph B.

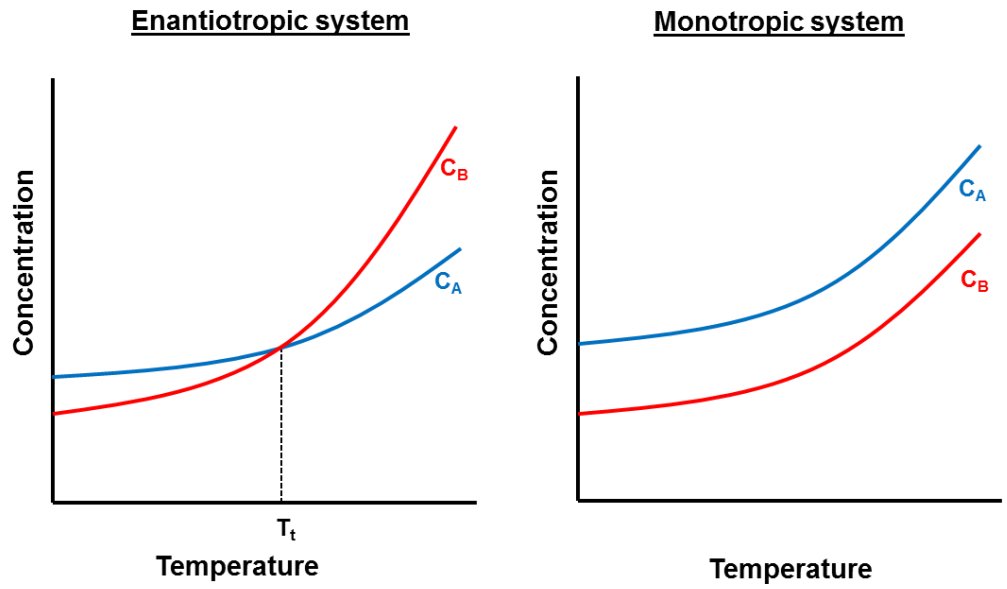

Figure 1.23 - Solubility curves of two polymorphs of a substance with respect to temperature in an enantiotropic system (curves cross) and a monotropic system (curves do not cross).

1.6.2 Co-crystallisation

Crystallisation is not restricted to single-component systems and a range of multi-component solid-state systems can be prepared. A co-crystal can be described as a multiple-component system in which two distinct molecular components combine, usually *via* hydrogen bonded interactions, in their neutral forms.[110] In these systems, the driving force for co-crystallisation is the formation of stronger hydrogen bonds between the two different components than hydrogen bonds in the individual single component systems.[110] As the molecular arrangement within the solid state plays a decisive role in the physical properties of a crystalline material, the presence of a second component in the crystal structure may lead to changes in the physical properties of the material.

Co-crystals have become of interest in the pharmaceutical industry in recent years. Pharmaceutical materials are commonly manufactured in their crystalline form for stability and ease of characterisation. However, due to their ordered nature, crystalline forms are often less soluble than amorphous forms. Typically, drug molecules contain multiple hydrogen bond donor and acceptor groups so have high affinity for co-crystallisation with suitable co-former molecules with similar groups. Co-crystallisation of pharmaceutical materials is particularly desirable if it results in improved physical properties, such as

solubility and compressibility, when compared to the parent drug.[110,111] Such improved properties come without compromising the structural integrity of the active pharmaceutical ingredient and may lead to improved bioavailability.[112] However, preparation of systems in a multi-component environment can lead to challenges in isolating the desired solid form; as such crystallisation can sometimes yield a mixed-phase product.

1.6.3 Salts

As well as incorporation of a guest molecule or co-former in this way, the formation of multi-component systems in the form of a salt may also be possible if the target material contains acidic or basic groups. A salt forms when a proton is transferred from one molecule to another. The likelihood of proton transfer occurring can be determined using the difference in the pK_a values of the acid and base components of the molecules as a guide. Proton transfer is likely to occur if ΔpK_a is greater than or equal to three where $\Delta pK_a = pK_a$ (base) – pK_a (acid). If the ΔpK_a is less than or equal to zero, a co-crystal may be expected to form. Within the intermediate region between zero and three, known as the salt-co-crystal continuum, it is difficult to predict whether a salt or neutral complex will form.[113,114]

In the pharmaceutical industry salt formation is often investigated if a compound does not crystallise or displays poor physical properties such as solubility. Many pharmaceutical ingredients are thus manufactured as salts as a result of access to improved physicochemical properties without affecting the chemical effect of the drug.[114] For example, ibuprofen lysine (marketed as, for example, Advil® and Nurofen®) is used for the treatment of the same conditions as ibuprofen. However, the lysine salt increases the water solubility of ibuprofen allowing for more rapid absorption by the body and subsequent onset of action and as a result is commonly used to treat migraines.

1.6.4 Solvates and hydrates

It is common for crystalline materials to incorporate solvent into their crystal lattice to form solvates, or hydrates in the case of incorporation of water. Identifying the ability of a potential active ingredient to form such so-called pseudopolymorphs is of practical importance in the process of manufacturing new substances. Hydrates may offer different properties to their anhydrous counterparts and although solvate formation is usually considered undesirable, especially in pharmaceutical materials, desolvation can sometimes enable access to new polymorphic forms.[115,116]

1.6.5 Crystalline defects

An important structural attribute in crystalline materials is the presence of defects in a crystal. In an ideal crystal structure (see Chapter 2), every asymmetric unit is equivalent and all of the unit cells are identical, but in a real system this is never the case and defects can be present. One type of crystal defect known as structural disorder occurs when a whole molecule, or parts of a molecule, in the structure adopt different orientations in different unit cells of the crystal. As the crystal structure shows the average asymmetric unit, the disorder is modelled as partially occupied sites representing two or more orientations of the molecule or part of the molecule.[96,117] Put simply, IUPAC defines structural disorder as "*any deviation from the ideal three-dimensional regularity of the crystal structure*".[99] Disorder is most commonly observed in molecules that have symmetry, enabling them to take on multiple orientations or, as in polymorphism, in molecules with conformationally flexible groups of atoms. In the latter case, the molecule in the crystal structure lies partially in either conformation, for example in the crystal structure of salicylsalicylic acid.[96,118] In this example, the hydroxyl group of the molecule occupies one *ortho* position in 72% of the molecules and the other *ortho* position in 28% of the molecules, as a result of the conformational flexibility of the phenol ring (Figure 1.24).[119]

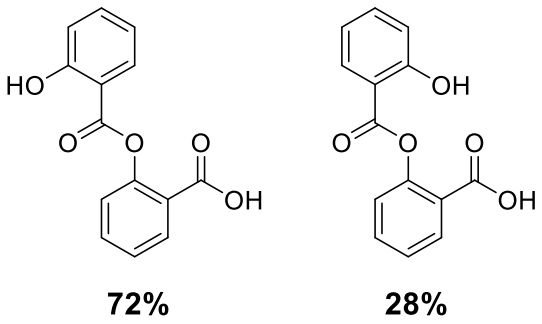

Figure 1.24 - The two *ortho* positions of the hydroxyl group in the disordered structure of salicylsalicylic acid with their relative occupancy of disorder.

Disorder can be divided into two categories known as static or dynamic disorder. Static disorder occurs when a molecule or part of a molecule occurs in one orientation or position in some unit cells and in another in other unit cells (as observed in the case of salicylsalicylic acid shown above). The amount of occupancy for each position is usually determined based on the distribution of electron density. Dynamic disorder occurs when the molecule or part of the molecule is constantly undergoing flux. This typically occurs in solvent molecules or alkyl chains.[96] Static and dynamic disorder can be distinguished by comparing the X-ray thermal parameters for collections carried out at different

temperatures as large amplitudes of vibration observed in dynamic disorder can be reduced by cooling the sample to lower temperatures.[117,118]

In some cases, the line between polymorphism and structural variation due to disorder is blurred. There are several examples in the literature that show disorder mistaken for polymorphism. In the case of eniluracil,[120] differences in PXRD patterns of different crystalline samples were first interpreted as polymorphism. Two different PXRD studies produced crystal structures with different relative positions of bonds in the molecule. It was found that the solid forms were more accurately described in terms of different degrees of disorder rather than polymorphism after single crystal X-ray diffraction (scXRD) data were collected using different single crystals prepared using different crystallisation conditions.

Disorder may have similar implications to polymorphism in product development. Disordered compounds with varying degrees of disordered components may display different physiochemical properties; resulting in batch to batch variations in many particle attributes of the bulk sample.[118] Poor understanding of this phenomenon may have accounted for problems in developing a robust production process for eniluracil.[120] Therefore, identifying disorder may be fundamental for relating the structures to their bulk properties as well as the manufacturing properties and processability.[121,122] However, there is limited literature on the link between crystalline disorder and the physical properties of organic solids.

1.7 Research scope

The underlying theme of the research presented in this thesis is the investigation of methods to alter physicochemical and bulk particle properties of organic solid forms through introducing a second component into the crystallisation (Figure 1.25). Alongside the material property modification, the work aims to investigate the production of such systems in both batch and continuous crystallisation environments in the context of the EPSRC Doctoral Training Centre for Innovative Manufacturing in Continuous Manufacturing and Crystallisation (CMAC).

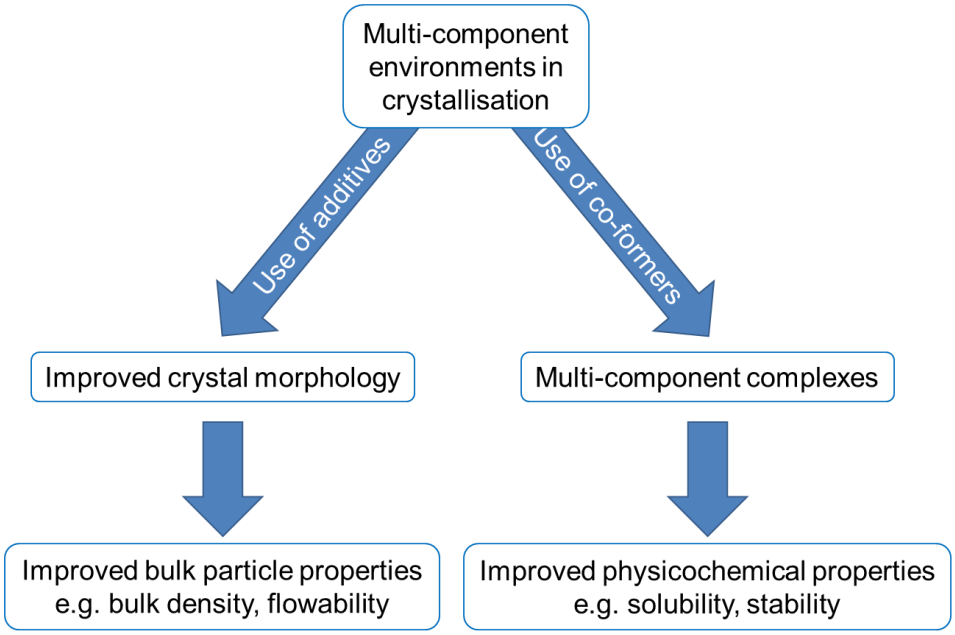

Figure 1.25 - Two types of multi-component environment in crystallisation explored in this work in seeking to improve properties of organic solid forms.

The way in which molecules are arranged in the solid-state can affect the physicochemical properties of the substance as well as the overall shape (morphology) adopted by the crystals of the solid material, which will affect its bulk particle properties. Both can be affected by the presence of a second component in the crystallisation. A second component (additive) may affect growth of the single-component structure of the target material by forming interactions with certain faces of the growing crystal. This slows down the growth rate of the specific faces and consequently results in an altered overall morphology of the crystal, which may in turn affect the bulk particle properties such as flowability and bulk density. Alternatively, often if present in larger quantities, a second component (co-former) may interact favourably with the target material at the molecular level, for example through intermolecular hydrogen bonding interactions, and become incorporated into the structure. This results in nucleation and growth of a multi-

component complex which may have different physiochemical properties to the single component structure.

1.8 Thesis outline

The research described in this thesis can be grouped into three main strands:

(i) Investigation of the use of additives in crystallisation to alter crystal morphology and the implementation of such systems for production in the continuous environment (Chapters 4-6). Two systems were studied in this work. Succinic acid was selected as a model system with a plate-like morphology suggested as an interesting system by industrial partners. Secondly, isoniazid was selected as a pharmaceutically relevant substance which showed a poor morphology in terms of particle properties.

(ii) Molecular-level investigations towards altering the physicochemical properties of a substance through the production of multi-component complexes (Chapter 7). The work, using the principles of crystal engineering targeted the production of disordered or layered solid forms as these attributes may introduce desired properties such as improved compressibility or enhanced solubility. Piroxicam was studied as prior work had shown the potential for this API to form solid forms displaying such structural attributes.

(iii) In order to understand further the phenomenon of molecular disorder, a single-component model system known to display disorder was studied. The level of orientational disorder in 5-chlorouracil was investigated with respect to the crystallisation conditions (Chapter 8). This understanding aimed to aid further studies into controlling disorder as a potentially important parameter in physical property optimisation.

Chapter 2

Theory of analytical methods

The work presented in this thesis has been carried out using a range of analytical methods, for characterisation of solid products of crystallisation experiments. Techniques used include a range of microscopies, crystallography, thermal analysis and spectroscopy. For the more detailed crystallisation studies carried out, *in situ* Process Analytical Technologies (PAT) were also used, which include a range of spectroscopies and light scattering methods. This chapter provides the theory behind the key analytical methods used.

2.1 Microscopy

2.1.1 Optical Microscopy

Optical microscopy is a useful tool in support of other analytical techniques in solid-state chemistry; in the present work it has been used to examine the crystalline products of experiments. An optical microscope fitted with polarising lenses can be used to determine the crystallinity of a sample, observe the crystal morphology and assess the suitability of crystalline samples for X-ray diffraction. When viewed under polarising light, single crystals extinguish, becoming darker when rotated. Optical microscopy is also useful for observing the morphology, colour and size of crystals. In materials discovery, the crystal morphology can provide visual indication as to whether a crystal is a known solid form, if it has a distinct shape and size. Likewise a change in colour can indicate the formation of a previously unknown complex.

2.1.2 Scanning Electron Microscopy (SEM)

A scanning electron microscope is an instrument that can be used to obtain a more detailed image of a substance than optical microscopy, employing an electron beam

rather than light to illuminate the sample. In SEM, the sample is exposed to a focused beam of electrons resulting in ejection of electrons or X-rays from the sample which are detected and converted to a signal to produce an image. In this work, the images were produced from detection of secondary electrons, weakly bound electrons of atoms on the surface of the sample ejected upon impact of the SEM electron beam. As secondary electrons are ejected from the surface of the sample, their detection allows visualisation of the crystal morphology and surface structure. Samples for SEM must not contain any water since the instrument operates under vacuum. Furthermore, non-metallic samples must be pre-coated with a thin layer of a conductive substance such as gold or chrome using a sputter coater. This is to prevent the sample accumulating charge when scanned by the electron beam and to increase the surface resolution.[123]

2.2 Crystallography

2.2.1 The crystalline state

A crystalline solid consists of a periodic arrangement of matter repeated in all directions giving rise to a highly ordered structure exhibiting long range order.[2,96,117] IUPAC defines crystallinity as *"the presence of three-dimensional order on the level of atomic dimensions".*[99]

If each structural unit in the regular array is represented by just a single point, a pattern of points all with the same surrounding environment can be generated. These points are named lattice points and the regular array of equivalent points is termed the lattice.[117] Linking up neighbouring lattice points in three-dimensions makes a volume which when repeated by translation, will produce the full three-dimensional crystal; this is termed the unit cell (Figure 2.1).

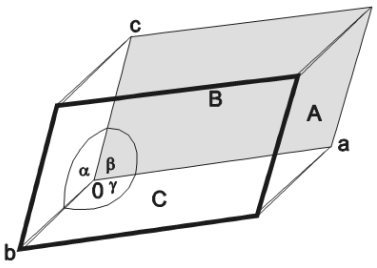

Figure 2.1 - The unit cell and definition of the unit cell parameters.[124]

There are multiple different choices possible for linking lattice points which gives rise to several possible shapes for the unit cell; however the unit cell with the highest internal symmetry is generally selected.[96] The unit cell represents the smallest repeating unit of

the three-dimensional crystal lattice and is described by unit cell parameters. These consist of three axes *a, b, c* and three angles *α, β, γ*. The lengths of the axes for organic compounds are generally of the order of 3 to 40 Å.[125]

In three-dimensional crystal structures, there are four different lattice types. The type of lattice depends on the position of the lattice points in the unit cell (Figure 2.2). The primitive (P) lattice type is the simplest with only one lattice point; therefore the only translational symmetry is that of the unit cell. The other lattice types, body centred (I), face centred (F) and centred (C), have additional lattice points contained within the unit cell volume, and thus show additional translational symmetry within the unit cell as well as the translational symmetry of the unit cell.[126]

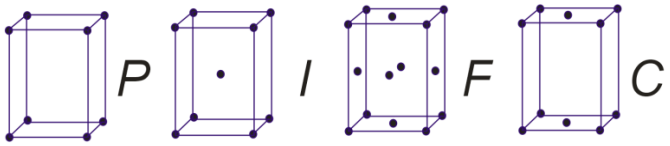

Figure 2.2 - Diagram showing the four lattice types.[124]

Assessing the possible symmetries for a lattice gives rise to seven possibilities for the shape of a unit cell; these are known as the seven crystal systems (Table 2.1).

Table 2.1 - The unit cell restrictions for each of the seven crystal systems and the distribution of the lattice types.

Crystal system	Unit cell parameters	Bravais lattice
Cubic	a=b=c α=β=γ=90°	P, I, F
Hexagonal	a=b≠c α=β=90° γ=120°	P
Trigonal	a=b≠c α=β=90° γ=120°	P
Tetragonal	a=b≠c α=β=γ=90°	P, I
Orthorhombic	a≠b≠c α=β=γ=90°	P, C, I, F
Monoclinic	a≠b≠c α= γ=90° β≠90°	P, C
Triclinic	a≠b≠c α≠β≠γ≠90°	P

The combination of the lattice type and the seven crystal systems forms the 14 Bravais lattices to one of which all crystal structures belong. It is worth noting that not all of the combinations give rise to a different Bravais lattice. This is as a result of there being an alternative description that would effectively describe the lattice as one that is already present in the 14 Bravais lattices.

2.2.2 Molecular symmetry

The unit cell can be reduced further to asymmetric units that are related by symmetry operations within the unit cell.[96] An asymmetric unit can be made up of several molecules, one molecule or part of a molecule depending on the symmetry present. There are multiple types of internal symmetry within the unit cell that are broadly described by two groups: non-translational and translational symmetry elements. Non-translational symmetry elements describe a form of rotation of the object. There are four types: the inversion centre, reflection, rotation and rotation-inversion. As the name suggests, translational symmetry elements are identified by a translation. There are two types: screw axis and glide plane, each combining two symmetry elements. A screw axis combines a translation followed by a rotation, while a glide plane describes a translation followed by a reflection. The combination of the symmetry elements with the Bravais lattice is expressed as the space group of the crystal. Considering the full range of lattices and internal symmetry elements yields a total of 230 possible space groups.

2.2.3 X-ray diffraction

As a result of their long range order, crystalline materials have the ability to diffract X-rays to produce regular patterns, which provides a wealth of structural information. Interatomic bond distances lie in the region of 0.8 - 3.0 Å which is comparable to the wavelength of X-rays enabling the contents of a crystal to be probed at the atomic level. In the laboratory, Cu or Mo are typically used as X-ray tube target anode materials, providing characteristic X-rays of wavelengths 1.5418 and 0.71073 Å, respectively, for use in diffraction experiments.[96,117,126]

In a diffraction experiment, a crystal is irradiated with X-rays and the interaction between the electrons in each atom and the incident X-ray beam causes the X-rays to diffract in all directions. The regularity of the crystalline structure gives rise to a diffraction pattern made up of distinct diffraction spots which is collected on an image plate or charge coupled device (CCD) detector.

2.2.4 Bragg's Law

W. L. Bragg studied the conditions at which diffraction is observed and considered diffraction as a reflection from sets of planes within the crystal. Diffraction occurs when an X-ray interacts with lattice planes known as Miller planes with a characteristic spacing, *d*. Miller planes refer to families of parallel planes that are described by Miller indices, a set of three integer values (*h k l*), the separation of which are termed d_{hkl}. The values represent the reciprocal of the intercepts of the plane with the crystallographic axes (a/*h*,

b/*k* and c/*l*) and are expressed as rational fractions. The path difference between the incident and diffracted X-rays can be calculated by considering X-rays reflected by two adjacent Miller planes separated by a distance of d_{hkl} (Figure 2.3). The path taken by the incident and diffracted beam is equal to the wavelength of the incoming X-ray beam, nλ and can be calculated as the sum of XY and YZ. If the angle of the incident beam to the *hkl* plane is θ, we can then calculate the path difference with respect to these terms (Figure 2.3).

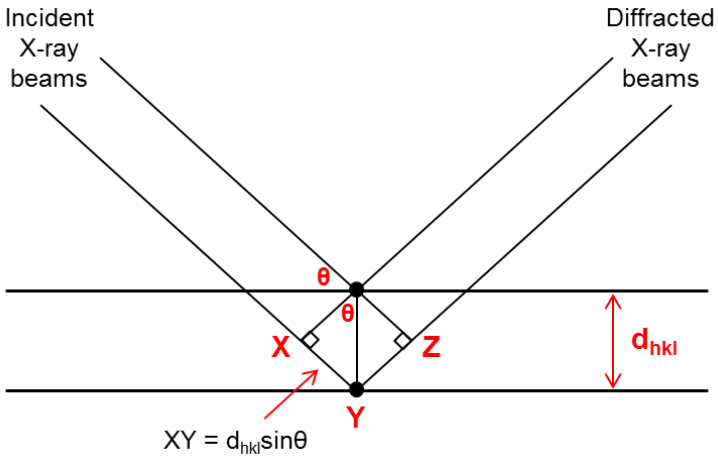

Figure 2.3 - Bragg's Law for diffraction of X-rays from a set of parallel Miller planes.

For constructive interference between these two beams to occur, this path difference must be equal to an integral number of wavelengths of the incident X-ray beam, nλ.[96] Therefore according to Bragg's Law, diffraction spots occur when the incident X-ray wavelength satisfies the Bragg equation, $2d\sin\theta = n\lambda$.

Each diffraction spot can thus be identified with an *hkl* value, since each spot represents diffraction from a specific Miller plane. During the data collection process, we measure the intensities, I_{hkl}, of the diffracted beam from each set of Miller planes (*hkl*). The frames of data that make up the diffraction pattern are processed to produce observed structure factor magnitudes, $|F_o\ (hkl)|$.[96]

Structure factors are a mathematical description of the interaction of the incident X-rays with the atoms in a crystal lattice and are affected by atomic scattering factors, f_j (Equation 2.2).[96] The f_j values account for the variation in scattering with the number of electrons in the atom and with the angle of scattering.[117] All atoms have different electron clouds and consequently interact differently with X-rays. At low Bragg angles the scattering power is proportional to the number of electrons, but the scattering reduces at

higher Bragg angles (Figure 2.4), as the scattering from different parts of the electron cloud become less constructive due to its finite extent. This occurs more slowly for atoms with more electrons, and this, combined with the dependence of atomic scattering on the number of electrons, makes it less easy to locate lighter atoms, such as hydrogen atoms, in the diffraction map.[96]

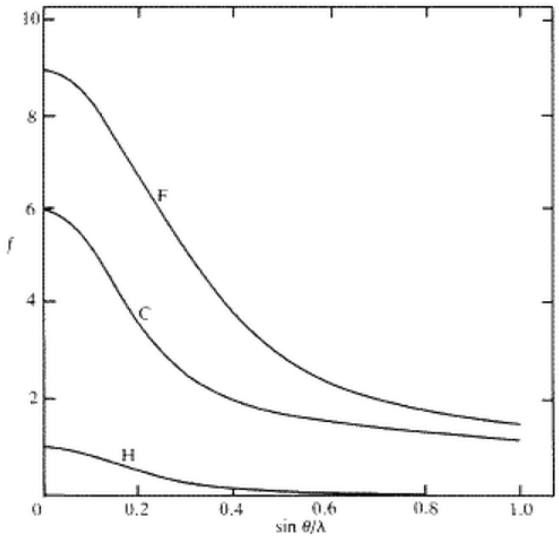

Figure 2.4 - Atomic scattering factors for hydrogen, carbon and fluorine, plotted against sinθ/λ.[127] The scattering factor for X-rays is related to the number of electrons in the scattering atom at sinθ/λ=0, then falls off with angle.

The intensity, I_{hkl}, is proportional to the structure factor squared and this relationship is used to produce experimental structure factor values for each reflection (Equation 2.1). The structure factors are needed to determine the distribution of electron density in the unit cell, through relations 2.1-2.3 below.[127]

$$I_{hkl}^{corr} \propto (F_{hkl}^{obs})^2$$

Equation 2.1

From the measured intensities, information is thus gained on the amplitude of the diffracted beam, however, the phase information cannot be determined, and this is needed in order to produce a three-dimensional image of the structure. This is known as the phase problem and is discussed below.

The structure factors are related to the atomic positions and scattering factors, and can be calculated for each reflection *hkl* using Equation 2.2; during structure determination,

structure factors calculated from the known atomic positions can thus be calculated and compared with their corresponding F_o value.[125]

$$F_{hkl} = \sum_{j=1}^{N} f_j \, exp\left[2\pi i(hx_j + ky_j + lz_j)\right]$$

Equation 2.2

The structure factor of each refection can also be related directly to the electron density at position (*x,y,z*) in the unit cell of the crystal structure by Fourier transformation[117] (Equation 2.3).

$$\rho_{xyz} = \frac{1}{V}\sum_{hkl} |F_{hkl}| . \exp[i\varphi_{hkl}] \, . \exp[-2\pi i(hx + ky + lz)]$$

Equation 2.3

The electron density, ρ_{xyz}, is expressed in units of electrons per cubic angstrom (e Å^{-3}), where *V* is the volume of the unit cell. All reflections in the diffraction pattern contribute to the electron density map. Evaluation of ρ_{xyz} shows the variation of electron density in the unit cell and the atoms will be located where the electron density is concentrated.[117] Once these atomic positions have been located, the phases of all the structure factors can be determined, but the problem remains that in order to calculate ρ_{xyz} from Equation 2.3, an initial set of phases for at least some of the reflections F_{hkl} must be obtained. There are several ways of achieving this, now largely automated in crystal structure analysis.

2.2.5 Structure solution

During structure solution, a molecular model must be obtained that will represent the contents of the crystal lattice. However, the phase information lost during the diffraction experiment must be regenerated in order to do this (by allowing the electron density to be evaluated through Equation 2.3). Two approaches, direct and Patterson methods, aim to overcome the phase problem and produce an initial set of estimated phases. Once such a solution is achieved, an initial electron density map is produced. If sufficiently accurate initial phase information has been generated, this provides a representation of the distribution of electron density that is sufficiently good to allow atomic positions to be identified. Various methods can then be used to improve and extend the number of phases available, leading to full structure determination and refinement.

2.2.5.1 Patterson methods

Patterson methods are commonly used for structures containing one atom or a small number of atoms that have significantly more electrons than the rest, named heavy atoms, so are often exploited in inorganic crystal structures. A Fourier transform of F_o^2 with all the phases set to equal zero produces a Patterson map[117] (Equation 2.4).

$$\rho_{uvw} = \frac{1}{V}\sum_{hkl}|F_{hkl}|^2.\exp[-2\pi i(hu + kv + lw)]$$

Equation 2.4

A Patterson map is a map that shows the vectors between pairs of atoms in the structure, including atoms paired with themselves and thus consists of peaks which show where atoms lie relative to one another, but not where they lie relative to the unit cell origin. Patterson peaks are proportional in size to the product of the atomic numbers of the pair of atoms. Consequently, large peaks that stand out on the map can be attributed to vectors involving heavy atoms in the structure. It is then possible to find a set of atom positions for the heavy atoms. The origin (0, 0, 0) will always correspond to the largest peak on the map as it is made up of the vectors of atoms paired to themselves which have zero length. The peak height will therefore, be proportional to the sum of the squares of the atomic numbers of all the atoms.[117,125] Once the heavy atoms have been found from a Patterson map, they can be used to obtain initial phases and the rest of the lighter atoms can be located in an iterative process using Equation 2.2 and Equation 2.3. Patterson methods are less appropriate for structures containing large numbers of atoms of equal atomic number as there are problems resolving overlapping peaks.

2.2.5.2 Direct methods

Direct methods are commonly used in small-molecule crystallography, often for crystal structures containing an organic molecule with no heavy atoms. However, as methods have become more advanced these increasingly automated methods have been used to solve more complex structures.[96]

Structure solution using direct methods exploits phase relationships between the intensities of various observed reflections in order to overcome the phase problem.[125] The initial strategy is based on a trial-and-error method which involves using normalised structure factors to ensure reflections measured at different θ values can be compared directly. Phases are then estimated for some of the strongest reflections (usually in a

parallel multiple solution method where sets of trial phases are assigned to reflections) and probable relationships between phases calculated. Constraints put restrictions on possible values for phases. These include that the value of electron density must never be negative and that the electron density maps must have high values at and near atomic positions but values close to zero elsewhere. The most probable phase set is then used to calculate an electron density map using a Fourier transform. The electron density map can then be examined and initial atom positions can be determined based on recognisable molecular features; these are used to generate an initial full set of estimated phases and the remainder of the atoms located in an iterative procedure using Equation 2.2 and Equation 2.3. Once a structure has been solved it can be carried through the refinement process.[96,117]

2.2.6 Structure refinement

The most common method used to refine a crystal structure is the method of least squares.[125] This method is used statistically to determine the fit between a model and the experimentally obtained data, with a specific value of certainty. In terms of crystal structure refinement, this provides a quantitative value as to the agreement between the structural model obtained during structure solution and the experimental diffraction dataset.[96]

During the refinement process, the positions of the atoms and associated displacement parameters are optimised through an iterative process of fitting against the experimental data. This enables better agreement between the calculated structure factors and the observed structure factors. This is monitored by a residual index known as the R-value or R-factor (Equation 2.5).

$$R_1 = \frac{\sum \left| \left| F^{\mathrm{calc}} \right| - \left| F^{\mathrm{obs}} \right| \right|}{\sum |F^{\mathrm{obs}}|}$$

Equation 2.5

The R-value is therefore related to the differences between the calculated and observed structure factor magnitudes and so the lower the R-value, the better the fit between the structural model and the experimental dataset. This provides an indication as to whether the refinements have reached convergence in which the structural model is at its best fit with the experimental data. Expected values for a good refinement lie in the region of 0.05-0.08.[96]

A weighted R-value is also calculated and reported which is often higher than the R-value, as it is based on the square of the structure factors and takes into account the errors in the diffraction experiment (Equation 2.6).

$$wR_2 = \sqrt{\frac{\sum w(F_{obs}^2 - F_{calc}^2)^2}{\sum w(F_{obs}^2)^2}}$$

Equation 2.6

Another statistical measure used to measure the quality of refinement is the goodness-of-fit (GOOF) (Equation 2.7; n = number of reflections and p = number of parameters). The GOOF of the structure, *S*, when refined to convergence should have a value close to 1.

$$S = \sqrt{\frac{\sum w(F_{obs}^2 - F_{calc}^2)^2}{n - p}}$$

Equation 2.7

2.2.7 Powder X-ray diffraction (PXRD)

Crystals large enough for single crystal X-ray diffraction are not always present in the products of a crystallisation experiment; often a polycrystalline powder is formed from which a PXRD pattern can be obtained. PXRD is therefore frequently used as a fingerprinting tool to determine the composition of a sample.

In a single crystal X-ray diffraction experiment, a complete diffraction pattern is obtained from one single crystal through measuring diffraction from the crystal as it adopts various orientations when rotated in the X-ray beam. In contrast, in a PXRD experiment the polycrystalline powder contains a large number of small, single crystallites lying in random orientations. Upon exposure to the sample the X-ray beam will therefore be diffracted in all directions and a cone of diffraction is produced for each Bragg reflection at an angle corresponding to its *d*-spacing and governed by Bragg's Law.[117] Each cone is made up of diffraction spots from many crystallites within the sample.[126] A PXRD pattern is produced by plotting the ring intensity against the 2θ angle and therefore instead of producing a three-dimensional diffraction pattern, a one-dimensional pattern is produced. The individual peak intensities may vary from those expected from the internal crystal structure, as effects such as preferred orientation can sometimes be present, increasing or decreasing the intensity of peaks. The peak positions are the most important feature

for the use of PXRD as a fingerprinting tool for identification of phases present in the solid sample; these reflect the unit cell dimensions, which are a critical parameter in phase identification.

In cases where it is not possible to grow single crystals large enough for scXRD, it is sometimes possible to refine the structure from high quality powder data using a Rietveld refinement, providing a good starting structural model can be achieved.[125] Rietveld refinement was not employed in this work.

2.3 Thermal analysis

2.3.1 Differential Scanning Calorimetry (DSC)

DSC is commonly used as a method to understand the thermal properties of a substance, identify different solid forms and study their phase transitions in combination with other thermal techniques. A small quantity of sample is weighed into a sample pan and the heat flow required to keep the two pans at the same temperature is measured whilst heating the two pans at a set rate. Thermal events can thus be identified from the heat flows required to achieve this; for example, in the case of an exothermic event, less heat is required to increase the temperature of the sample pan relative to the reference pan. Thermal events are therefore shown as changes in heat flow with respect to temperature. As a result, the temperature at which exothermic and endothermic events occur can be identified as well as determination of the associated enthalpy of each thermal event through integration of the area under the curve.[128,129] Typical thermal events that can be assessed using DSC are shown in Figure 2.5.

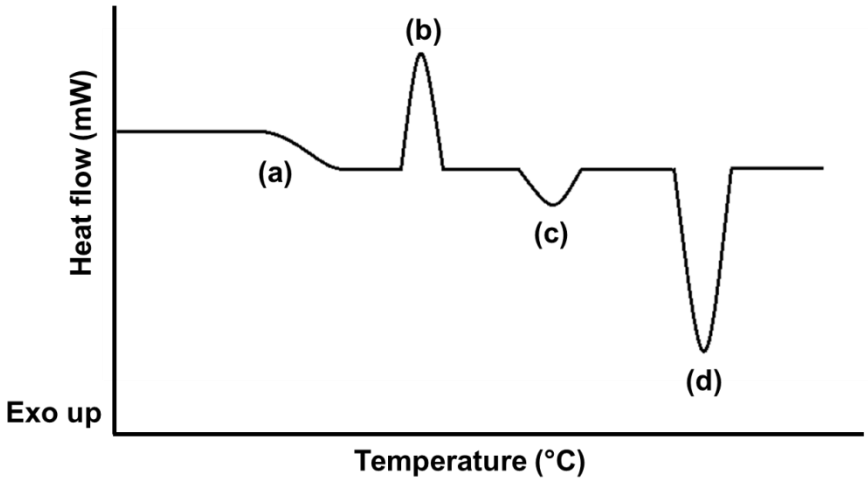

Figure 2.5 - Graph showing typical thermal events in a DSC trace: (a) glass transition, (b) recrystallisation, (c) desolvation or phase transition and (d) melting.

2.3.2 Thermogravimetric Analysis (TGA)

TGA is used to measure the change in mass of a sample as a function of temperature. In solid-state chemistry the technique is often used to determine the stoichiometry of solvates or hydrates and can also be used to study the decomposition of a material.[129] Combination of TGA with mass spectroscopy can allow for identification of degradation products. In TGA a known mass of sample is weighed into a sample pan (different types of pans can be used including aluminium and ceramic) and the mass is recorded as the temperature is increased at a programmable rate. A weak nitrogen flow is sometimes applied over the sample during the experiment to maintain an inert atmosphere.[130] The percentage of mass change can be plotted with respect to temperature (Figure 2.6); this quantification allows, for example, events such as desolvation to be determined with a high degree of certainty.

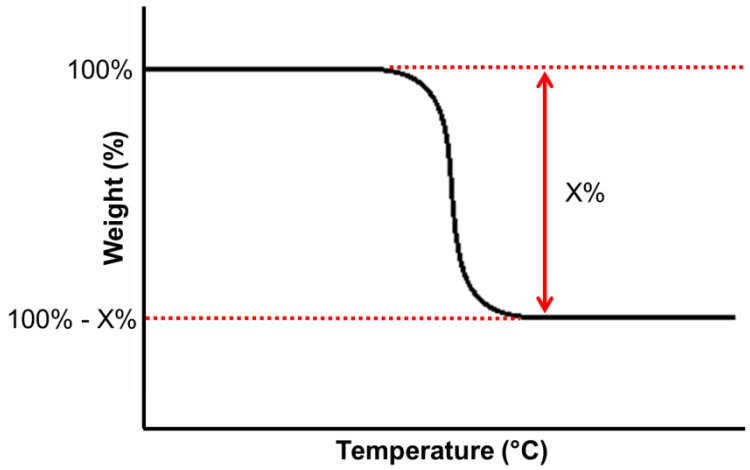

Figure 2.6 - Graph showing solvent loss in a typical TGA trace.

2.3.3 Hot-stage Microscopy (HSM)

Hot-stage microscopy is a useful thermal analytical tool in which the effect of temperature on a substance can be visualised and recorded. It is often used to complement DSC and TGA allowing for thermal events such as melting and phase transitions to be interpreted visually. HSM is also a useful tool for identifying properties such as colour change in thermochromic materials or the phenomenon of thermosalience in which crystals display a mechanical jumping effect with temperature.

2.4 Spectroscopy

2.4.1 Fourier Transform Infra-red spectroscopy (FTIR)

Infra-red spectroscopy results from the absorption of infra-red light by a sample. The amount of infra-red light of each frequency that passes through the compound is measured as the percentage transmittance. Bonds are constantly vibrating and the incident beam can be absorbed by the sample when the incident frequency matches the frequency of vibration of the bond, which is therefore excited into a higher vibrational energy state. Specific bonds in a molecule thus absorb infra-red light at characteristic frequencies enabling the identification of functional groups from a spectrum of an unknown sample.

Modern IR spectrometers often adopt Fourier transform techniques. Infra-red light passes through an interferometer which splits the beam from the sample into two beams. One beam reflects off a mirror which is fixed in place and the other beam reflects off a moveable mirror that can alter the path difference of the beam. When the two beams recombine their interference pattern is converted to a spectrum by applying a Fourier transformation. This method increases the sensitivity of the measurements and allows for all the frequencies to be collected simultaneously, decreasing the data collection time.[97] FTIR spectroscopy is a non-destructive and versatile technique in which only a small quantity of the liquid or solid sample is required.

2.4.2 Raman spectroscopy

Raman spectroscopy is another type of vibrational spectroscopy which involves shining a high energy incident beam (laser) on a sample and monitoring the light scattered by the molecules. Most of the scattered light emerges from the sample in the same frequency as the source, known as Rayleigh radiation. However, a small quantity of the scattered light emerges from the sample with lower or higher energy as a result of vibrational motions in the target material; this results in a change in frequency of the detected photons, and the resulting signals are named Stokes or anti-Stokes lines, respectively. Laser beams are required to provide highly monochromatic incident radiation for Raman spectrometers to observe the small shifts in the frequency of the low intensity scattered radiation.[97]

Vibrational spectroscopy can sometimes be used to distinguish polymorphic forms by identification of subtle differences in their spectra. A bond that is involved in a hydrogen bond will vibrate differently than a free bond, creating a downshift in the frequency of the vibration. Polymorphs often exhibit different hydrogen bonding environments and thus different frequencies of relevant vibrational modes can be observed.

2.4.3 Process Analytical Technologies (PAT)

In-line tools are increasingly being implemented to monitor reactions and crystallisations in real time. Use of PAT allows for spectroscopic data such as FTIR, UV-vis and Raman and other information to be collected during an experiment without the need for sampling from the reaction vessel for off-line analysis. In crystallisation, FTIR and UV-vis probes can be used to monitor the solution concentration of a compound over time. A Raman probe can be used to monitor changes in the solid form of a substance by observing subtle changes in the spectrum. Additional PAT methods such as Particle Vision and Measurement (PVM) and Focused Beam Reflectance Measurement (FBRM) can also be applied. PVM is used to observe the crystal shape, morphology and size as well as to monitor processes such as agglomeration. FBRM is a laser-based method used to monitor the particle counts per second based on the chord length distribution of particles in solution. In an FBRM probe a focused laser beam is rotated to allow for a circular path of laser light to interact with particles in a flowing suspension.[131] Upon scanning across a particle, light is backscattered to a detector and the duration of each pulse of backscattered light is multiplied by the scan speed to calculate the distance across each particle. This distance is defined as the chord length. Thousands of particles are counted per second allowing for measurement of chord length distribution in real time.[132] Chord length distribution describes the frequency at which particles of a particular chord length are detected and gives an indication of particle size.[131] In this work *in situ* PAT incorporating FBRM, PVM and Raman probes were used to monitor the crystallisation of succinic acid.

Chapter 3

Techniques and instrumentation

This chapter describes the routine techniques used in the preparation of crystalline materials as well as the instrumentation used for analysis and characterisation of the products. More detailed experimental information is provided in each chapter relevant to the particular materials studied. Additional analytical techniques were also used for individual materials studied; these are described in the chapter which describes the materials for which they were solely used.

3.1 Solubility and metastable zone width (MSZW) measurements

Knowledge of the solubility of the substance is an important parameter in crystallisation from solution, as well as being in many cases a key physical property of product solid forms, for example for APIs and their complexes. Solubility and MSZW determinations were carried out using the Crystal16 and Crystalline platforms from Technobis Crystallization Systems in the CMAC laboratory at the University of Strathclyde.

Both platforms operate on the principle of using turbidity to detect the clear and cloud point temperatures of a solution. Varying concentrations of the substance are prepared into vials and the relevant solvent added. The transmissivity of the solution is then measured as the temperature is changed; this is used to indicate the clear and cloud points of the solution for each concentration. The clear point represents the temperature of dissolution; the temperature at which the solution becomes transparent (100% transmissivity) and the solid has all dissolved. The cloud point represents the temperature of recrystallisation; the temperature at which the percentage transmissivity of the solution begins to decrease. Data were analysed using the CrystalClear[133] software in which the clear and cloud point temperatures can be determined for each solution (Figure 3.1). The

combination of these points from each solution prepared with different concentrations of substance can be used to produce solubility and cloud point curves with respect to temperature.

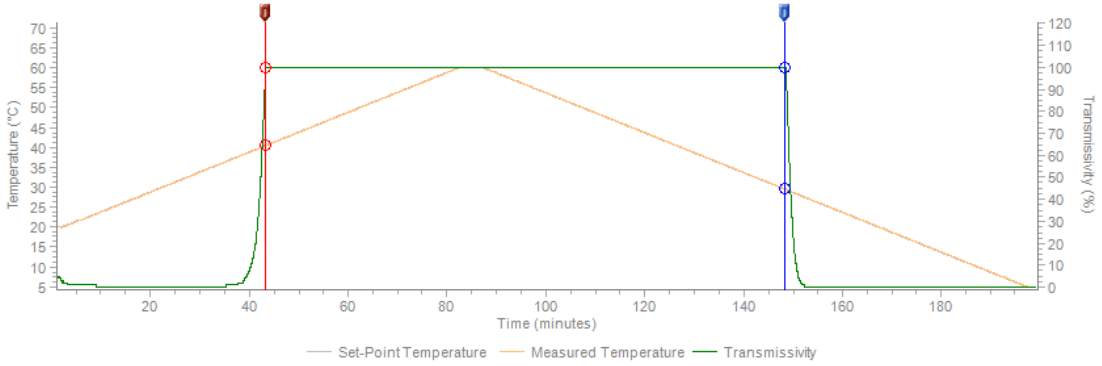

Figure 3.1 - Determination of the clear (red) and cloud (blue) point temperatures with respect to transmissivity of a solution in the Technobis Crystallization Systems platforms. In this example, the clear point temperature lies at 40.5 °C and the cloud point temperature lies at 29.5 °C.

The Crystal16 operates at 1.5 ml scale with magnetic bottom stirring and relies solely on turbidity to detect clear and cloud points for 16 vials in parallel. The Crystalline can operate at up to 8 ml scale with eight vials running in parallel and magnetically controlled overhead stirring can also be implemented. The Crystalline is also equipped with PAT capability in the form of *in situ* cameras and the capability for *in situ* Raman probes for additional detection of the clear and cloud points of a solution with respect to temperature.

3.2 Crystallisation platforms and methods

3.2.1 Evaporative crystallisation

Small scale evaporative crystallisation was used as an initial screening method in the preparation of multi-component molecular complexes and to obtain single crystals of sufficient size and quality for single crystal X-ray diffraction. It was also used in studies of the effect of additives on crystal morphology. The crystallisations were prepared in 7 ml glass vials in which milligram quantities of the substances were dissolved in a suitable solvent (usually the minimum quantity of solvent required for dissolution to be achieved). Sonication and a short period of heating were sometimes used to aid dissolution. Small holes were then pierced in the lids to allow for slow evaporation of the solvent and the vials were left to crystallise at controlled temperatures using temperature controlled hot-plates (Figure 3.2). Crystallisations were also carried out at room temperature as well as

at 4 °C by placing the vials in the refrigerator. Multiple crystallisations were prepared in order to access different conditions for crystal growth; changes to the conditions were made by altering the solvent system, the stoichiometric ratios of the starting materials and the temperature of crystallisation.

Figure 3.2 - Temperature controlled hot-plates for evaporative crystallisation.

3.2.2 Cooling crystallisation

Two platforms were used routinely in this work to carry out cooling crystallisation at small scale.

3.2.2.1 Cambridge Reactor Design Polar Bear Plus Crystalliser

The Polar Bear Plus crystalliser from Cambridge Reactor Design was used in this work for batch crystallisations at various scales. The crystalliser allows for programmable heating and cooling profiles and magnetic bottom stirring at different rates. The platform also allows for operation at different scales by the use of changeable inserts allowing for scales of 1 ml and 20 ml vials and 50 ml and 500 ml round bottomed flasks (Figure 3.3).

Figure 3.3 - (left) The Polar Bear Plus crystalliser and (right) changeable inserts to allow for crystallisation experiments at different scales.

Overhead stirring was also implemented for crystallisations carried out using this platform by use of a magnetically controlled overhead stirrer from Technobis Crystallization Systems which was clamped above a 20 ml vial, or by using an overhead shaft and motor which was clamped above a round bottomed flask. The Polar Bear was also used for solution mediated (slurrying) crystallisations to enable temperature control and input of specific magnetic stirring speeds.

3.2.2.2 ReactArray Microvate

The ReactArray Microvate was also used for a number of cooling crystallisations; this device allows for programmable temperature regimes for rows of four 2.5 ml vials (Figure 3.4). The compound was dissolved in a suitable solvent in the vial which was then placed in the reactor block with sealed lids. The cooling profile was set using the supplied computer software. Evaporation was also enabled in this device, by removing the lids of the vials for the relevant crystallisations.

Figure 3.4 - The ReactArray Microvate for controlled cooling crystallisation.

3.3 X-ray diffractometers

3.3.1 Single X-ray diffraction

During this work crystallographic data were collected using four in-house laboratory diffractometers: a Rigaku Oxford Diffraction (formerly Agilent Technologies) SuperNova, a Rigaku Oxford Diffraction Xcalibur, a Rigaku Oxford Diffraction Gemini A Ultra and, for a small number of data collections, a Rigaku R-AXIS/RAPID.

The Rigaku R-AXIS/RAPID diffractometer has a four-circle goniometer and uses a sealed tube Mo-K_α source with a graphite monochromator. The diffractometer differs from the other three diffractometers in that it features an image plate detector while the others are

equipped with a Charged Coupled Device (CCD) area detector. The SuperNova diffractometer has a four-circle kappa goniometer and dual micro-focus sources (Mo-K_α and Cu-K_α) with a graphite monochromator and is equipped with an Eos S2 detector. The Xcalibur has a four-circle kappa goniometer, is also equipped with an Eos S2 detector and has a sealed tube Mo-K_α source with a graphite monochromator. The Gemini A Ultra diffractometer has a four-circle kappa goniometer and is equipped with a dual sealed tube source with a graphite monochromator (Mo-K_α and Cu-K_α radiation). The diffractometer has an Atlas CCD detector.

Figure 3.5 shows a general set-up for a laboratory diffractometer (Rigaku Oxford Diffraction Xcalibur) with the main features highlighted. With the exception of the detector type, the general set-up for each of the diffractometers is the same. The four-circle goniometer can enable movement of the crystal through the diffractometer positions (κ, φ, ω, 2θ) required to collect a complete set of diffraction data. The distance between the sample and the detector can also be altered by movement of the detector.

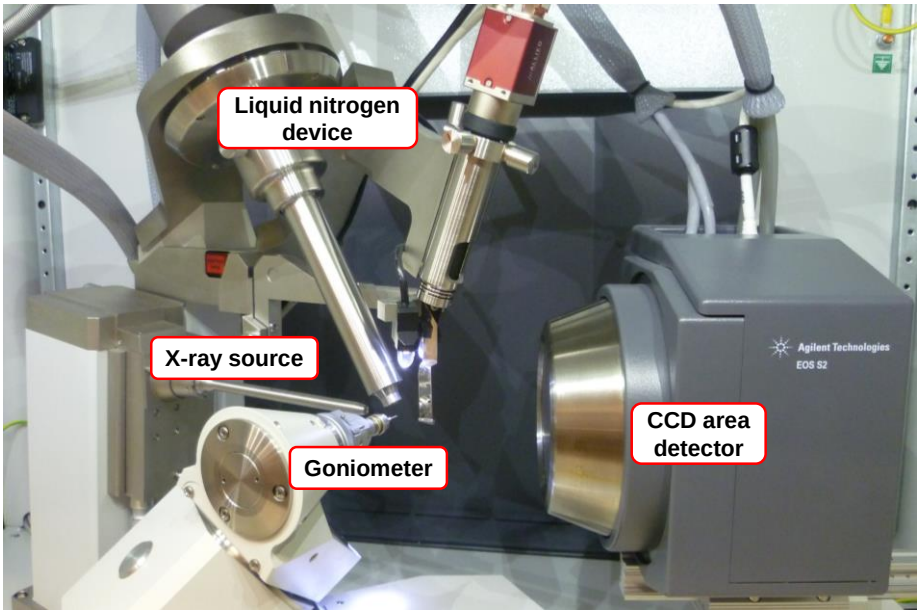

Figure 3.5 - A photograph of the Rigaku Oxford Diffraction Xcalibur diffractometer with the main features labelled.

Each diffractometer utilises a liquid nitrogen flow device (either an Oxford Cryosystems Cryostream 700 or an Oxford Instruments CryoJetXL) in order to control the temperature of the sample during the data collection. In standard data collections the flow of nitrogen gas from the device is used to cool the sample. The device also incorporates the ability to heat the nitrogen gas and can thus be used to heat the sample to carry out data collections at higher temperatures.

Data collection and processing was carried out using the CrysAlisPro[134] software for the Rigaku Oxford Diffraction Gemini, Xcalibur and SuperNova diffractometers and the Rigaku CrystalClear 2.0[135] software for the R-AXIS/RAPID diffractometer. When used, face indexing was carried out using the CrysAlisPro[134] software. XPREP[136] was also used in some cases to process data and verify space group assignment. All structures were solved by direct methods using SHELXS (-97 or -2013)[137] and refined using SHELXL (-97 or -2013)[138] within the WinGX[139,140] program. Visualisation of the crystal structures and calculation of the BFDH morphology was carried out using Mercury 3.8.[141] Specific experimental and special refinement details are reported within each chapter.

A synchrotron source (Advanced Light Source, Lawrence Berkeley National Laboratory, Beamline 11.3.1) was also used to collect single crystal X-ray diffraction data for one of the crystal structures discussed in this work. This involved a variable temperature experiment, benefiting from the high intensity, rapid data collection times and enhanced sample environment available at the synchrotron beamline, and was carried out on behalf of the author. Use of the synchrotron allowed for the collection of high quality data from the high intensity of the synchrotron X-rays and also for data to be collected at temperatures higher than could be accessed using in-house laboratory diffractometers. In the experiment data were collected using a Bruker AXS D8 three-circle diffractometer, equipped with a Bruker AXS PHOTON 100 complementary metal-oxide semiconductor (CMOS) detector, using Si (111) monochromated radiation (λ = 0.9538 Å). The temperature of the sample was controlled using an Oxford Cryosystems Cryostream Plus. Data collection was carried out using the Bruker AXS APEX2[142] software and data processing was carried out using the Bruker AXS APEX2[142] with SADABS-2014/5[143] software packages. Further experimental information is provided in Chapter 7.

3.3.2 Powder X-ray diffraction (PXRD)

Routine PXRD data were collected in flat-plate mode using a Bruker D8 Advance laboratory diffractometer equipped with monochromatic Cu-K_α (λ=1.54056 Å) radiation in reflection geometry at 298 K. With the exception of samples of succinic acid, all samples were ground using a mortar and pestle to produce a microcrystalline powder prior to preparation for flat-plate analysis. Samples of succinic acid were prepared without grinding in order to prevent a polymorphic transformation (see Section 4.3.1).

Variable temperature PXRD data were also collected at a synchrotron source (Diamond Light Source, Beamline I11) for one complex in order to study a phase transition; again this was carried out on behalf of the author. The microcrystalline sample was loaded into

a borosilicate glass capillary and secured in a brass holder using glue. The beamline uses Si (111) monochromated radiation with an energy of 15 keV (λ = ~0.826 λ), and is equipped with two detector arrays: the PSD (position-sensitive detector) is used for high throughput experiments and was used in this work, and the MAC (multi-analyser crystal) for high resolution. The sample temperature was controlled using an Oxford Cryosystems Cryostream Plus. Further experimental information is again detailed in Chapter 7.

3.4 Thermal analysis

3.4.1 Differential Scanning Calorimetry (DSC)

DSC studies were performed using a Thermal Advantage Q20 DSC from TA Instruments, equipped with Thermal Advantage Cooling System 90 and operated with a dry nitrogen purge gas at a flow rate of 18 cm^3 min^{-1}. 2-4 mg samples were placed in sealed Tzero aluminium pans and heated at a rate of 5 °C min^{-1}, to various maximum temperatures depending on the sample being studied. Data were collected using the software Advantage for Qseries version 5.4.0 © 2001-2011 TA Instruments-Waters LLC. Analysis of the data was carried out using TA Universal Analysis software.

3.4.2 Thermogravimetric Analysis (TGA)

In this work TGA was carried out by placing 2-5 mg of sample in a Perkin Elmer TGA4000 with a nitrogen flow rate of 20 ml min^{-1}. The TGA data were accumulated while the temperature was ramped to 400 °C at a heating rate of 5 °C min^{-1}.

3.4.3 Hot-stage Microscopy (HSM)

HSM was carried out using a Mettler Toledo FP82 hot stage equipped with a Leica DM1000 microscope. Each crystal was subjected to a temperature program of 30 °C to various maximum temperatures depending on the sample at 5 °C min^{-1} using the FP90 Central Processor. The crystals were filmed using a Lumenera Infinity 2 microscopy camera and recorded using Studio Capture software version 4.0.1 © 2001-2010 Studio86Designs.

3.5 Spectroscopy

3.5.1 Fourier Transform Infra-red spectroscopy (FTIR)

The FTIR spectra in this work were recorded using a Perkin Elmer FTIR Spectrometer in the range 4000–500 cm^{-1} with an ATR sampling accessory at room temperature.

3.5.2 Raman spectroscopy

Raman spectra in the succinic acid study were collected using a Thermo Scientific DXR Raman microscope (laser at 780 nm and OMNIC software version 8). For variable temperature Raman studies a Renishaw inVia Raman Microscope combined with a Mettler Toledo FP82 hot stage were used.

3.5.3 ^{1}H Nuclear Magnetic Resonance (NMR)

For all proton NMR studies in this work, samples were dissolved in a suitable deuterated solvent and an Agilent Technologies 500 MHz ^{1}H-NMR instrument was used. The data were analysed using ACD labs.

Chapter 4

Tuning crystal morphology of β-succinic acid using a polymer additive

This chapter has been published in part as a journal article:
A. R. Klapwijk, E. Simone, Z. K. Nagy and C. C. Wilson, Tuning Crystal Morphology of Succinic Acid Using a Polymer Additive. *Cryst. Growth Des.*, 2016, 16, 4349-4359.

Some of the other findings presented in this chapter are reported in the following paper:
E. Simone, A. R. Klapwijk, C. C. Wilson and Z. K. Nagy, Investigation of the Evolution of Crystal Size and Shape during Temperature Cycling and in the Presence of a Polymeric Additive Using Combined Process Analytical Technologies. *Cryst. Growth Des.*, 2017, 17, 1695-1706.

4.1 Introduction and aims

In the context of this study, an additive is defined as a soluble, polymeric or structurally similar impurity deliberately added to a crystallisation with the aim of modifying crystal morphology or solid form. The aim of this work was to identify an additive compound which, when present in solution, results in changes in the crystal morphology of a target compound and to study the effect of the additive under various crystallisation conditions. As noted earlier, the avoidance of plate-like or thin needle morphologies is advantageous in processing, and an ideal additive would favour more isometric particles such as block shaped crystals. Succinic acid was selected as a relevant model target compound and various polymer additives were initially studied in order to select an additive system that can be seen to affect the morphology adopted. Indexing of the crystal faces using single crystal X-ray diffraction and analysis of the crystal structure were used as tools to

understand the mechanism by which the morphology change occurs. Ultimately, the aim is to move such an additive-mediated process into continuous crystallisation environments, discussed in Chapter 5 below.

Succinic acid (Figure 4.1; SA) is a dicarboxylic acid used in the food industry and is a Generally Recognized as Safe (GRAS) compound[144] commonly used as a co-former in multi-component crystallisation of APIs and other functional molecular systems.[112,145,146] SA was selected as a target system in this study as it grows into large plate-like crystals from water in which the morphology can be easily observed under the microscope and the morphology has previously been shown to be sensitive to crystallisation conditions, such as the choice of solvent.[32,147]

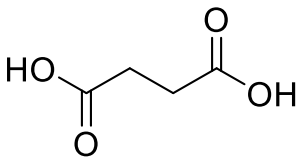

Figure 4.1 - Chemical structure of succinic acid.

There are two reported polymorphic forms of SA. The monoclinic β-form can be obtained from various solvents and is the stable form at ambient conditions. Above approximately 137 °C the β-form converts to the high temperature triclinic α-form,[148] which is metastable at room temperature.[149,150] This polymorphic transition can be observed across a single crystal using hot-stage microscopy, as shown in Figure 4.2. The α-form of SA has previously been obtained by sublimation crystallisation[151] and was also observed during milling experiments[149,152] and through monodisperse droplet evaporation.[150]

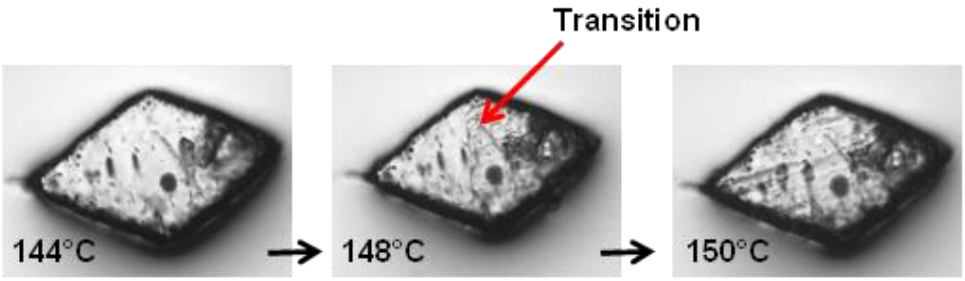

Figure 4.2 - Hot stage microscopy images of β-SA converting to α-SA. Images taken during the present work.

The crystal morphology adopted by β-SA depends upon the solvent from which it is crystallised. Aqueous crystallisation results in plate-like crystals (Figure 4.3; the

experiments described here of β-SA are from crystals grown in the current study) whereas crystallisation from isopropanol results in a more needle-like morphology.[32,147]

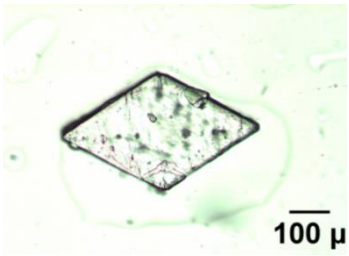

Figure 4.3 - Microscope image of crystal morphology of SA crystallised from water.

The faces of a β-SA crystal grown from aqueous solution were indexed using single crystal X-ray diffraction and the results correlate with those previously reported in the literature.[147,153] In addition to the experimentally observed morphology, the BFDH morphology of β-SA was calculated. The observed and predicted morphologies are shown in Figure 4.4 with the crystal faces labelled with the corresponding Miller indices.

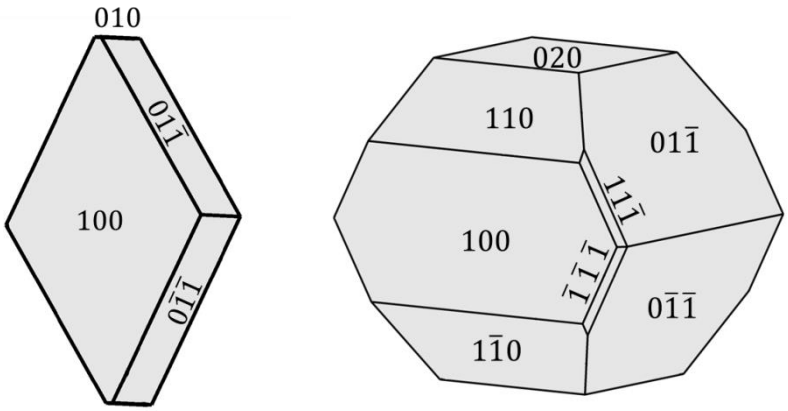

Figure 4.4 - (left) Observed morphology of β-SA when crystallised from water and (right) predicted morphology of β-SA using the BFDH tool in Mercury.[141]

The predicted morphology correlates reasonably well with the observed morphology; all of the faces in the observed morphology are present in the predicted morphology. However, the overall shape of the predicted morphology is block-like and there are additional faces present in comparison with the observed plate-like morphology. This can partly be accounted for by the neglect of molecular-level solvent interactions in the BFDH model. As discussed in previous literature,[32,51,154] in the crystal structure of β-SA the (100) face intercepts chains of SA molecules linked by hydrogen bonded carboxylic acid dimers (Figure 4.5). This makes the (100) face a polar face with which water molecules would be likely to interact, inhibiting growth along the direction perpendicular to this face

and suggesting why the (100) face is the largest, slowest growing face in crystallisations carried out from water and the final crystal shape is plate-like. The BFDH model does not account for such solvent interactions, which can have a large effect on the crystal morphology, and therefore may not always make accurate predictions of crystal shape.[27]

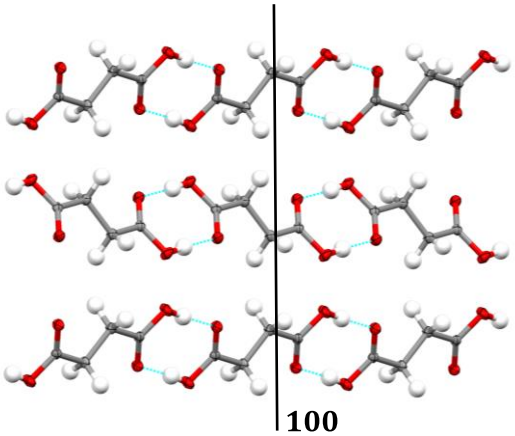

Figure 4.5 - Packing arrangement of β-SA through the (100) face, showing the hydrogen bonded carboxylic acid dimers propagating the crystal structure perpendicular to this face.

After initial crystallisation experiments, Pluronic P123 (PP123) was selected as the polymer additive to be used in this study. PP123 (Figure 4.6) belongs to a family of triblock co-polymers composed of a hydrophobic chain of poly(propylene glycol) (PPG) flanked by two hydrophilic chains of poly(ethylene glycol) (PEG) where the composition of PEG and PPG blocks is $PEG_{20}PPG_{70}PEG_{20}$. Polyethylene glycol is widely used in many industrial applications and can be obtained in many different chain lengths. Pluronic F127 (PF127) was also utilised in this study for comparison. This polymer contains the same blocks as PP123 however, in a different composition richer in the hydrophilic blocks ($PEG_{101}PPG_{56}PEG_{101}$).

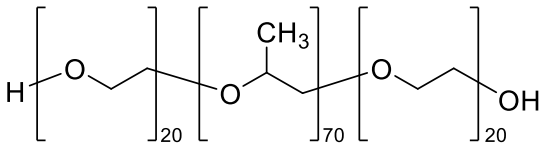

Figure 4.6 - Molecular structure of Pluronic P123.

4.2 Experimental information

SA, PP123, PF127 and poly(propylene glycol) 4000 (PPG4000) were obtained from Sigma Aldrich. Poly(ethylene glycol) 1000 (PEG1000) was obtained from Alfa Aesar. Deionized water was used as the solvent for all crystallisations.

4.2.1 Solubility and MSZW measurements

Solubility and MSZW measurements of SA in water and in the presence of 0.5% PP123 in water were carried out using the Technobis Crystallization Systems Crystalline at 3 ml scale. Vials containing different concentrations of SA and polymer were heated and cooled between temperature ranges of 5 °C and 70 °C using a heating/cooling rate of 0.5 °C min^{-1} using magnetic bottom stirring at 400 rpm and magnetically controlled overhead stirring at 700 rpm. The data were analysed using CrystalClear software.[133]

4.2.2 SA and additive concentrations

Table 4.1 outlines the concentrations of SA and PP123 used in the crystallisations from water. The dissolved polymer concentrations used are defined here, and for all other crystallisations in this chapter, as the percentage of the saturation concentration of SA by weight, expressed in g ml^{-1} of water. These express the very low concentrations of polymer used, for example, for T_{sat} = 20 °C (0.06 g ml^{-1} of SA), 0.5% polymer concentration would be 0.00030 g ml^{-1}, 0.25% would be 0.00015 g ml^{-1} and 0.17% would be 0.00010 g ml^{-1} of polymer; the T_{sat} concentrations are taken from the solubility curve detailed in the next section (Figure 4.14 below). It is known that Pluronic P123 assembles in micelles at low concentrations; the polymer concentrations used here are in the region where micellar formation is favoured, but it is unclear how this might influence the possible interaction with the growing crystal faces of the SA crystal.[155]

Table 4.1 - Concentrations of SA and PP123 additive used, in mg ml^{-1} for crystallisations from water.

T_{sat} (°C)	Concentration of SA (mg ml^{-1})	Concentration of PP123 (mg ml^{-1})			
		0.17%	0.25%	0.50%	1.0%
20	60	0.10	0.15	0.30	0.60
27	80	0.13	0.20	0.40	0.80
30	90	0.15	0.23	0.45	0.90
32	100	0.17	0.25	0.50	1.00
34	110	0.18	0.28	0.55	1.10
37	125	0.21	0.31	0.63	1.26
40	145	0.24	0.36	0.73	1.46

4.2.3 Crystallisations at 1 ml scale

The Cambridge Reactor Design Polar Bear Plus crystalliser was used for 1 ml scale screening crystallisations, which were carried out in 1.5 ml vials with magnetic bottom stirring at a stirring speed of 325 rpm. This set-up was also used for the crystallisations of SA at 1 ml scale in the presence of the PP123 additive. The experiments were carried out at seven saturation concentrations of SA (T_{sat} = 20, 27, 30, 32, 34, 37 and 40 °C) with four different concentrations of PP123 (0%, 0.17%, 0.25% and 0.5%). All 1 ml crystallisations were subject to a linear cooling profile from 10 °C above the saturation temperature of the given SA concentration to 5 °C with a cooling rate of 0.5 °C min^{-1}. The crystalline product was filtered at the end of the cooling profile and visual analysis carried out using optical microscopy.

4.2.4 Initial crystallisations at 10 ml scale

The Cambridge Reactor Design Polar Bear Plus crystalliser was used for the 10 ml cooling crystallisations, carried out in in 20 ml glass vials with each of overhead and magnetic bottom stirring. Crystallisations with overhead stirring at 10 ml scale, implemented using magnetically controlled overhead stirrers from Technobis Crystallization Systems, were carried out at four saturation concentrations of SA from water (T_{sat} = 20 , 27, 30 and 40 °C), with four concentrations of PP123 (0%, 0.17%, 0.25% and 0.5%). Crystallisations from water with magnetic bottom stirring at a rate of 325 rpm were carried out under a more limited set of conditions: with no polymer and 0.17% of polymer for T_{sat} = 30 °C. Crystallisations from ethanol with overhead stirring were carried out at T_{sat} = 30 °C with 0% and 0.5% of PP123 additive. All 10 ml crystallisations were subject to a linear cooling profile from 10 °C above the saturation temperature of the given SA concentration to 5 °C with a cooling rate of 0.5 °C min^{-1}. The crystalline product was filtered at the end of the cooling profile and visual analysis carried out using optical microscopy.

4.2.5 Crystallisations at 200 ml scale

Further experiments were carried out at 200 ml scale. The crystallisations were carried out in a 250 ml round bottom flask in the Cambridge Reactor Design Polar Bear Plus crystalliser. Overhead stirring was implemented by attaching a motor driven impeller to the platform and a stirring speed of 325 rpm was used (Figure 4.7). Experiments with magnetic bottom stirring were also carried out at this scale at 325 rpm. A saturation concentration of SA at 30 °C was used for all experiments with concentrations of 0% and 0.17% PP123 investigated. The crystallisations were subject to a linear cooling profile

from 10 °C above the saturation temperature of the given SA concentration to 5 °C with a cooling rate of 0.5 °C min^{-1}. The crystalline product was filtered at the end of the cooling profile and visual analysis carried out using optical microscopy.

Figure 4.7 - Experimental set up for 200 ml crystallisations with overhead stirring.

4.2.6 Crystallisations at 350 ml scale

The 350 ml cooling crystallisations were carried out at Loughborough University using a 400 ml jacketed glass vessel equipped with overhead stirring at 325 rpm (PTFE pitch blade turbine). The set-up is shown in Figure 4.8 and Figure 4.9. The temperature was controlled using a PT-100 temperature probe connected to a Huber Ministat 230 thermoregulator. A PAT array was used, consisting of an RXN2 Hybrid Raman analyser with immersion probe and 785 nm laser (Kaiser with iC Raman 4.1 software), D600L Lansentec Focused Beam Reflectance Measurement (FBRM) probe (equipped with control interface software version 6.7) and a particle vision and measurement (PVM) V819 probe (Mettler Toledo) with on-line image acquisition software (version 8.3). The pre- and post-processing of the data was carried out with Matlab R2013, iC Raman 4.1 and Excel. The data from the FBRM and the Huber instrument are transmitted in real-time to the CryPRINS software (Crystallisation Process Informatics System). This software was used for real-time monitoring of the FBRM counts and the temperature, as well as input of a temperature profile.

Different saturation concentrations of SA (T_{sat} = 20, 27, 30, 32, 34, 37 and 40 °C) in the presence of different concentrations of PP123 (0%, 0.17%, 0.25% and 0.5% of the saturation concentration of SA) were used. From each crystallisation a 6 ml sample was

taken at the end of each experiment for off-line analysis (PXRD, Raman and SEM imaging). At this scale up to six experiments were carried out consecutively such that at the end of each crystallisation, the contents were redissolved and additional quantities of SA and PP123 were added to the vessel to increase the concentration for the next experiment, also accounting for the 6 ml sample taken after each experiment. The feed solution was then replaced at the beginning of each day. All crystallisations were subject to a linear cooling profile from 10 °C above the saturation temperature of the given SA concentration to 5 °C with a cooling rate of 0.5 °C min^{-1}. The MSZW was determined at this 350 ml scale from the *in situ* FBRM data.

Figure 4.8 - 400 ml stirred tank reactor with PAT used for 350 ml scale crystallisations.

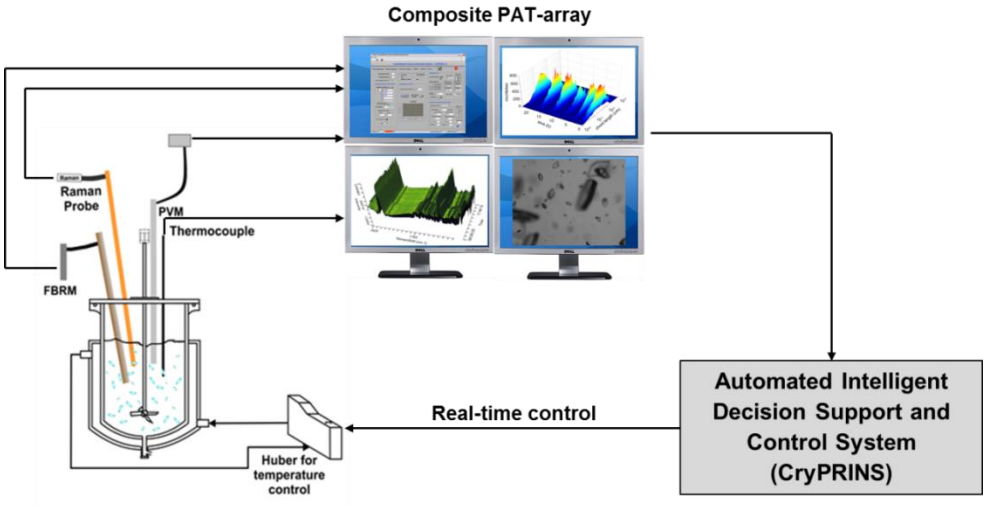

Figure 4.9 - Schematic of experimental set-up for 350 ml crystallisations at Loughborough University.

4.2.7 Additional crystallisations at 10 ml scale

Additional studies investigating the cooling rate of the crystallisation, use of different polymer additives, and for washing / recrystallisation experiments were also carried out at 10 ml scale with overhead stirring. For all experiments the crystalline product was filtered at the end of the cooling profile and visual analysis was carried out using optical microscopy. Experiments investigating the effect of the cooling rate on the crystal morphology of SA produced in the presence of PP123 were carried out at one saturation concentration of SA (T_{sat} = 30 °C) and four concentrations of PP123 (0%, 0.17%, 0.25% and 0.5%) with overhead stirring. All crystallisations were subject to a linear cooling profile from 10 °C above the saturation temperature of the given SA concentration to 5 °C with a cooling rate of 0.1 °C min^{-1}.

Experiments performed using different polymer additives involved the use of Pluronic F127 (PF127) as well as the separate blocks of PP123: PEG1000 and PPG4000 as additives. Crystallisations in the presence of PF127 were carried out for SA concentration T_{sat} = 30 °C using 0.17% and 0.5% of polymer. Crystallisations carried out in the presence of PEG1000 were implemented for SA concentrations T_{sat} = 30 °C and 40 °C initially using 0.5% polymer. However, as no effect was observed, crystallisations with 1% of polymer were also carried out. Crystallisations carried out in the presence of PPG4000 were implemented for SA saturation concentrations T_{sat} = 20, 27, 30 and 40 °C using 0.17%, 0.25% and 0.5% of polymer. The same cooling profile was used as for the previous 10 ml crystallisations at a cooling rate of 0.5 °C min^{-1}.

For the washing and recrystallisation experiments, crystals of a sample from a 350 ml scale experiment (T_{sat} = 50 °C; 0.5% PP123) were recrystallised from water at 10 ml scale for SA concentration T_{sat} = 30 °C using overhead stirring. A second sample was washed, in combination with filtration, with deionised water at 4 °C and then recrystallised after drying. This procedure was repeated with other crystals from the same sample but using diethyl ether as the washing solvent. Additionally, 1.5 g of crystals from the original morphology-modified sample were slurried in 10 ml of diethyl ether for one hour and the dry product recrystallised from water for SA concentration T_{sat} = 30 °C. The same cooling profile was used as for the previous 10 ml crystallisations at a cooling rate of 0.5 °C min^{-1}.

4.2.8 Direct nucleation control (DNC) and temperature cycling experiments

The DNC and temperature cycling experiments were carried out using the experimental set-up used for previous experiments at 350 ml scale at Loughborough University (Figure 4.8). All DNC experiments were carried out from water at 350 ml scale with a SA concentration of 0.06 g ml^{-1} (T_{sat} = 20 °C) and in experiments with the additive present an additive concentration of 0.5% was used. The initial cooling rate was 0.5 °C min^{-1}. Two set points of 100 and 200 counts/second were chosen for experiments with and without the additive present and set in the CryPRINS software. The value of total counts/second measured by the FBRM is sent to the CryPRINS software and temperature is decreased if the measured total counts/s is lower than the set point range, or increased if it is higher, causing small crystals to dissolve. In each case a sample was taken before and after DNC for visualisation of the crystal morphology.

In the temperature cycling experiments a 350 ml solution (0.06 g ml^{-1}, T_{sat} = 20 °C) of SA in water was heated up to 30 °C and cooled to 10 °C at a rate of 0.5 °C min^{-1}. After nucleation the temperature cycling was started and experiments were stopped when the statistics from the FBRM and PVM reached a constant value (equilibrium state). A constant heating/cooling rate of $\pm$0.3 °C min^{-1} was used and various parameters were investigated including the effect of the amplitude of the cycle where three different amplitudes were tested (4.5, 6 and 7.5 °C). The 4.5 °C amplitude temperature cycle experiment was repeated in the presence of the PP123 polymer additive in two concentrations (0.25% and 0.5%).

4.2.9 Crystallisation of adipic acid

Preliminary crystallisations of adipic acid (AA) were also carried out as part of this work. AA was obtained from Sigma Aldrich and deionised water was used as the solvent for all of the crystallisations. The solubility of AA was extracted from the literature.[7,156] The crystallisations were carried out at 10 ml scale at four saturation concentrations of AA (T_{sat} = 20, 27, 30 and 40 °C) and one concentration of PP123 (0.5%) with overhead stirring. All crystallisations were subject to a linear cooling profile from 10 °C above the saturation temperature of the given AA concentration to 5 °C with a cooling rate of 0.5 °C min^{-1}. The crystalline product was filtered at the end of the cooling profile and visual analysis was carried out using optical microscopy.

4.2.10 Characterisation methods

Microscope images of crystals from 1 ml, 10 ml and 200 ml scale crystallisations were taken using a Leica DM1000 microscope equipped with an Infinity 2 microscopy camera at 4x magnification. In addition to the *in situ* PVM images, Raman spectra and images of the crystals from 350 ml scale crystallisations were obtained using a Thermo Scientific DXR Raman microscope (laser at 780 nm and OMNIC software version 8). All images were taken at 4x magnification. Scanning Electron Microscopy (SEM) images were obtained using a JEOL SEM6480LV SEM in which samples were coated with gold using an Edward Sputter Coater S15OB.

Face indexing was carried out using a Rigaku Oxford Diffraction (formerly Agilent Technologies) Xcalibur diffractometer with Mo-K_α (λ=0.71073 Å) radiation. Unit cell screenings were carried out at 150 K with the temperature controlled using an Oxford Cryosystems Cryostream 700. Face indexing was then carried out using the CrysAlisPro 171.37.33 software.[134] Analysis of the crystal structure and morphology of β-SA and use of the BFDH morphology tool was carried out using Mercury 3.5.[141]

MALDI-TOF mass spectrometry was carried out using a Bruker autoflex speed instrument. The samples were run using dithranol in THF as a matrix and NaTFA as a cationizing agent and data were acquired in reflectron positive mode. Samples of SA from a 350 ml scale experiment (T_{sat} = 50 °C; 0.5% PP123) and PP123 starting material were each dissolved in THF (5 mg ml^{-1}) and spotted on a MTP384 polished steel plate and calibrated using PEG4000. Data were also collected for concentrations of 0.5 mg ml^{-1} and 0.05 mg ml^{-1} of the PP123 starting material in order to determine the detection limit of the technique for the polymer.

Experimental information for the DSC, PXRD, NMR and FTIR measurements undertaken are detailed in Chapter 3.

4.3 Characterisation of SA starting material

4.3.1 Polymorphism

The two polymorphic forms of SA are distinguishable through PXRD; Figure 4.10 shows the diffraction patterns of each form calculated from single crystal data, along with experimental patterns from the SA sample used. Figure 4.10c shows the PXRD pattern of the starting material indicating that it is the β polymorphic form of SA.

Often samples are ground using a mortar and pestle in preparation for PXRD analysis in order to produce a more uniform particle size and shape and prevent preferred orientation effects in the diffraction pattern. However, care must be taken when applying this sample preparation method as sometimes dry grinding can induce changes in the solid form of the sample and subsequently produce misleading results. It was reported by Trask *et al.* that upon dry or liquid assisted (with a polar solvent) grinding of β-SA in a mechanical mill no polymorphic transformation is observed. However, it was also shown that grinding in a mechanical ball mill in the presence of several drops of a less polar solvent induces a transition to the metastable α-SA.[152] In contrast to these findings, it was found in the present study that dry grinding of a sample of SA using a mortar and pestle for 5 minutes drove the partial transition from β-SA to α-SA. Moreover, within as little as 30 seconds of grinding, peaks representative of the α-form were observed in the PXRD pattern. Diffraction peaks from the β-SA pattern remain dominant in the PXRD pattern; however, the presence of the additional low intensity peak at 22° 2θ is characteristic of α-SA (Figure 4.10d). An additional experiment was carried out in which the sample was ground in a mortar and pestle for 20 minutes in attempt to drive the transition to completion. The peaks for β-SA remain dominant but in addition to the α-SA peak at 22° 2θ, a weak peak characteristic of α-SA is evident at 27° 2θ (Figure 4.10e).

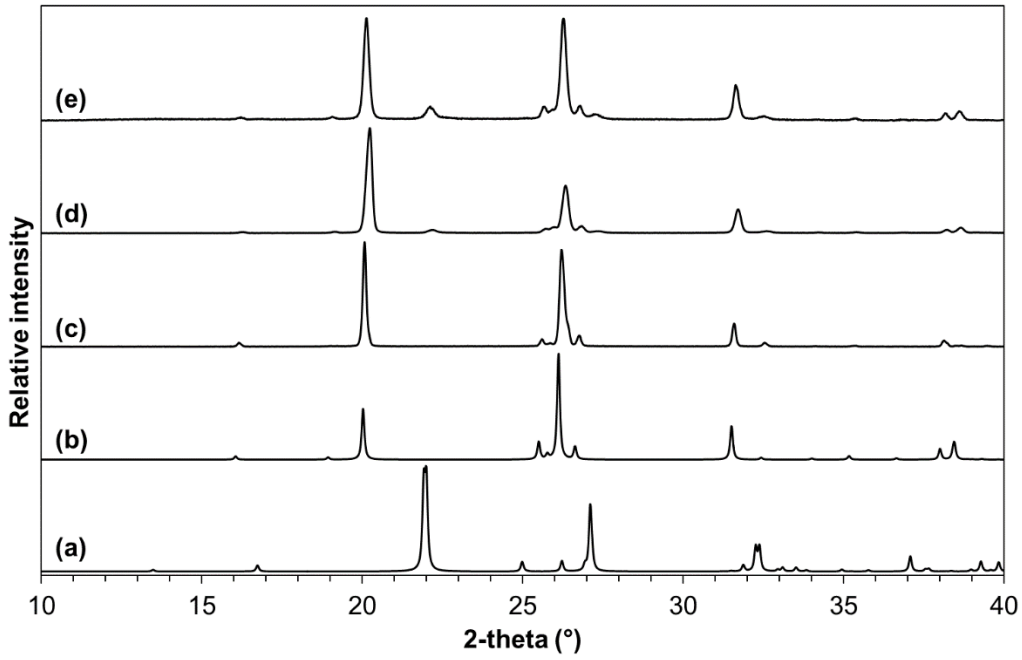

Figure 4.10 - PXRD patterns of SA: (a) calculated from the structure of the triclinic α-polymorph (CSD ref. code = SUCACB07), (b) calculated from the structure of the monoclinic β-polymorph (CSD ref. code = SUCACB02), (c) β-SA starting material, (d) after 5 minutes grinding and (e) after 20 minutes grinding.

As a result of this observation all samples for PXRD analysis were prepared without grinding, although preferred orientation of varying degrees of severity was evident in these, due to the different crystal morphologies produced in this study.

The polymorphic forms of SA are also distinguishable through Raman spectroscopy (Figure 4.11 and Figure 4.12).

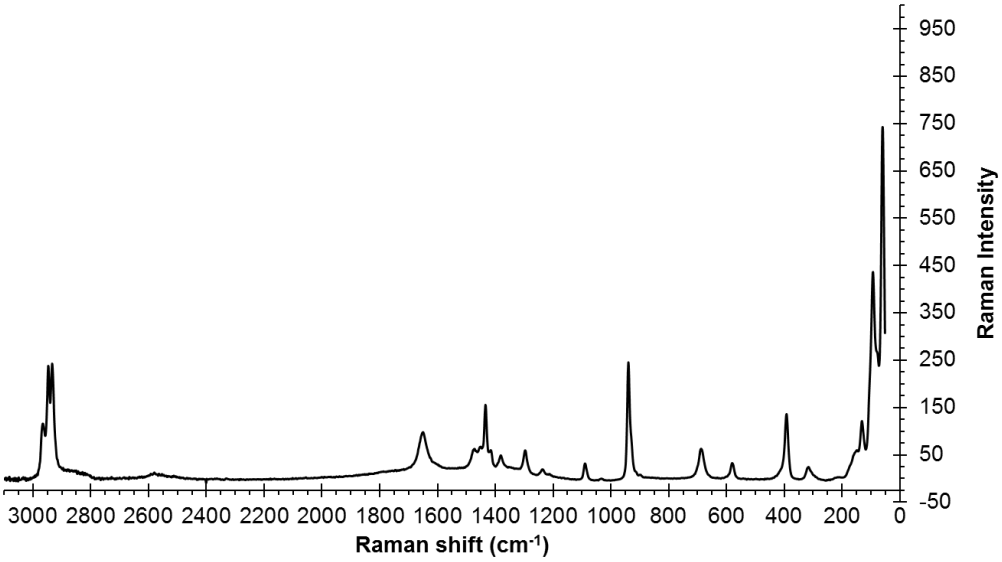

Figure 4.11 - Raman spectrum of α-SA.

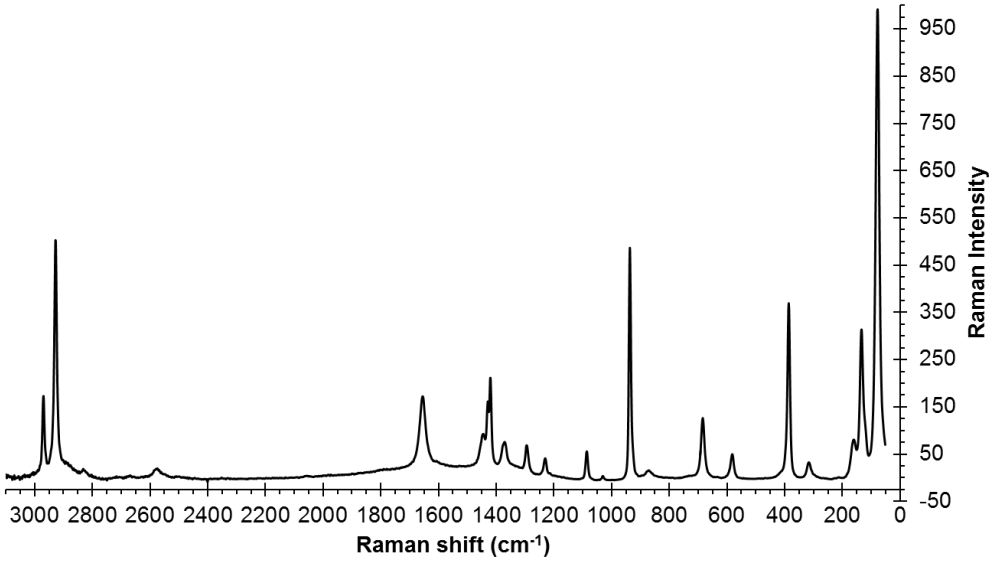

Figure 4.12 - Raman spectrum of SA obtained from Sigma Aldrich (β-SA).

Differential scanning calorimetry (Figure 4.13) shows the melting of α-SA (onset: 186.7 °C) which is followed by decomposition. The melting point of β-SA is not observed since the polymorphs are enantiotropically related and the β-form converts to the α-form prior to melting between 140-160 °C (as shown in the insert).

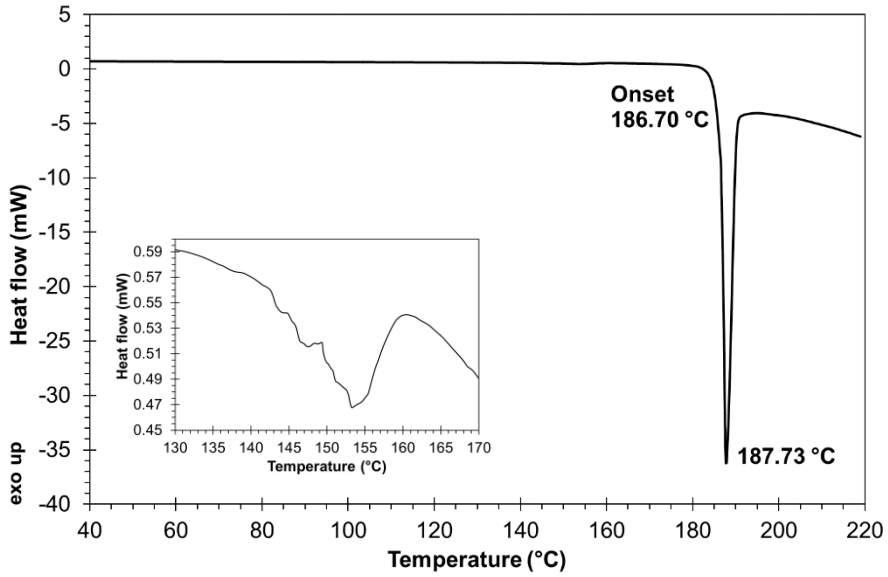

Figure 4.13 - DSC trace of SA obtained from Sigma Aldrich, with the inset indicating the thermal event corresponding to the transformation from β to α-SA.

4.3.2 Solubility

The solubility of β-SA was measured using turbidity and imaging in the Crystalline platform from Technobis Crystallization Systems in two solvents: water and ethanol (Figure 4.14).

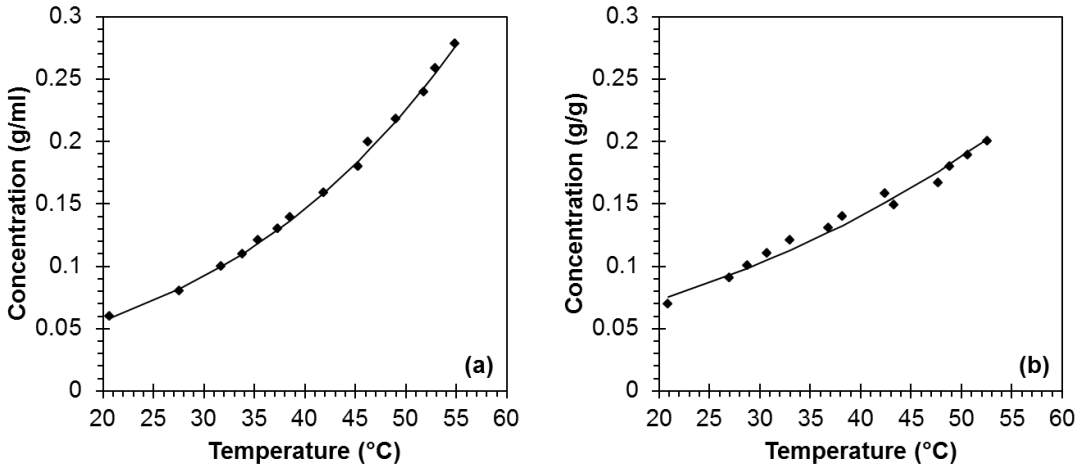

Figure 4.14 - Solubility curve of β-SA in (a) water and (b) ethanol with lines of fit based on a Van't Hoff functional form as a guide to the eye.

4.3.3 Crystal morphology

The morphology of the SA raw material is non-uniform and exhibits rounded, irregular edges, as shown in Figure 4.15.

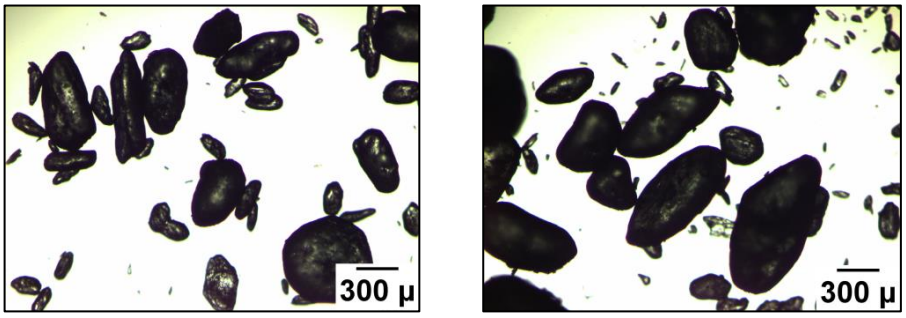

Figure 4.15 - Microscope images showing crystal morphology of SA obtained from Sigma Aldrich.

4.4 Identification of a polymer additive: initial crystallisations (1 ml scale)

Initial 1 ml scale cooling crystallisations were carried out using magnetic bottom stirring in order to identify a suitable polymer additive to use in the planned morphology modification study. Experiments were carried out in water and in ethanol with two initial polymers selected; these were polyethylene glycol 200 (PEG200) and Pluronic P123 (PP123), used at a starting concentration of 1% as well as a control with no polymer present.

The PEG200 had very little effect on the resulting crystal morphology from both solvents and in crystallisations from ethanol, the presence of the PP123 additive also had little effect on the crystal morphology. In contrast, in aqueous solutions containing PP123, a large change in crystal morphology was observed: it was found that the presence of the PP123 additive at the high initial concentration used in this screening experiment effectively modified the crystal morphology of SA from plates to needles (Figure 4.16).

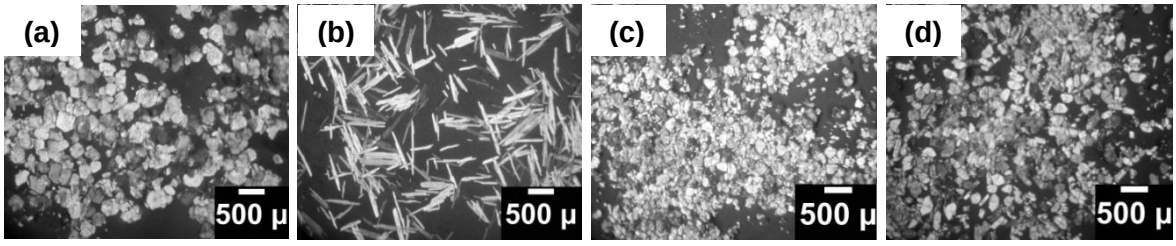

Figure 4.16 - Microscope images of SA crystals from: (a) water, no additive, (b) water, 1% PP123, (c) ethanol, no additive and (d) ethanol, 1% PP123.

As a result of the obvious morphology change produced with the PP123 additive, investigations into the effect of this polymer on the crystallisation of SA were pursued and a broader range of parameters investigated.

Preliminary investigations into the effect of PP123 on the morphology of SA were carried out by changing the concentration of SA and the concentration of PP123 at 1 ml scale with magnetic bottom stirring. Crystallisations were carried out with different concentrations of SA with 1.0% of PP123 present in solution. Figure 4.17 shows the crystals produced from these experiments. The images show that needle-like crystals are observed in each case, however, as the initial concentration of SA is increased, the crystals produced become broader and more rod-like.

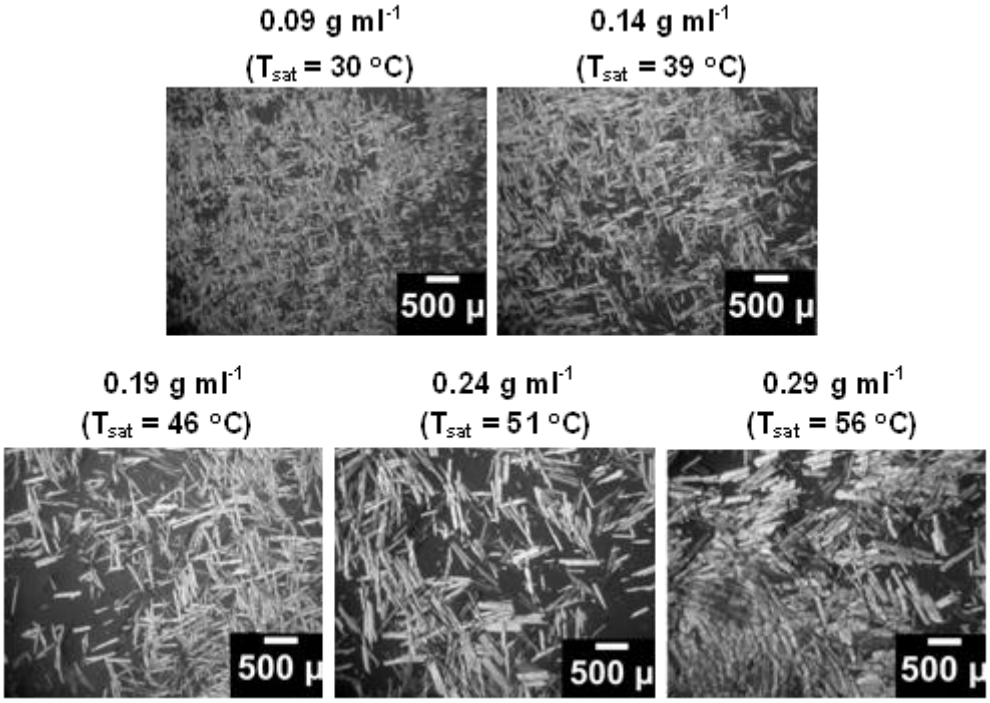

Figure 4.17 - Microscope images of SA crystals from crystallisation of different concentrations of SA in the presence of 1.0% PP123.

The concentration of PP123 was also varied to observe whether a smaller concentration of polymer additive could be used to produce the same effect. Interestingly, with smaller quantities of PP123, the crystals produced were broader and less needle-like (Figure 4.18).

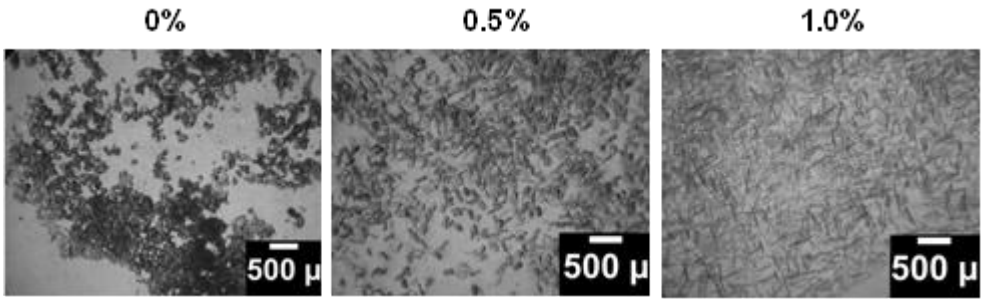

Figure 4.18 - Microscope images of SA crystals from crystallisation in the presence of different concentrations of PP123. The SA concentration is 0.12 g ml^{-1} (T_{sat} = 35 °C) in all cases.

The information obtained in these preliminary screening experiments was used to design the subsequent study.

4.5 Cooling crystallisation from water (1 ml scale)

As a result of the findings from the initial experiments, further analysis of the effect of the PP123 additive investigated concentrations of PP123 of 0-0.5% across a range of SA concentrations, at 1 ml scale. The crystal morphology was analysed using optical microscopy (Figure 4.19).

Crystallisations of SA from water with no additive present in solution produced plate-like crystals which increased in size with increasing saturation concentration of SA. In the presence of the smallest quantity of polymer additive (0.17%), limited effect of the additive is apparent on the crystal morphology observed at low saturation concentrations of SA. However, at a SA concentration of above 0.10 g ml^{-1} (T_{sat} = 32 °C), the crystal morphology becomes more block-like and at increasing saturation concentrations, the crystals become rod-like; this agrees with observations made in the initial experiments. When the concentration of PP123 in solution is increased a similar trend is observed, however needle-like crystals are produced at lower saturation concentrations of SA with higher concentrations of PP123 present.

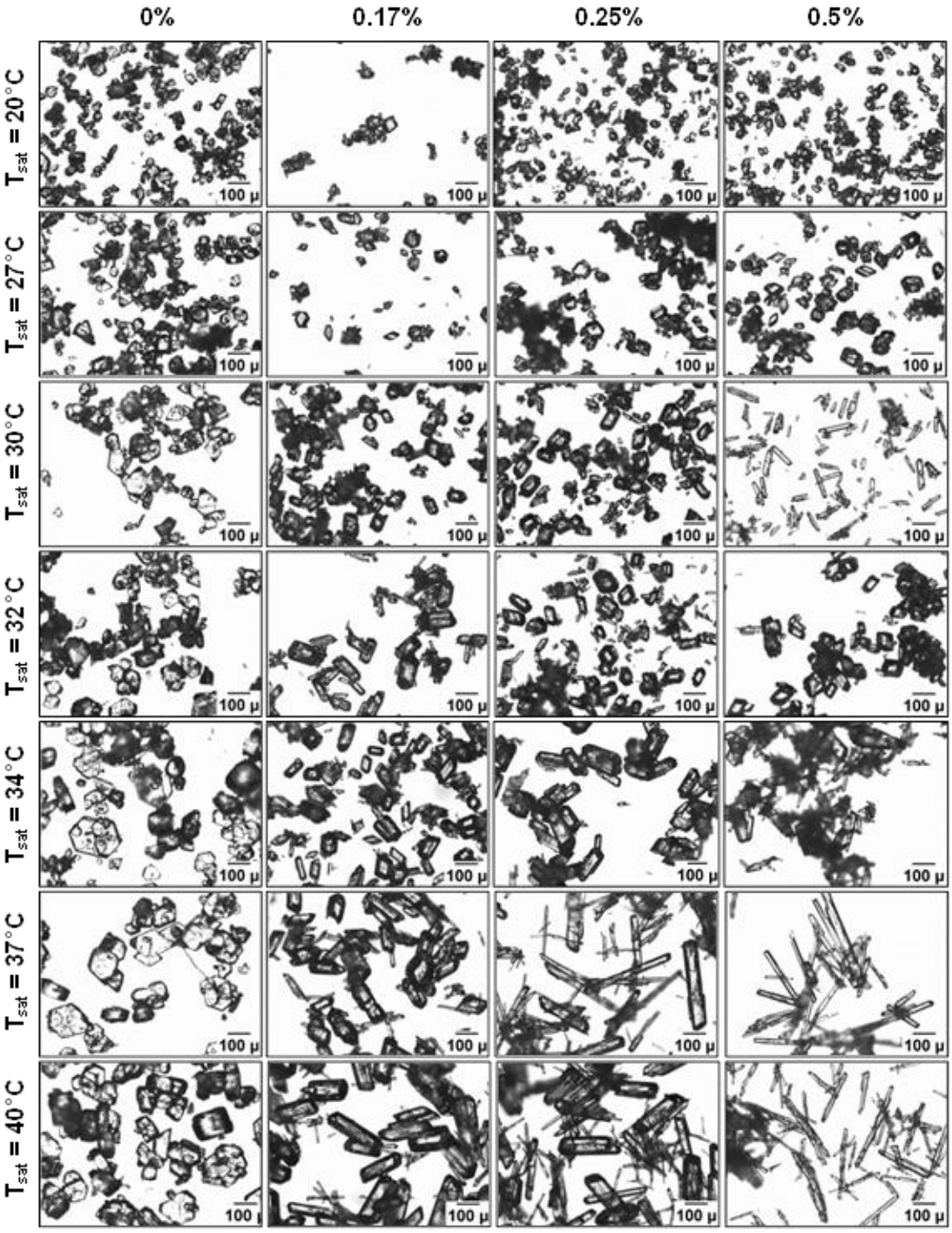

Figure 4.19 - Microscope images of SA crystals crystallised at 1 ml scale.

4.6 Effect of PP123 additive on solubility and MSZW at 3 ml scale

4.6.1 Experiments with magnetic bottom stirring

In experiments carried out at 1 ml scale, it was evident visually that solutions containing the PP123 additive nucleated at a lower temperature than those without the additive present. Solubility and MSZW measurements were thus carried out at 3 ml scale using magnetic bottom stirring with and without the polymer additive present in order to investigate this effect quantitatively. The solubility and cloud points were determined

using the combination of turbidity measurements and on-line imaging (Figure 4.20). It is clear that the presence of 0.5% PP123 additive in solution has no effect on the solubility of SA in water (Figure 4.20c). However, the cloud point results suggest that the addition of PP123 generates a shift in the MSZW of around 7-10 °C (Figure 4.20d) indicating an inhibiting effect of the additive on nucleation. The shift appears more prominent at low concentration of SA. A delay in nucleation has been observed in other studies into the effect of impurities on crystallisation.[42,44,60,157] This may be a result of the impurity supressing the development of the nucleus of critical size.[158] It was also confirmed through PXRD analysis that this shift was not due to nucleation of a different polymorphic form; the product remained the β-form. However, it should be noted that these measurements were performed at 3 ml scale and in small volumes primary nucleation is mainly a stochastic process. Findings by Kadam *et al*[159] have shown significant variation in the nucleation temperature at small scale; therefore repeat determinations would be essential to establish if this temperature shift is statistically relevant.

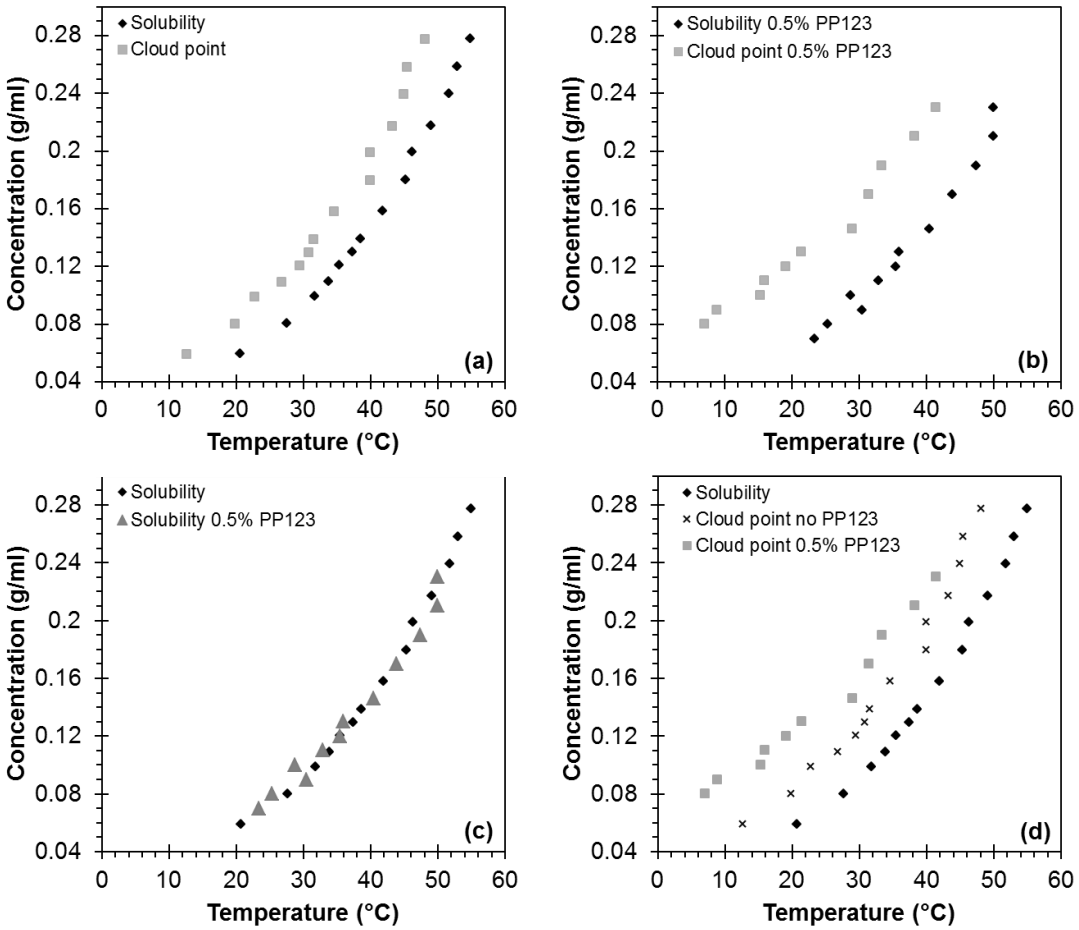

Figure 4.20 - Solubility and MSZW curves for SA in water at 3 ml scale with magnetic bottom stirring with (a) no PP123, (b) 0.5% PP123 and comparisons between (c) solubility with and without PP123 present and (d) MSZW with and without PP123 present.

Table 4.2 shows the nucleation temperature data for experiments without and with 0.5% PP123. The supersaturation ratio at nucleation does not change significantly with increased concentration of SA. In contrast, in the experiments with PP123 present the supersaturation ratio is higher at low concentrations of SA and falls as the concentration of SA increases.

Table 4.2 - Crystallisations at 3 ml scale (top) with no polymer and (bottom) with 0.5% PP123.

	T_{sat} (°C)	Initial conc. (g ml^{-1})	Temp. of nucleation (°C)	Equilibrium conc. at nucleation temp.	Supersaturation ratio at nucleation
3ml no polymer	20	0.059	12.60	0.04	1.56
	27	0.080	19.90	0.06	1.44
	32	0.099	22.80	0.06	1.54
	34	0.109	26.80	0.08	1.39
	35	0.120	29.50	0.09	1.34
	38	0.129	30.80	0.10	1.35
	39	0.139	31.60	0.10	1.40
	42	0.158	34.60	0.11	1.39
	45	0.180	40.00	0.15	1.23
	47	0.199	40.00	0.15	1.36
	49	0.217	43.30	0.17	1.28
	51	0.239	45.00	0.18	1.31
	53	0.258	45.40	0.19	1.39
	55	0.278	48.10	0.21	1.33

	T_{sat} (°C)	Initial conc. (g ml^{-1})	Temp. of nucleation (°C)	Equilibrium conc. at nucleation temp.	Supersaturation ratio at nucleation
3ml 0.5% PP123	27	0.080	7.10	0.03	2.85
	30	0.090	8.90	0.03	2.90
	32	0.100	15.30	0.04	2.28
	34	0.110	16.00	0.05	2.42
	35	0.120	19.10	0.05	2.24
	38	0.130	21.40	0.06	2.16
	40	0.146	29.00	0.09	1.67
	44	0.170	31.40	0.10	1.73
	46	0.190	33.40	0.11	1.76
	48	0.210	38.20	0.13	1.56
	50	0.230	41.40	0.16	1.48

4.6.2 Experiments with overhead stirring

Solubility and cloud point determinations were also carried out at 3 ml scale with magnetically controlled overhead stirring (Figure 4.21). In contrast to the results obtained

with magnetic bottom stirring, the cloud points determined show significant spread, making it difficult to draw accurate conclusions on the effect of the additive on the nucleation temperature. This may be due to the geometry of the stirrer being positioned too high in the solution to suspend the volume of solution in the vial resulting in non-uniform mixing conditions, a deduction supported by the non-uniform crystal morphology observed (Figure 4.23). Due to the apparatus being at another institution, repeat determinations were not possible in the timescales available. In contrast to the experiments with magnetic bottom stirring, no difference in MSZW is observed with 0.5% PP123 present (Figure 4.21c).

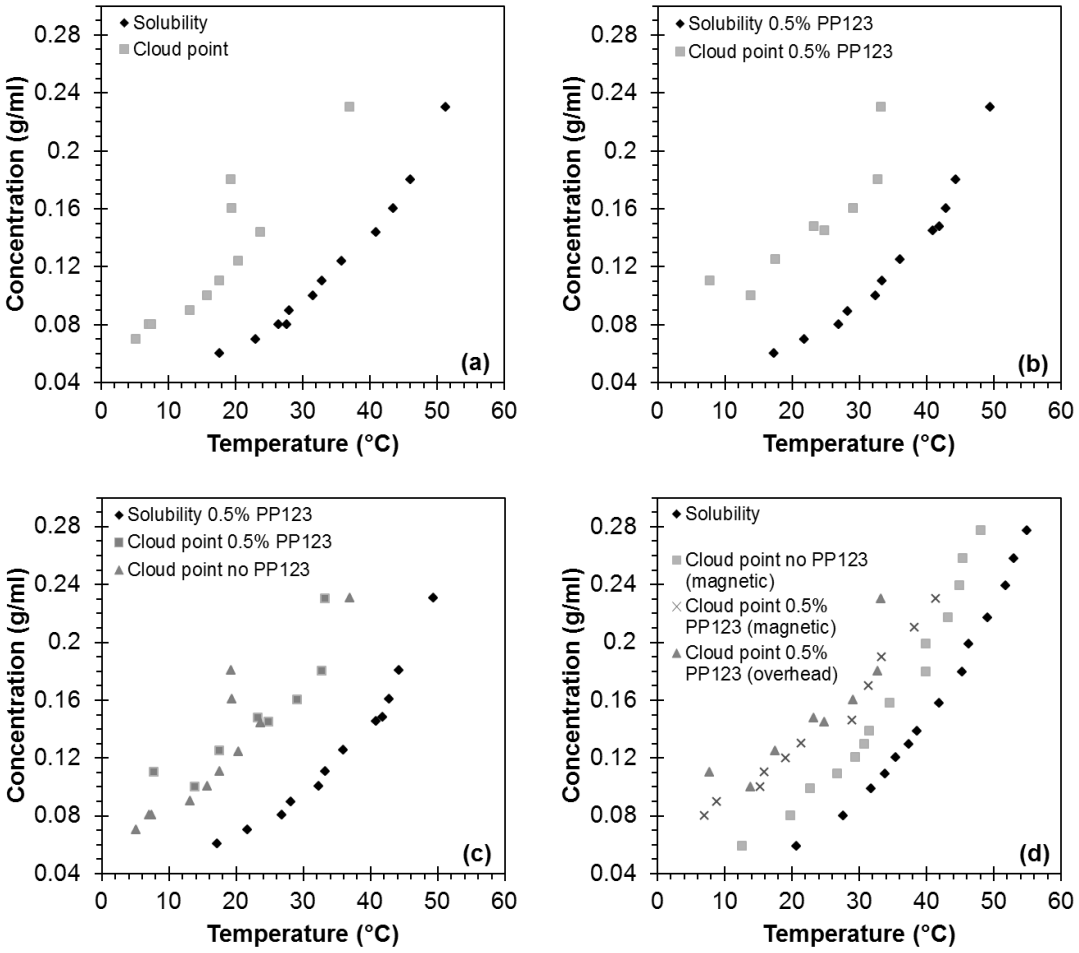

Figure 4.21 - Solubility and MSZW curves for SA in water at 3 ml scale with overhead stirring with (a) no PP123, (b) 0.5% PP123 and comparisons between (c) MSZW with and without PP123 present and (d) MSZW with type of stirring.

4.7 Effect of PP123 additive on morphology at 3 ml scale

On-line imaging was implemented for the duration of the heating and cooling profiles in the solubility and cloud point measurements at 3 ml scale. Images from crystallisations are shown in Figure 4.22 and Figure 4.23.

4.7.1 Experiments with magnetic bottom stirring

With magnetic bottom stirring (Figure 4.22), at low saturation (T_{sat} = 30 °C) the images suggest that there is no change in crystal morphology with 0.5% PP123 present. However, at higher saturation (T_{sat} = 40 °C) in the presence of polymer the SA crystals are elongated and needle-like whereas with no polymer present they remain non-uniform plates. These observations correlate with initial observations made in 1 ml scale crystallisations (Section 4.5). As the concentration of SA is increased to T_{sat} = 50 °C, the crystals grown in the presence of polymer are more rod-like. It is clear that in the presence of the PP123, the concentration of SA affects the morphology of the resulting crystals whereas with no polymer present the crystal shape is unchanged with increasing SA concentration.

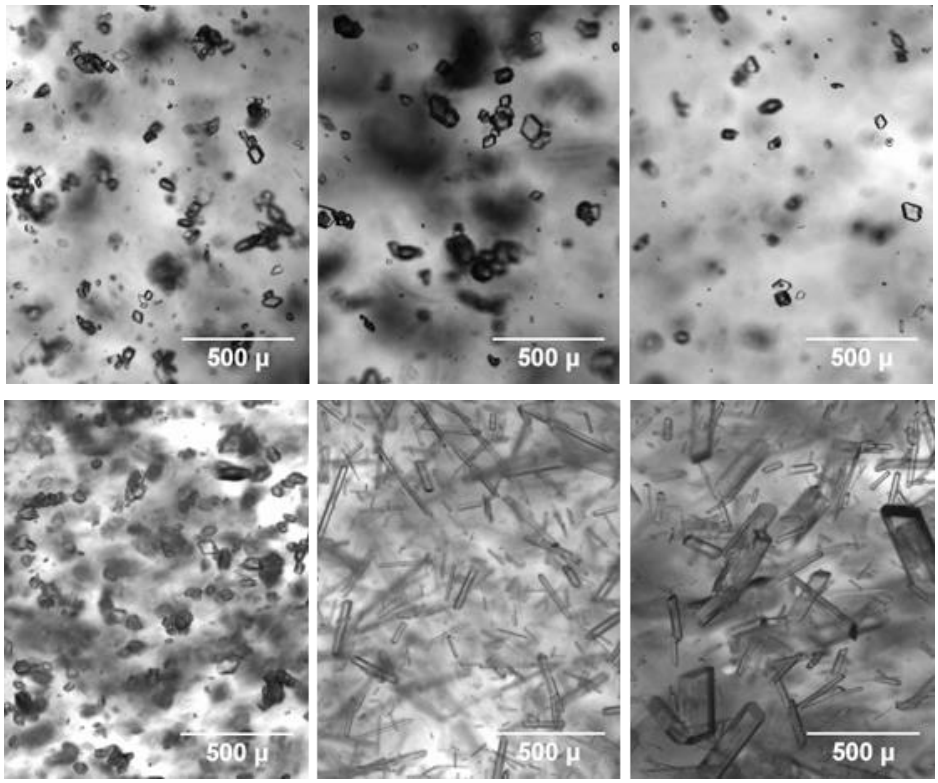

Figure 4.22 - On-line images from experiments with magnetic bottom stirring: (top) crystals of SA from T_{sat} = 30 °C, 40 °C and 50 °C with no polymer present; (bottom) crystals of SA from T_{sat} = 30 °C, 40 °C and 50 °C all with 0.5% PP123 present.

4.7.2 Experiments with overhead stirring

The images from the experiments carried out with overhead stirring are shown in Figure 4.23. It is clear that the mixing conditions were not optimal in these experiments as the crystal morphology and particle size is non-uniform. Although overhead stirring offers the benefit of lack of attrition of crystals at the bottom of the vessel, this outcome again highlights the importance of the geometry and height of the stirrer in the vessel. There is still, however, a clear change in crystal shape in the presence of 0.5% PP123 with overhead stirring; the crystals become more elongated as the saturation concentration of SA is increased. Due to the lower nucleation temperature with overhead stirring, crystallisation was not observed for the 0.5% PP123, T_{sat} = 30 °C experiments.

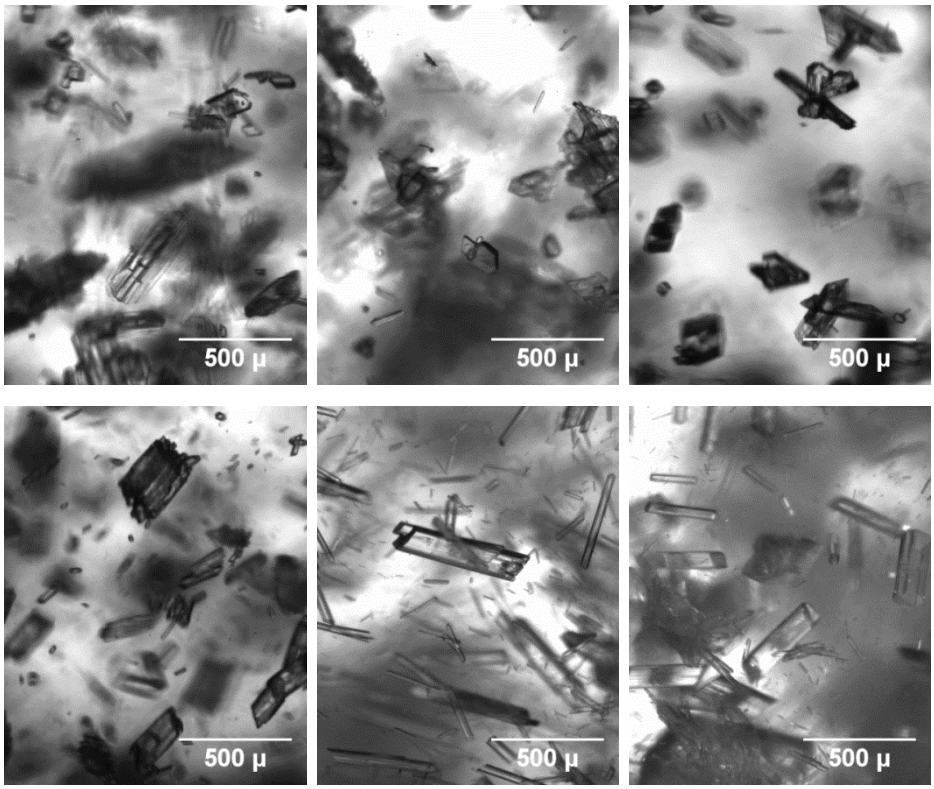

Figure 4.23 - On-line images from experiments with overhead stirring: (top) crystals of SA from T_{sat} = 30 °C, 40 °C and 50 °C with no polymer present; (bottom) crystals of SA from T_{sat} = 32 °C, 40 °C and 50 °C with 0.5% PP123 present.

4.8 Cooling crystallisation from water (10 ml scale)

One of the limitations of working at 1 ml scale lies in the accuracy of weighing very small quantities of the PP123 additive into the 1.5 ml vials. This limits the ability to draw accurate conclusions about the effect of the different crystallisation conditions on the crystal morphology produced. The scale of the crystallisations was therefore increased to 10 ml.

Initial experiments at this scale were carried out using magnetic bottom stirring. A morphology change was observed when the additive was present, but with this mode of stirring the crystals were very non-uniform, both with and without the PP123 present (Figure 4.24). This suggests that the mixing conditions are non-uniform and crystal breakage may be occurring due to the abrasive action of the stirring bar.[160]

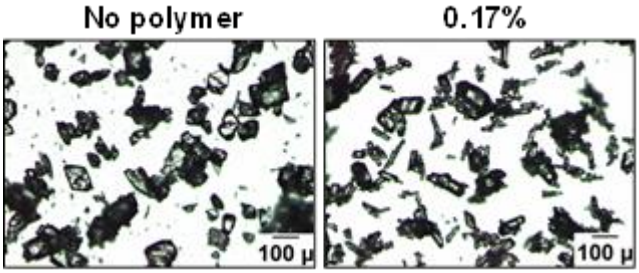

Figure 4.24 - Microscope images of crystals produced with magnetic bottom stirring at 10 ml scale.

As a result, subsequent crystallisations at this scale were carried out using overhead stirring (with the impeller positioned effectively in the solution for these experiments) with a range of SA and polymer additive concentrations investigated. The overhead stirring at this scale produced larger and more uniform particles than the magnetic bottom stirring, enabling more reliable analysis of trends in the crystal morphology with the different conditions. Microscope images of the crystals produced in the experiments carried out are shown in Figure 4.25.

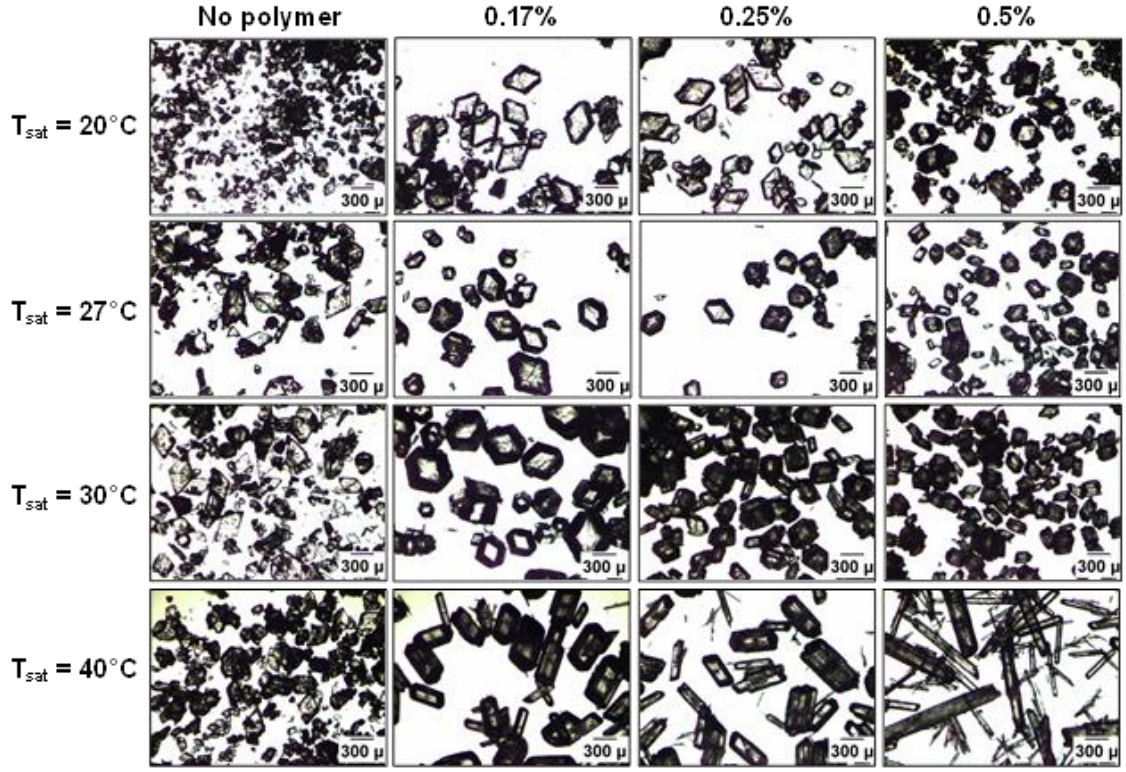

Figure 4.25 - Microscope images of product of crystallisations at 10 ml scale.

It is clear that the effect of the polymer is dependent on both the concentration of SA and the concentration of PP123 present. With no PP123 present in solution, SA crystallises from water in a non-uniform plate-like morphology, in agreement with previous reports.[153,154,161] At a concentration of 0.5% PP123 and a low concentration of SA (T_{sat} = 20 °C) block-like crystals are produced, however they are relatively non-uniform in terms of their morphology and size. This may be due to poor mixing; at higher concentrations of SA the morphology is more uniform. As the concentration of SA is increased to T_{sat} = 30 °C, the crystals remain block-like, however, the faces appear to have a more irregular surface. Crystallisation carried out at T_{sat} = 40 °C at 0.5% polymer yielded crystals of needle-like morphology. This trend of changing morphology with changing saturation of SA can also be observed at lower concentrations of PP123; the block-like crystals are accessible at higher saturations with lower concentration of PP123, with significantly improved uniformity in crystal size. As noted above, formation of block-like crystals is very favourable in terms of ease of downstream processing of a solid form. Crystals of this favourable block-like morphology observed at low saturation concentrations of SA with overhead stirring were not previously observed with magnetic bottom stirring under the same conditions.

It is interesting to note that very low concentrations of the PP123 additive are required to exert a large effect on the crystal morphology. Despite these substantial morphology changes, the polymorphic form of SA remained the β-form in all crystallisations, as confirmed by PXRD.

4.9 Cooling crystallisation from ethanol (10 ml scale)

Cooling crystallisations with overhead stirring were also carried out from ethanol at 10 ml scale in the presence of the PP123 additive at a saturation concentration of T_{sat} = 30 °C. As observed previously with magnetic bottom stirring, the polymer was found to have no effect on the crystal morphology on recrystallisation from ethanol (Figure 4.26).

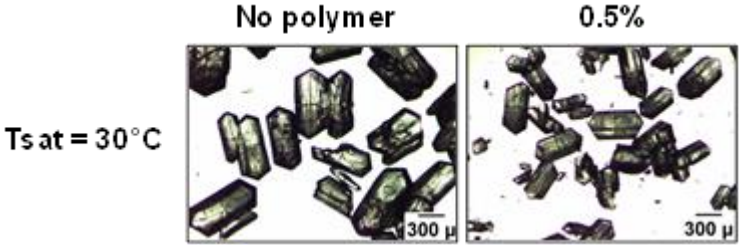

Figure 4.26 - Microscope images of crystallisations of SA from ethanol in the presence of different concentrations of PP123.

4.10 Cooling crystallisation from water (200 ml scale)

Further scaling-up of the crystallisation was carried out and it was found to be possible to produce the desirable block-like crystals at 200 ml scale under the same conditions as at 10 ml scale. Experiments were also carried out with magnetic bottom stirring for comparison and, as observed at 10 ml scale, the resulting crystals were smaller and non-uniform in shape and size.

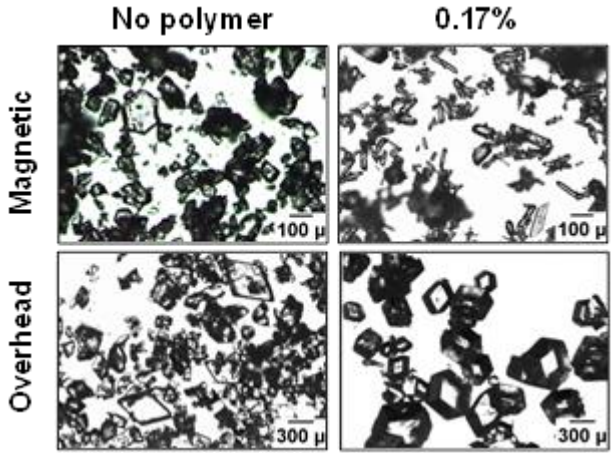

Figure 4.27 - Microscope images of crystals produced at 200 ml scale.

4.11 Scale-up of cooling crystallisation from water to 350 ml scale and implementation of Process Analytical Technologies (PAT)

4.11.1 Aims

This work was carried out in the Department of Chemical Engineering at Loughborough University in collaboration with Dr Elena Simone and Professor Zoltan Nagy. The aim was to scale up crystallisations of SA from water in the presence of PP123 (previously carried out at the University of Bath at smaller scales) and to implement PAT (FBRM, PVM and Raman) to monitor the crystallisation. Such PAT is used increasingly as it allows reactions and crystallisations to be monitored and provide real-time information. Use of PAT also enabled data to be collected on the nucleation temperature of the experiments, allowing for comparisons to be made with small scale crystallisations carried out in the Technobis Crystallization Systems Crystalline device.

In this work several PAT tools were used in combination to follow the crystallisation (Figure 4.28). Particle vision and measurement (PVM) was used to observe the crystal shape and size *in situ*. Focused Beam Reflectance Measurement (FBRM) was used to detect the nucleation temperature and monitor the particle development. Raman

spectroscopy was used to detect any changes in solid form and provide an additional method of detecting the nucleation temperature.

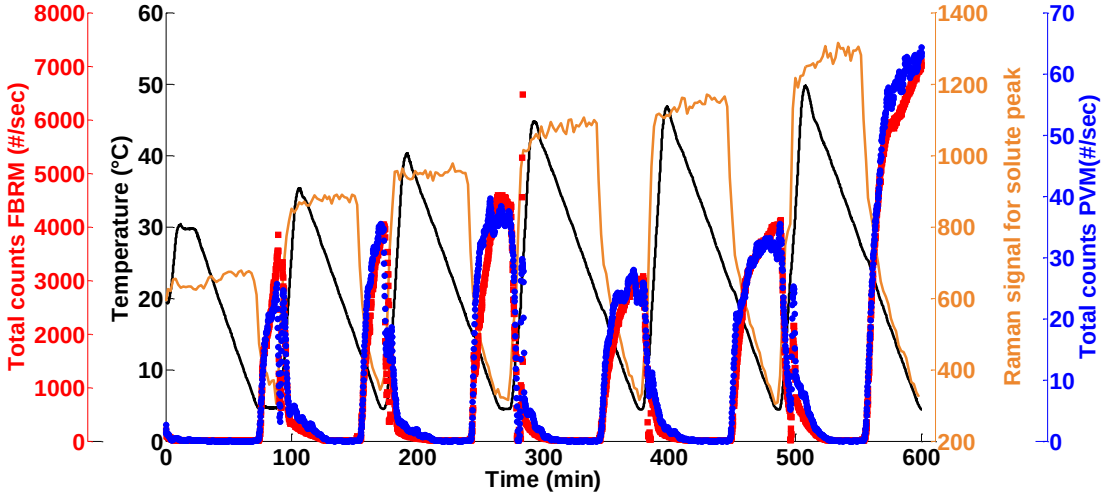

Figure 4.28 - A combination of PAT tools were used to follow up to six consecutive crystallisation experiments containing 0.17% PP123 with increasing concentration of SA; the FBRM, Raman and PVM measurements during six cycles are shown here (see experimental section for details of how the cycling was carried out).

4.11.2 Raman analysis

For the Raman measurements, a characteristic peak for each of the solute (840 cm^{-1}) and the solid (937 cm^{-1}) were identified (Figure 4.29). These peaks were used to detect the point of nucleation and dissolution in the crystallisation. Upon dissolution of the solid the solid peak decreases in intensity and the solute peak increases in intensity and *vice versa* for nucleation.

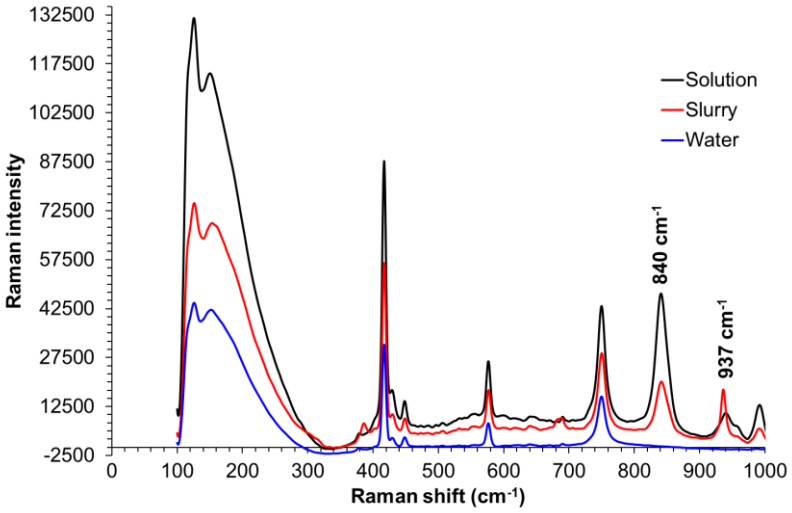

Figure 4.29 - Raman spectra for water, the SA solution and the SA slurry.

It is thus possible to produce a solubility curve using the Raman data. A SA solution was heated from 10 °C to 50 °C at 0.1 °C min^{-1} and the Raman intensity of the solute peak was monitored as the solid dissolved (Figure 4.30, left). The Raman intensity of the solute peak was also plotted at four concentrations of SA (Figure 4.30, right), and these data related to produce the solubility curve; this is seen to be in reasonable agreement with that determined through imaging and turbidometric analysis in the Technobis Crystallization Systems Crystalline (Figure 4.31).

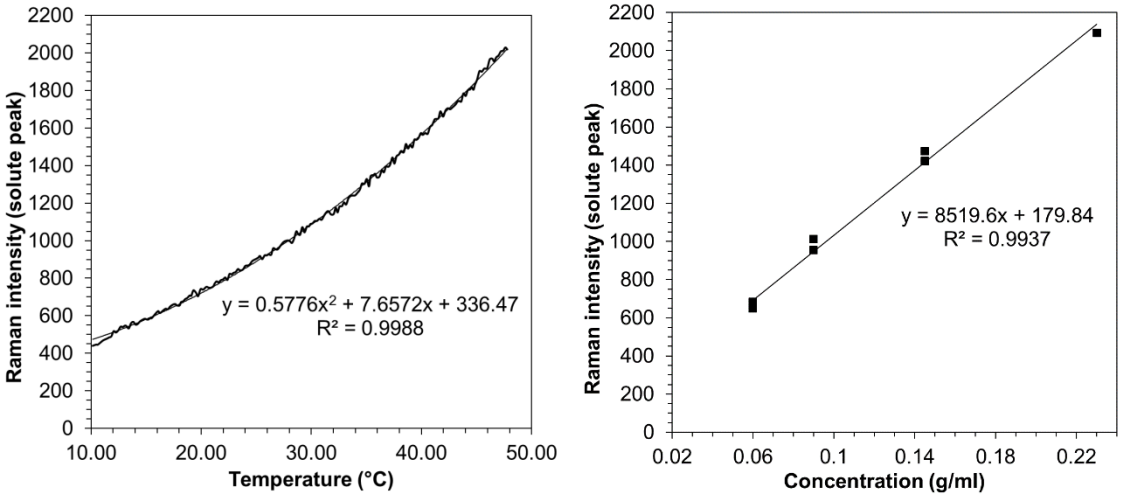

Figure 4.30 - Variation of Raman intensity with (left) temperature and (right) SA concentration.

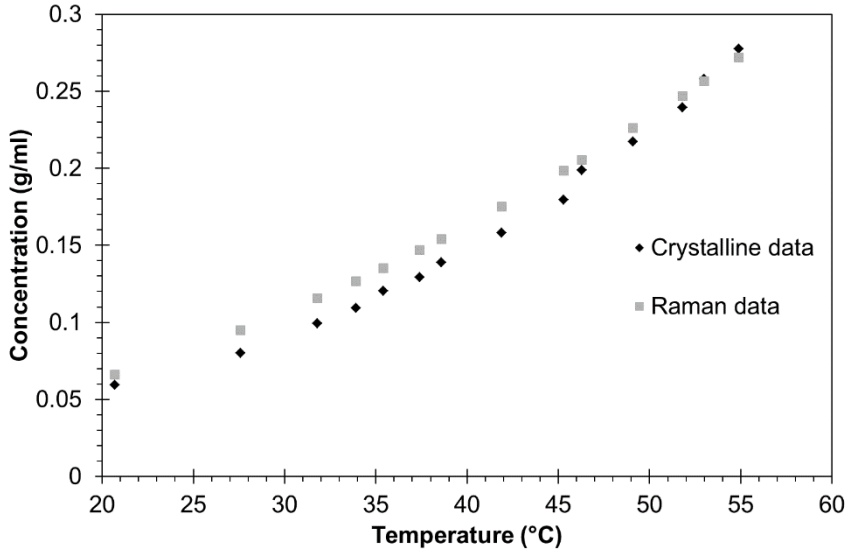

Figure 4.31 - Comparison of SA solubility curve in water using Raman data and turbidometric analysis and imaging (Crystalline data).

4.11.3 Effect of PP123 additive on MSZW at 350 ml scale

The MSZW of SA in water at 350 ml scale is shown in Figure 4.32a. The nucleation temperature was detected using the FBRM data. The results suggest that at this larger scale, the addition of PP123 in the range of concentrations studied (0.17%, 0.25% and 0.50%) does not significantly change the cloud point. This is in contrast to the findings at smaller scale and may result from the different mechanisms of primary nucleation at the two scales. In small volumes primary nucleation is mainly a stochastic process which, for this case, seems to be inhibited by the additive. At larger scales, where primary nucleation mainly follows a deterministic mechanism, the additive seems not to have a significant effect.[159] In Figure 4.32b the two MSZW curves in the absence of polymer, at 3 ml and 350 ml, are shown together. At a temperature higher than 27 °C the two curves start to overlap while, at lower temperature, the cloud point at the small scale is higher compared to the larger scale. The opposite is true for the MSZW with PP123 present; the cloud point at the small scale is lower compared to the large scale (Figure 4.32c).

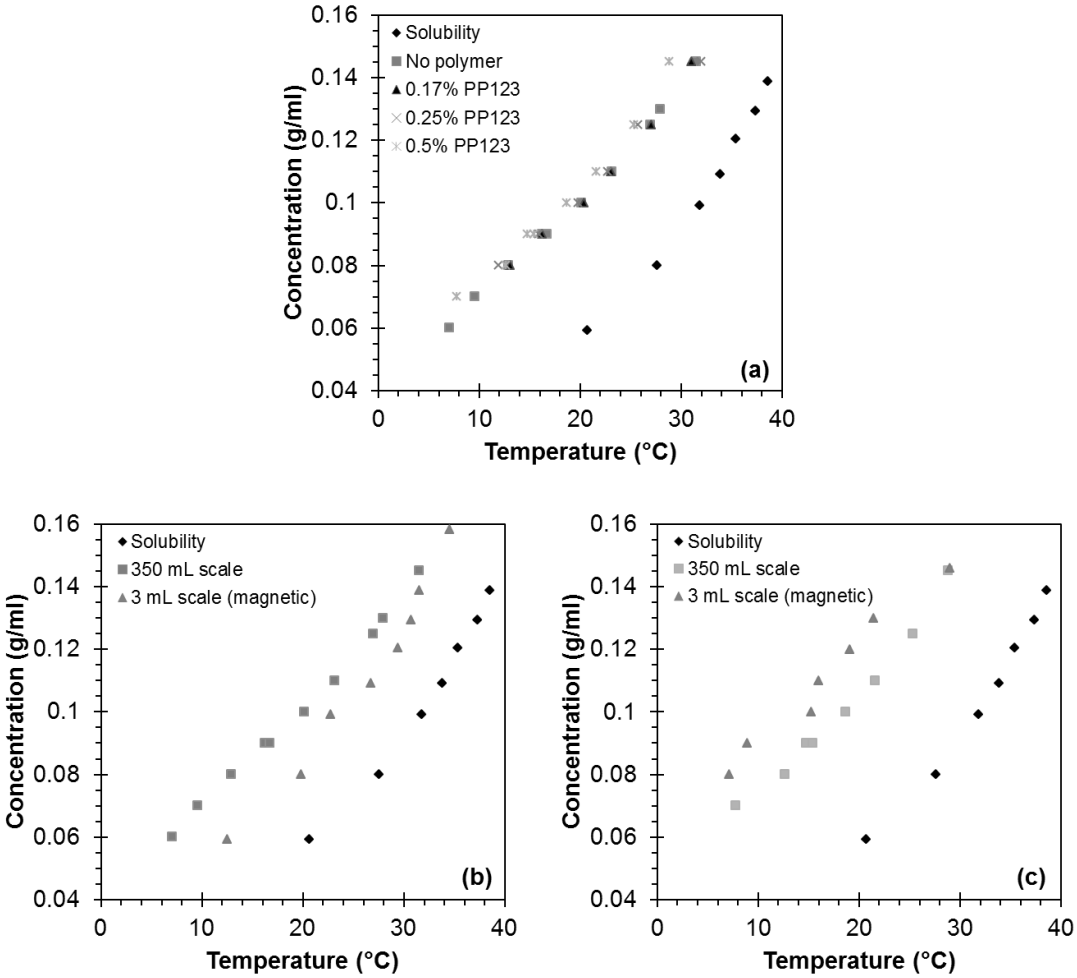

Figure 4.32 - MSZW curves for SA in water at 350 ml scale with overhead stirring with (a) different concentrations of PP123 present and comparisons between (b) MSZW at 3 ml and 350 ml scale without PP123 present and (c) MSZW at 3 ml and 350 ml scale with PP123 present.

However, it should be noted that measurements of cloud point were carried out using different techniques for each scale (turbidity and on-line imaging for the 3 ml experiments, FBRM for the 350 ml experiments); therefore a fair comparison between the two sets of data is not possible.

4.11.4 Crystal morphology at 350 ml scale

Microscope images of the dry product from crystallisations carried out at 350 ml scale are shown in Figure 4.33 and Figure 4.34 and *in situ* images from the PVM probe are shown in Figure 4.35. The trend in the morphology change observed at this scale is similar to that described above for the 10 ml batch experiments. The morphology modification induced by the polymer additive is thus seen to be scalable. Additionally, a broader range of concentrations of SA were investigated at this scale allowing for more detailed analysis of the crystal morphology.

As observed in the 10 ml crystallisations with overhead stirring, in the absence of polymer SA crystallises in non-uniform, diamond shaped plates (Figure 4.34). At higher temperatures (e.g. T_{sat} = 40°C) the resulting crystal faces are rounded and less well-defined than those of crystals produced at lower temperatures suggesting that the surfaces may have undergone roughening (see Section 1.2.3). Upon addition of 0.5% PP123 at low saturation of SA, crystals grow in a block-like morphology where the crystal faces appear to be growing at approximately equal rates. The shape of these block-like crystals is more uniform compared to those obtained in the equivalent 10 ml experiments. At higher saturations and high polymer concentration the shape of the crystals changes from block-like to needles. Figure 4.33 shows crystals obtained for T_{sat} = 30 °C, 0.5% polymer: the shape is still block-like but the surface of the crystals appears irregular, presumably because of the inhibiting effect of the polymer on growth. At higher saturation and the same polymer concentration (0.5%), the crystals grow as needles. Again, as observed in the 10 ml experiments, crystallisations carried out with a lower concentration of PP123 present showed the same trend in morphology change as the saturation of SA is increased. The block-like crystals can once again be accessed at higher saturation with less polymer present.

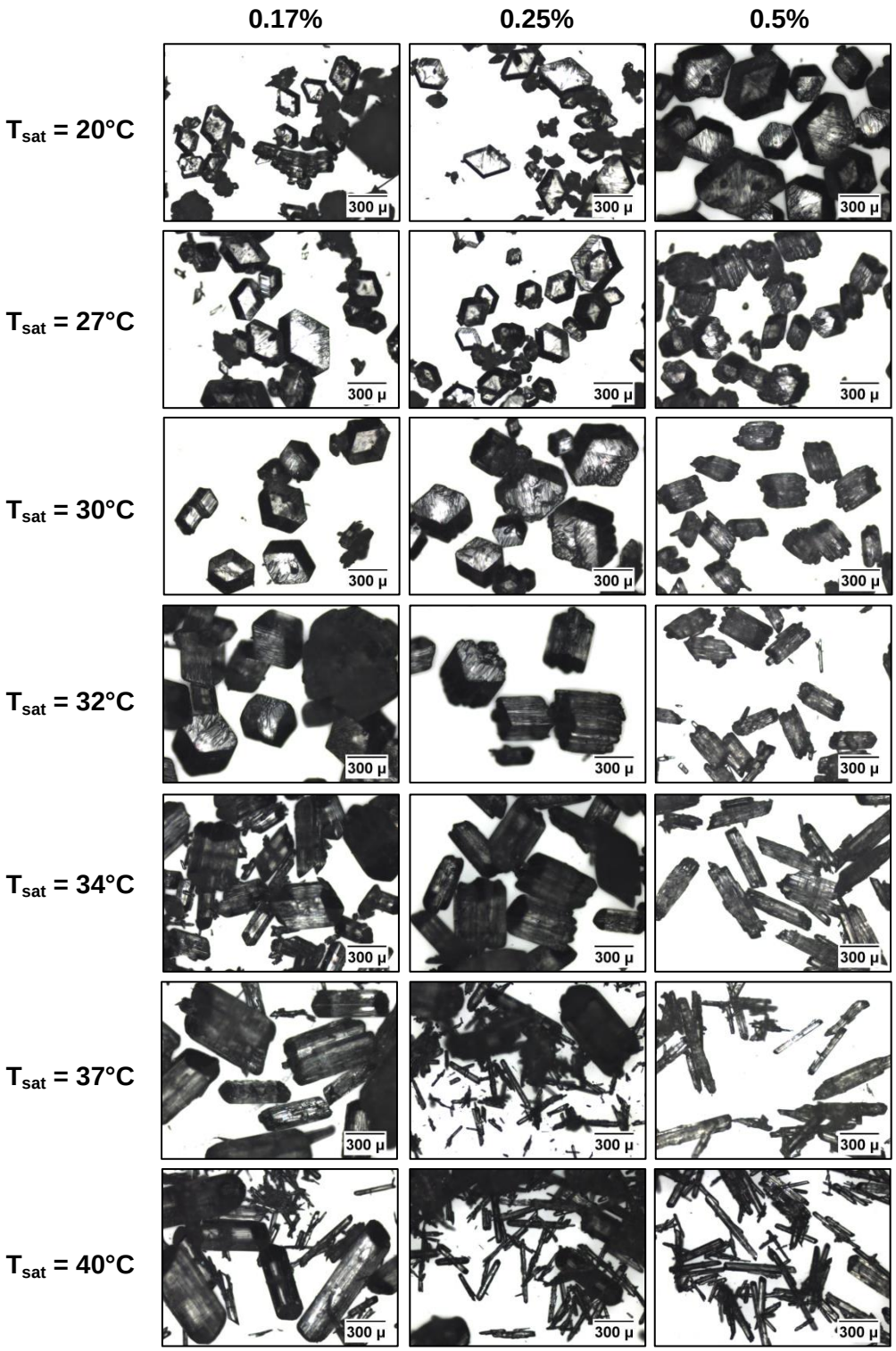

Figure 4.33 - Microscope images of products of crystallisations at 350 ml scale with different concentrations of PP123 present.

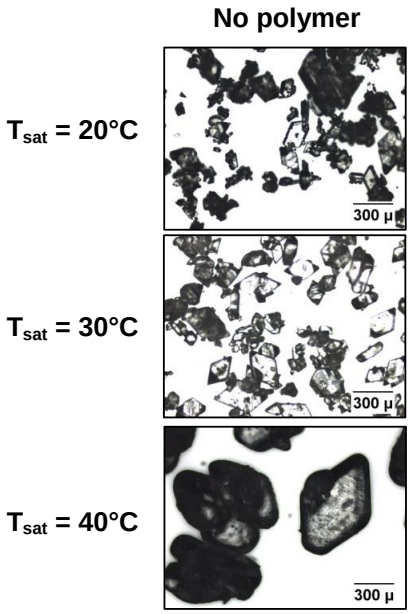

Figure 4.34 - Microscope images of products from crystallisations at 350 ml scale with no polymer.

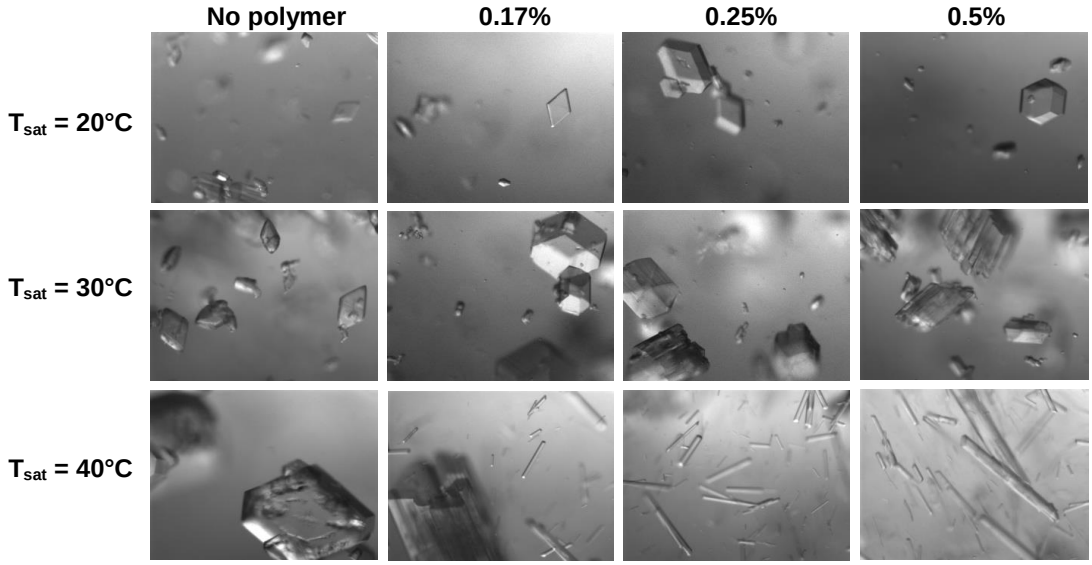

Figure 4.35 - PVM images from 350 ml crystallisations under different conditions.

The calculated initial supersaturation ratio at nucleation, in crystallisations both with and without additive present, was found to be higher for low saturation concentrations of SA, decreasing as the saturation temperature rises (Table 4.3). This may explain why at high saturation concentrations, an enhanced effect of the additive was observed compared to lower saturation concentrations. At low supersaturation fewer crystals form, however with high initial concentrations more material is available in solution for the crystals to grow, which may explain why the particles obtained were considerably larger (or, in the case of needles, longer) compared to those produced at low saturation concentrations.

Table 4.3 - Calculation of supersaturation ratio for each experiment carried out 350 ml scale.

	T_{sat} (°C)	Initial conc. (g ml^{-1})	Temp. of nucleation (°C)	Equilibrium conc. at nucleation temp.	Supersaturation ratio at nucleation
350ml no polymer	20	0.060	7.03	0.03	2.14
	27	0.080	12.89	0.04	2.07
	30	0.090	16.22	0.05	1.95
	32	0.100	20.11	0.06	1.78
	34	0.110	23.11	0.07	1.68
	37	0.125	26.94	0.08	1.58
	38	0.130	27.93	0.08	1.56
	40	0.145	31.52	0.10	1.47

	T_{sat} (°C)	Initial conc. (g ml^{-1})	Temp. of nucleation (°C)	Equilibrium conc. at nucleation temp.	Supersaturation ratio at nucleation
350ml 0.5% PP123	27	0.080	12.66	0.04	2.10
	30	0.090	15.43	0.04	2.04
	32	0.100	18.66	0.05	1.91
	34	0.110	21.57	0.06	1.81
	37	0.125	25.36	0.07	1.70
	40	0.145	28.83	0.09	1.67

	T_{sat} (°C)	Initial conc. (g ml^{-1})	Temp. of nucleation (°C)	Equilibrium conc. at nucleation temp.	Supersaturation ratio at nucleation
350ml 0.25% PP123	27	0.080	11.95	0.04	2.18
	30	0.090	15.93	0.05	1.98
	32	0.100	19.77	0.06	1.81
	34	0.110	22.71	0.06	1.71
	37	0.125	25.75	0.07	1.67
	40	0.145	32.00	0.10	1.44

	T_{sat} (°C)	Initial conc. (g ml^{-1})	Temp. of nucleation (°C)	Equilibrium conc. at nucleation temp.	Supersaturation ratio at nucleation
350ml 0.17% PP123	27	0.080	13.07	0.04	2.05
	30	0.090	16.2	0.05	1.96
	32	0.100	20.39	0.06	1.75
	34	0.110	23.09	0.07	1.68
	37	0.125	27.06	0.08	1.57
	40	0.145	31.01	0.10	1.50

NB. T_{sat} = 20 °C has been omitted for experiments with PP123; in these the temperature was held at 5 °C for nucleation to occur, therefore no measurement was made of nucleation temperature.

4.12 Effect of cooling rate on crystal morphology at 10 ml scale

Preliminary investigations into the effect of the cooling rate on the crystal morphology produced in the presence of different concentrations of the PP123 additive were also carried out at the lower cooling rate of 0.1 °C min^{-1} (the previous experiments having used a cooling rate of 0.5 °C min^{-1}). Figure 4.36 shows the morphology of the crystals produced at these two cooling rates, and it can be seen that at slower cooling rates, the polymer additive has an enhanced effect. For example, with a starting concentration of 0.09 g ml^{-1} of SA (T_{sat} = 30 °C) and 0.17% PP123, at a cooling rate of 0.5 °C min^{-1} block-like crystals were produced. However, at the slower cooling rate with the same concentrations of SA and polymer additive, rod-like crystals were produced, resembling those produced at higher saturation concentrations (e.g. T_{sat} = 40 °C) of SA (at 0.17% PP123).

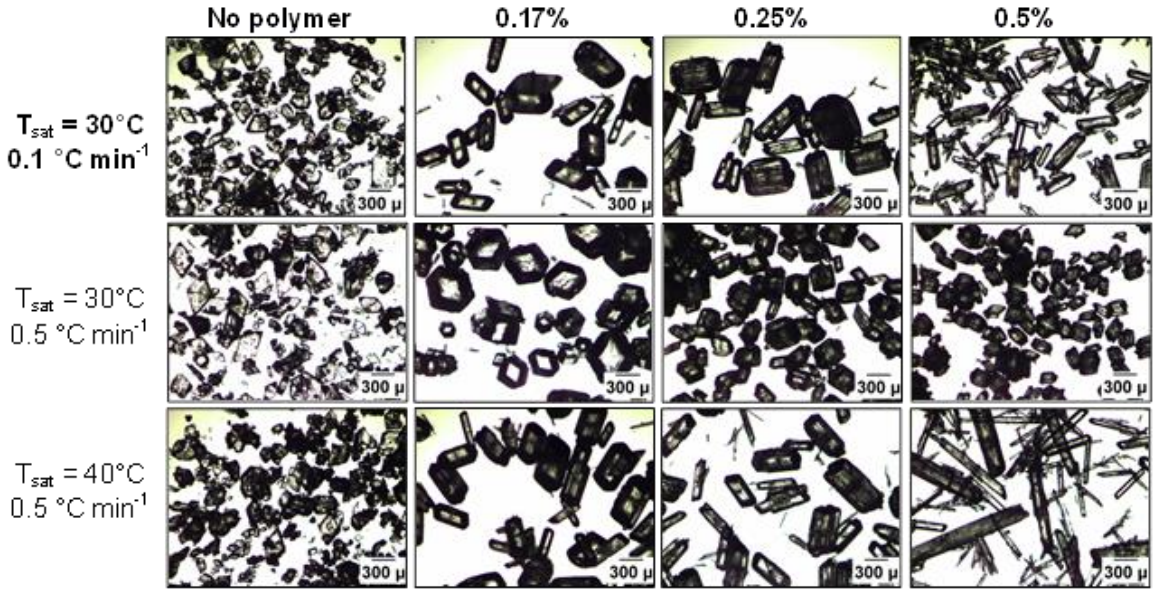

Figure 4.36 - Microscope images of SA crystals from experiments with a cooling rate of 0.1°C min^{-1}. Relevant images from crystallisations carried out with a cooling rate of 0.5 °C min^{-1} are also shown for comparison.

It is postulated that at slower cooling rates nucleation may occur at higher temperatures and thus a lower supersaturation ratio would exist at nucleation. The supersaturation ratio in experiments carried out with the fast cooling rate at higher saturation concentrations of SA would be comparable with the supersaturation in experiments carried out with the slow cooling rate at lower saturation concentrations of SA. In order to investigate this postulate, direct measurement of the nucleation temperature would be required and a broader range of SA and additive concentrations studied, at a range of cooling rates.

4.13 Understanding the effect of the PP123 additive on crystal growth

4.13.1 Indexing the crystal faces

The crystal faces involved in the morphology change were identified *via* face indexing (Figure 4.37).

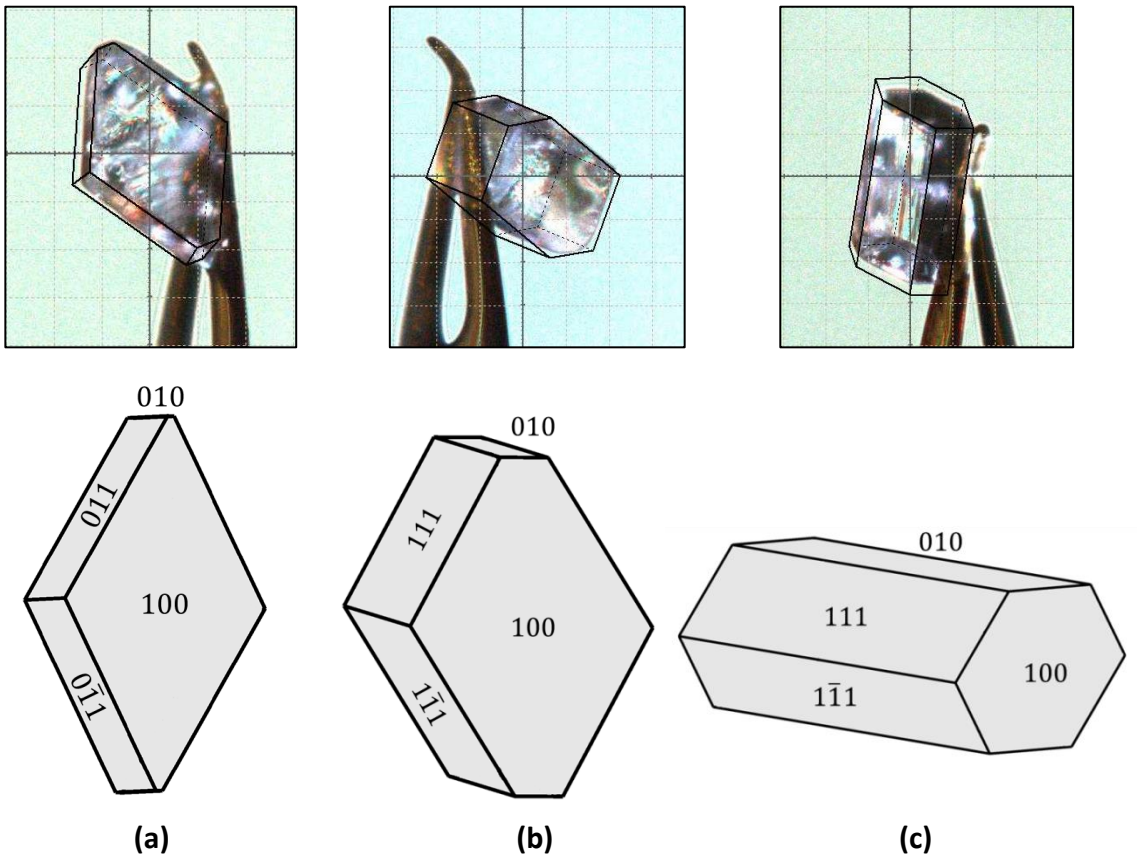

Figure 4.37 - Faces of SA crystals: (a) plate-like crystals from crystallisations with no polymer; (b) block-like crystals from low saturation crystallisations and (c) rod or needle-like crystals from high saturation crystallisations.

Upon addition of the PP123, the (100) face remains prominent. However, its prominence decreases with increased saturation concentration of SA and concentration of polymer as the crystal shape moves towards a needle-like morphology. This suggests that the growth rate in the direction of this face (along the crystallographic *a* axis) is faster than those of the other faces under these conditions. This is also evident in peak intensity changes due to preferred orientation in the experimental PXRD patterns (Figure 4.38).

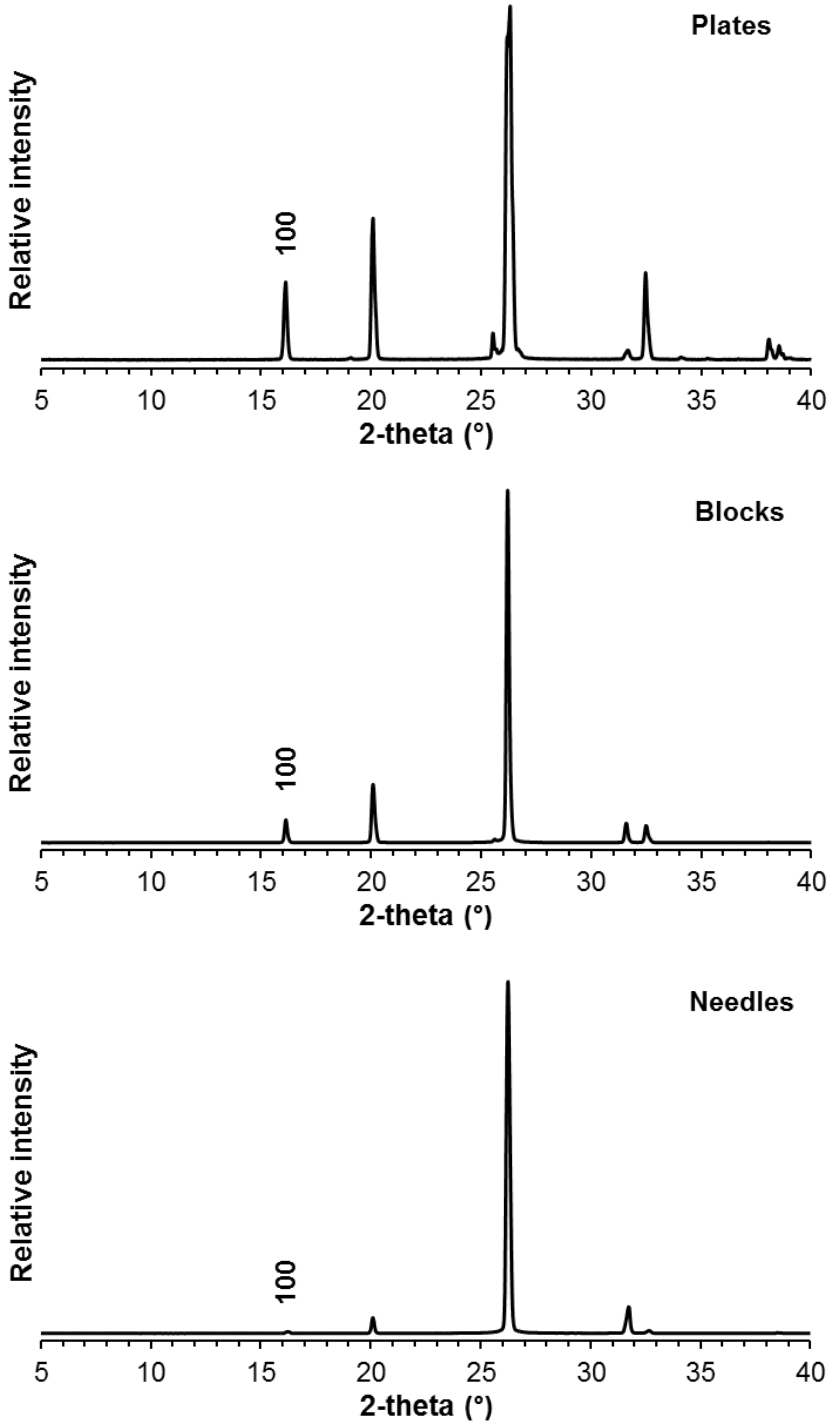

Figure 4.38 - PXRD of samples of each morphology showing preferred orientation.

As described in Section 4.3.1, due to polymorphic transitions induced by the grinding process, the PXRD samples were prepared without grinding; the habit change is thus evident through preferred orientation. In the PXRD pattern for crystallisations in the absence of polymer, the (100) peak is more intense than in the PXRD pattern for the block-like crystals produced in the presence of polymer at low saturation concentrations of SA. Furthermore, in the pattern for the needle-like crystals produced in the presence of

the polymer at high saturation concentrations of SA, in which the (100) face is much diminished, the (100) peak is barely discernible. This change in crystal shape, and observed increase in the growth rate of the (100) face, suggests that the growth of the side faces is being inhibited by the presence of the PP123, slowing down growth in the direction perpendicular to the face and leading to needle-like growth along the (100) direction.

Looking at the side faces, the (010) face is present in all of the morphologies, however it increases in size in crystals produced in the presence of the additives. It is also evident that in the presence of the PP123, the (111) faces become more dominant over the (011) faces. This face change can be observed in crystals obtained from crystallisations at low saturation of SA and low concentration of polymer which retain a plate like morphology but in which both the (011) and the (111) faces are present. Scanning electron microscopy (SEM) images show this (Figure 4.39b) and also that at higher saturation of SA only the (111) and $(1\bar{1}1)$ faces are observed (Figure 4.39c). This suggests that the growth along the (111) and $(1\bar{1}1)$ directions is being inhibited by the presence of the polymer, allowing these to become more prominent faces.

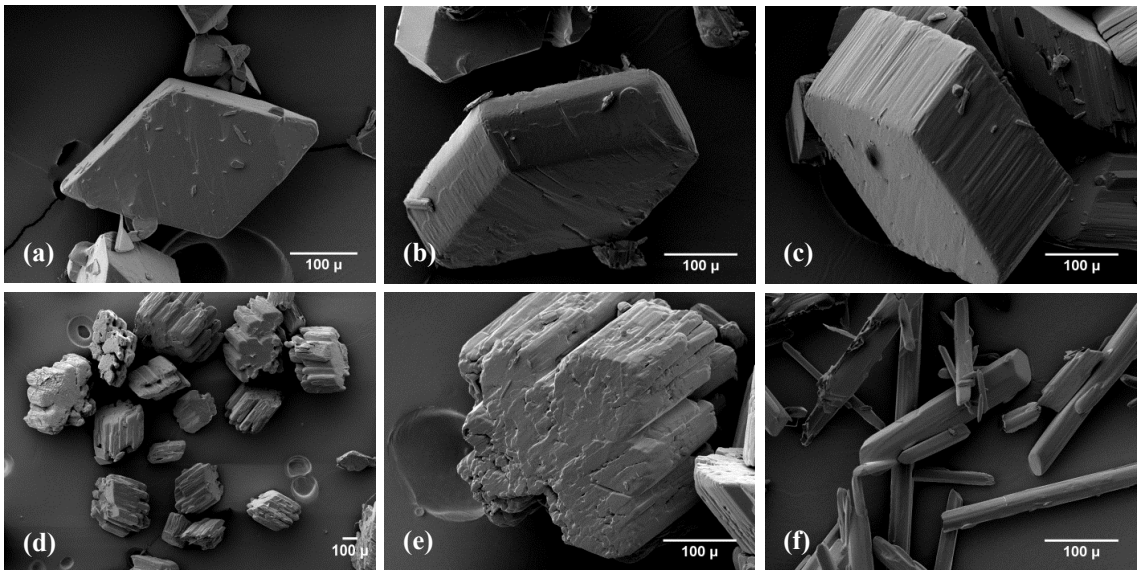

Figure 4.39 - SEM images of SA crystals crystallised under the following conditions: (a) T_{sat} = 30 °C, no polymer; (b) T_{sat} = 20 °C, 0.25% PP123 (side view); (c) T_{sat} = 30 °C, 0.17% PP123; (d) T_{sat} = 30 °C, 0.5% PP123; (e) T_{sat} = 27 °C, 0.5% PP123; (f) T_{sat} = 40 °C, 0.5% PP123.

The SEM images also reveal a more detailed picture of the surface of the crystals. On the block-like crystals the (100) face has a smooth surface, however, the (111), $(1\bar{1}1)$, (010) and $(0\bar{1}0)$ faces are more irregular, with well-defined steps. These irregularities are more

evident on the crystals produced from higher saturation experiments (Figure 4.39d). It is clear that these crystals remain single crystals; the crystals extinguish polarised light uniformly under a microscope. Diffraction patterns from these generally show single, sharp spots characteristic of single crystals but with some diffuse streaky spots also evident. Furthermore, the surface of the (100) face remains smooth and appears too uniform for the crystals to be agglomerates. The cause of this phenomenon is undetermined at present.

4.13.2 Analysis of the crystal structure of β-SA

The crystal structure of SA was analysed with respect to the results from the face indexing to investigate which functional groups of the molecule are present on the crystal surface that may be interacting with the polymer. In the crystal structure of β-SA, the molecules arrange themselves in hydrogen bonded chains linked by carboxylic acid dimers. The chains lie in two orientations, forming consecutive layers. One orientation runs parallel to the (111) plane, the other parallel to the $(1\bar{1}1)$ plane (Figure 4.40). The only intermolecular interactions between these planes are short contact interactions between the layers of SA molecules. The hydrophobic CH_2 groups lie on the surface of both the (111) and the $(1\bar{1}1)$ faces suggesting that the polymer is interacting with these groups. These groups are also present on the surface of the (010) face which is slightly larger on crystals grown in the presence of the PP123 additive, suggesting that growth in the direction perpendicular to the (010) face may also be inhibited by the additive.

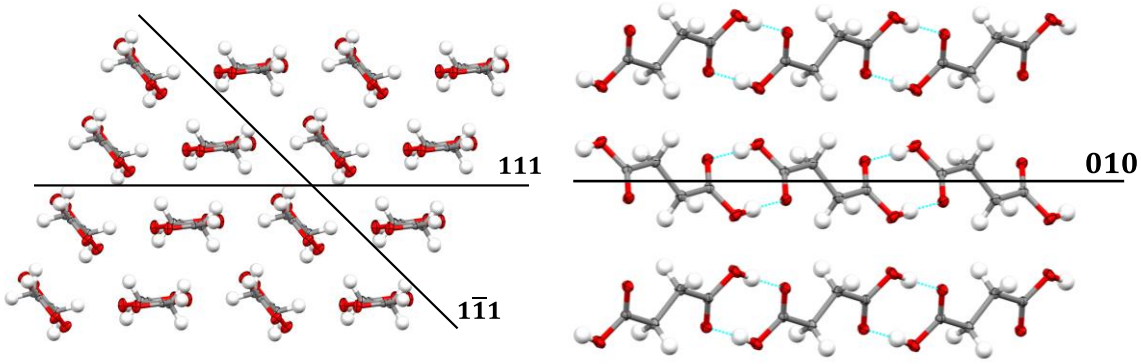

Figure 4.40 - Packing arrangement of β-SA: (left) view along the (111) and $(1\bar{1}1)$ planes and (right) view along the (010) plane.

4.13.3 Additional experiments with PEG and PPG

As noted above, PP123 is a triblock co-polymer comprising blocks of hydrophilic polyethylene glycol (PEG) and hydrophobic polypropylene glycol (PPG). To investigate which part of the polymer may be interacting with the surface of the growing crystals,

additional crystallisations were carried out at 10 ml scale with the individual blocks of PP123 (PEG and PPG) as additives; the resulting crystal morphologies from these experiments are shown in Figure 4.41.

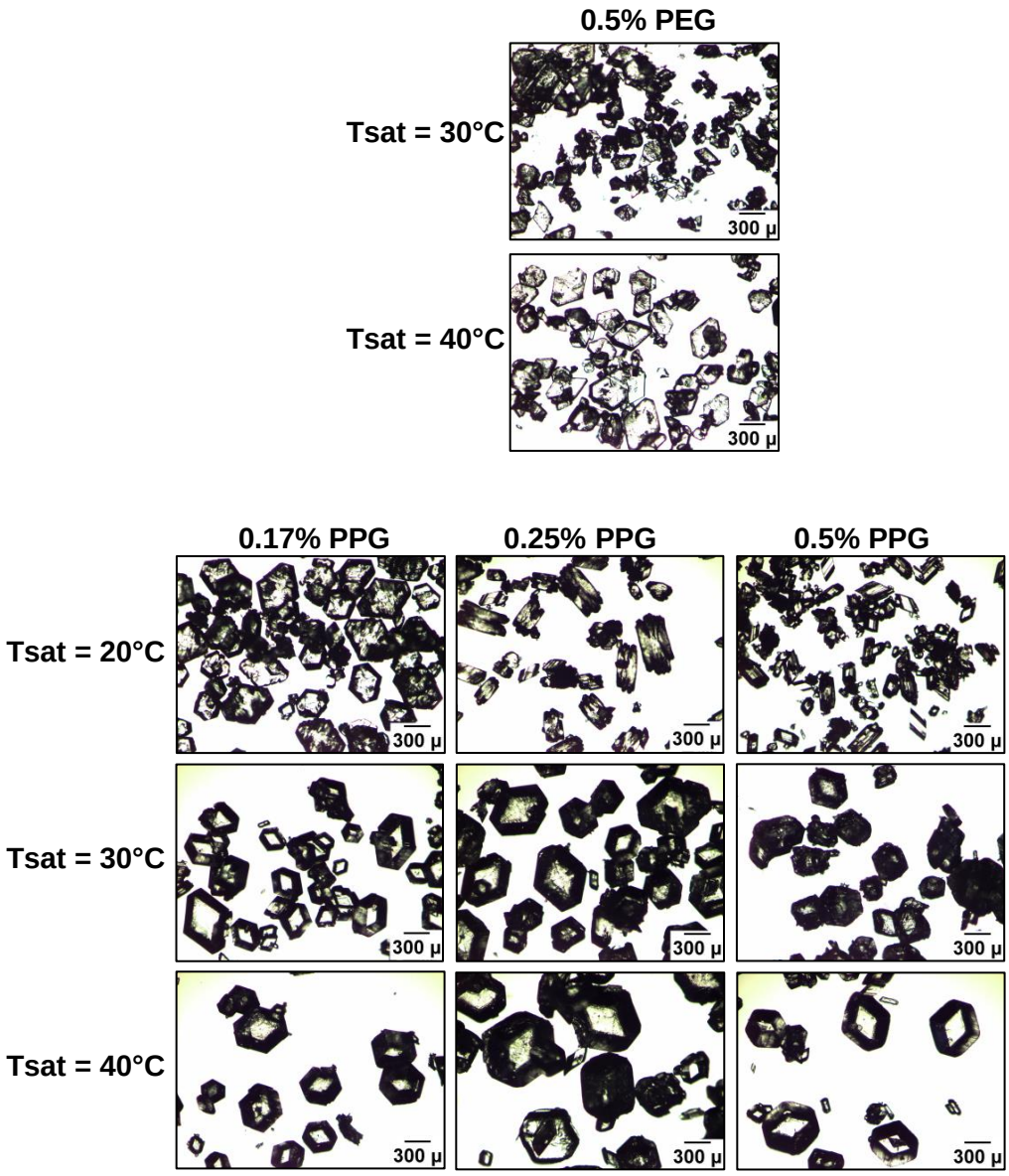

Figure 4.41 - Microscope images of SA crystals from crystallisations carried out with (top) PEG1000 and (bottom) PPG4000 at 10 ml scale.

It was found that the presence of the hydrophilic block, PEG1000, had no effect on the morphology of SA even when the concentration of polymer was increased to 1%. In contrast, the crystallisations with the hydrophobic block, PPG4000, mostly resulted in block-like crystals with the same faces as the crystals produced from experiments at low saturation of SA or low concentration of PP123, as confirmed by microscopy and face indexing. This suggests a possible mechanism for the additive effect of PP123 in which the hydrophobic PPG4000 block of the co-polymer is interacting with the hydrophobic

faces of the crystals, on which the CH_2 groups are present, causing inhibition of growth on these faces.

Use of PPG4000 alone as an additive appears to have some additional benefits. In contrast to the experiments with PP123, the crystals produced at high saturation of SA remain block-like rather than needle-like, extending the concentration range over which the favourable block-like morphology can be obtained. At T_{sat} = 40°C and as the concentration of PPG is increased the surface of the crystals is increasingly more rounded suggesting that under these conditions the crystals may be growing *via* a continuous growth mechanism.

Crystallisation in the presence of Pluronic F127 (PF127) was also carried out at 10 ml scale. PF127 has a shorter PPG and longer PEG block than PP123. As observed with the PEG1000, PF127 had no effect on crystal morphology, indicating again that the PPG block is important in the morphology change.

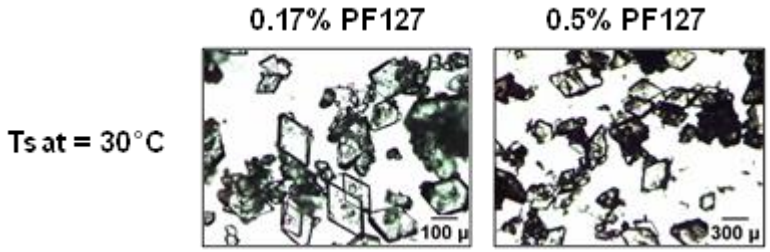

Figure 4.42 - Microscope images of SA crystals from crystallisations carried out with PF127 at 10 ml scale.

4.14 Investigating the purity of the crystalline product

The aim of crystallisation in the presence of additives is to improve the shape of the crystals whilst the additive remains in solution. In crystallisation in the presence of structurally similar additives the solution is designed to remain undersaturated with respect to the additive meaning that the additive will stay in solution and should not be present in the final solid product after filtration. Although some polymer additives offer the benefit of being non-toxic and are often used as excipients in pharmaceutical formulations, it is important to understand whether any additive is left behind in the product. The additive may adhere to the surface of the crystals meaning that washing steps may be required to remove the compound. Several techniques were used in order to investigate whether the polymer additive was present in the product of the

crystallisations carried out here. Both analytical methods and a non-quantitative method of recrystallising the product after washing steps to observe residual effects on crystal morphology were employed.

4.14.1 Analytical methods

FTIR spectra of samples crystallised with and without additive present were recorded (Figure 4.43); these display no differences from each other, or correlation with the spectrum produced from the PP123 polymer. The polymorphic form of the product from each crystallisation was analysed using PXRD and Raman spectroscopy; the latter are shown in Figure 4.44 and again are the same with and without polymer, matching that of β-SA.

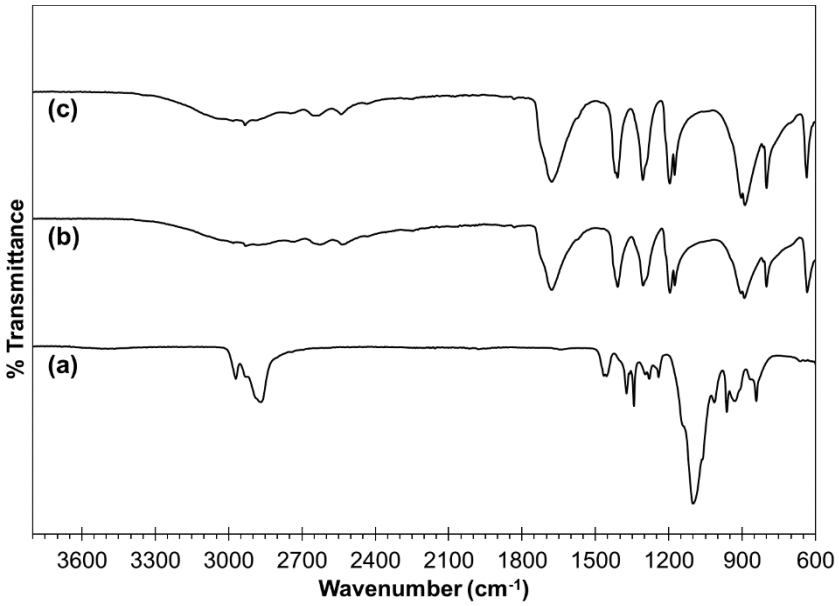

Figure 4.43 - FTIR spectra for (a) PP123, SA samples crystallised (b) without and (c) with PP123 present in solution.

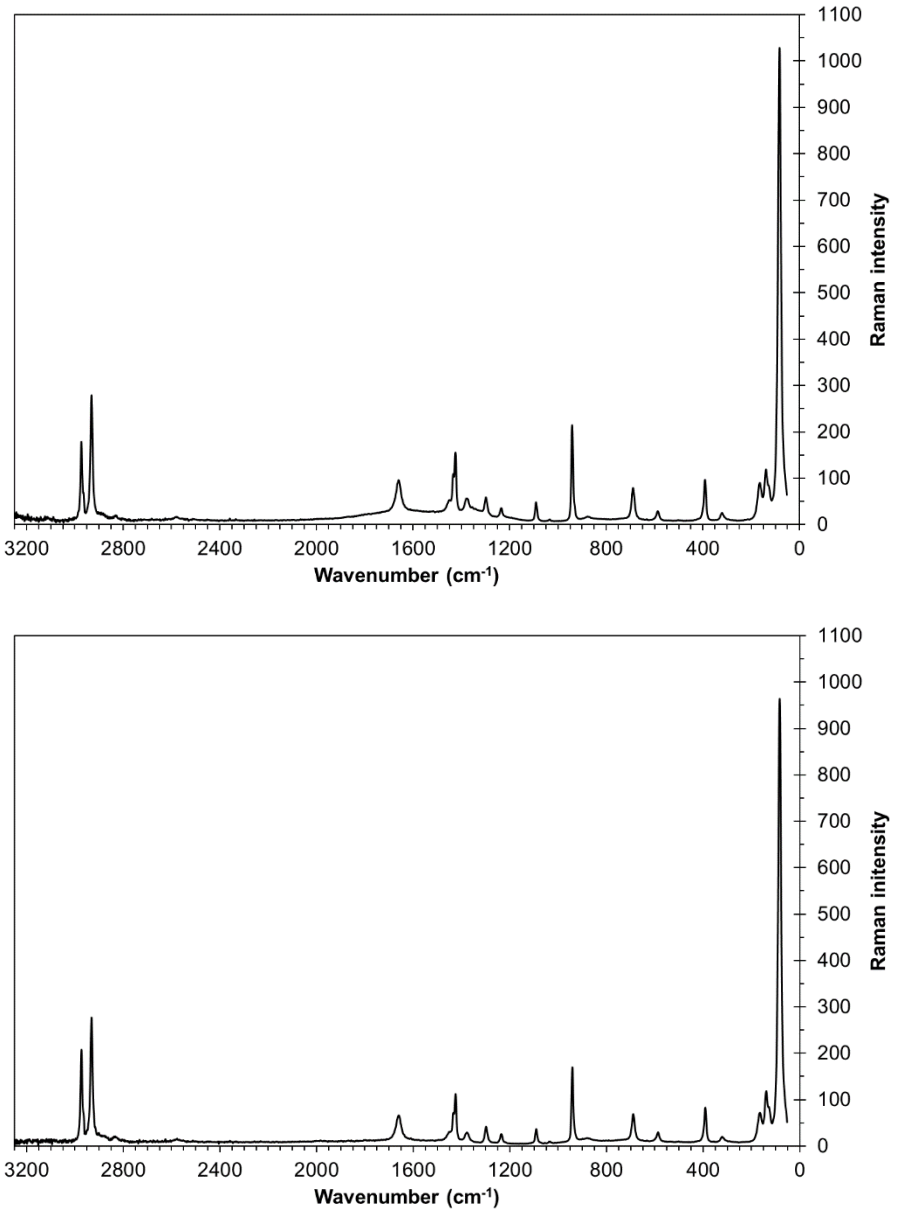

Figure 4.44 - Raman spectra of SA crystallised (top) without and (bottom) with PP123 present in solution; the spectra are consistent with β-SA.

DSC and NMR were also used (Figure 4.45, and Appendix A4.1), as well as MALDI-TOF mass spectroscopic analysis (Appendix A4.2), again showing no evidence of the presence of residual polymer additive in the samples.

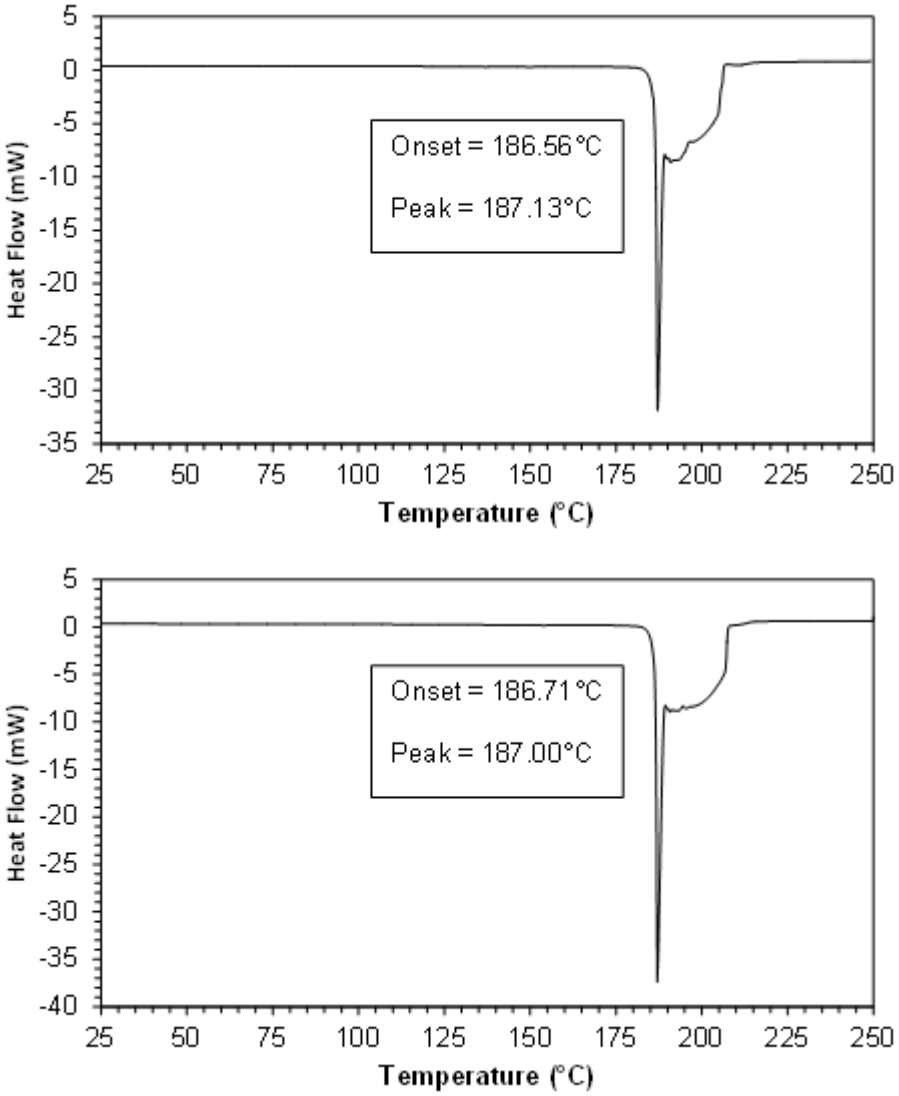

Figure 4.45 - Differential scanning calorimetry for SA samples crystallised (a) without and (b) with PP123 present in solution.

The small quantity of polymer initially added to the crystallisation (1.15 mg ml^{-1}) was within the defined detection limit (0.05 mg ml^{-1}) of the MALDI-TOF method. That the polymer was not detected in the samples suggests that the polymer is not incorporated into the crystal lattice. However, it may be present on the surface of the crystals, but in lower concentrations than those detectable by the method (< 0.05 mg ml^{-1}).

As a result of the limited success of using analytical techniques, an alternative approach was also adopted that involves washing experiments, using the presence of morphology modification as a diagnostic to indicate the presence of polymer in the relevant products.

4.14.2 Recrystallisation and slurrying experiments

A series of preliminary crystallisation experiments were carried out on a sample previously crystallised from solution containing the highest concentration of PP123 additive (and whose morphology had been modified to rod-like (Figure 4.46)) to assess whether trace amounts of PP123 were present in the crystals or on their surfaces. In theory, if no polymer is left behind on the crystals, subsequent recrystallisation of the sample from water would result in crystals of the original plate-like morphology.

Recrystallisation of this sample from water produced crystals of block-like morphology (Figure 4.46 I), indicating that PP123 may remain on the surface of the crystals, in quantities smaller than those detectable by the analytical techniques implemented (Figure 4.43, Figure 4.44, Figure 4.45 and Appendix A4.1-A4.2). As a result of this observation, a number of washing experiments were carried out. Recrystallisation of samples that had been repeatedly washed with cold water, in combination with filtration, again continued to produce the morphology-modified crystals (Figure 4.46 II). Washing with water also resulted in a significant decrease in crystal yield due to dissolution. This suggests that a small quantity of the polymer still remains bound to the crystal surfaces of the SA following dissolution or washing in a polar solvent. When this method was repeated with a less polar solvent (diethyl ether), however, the resulting crystals were less block-like (Figure 4.46 III) indicating that diethyl ether washing is removing residual polymer from the crystal surfaces. Slurrying of the crystals in diethyl ether for one hour prior to recrystallisation from water was found to be a more successful washing technique than washing with filtration. Washing by reslurrying the product in a solvent allows crystal agglomerates, which may entrap mother liquor, to break up whereas channelling may occur by washing on a filter so not all of the crystals have contact with the washing solvent.[162] The crystals resulting from the slurry-washing experiments were of plate-like morphology as previously observed in the crystallisations of SA with no polymer present (Figure 4.46 IV). This experiment was repeated and again resulted in crystals of plate-like morphology (Figure 4.46 V). Thus the non-polar solvent had the effect of removing the polymer from the crystal surfaces, suggesting it is acting as a competitor for the polymer-crystal surface hydrophobic binding interaction. This also supports the conclusion that PP123 is not incorporated in the crystals of SA, and that the residual polymer can easily be removed in an appropriate washing step.

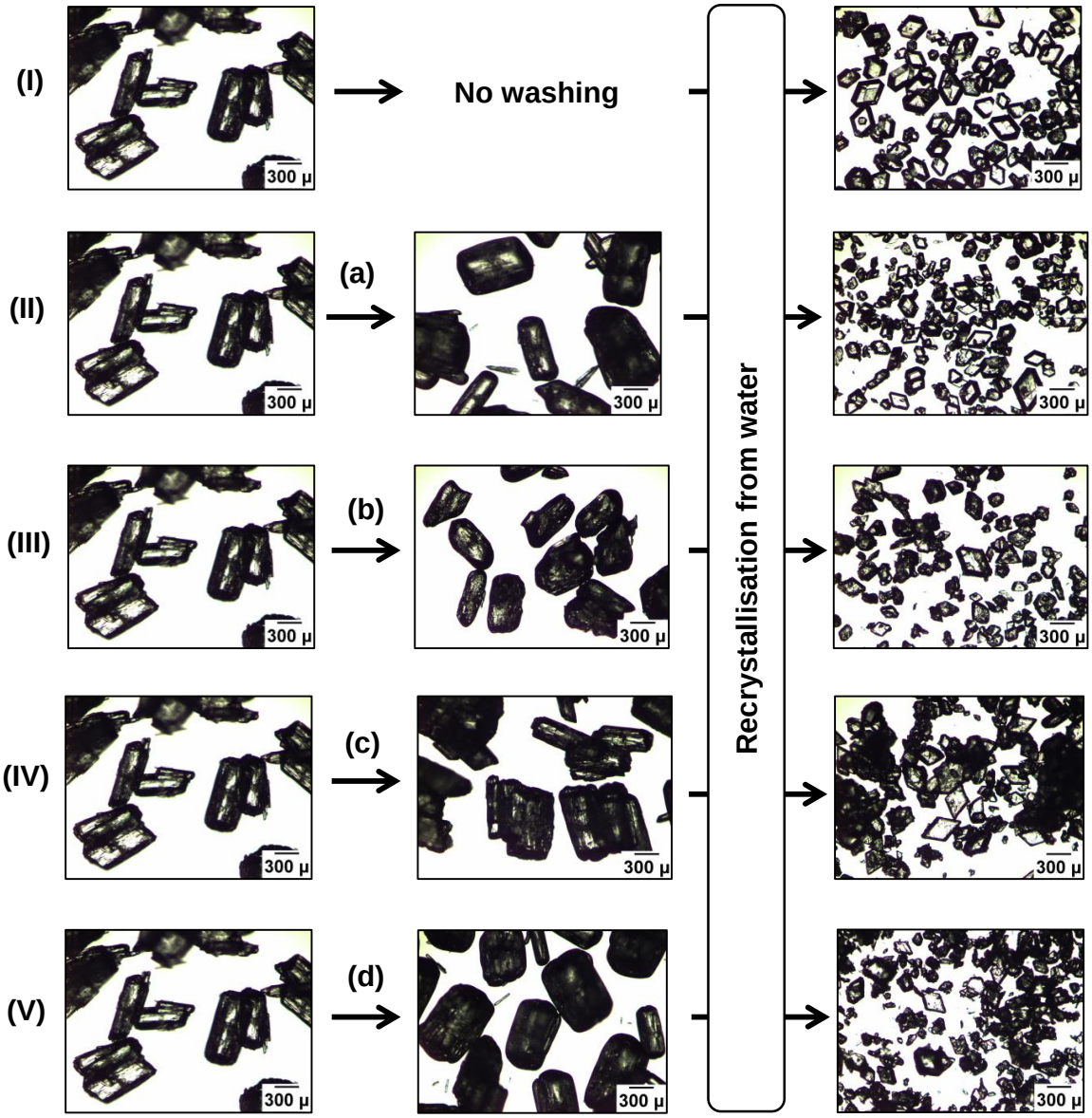

Figure 4.46 - Microscope images of SA crystals from washing experiments: (a) washing with filtration with cold water, (b) washing with filtration with diethyl ether, (c) slurrying in diethyl ether and (d) repeat of slurrying in diethyl ether.

4.15 Further experiments carried out at 350 ml scale

4.15.1 Direct nucleation control (DNC) experiments

Feedback control strategies can be effective in improving crystal quality and size uniformity by controlling the number of nuclei present in the system.[163-165] Such a strategy is implemented by maintaining the number of particle counts detected by the FBRM probe during a crystallisation process constant by heating and cooling the solution. If the particle counts are higher than the target number of counts, the control software reacts by increasing the temperature of the crystalliser jacket in order to dissolve the smaller, fine

particles. If the number of counts is too low the temperature is decreased to enable growth of the existing particles and nucleation of new particles. This process continues until the crystallisation reaches the set point of counts per second.

An automated DNC strategy for crystallisation of SA from water was implemented using the CryPRINS software, based on FBRM data. Additional DNC experiments were also carried out in the presence of the PP123 polymer to observe the combined effect of the additive and the DNC strategy on the crystal morphology. These initial DNC experiments were carried out in collaboration with Dr Elena Simone and Professor Zoltan Nagy at Loughborough University following on from the scale-up work detailed in Section 4.11. An additional, more detailed and optimised DNC study on this system was carried out subsequently by Dr Elena Simone.[166]

4.15.1.1 DNC with no additive present

Figure 4.47 and Figure 4.48 show the results from the two experiments with set points 200 and 100 particle counts/second, respectively. The results show that with no additive present, two heating/cooling cycles were required to reach each set point.

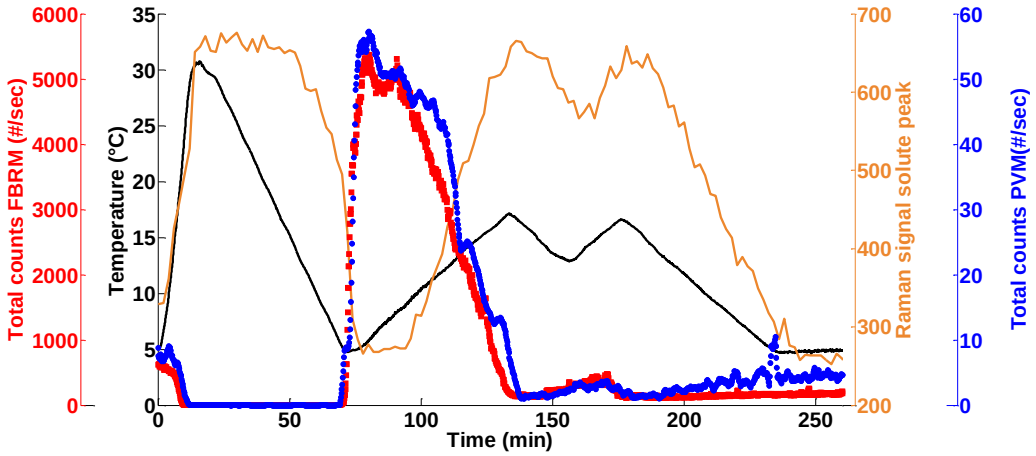

Figure 4.47 - Graph showing the temperature profile (black) used for the DNC experiment of SA crystallised with no additive present with an FBRM set point of 200 counts/sec (red). Data from the Raman and PVM probes are also shown (blue and orange, respectively).

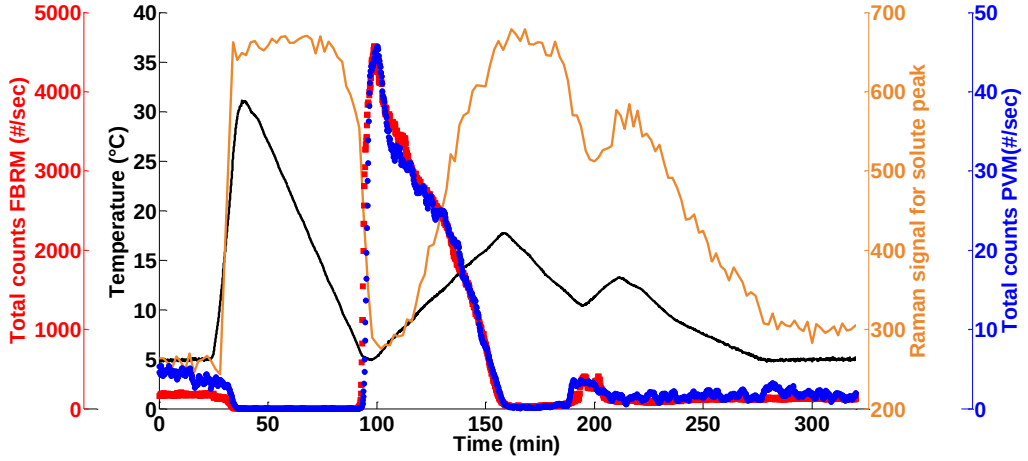

Figure 4.48 - Graph showing the temperature profile (black) used for the DNC experiment of SA crystallised with no additive present with an FBRM set point of 100 counts/sec (red). Data from the Raman and PVM probes are also shown (blue and orange, respectively).

Upon inspection of the crystal morphology before and after DNC it can be concluded that the DNC process has generated large, plate-like crystals of more uniform morphology than those observed without DNC (Figure 4.49). Face indexing was also used to confirm the morphology was the same as that observed with no DNC (Figure 4.50).

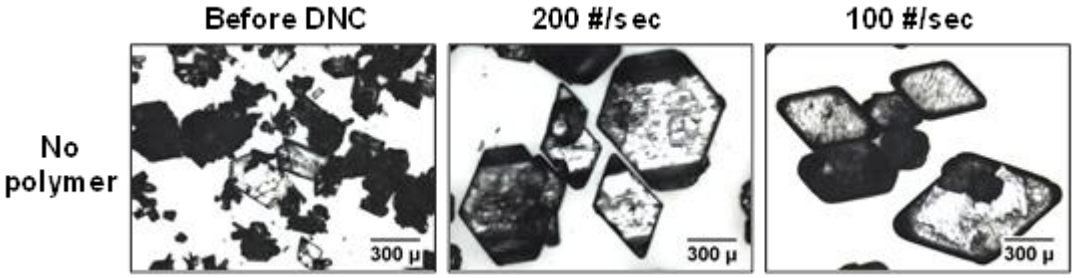

Figure 4.49 - Microscope images of crystals obtained from DNC experiments with no additive.

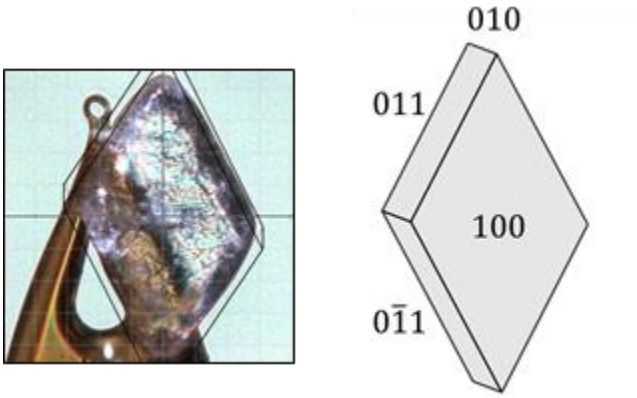

Figure 4.50 - Indexing of crystal from DNC crystallisation in the presence of no additive.

4.15.1.2 DNC with 0.5% PP123 additive present

DNC was also carried out on crystallisations containing 0.5% PP123 present in solution (Figure 4.51 and Figure 4.52). When comparing the results from these experiments with those with no additive present it is evident that more cycles are required for the particle counts to reach the same set point in the presence of the additive (in both cases of 200 and 100 counts/second, three cycles were required to reach the set point). This may be a result of the inhibiting effect of the PP123 additive on the growth of the crystals increasing the cycles required to reach the desired number of particle counts.

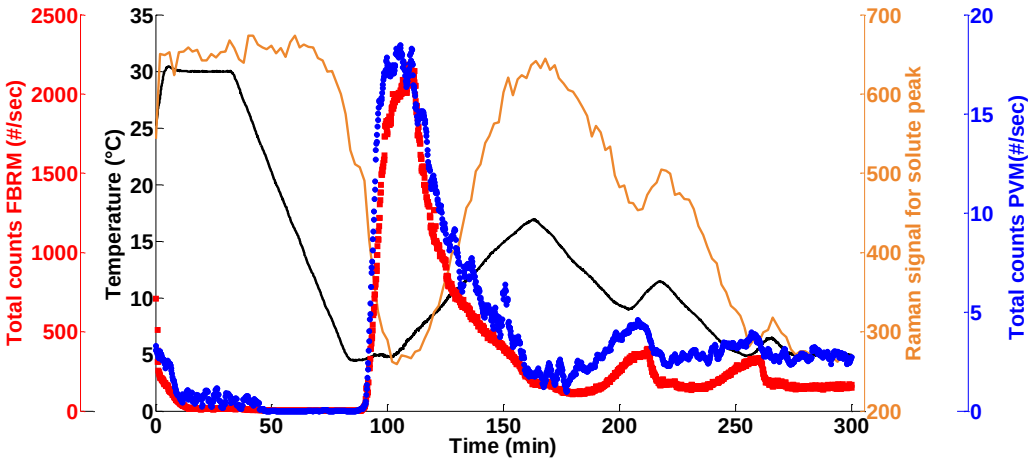

Figure 4.51 - Graph showing the temperature profile (black) used for the DNC experiment of SA crystallised with 0.5% PP123 present with an FBRM set point of 200 counts/sec (red). Data from the Raman and PVM probes are also shown (blue and orange, respectively).

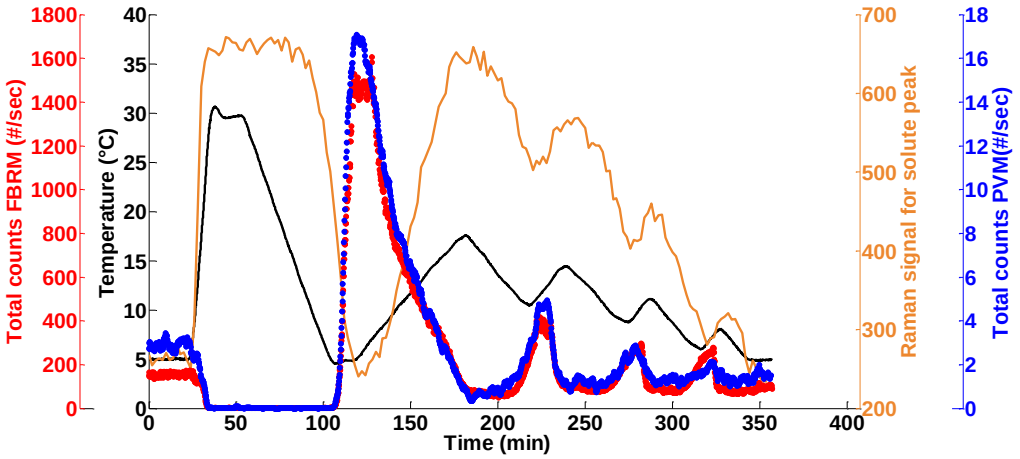

Figure 4.52 - Graph showing the temperature profile (black) used for the DNC experiment of SA crystallised with 0.5% PP123 present with an FBRM set point of 100 counts/sec (red). Data from the Raman and PVM probes are also shown (blue and orange, respectively).

Figure 4.53 shows the crystal morphology produced from the DNC experiments with 0.5% PP123 present. After DNC the crystals are larger and more uniform in size. Interestingly,

however, they are more rod-like than those produced without DNC; in the latter the crystals are block-like in the presence of polymer additive. Indexing of the faces of the crystals from the DNC experiments showed that the dominant faces remain the same as those observed in the absence of DNC and the same face change is observed from when no additive is present. Thus the combination of DNC and polymer additive is affecting the relative rates of face growth, while generating a similar trend of morphology modification.

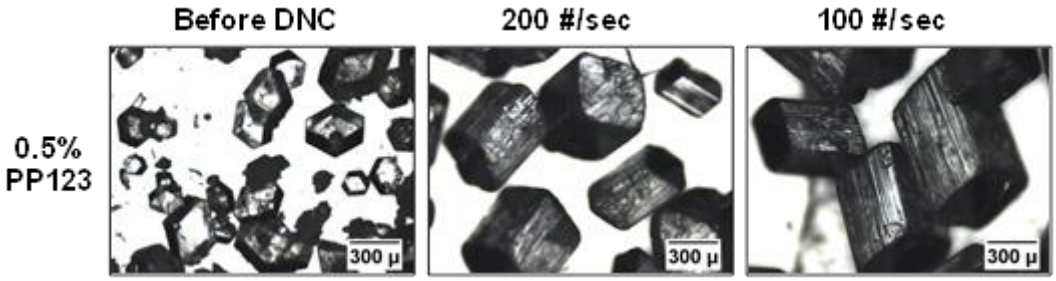

Figure 4.53 - Microscope images of crystals obtained from DNC experiments with 0.5% PP123 additive present in solution.

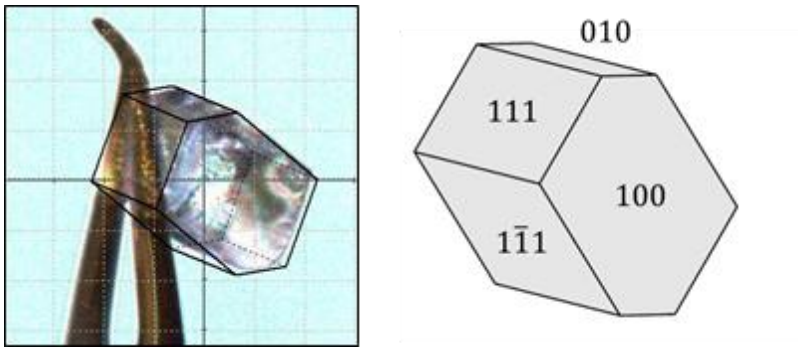

Figure 4.54 - Indexing of crystal from DNC crystallisation in the presence of 0.5% PP123 additive.

4.15.2 Temperature cycling experiments

Temperature cycling with no feedback control can also be used as a strategy to obtain improved particle shape and narrow size distributions, though it is often less efficient in process terms. Heating and cooling cycles allow for dissolution of fines and growth of larger particles to produce narrow particle size distributions.[167] In addition, temperature cycling may impact the shape of the crystals since different faces have different relative growth and dissolution rates.

The crystallisation experiments presented in this section were carried out by Dr Elena Simone at Loughborough University using the SA system in which prior collaborative work had been carried out (Section 4.11 and Section 4.15.1). The work is presented here as the outcomes of the experiments were analysed by the author in terms of the particle

morphology and indexing of the crystal faces. Results from temperature cycling experiments are presented in more detail in Simone *et al*.[166]

Crystallisations of SA with temperature cycling were carried out with and without the PP123 additive present in solution. In the initial experiment with no additive present, following nucleation at 10 °C heating and cooling cycles of 4.5 °C were applied. After a period of two consecutive days, an equilibrium state was identified using the PAT data. Figure 4.55 shows an overlay of the temperature profile and the total counts per second from the FBRM probe over the two day period of temperature cycling. The total counts per second from the FBRM probe decreases until it reaches a constant value of 50 counts per second.

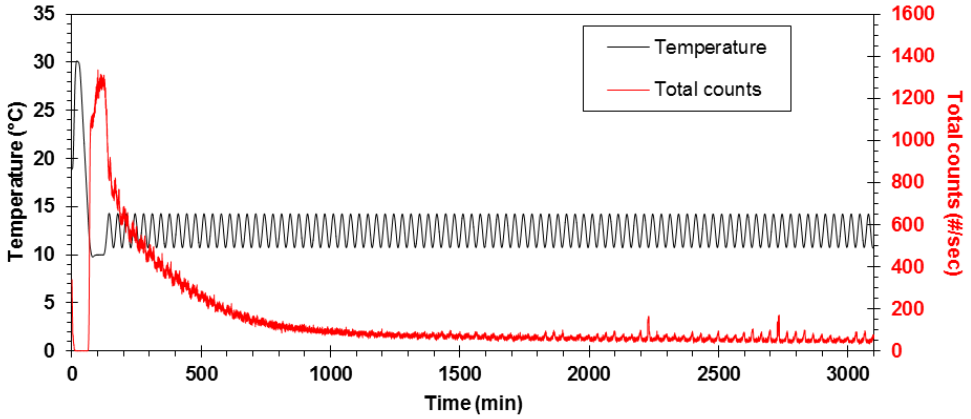

Figure 4.55 - Temperature profile and total counts per second recorded from the FBRM statistics during temperature cycling over a period of two days.

During and after the experiment, samples were taken from the vessel and microscopy was used to observe the effect of the temperature cycling on the crystal morphology. Figure 4.56 shows the crystal morphology after temperature cycling. In contrast to the DNC experiments, temperature cycling with no additive present in solution resulted in a significant change in the shape of the SA crystals to square bipyramidal shaped crystals.

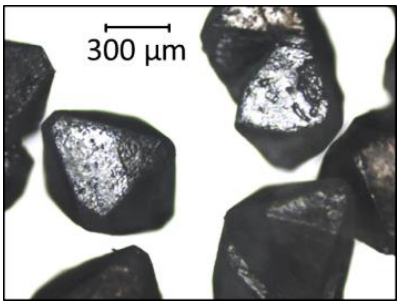

Figure 4.56 - Microscope image of square bipyramidal morphology produced from temperature cycling experiments with no additive present.

In addition, the crystals were examined in more detail using face indexing. The temperature cycling appears to promote the growth of the (110) and $(1\bar{1}0)$ faces over the (100) which is prominent in the plate-like crystals produced prior to temperature cycling (Figure 4.57).

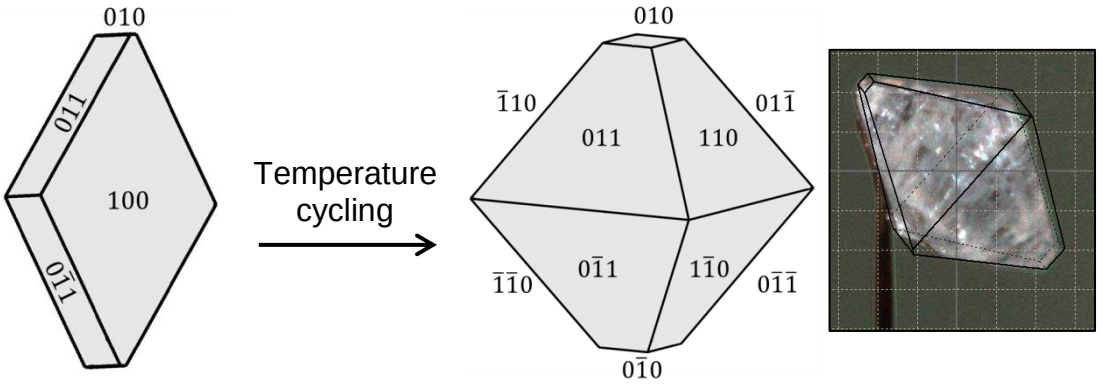

Figure 4.57 - Face indexing of SA crystals produced in the presence of no additive before (left) and after (right) temperature cycling.

It is also interesting to note that the final equilibrium shape produced in the temperature cycling experiments is more comparable with the shape calculated by the BFDH method than any other morphology presented herein. The (100) face present in the BFDH shape is accompanied by the (110) and $(\bar{1}10)$ faces present in the crystals produced from temperature cycling which are not present in the original morphology (Figure 4.58).

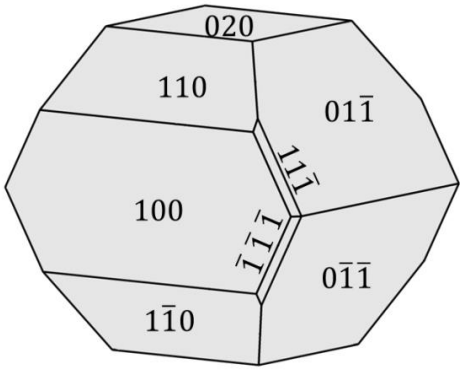

Figure 4.58 - BFDH morphology of β-SA.

The equilibrium shape could also be obtained using larger cycling amplitudes in which the time required to reach steady state was reduced. Larger heating and cooling cycles enables more rapid dissolution of the smaller particles and quicker adjustment to the equilibrium shape.

Temperature cycling was also carried out with the PP123 additive present in solution; the time required for the particle counts per second to reach a constant value was greater in the presence of the additive and the equilibrium square bipyramidal shape was not observed. Instead, rod-like crystals were produced which, in addition to the longer time required to reach equilibrium, may be a result of the inhibiting effect of the additive on the growth of SA. Analysis of the rod-like crystals was also carried out using face indexing which showed the morphology to be the same as that produced in the additive experiments with no temperature cycling.

Significant differences were thus observed between the morphology obtained using DNC and using temperature cycling without DNC, specifically with no polymer present. In the preliminary DNC experiments presented here, the predicted equilibrium shape was not produced and instead, large plate shaped crystals formed.

It should also be noted that, in practical terms with respect to the potential implementation of morphology modification strategies in industrial processing contexts, the need for repeat crystallisation cycles may be unfavourable. The polymer additive effect has been found in a single cooling run and offers a certain degree of control over particle size and shape (*via* polymer concentration, SA concentration and cooling rate) in the SA crystallisations presented here. However, in terms of particle size uniformity, the combination of the use of additives and temperature cycling techniques may enable access to desirable morphologies in more narrow size distributions.

4.16 Application of PP123 additive to other dicarboxylic acids

The aim of this experiment was to observe the possible effect of the PP123 polymer additive on the crystallisation of a longer chain dicarboxylic acid, adipic acid (AA) (Figure 4.59).

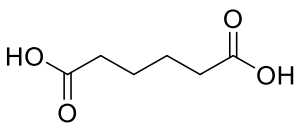

Figure 4.59 - The structure of adipic acid.

AA crystals grow into hexagonal plates when crystallised from water (Figure 4.60).

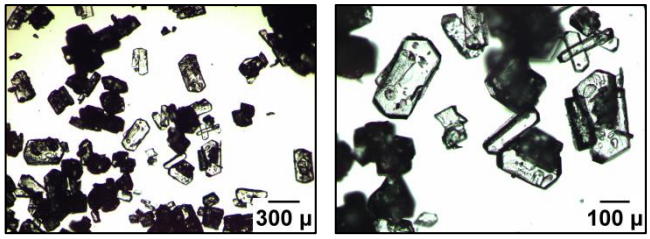

Figure 4.60 - Microscope images of AA crystallised from water (T_{sat} = 40 °C).

In the presence of PP123 additive the AA crystals become increasingly elongated at high saturation concentration of AA (Figure 4.61). The crystallisations at low saturation (T_{sat} = 20 °C) show a variable crystal morphology suggesting that the mixing rate was not sufficient to establish uniform mixing conditions. The needle-like crystals observed at T_{sat} = 40 °C are comparable with those produced under the same conditions with SA.

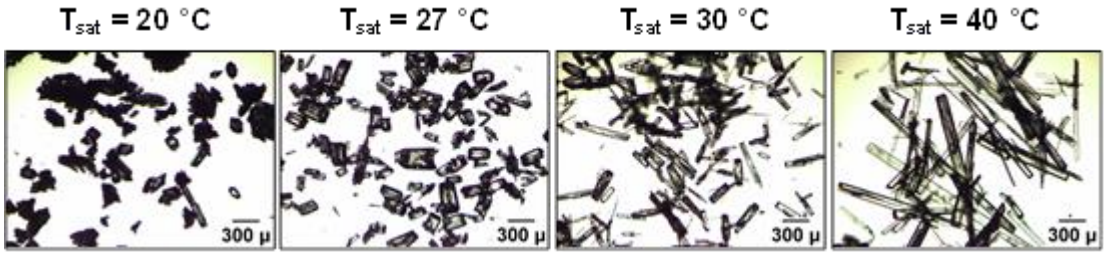

Figure 4.61 - Microscope images of AA crystallisations carried out in the presence of 0.5% of PP123 additive.

The results from these additional crystallisations indicate that the PP123 polymer additive can be applied to modify crystal morphology in other systems with a similar chemical structure.

4.17 Conclusions

In this work the presence of very small quantities of a polymer additive (Pluronic P123) have been shown to be effective in reproducibly modifying the crystal morphology of SA from plates to blocks when grown from aqueous solutions. The production of block-like crystals is more desirable in terms of ease of downstream processing and despite the large change in crystal morphology the solid form remains β-SA in all cases.

The additive effect was investigated at various batch scales from 1 ml to 350 ml. The effect of the polymer is shown to be dependent on both the concentration of SA and the concentration of polymer in solution. At high saturation of SA or high concentration of

polymer, needle-like crystals are produced whereas at low saturation of SA or low concentration of polymer, more desirable block-like crystals are produced. Fine tuning of the crystallisation conditions enabled identification of the conditions required to produce the most desirable block-like morphology. Block-like crystals are shown to be produced at scales from 10 to 350 ml scale, where overhead stirring can be implemented. The chosen method of mixing and geometry of the impeller was found to be crucial in terms of the crystal shape and uniformity; experiments with magnetic bottom stirring resulted in needles at high saturation and non-uniform crystals at low saturation. In addition to the concentration of SA and concentration of additive, the effect of cooling rate was also investigated. It was found that at slower cooling rates, a more enhanced effect of the additive was observed.

Where the nucleation temperature could be measured accurately using in-line analysis (turbidity or FBRM), it was found in all cases that, in the presence of the polymer additive PP123, a decrease in the supersaturation ratio with increasing saturation concentration of SA was observed. At low supersaturation fewer crystals formed but the high initial concentrations of SA mean that more material is available in solution for the crystals to grow, enabling the production of larger (or longer for needles) crystals compared to those produced at low saturation temperatures. On-line and in-line analysis also allowed for investigation of the effect of the polymer additive on the nucleation temperature. It was found that, at 3 ml scale, the additive appeared to widen the MSZW by 7-10 °C, whereas at 350 ml scale the additive had little effect on the nucleation temperature.

Experiments were also carried out to investigate the mechanism by which the polymer is affecting crystal growth. Further experiments using the individual blocks of the triblock co-polymer suggest that the PPG block of the polymer interacts with the interface of the growing crystal *via* hydrophobic interactions. Face indexing of the crystals produced and subsequent analysis of the crystal structure of β-SA showed that the faces being inhibited are hydrophobic faces, which are likely to interact with the PPG block of the triblock co-polymer. Interestingly, when the PPG block alone was used as the additive in high concentrations or at high saturation of SA, block-like crystals were produced whereas with PP123, needle-like crystals would be produced under these conditions. This extension of the concentration range over which the favourable block-like crystals are produced is a significant benefit in terms of the goal of this work; to produce particles reliably that are easier to handle in process environments.

A range of analytical techniques were implemented to investigate whether the polymer was present in the final filtered product. However, the techniques used did not show the presence of any polymer at their level of sensitivity. To investigate this further, an alternative experimental method to deduce the presence of residual trace amount of polymer was implemented; using morphology-modification as a diagnostic of the presence or absence of polymer. Multiple recrystallisation and washing experiments were carried out which showed that polymer was present on the surface of the crystalline product. This derivative technique was successful in the identification of quantities of polymer smaller than those detectable by the analytical techniques previously employed. Washing the crystals in a low polarity solvent allowed for removal of the residual polymer present, in particular slurry-washing was shown to the most effective method for achieving this.

Additives can be effective in modifying crystal morphology; however one of the limitations of this method is the addition of an impurity into the system which will require extra washing steps to remove. Direct nucleation control (DNC) and temperature cycling are presented as an alternative method of obtaining improved crystal size distributions and different morphologies. Implementation of DNC was effective in modifying the size of the crystals but not their shape. In the absence of the PP123 additive, large plate-like crystals were produced whereas large rod-like crystals were produced in the presence of the PP123 additive showing that the additive effect was reproduced with DNC methods. Unlike in the DNC experiments, temperature cycling of SA in the absence of additives produced a square bipyramidal shaped equilibrium morphology which was analysed by indexing the crystal faces and found to be more in agreement with the BFDH-predicted morphology. Temperature cycling with the additive present resulted in the rod-like morphology produced previously. It is also noted that these additive-free methods have the disadvantage of requiring repeat crystallisations, which may be unfavourable in terms of implementing efficient processes. However, combining the use of additives with such methods may enable access to desirable morphologies in more narrow size distributions.

Initial studies into application of the PP123 additive to the crystallisation of adipic acid, a longer chain dicarboxylic acid than SA, were also carried out. Under the conditions explored, the additive had a similar influence on the crystal shape as SA where needle-like crystals were produced. This indicates that the polymer-additive effect may be transferable across other target systems of structural similarity.

Chapter 5

Continuous crystallisation of succinic acid

Traditionally, batch methods of crystallisation have been utilised in the pharmaceutical and fine chemical industries. Unlike others, these industries have not kept pace with advances in continuous modes of operation, relying heavily on the use of stirred tank reactors which, as noted above, can bring batch to batch variations and limited control over particle attributes.[75] In recent years, there has been significant drive towards developing continuous methods of crystallising pharmaceuticals and other fine chemicals due to the opportunity to exploit improved mixing and heat transfer and other benefits the mode of operation may offer (discussed in Chapter 1). This chapter explores the use of two continuous crystallisation platforms for the cooling crystallisation of succinic acid (SA) from water, including continuous runs with polymer additives present, with the capability to modify morphology as discussed in Chapter 4.

Part of the work presented in this chapter has been published as a journal article:
K. Robertson, P.-B. Flandrin, A. R. Klapwijk and C. C. Wilson, Design and Evaluation of a Meso-scale Segmented Flow Reactor (KRAIC). *Cryst. Growth Des.*, 2016, 16, 4759-4764.

5.1 Crystallisation in segmented flow

5.1.1 Introduction and aims

There are multiple existing platforms designed to facilitate crystallisation processes in flow at large macro-volume scale, such as continuous oscillatory baffled crystallisers (COBCs) and mixed-suspension, mixed-product removal (MSMPR) crystallisers. Reactors that enable production at micro-volume scales such as microreactors have been

studied significantly for enabling chemical reactions in flow[168] and have also been applied to the synthesis of nanometre sized particles.[169] However due to the narrow internal diameter of such reactors they are often deemed unsuitable for the processing of larger sized particles where problems with blockages are likely to occur.[168] As a result there has been significant interest in tubular mesoscale reactors with larger internal diameters than microscale for the processing of solids without the need for large quantities of starting materials. Such mesoscale crystallisers often employ segmented flow – immiscible fluid, or gas, and a saturated feed solution are independently pumped into the system creating discrete segments (or slugs) of each phase. The barrier between the segments helps to prevent back-mixing and create homogeneity in the crystallisation conditions in each slug.[170] Control of the flow rates of the two feeds can optimise the segment size and thus maximise the efficiency of mixing.[171] The solution segments then flow through the reactor where mixing within the segments is facilitated by generation of an internal fluid vortex by the non-slip boundary between the immiscible phases.[172,173] Segmented flow can be operated with air or with a suitable liquid immiscible with the crystallisation solvent, known as the carrier fluid, as shown in Figure 5.1.

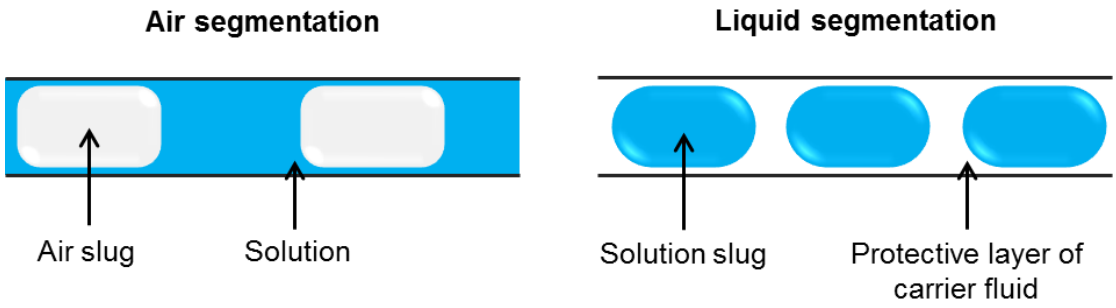

Figure 5.1 - Diagram comparing air and liquid segmentation.

In air segmentation, the solution flow is interrupted by the presence of slugs of air and several studies have reported the use of this method in combination with cooling crystallisation within the solution segments.[171,174] However, use of air segmentation (Figure 5.1, left) leaves the solution exposed to the walls of the crystalliser which may result in problems in the crystallisation of a compound which has a high affinity to nucleate on the walls of the tubing; the resulting fouling may ultimately promote the formation of blockages. In contrast, liquid segmentation overcomes this issue by generating slugs of solution which are separated from the walls of the reactor with a carrier fluid with suitable wetting properties (Figure 5.1, right), avoiding solid build-up on the crystalliser walls. Several studies have reported the precipitation of solids using this method.[170,175] However, one of the main challenges of using liquid segmentation is

separation of the carrier fluid from the product at the end of the crystalliser tubing; this is tackled in the present work.

The Kinetically Regulated Automated Input Crystalliser (KRAIC) is a mesoscale flow reactor designed by Dr Karen Robertson and developed in the Wilson group at the University of Bath (Figure 5.2). It is a versatile platform which can be used for many functions such as cooling and anti-solvent crystallisation as well as chemical synthesis in flow. In the configuration used here, a single, continuous, stream of solution is segmented by a flow of immiscible carrier fluid and cooled through passive insulated temperature controlled regimes. This results in nucleation and growth of crystals prior to separation of carrier fluid and filtration of product.

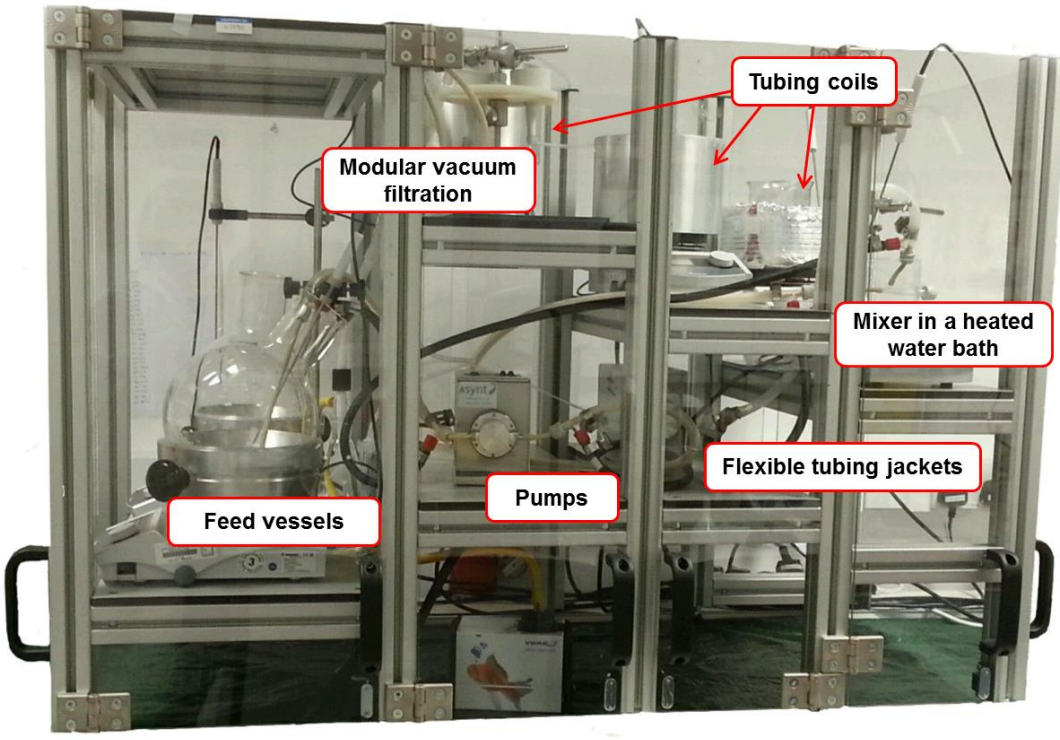

Figure 5.2 - Schematic of the KRAIC segmented flow crystalliser.[176]

The KRAIC is constructed from 15 m of fluorinated ethylene propylene (FEP) tubing with an internal diameter of 3.2 mm which is assembled in three progressively elevating coils. The solution and carrier fluid are independently pumped using gear pumps from temperature controlled feed vessels to a glass mixer piece (Y or T-piece) to produce liquid-segmented flow. Pumping the two feeds independently allows for greater control over the segment size and thus mixing conditions. The inlet of each feed line is also fitted with a solvent filter to ensure that dust or nuclei from the feed vessels do not enter the

system. The coils of the reactor are placed within vessels that can be temperature-controlled, providing three temperature zones through which the segments flow, allowing the generation of supersaturation through cooling, before emerging at the filtration unit at the end of the crystalliser for recovery of the product. The temperature inside the KRAIC platform is controlled using various methods. The temperature of the feed vessels, mixer piece and tubing coils is controlled using hot-plate stirrers with Drysyn® formers, water and graphite baths, respectively. During the development of the crystalliser, flexible jackets for the tubing between the feed vessel and pump and pump and mixer piece were designed in collaboration with Asynt;[177] these allow for temperature control of the tubing using a bath circulator. The jackets comprise two glass ends connected by outer silicone tubing through which the feed tubing is threaded. In addition, the outlet of the reactor features an end piece to aid propulsion of the solid product into the filtration unit and to recover the carrier fluid from the solution. The design of this end piece was evolved through several iterations which will be discussed in the development of the KRAIC platform.

A standard crystallisation experiment in the KRAIC is achieved by the following procedure:

- The tubing is primed with pure solvent and carrier fluid for 2 hours in order to activate temperature control for all active temperature zones (tubing jackets and water baths) and enable equilibration of the temperature within the KRAIC including areas of passive insulation (tubing coils);
- Relative flow rates of the solution and carrier fluid are chosen to optimise the segment size and residence time;
- Pure solvent is switched over to the solution feed to begin the experiment;
- Supersaturation is generated within each segment by cooling over the length of the KRAIC;
- Upon reaching the end of the crystalliser, recovery of the carrier fluid is followed by filtration of the crystals from the solution. The carrier fluid is recycled back into its feed vessel.

The work reported herein was carried out as part of, and in parallel to, the development of the KRAIC platform. SA was selected as a model system to understand the capabilities of the crystalliser due to its fast growth rates when crystallised from water. Selection of this compound aimed to highlight areas of investigation for operational issues such as encrustation. The second aim of this study was to investigate the possibility of

transferring the additive controlled crystallisation of SA detailed in Chapter 4 into the continuous environment.

5.1.2 Development of the KRAIC platform

As SA was used as a model system to aid the development of the custom built KRAIC platform, multiple experiments were carried out to evaluate the capabilities of the crystalliser and to identify issues that required resolution. The initial design of the KRAIC comprised one feed vessel containing the solution which was pumped *via* a peristaltic pump through unjacketed tubing to a Y-piece in which segmentation with a continuous flow of air was facilitated. Upon reaching the end of the crystalliser the crystals were deposited directly from the end of the tubing into the filtration unit. Although use of air segmentation avoided issues with separation of the product from a carrier fluid, contact of the solution with the crystalliser walls rapidly resulted in encrustation as shown in Figure 5.3.

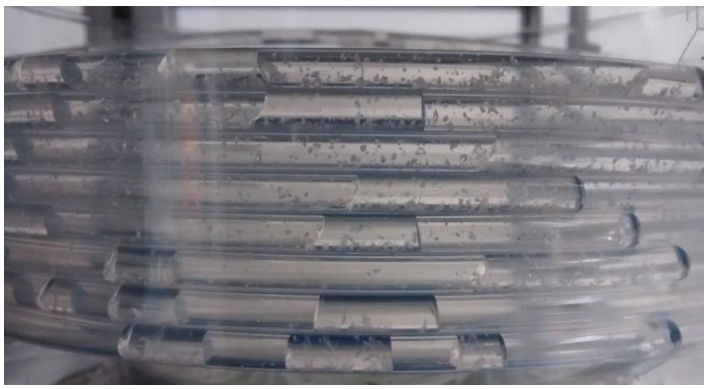

Figure 5.3 - Image showing encrustation on the walls of the crystalliser in experiments using air segmentation.

The fouling disrupted the flow of the segments of solution, caused back-mixing, encouraged further nucleation and growth and ultimately led to a blockage in the system. This type of segmentation was thus deemed unfeasible for future crystallisations. The solid form produced from the experiments was confirmed as the β-form of SA using PXRD analysis, as shown in Figure 5.4.

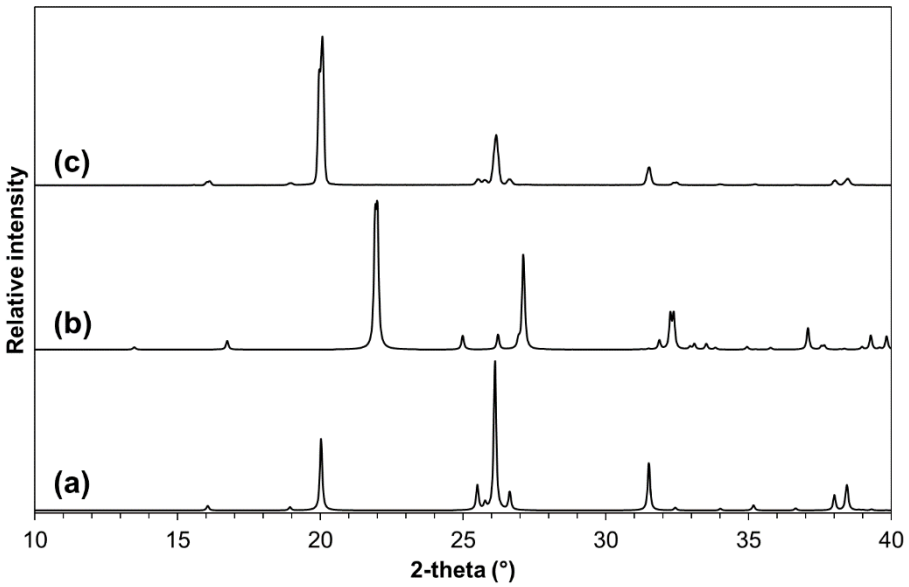

Figure 5.4 - PXRD patterns of (a) β-SA (SUCACB02), (b) α-SA (SUCACB07) and (c) SA obtained from the KRAIC with air segmentation.

As a result of the fouling experienced with air segmentation, liquid segmentation was then implemented as an alternative and a second feed vessel was added from which the carrier fluid was pumped to the mixer piece. The first experiments used dichloromethane (DCM) as the carrier fluid due to its immiscibility with water and low solubility of SA in DCM. Since the carrier fluid coats the walls of the crystalliser and thus prevents contact of the solution with the internal walls of the tubing, in experiments with liquid segmentation no encrustation on the walls of the crystalliser was observed once segmentation was achieved. Furthermore, the solution slugs were almost spherical in size enabling good mixing within the segments (Figure 5.5).

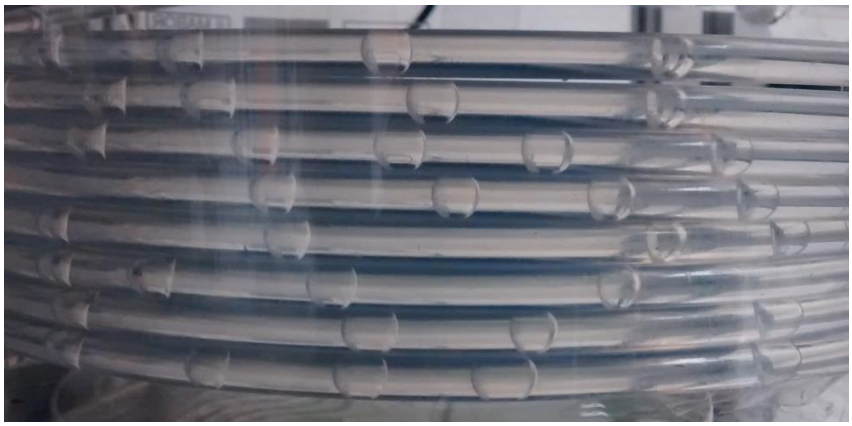

Figure 5.5 - Spherical solution segments produced by liquid segmentation in the KRAIC.

However, after one hour of operation, the glass Y-piece showed signs of encrustation, segment size had become more inconsistent and fewer crystals were observed in each segment. Several minutes later a blockage in the tubing supplying the feed solution was detected at the exit of the peristaltic pump and prior to the segmenter piece. In this experiment the feed solution, containing a concentration of SA of 0.1 g ml^{-1} (T_{sat} = 32 °C), was maintained at a temperature of 40 °C. It was supposed that the solution was sufficiently undersaturated for the SA to remain in solution until reaching the crystalliser. However, the rate of heat loss was underestimated and the solution temperature decreased sufficiently to induce nucleation within the tubing prior to segmentation.

A series of experiments were then carried out in which the temperature of the feed solution was increased in attempt to prevent nucleation in the feed tubes prior to the segmentation. The temperature of the carrier fluid was also reduced to room temperature to counteract the higher start temperature of the solution thus maintaining expected yield. The concentration of the succinic acid solution was kept at 0.1 g ml^{-1}. However, no crystallisation was achieved with the feed solution at either 60 °C or subsequently at 50 °C. As a result, the SA solution concentration was increased to 0.12 g ml^{-1}. With the feed temperature at 60 °C, solids were observed in the second coil. However, after 14 minutes of operation, encrustation at the outlet of the tubing and after the peristaltic pump before the Y-piece was again observed. With the feed vessel at both 40 °C and 50 °C precipitation was observed in the first coil but this was accompanied by encrustation on the Y-piece within minutes. It was thought that the crystallisation in the Y-piece may have resulted from the difference in temperature between the solution and the carrier fluid. This experiment was then repeated with the carrier fluid set at 32 °C, but this again resulted in heavy encrustation to the Y-piece. Liquid segmentation was therefore effective in preventing the encrustation to the FEP body of the reactor tubing once segmentation had been achieved. However, encrustation was still possible prior to segmentation, in the Y-piece as well as in the feed tube. In both cases these are positions at which the solution has contact with the reactor walls and is not protected by the carrier fluid. This fouling causes multiple issues such as reduction in solid recovery, disruption of segmentation, encouragement of further nucleation and growth and ultimately hindered the prolonged running of the platform.

The carrier fluid was then changed to a perfluoropolyether liquid (Galden SV110); the inert nature of this fluid offers the benefits of being immiscible with a wider range of

solvents than DCM and less likely to solubilise the target compound, as well as having favourable contact angle with the FEP.

Steps were also taken to try to prevent problems with encrustation (Figure 5.6):

- The Y-piece segmentation unit was submerged in a glass water bath;
- The tubes from the feed vessels to the pumps were jacketed with tubing connected to a bath circulator, designed in collaboration with Asynt,[177] to prevent nucleation prior to the segmenter piece.

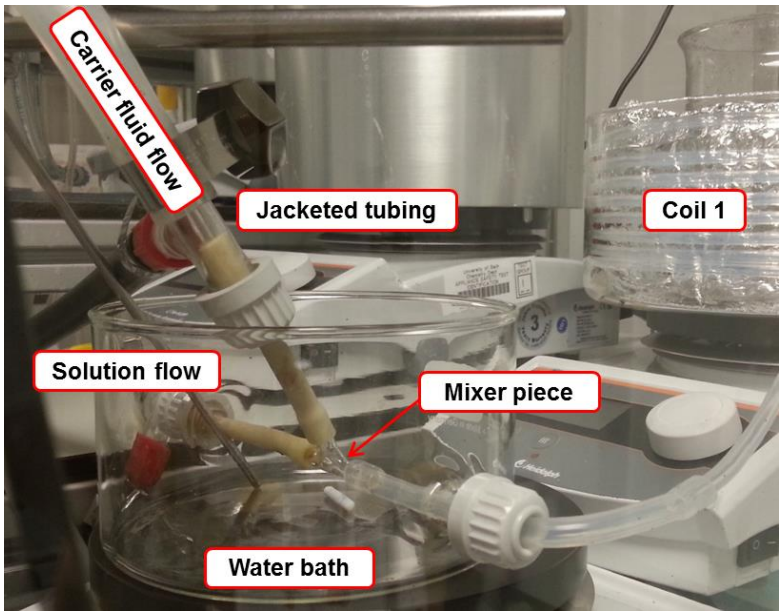

Figure 5.6 - Image showing the water bath for the mixer piece and the tubing jackets.

In previous experiments a double headed peristaltic pump was used to pump the solution and carrier fluid into the system. This was replaced with two gear pumps which offered the benefit of individual control of flow rates as well as producing more uniform segment sizes and less disruption to the flow due to the lower pulsation. The tubing conveying the carrier fluid from the feed vessel to the segmenter piece was also altered to 1 mm ID FEP tubing in place of 3.2 mm ID Masterflex® tubing. This change in internal diameter was implemented in order to avoid problems with air bubbles in the flow; the wetting properties of the tubing are such that a continual stream of carrier fluid is impossible in tubing with a larger diameter. The transparency of the FEP tubing enabled identification of any air in the system. To avoid blockages, the solution tubing was not changed to smaller diameters. Additionally, the mixer was changed to a T-piece which resulted in improved segment uniformity.

The feed and carrier solutions were maintained at 40 °C and room temperature, respectively, and a SA solution concentration of 0.12 g ml^{-1} was used. The tubing jackets were set at 40 °C meaning that the carrier fluid did not require preheating due to the efficacy of tubing jackets around the feed lines and the large surface area for heat transfer provided by the small bore tubing. The water bath (40 °C) was effective in preventing encrustation to the segmenter piece and the tubing jackets prevented a build-up of solids in the tubing prior to the segmenter. However, after 30 minutes of operation a build-up of solids was detected at the outlet of the crystalliser. At the end of the tubing the carrier fluid is able to slip past the solution slugs due to its high density, low viscosity and good wetting properties with the FEP tubing, allowing the surface of the tubing to become exposed to the suspended crystals. This problem led to the design of an end piece to help propel the solution into the collection vessel. An end piece with a split mouth was added to the outlet, designed to induce turbulence. This design enabled a run for one hour with no encrustation observed on the end of the tubing.

Despite implementation of changes to prevent issues with encrustation one of the major continual problems encountered with the set-up was with filtration and the concomitant removal of the carrier fluid from the product. In previous experiments a Whatman glass frit filter was used to collect the solid product, however the bulk of this hindered the changeover of filter paper between residence times and the presence of the carrier fluid caused the filter paper to stick to the sintered glass. Problems with changing over the filtration unit were resolved by implementing a carousel of Buchner funnels. However, the presence of the carrier fluid facilitated adhesion of the particles as well as adhesion of the filter paper to the funnel. Together, these problems hindered filtration efficiency which resulted in continual growth of the crystals in a slurry in the filter funnel and therefore inconsistent measurement of solid recovery and poor recovery of the carrier fluid. A method of removing the carrier fluid prior to filtration was therefore desirable.

The end-piece was therefore modified to feature carrier fluid recovery holes designed to separate the immiscible fluids through the difference in their wetting properties of the FEP tubing. This enabled the carrier fluid to be collected prior to filtration and the solution to continue to the filtration unit. This design was effective in removing the carrier fluid and reducing the adhesion of the filter paper to the filter funnel. However, after 45 minutes of operation, fouling was observed on the end piece at the point of separation of the two solution phases. This separation resulted in removal of the barrier between the solution and the crystalliser walls allowing encrustation and an eventual blockage to occur at this site.

A third end-piece design was then implemented which included an inlet for a neutral solvent prior to the carrier fluid recovery holes. The term neutral solvent here describes a solvent that does not dissolve the product or encourage further precipitation. This solvent was pumped into the end piece with the aim of increasing the slurry velocity to prevent adhesion of particles to the walls of the crystalliser. This method was effective in preventing the encrustation at the site of separation of the solution and carrier fluid for over an hour of operation. Furthermore, a test was carried out in which the flow of the neutral solvent was stopped; within minutes a blockage formed on the end piece, highlighting the importance of this feature. Images of the end pieces are shown in Figure 5.7.

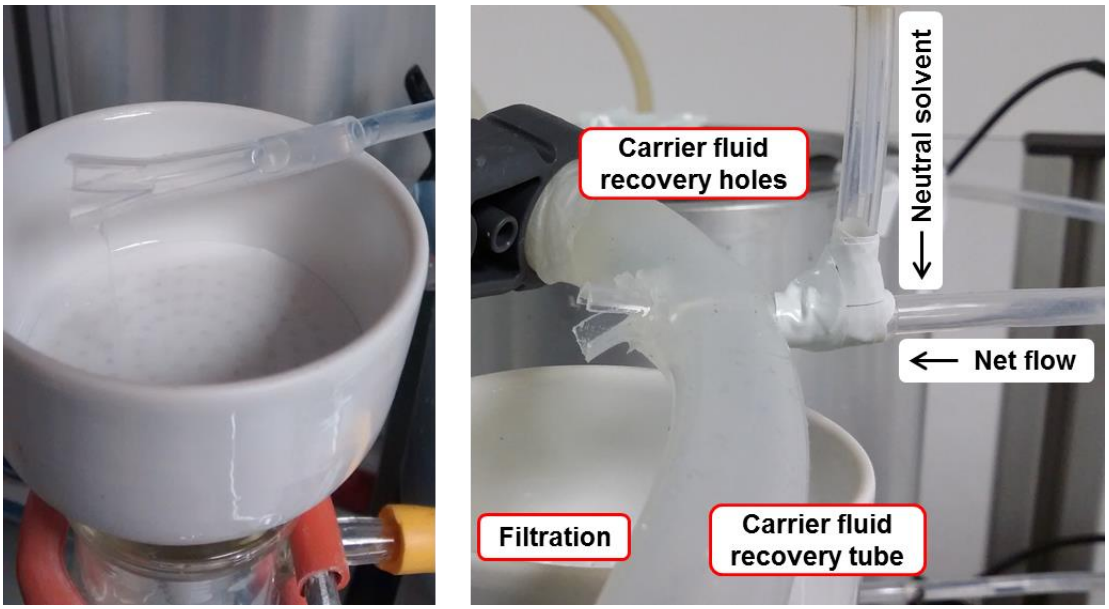

Figure 5.7 - Photograph of (left) the initial end piece design and (right) end piece with carrier fluid recovery and input of neutral solvent.

In subsequent experiments, insulation (graphite or sand) was added to the cylinders housing the coils of tubing to aid efficient temperature control within the tubing. This was effective in insulating the coils and as a result the concentration of SA solution in the feed vessel was increased to 0.13 g ml^{-1} to account for this.

Interestingly, it was evident from the PXRD patterns of solid collected from the experiments that both the α and β polymorphs of SA were present in all of the samples produced with liquid segmentation with both types of carrier fluid (Figure 5.8). In both cases the majority of the obtained pattern matches that of the pattern for β-SA, however it also features multiple additional peaks. The most intense of these peaks at approximately

22° and 27° 2θ correlate with peaks present in the pattern for α-SA. The α-polymorph was not previously observed in the product from batch experiments or in KRAIC experiments with air segmentation. Furthermore, α-SA has only previously been produced though solution-based methods by use of spray drying.[150] In both the liquid-segmentation in the KRAIC and in spray drying techniques there is no interaction of the solution with a solid interface; the lack of such an interface may be a factor in the solution-based production of α-SA. Alternatively, it is possible that the nucleation of the α-SA may be a result of an interaction of the solution with the carrier fluid. In order to investigate this further, a 10 ml scale batch cooling crystallisation with overhead stirring was carried out with an 8 ml saturated solution of SA in water with the same initial concentration as in the KRAIC (0.12 g ml^{-1}), with the vessel also containing 2 ml of the GaldenSV 110 carrier fluid. A cooling profile of 40 °C to 10 °C at 0.5 °C min^{-1} was used. However; this crystallisation produced a sample containing only β-SA.

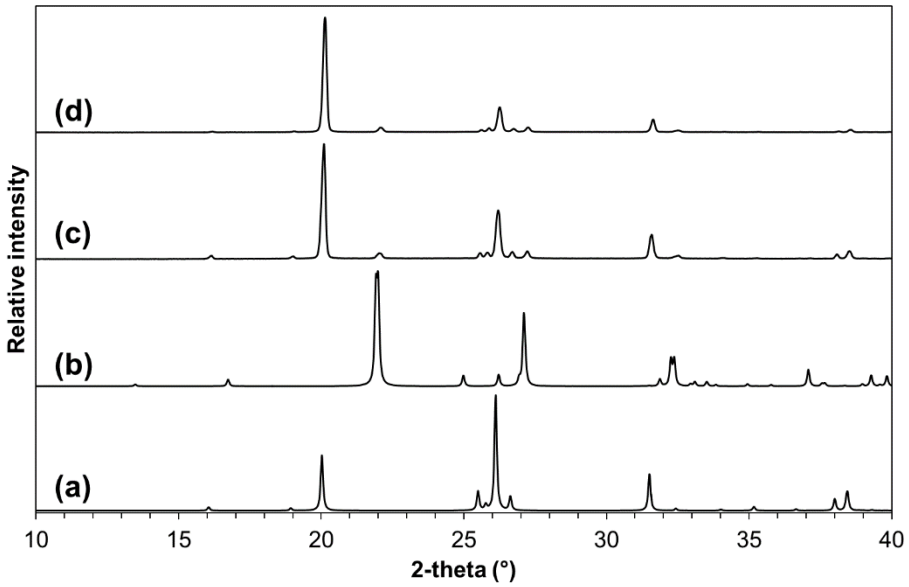

Figure 5.8 - PXRD patterns of (a) β-SA (SUCACB02), (b) α-SA (SUCACB07), (c) sample from experiment with DCM as the carrier fluid and (d) a sample from experiment with GaldenSV 110 as the carrier fluid.

The presence of two polymorphs in the samples can also be inferred from inspection of the crystal morphology of the product. The samples shown to contain α-SA and β-SA feature crystals of two distinct morphologies: plate-like crystals resembling those produced in batch experiments (β-SA) as well as fine and striated plate-like crystals only observed in samples containing α-SA (Figure 5.9). Unit cell determination for the striated

plate-like crystals by scXRD found such crystals to be α-SA. This suggests that the two morphologies observed may represent the two polymorphs of SA.

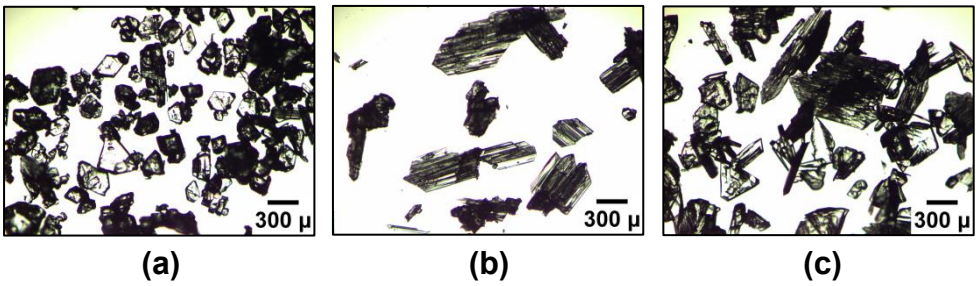

Figure 5.9 - Microscope images showing the different crystal morphologies ((a) plate-like crystals and (b) striated plate-like crystals) which are present concomitantly in the samples (image (c)).

5.1.3 Experiments carried out in the optimised design of the KRAIC

Figure 5.10 shows a schematic of the optimised design of the KRAIC. The two feed solutions are independently pumped (using gear pumps) to the mixer piece *via* jacketed tubing. Upon reaching the mixer piece, the two phases are segmented and continue to flow through the three coils. Supersaturation is generated within the solution segments through cooling and upon reaching the end of the crystalliser the carrier fluid is recovered and the crystalline product isolated using vacuum filtration.

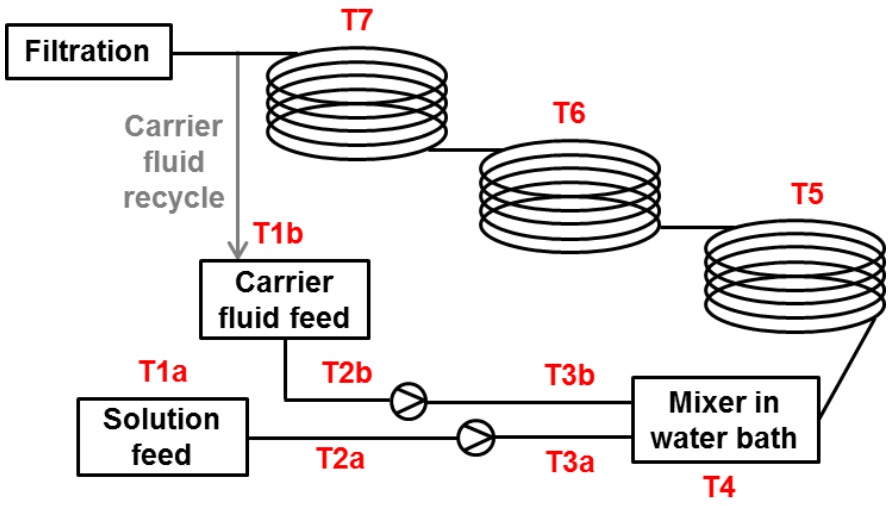

Figure 5.10 - Schematic of the KRAIC set-up with temperature zones labelled (T1-7).

5.1.3.1 Experimental information

The experimental parameters used for all experiments in the optimised set-up are summarised in Table 5.1. Prior to the experiment the tubing was primed with pure solvent and carrier fluid (40 °C) for 2 hours. The residence volume in the KRAIC is the volume of the solution in each residence time and does not include the carrier fluid.

Table 5.1 - Table summarising the experimental information for the crystallisation of SA from water with no additive present in the KRAIC.

SA conc. (g ml^{-1})	Segmentation type	Flow rate (ml min^{-1})	Mixer type	RT	RV
0.13	Liquid (GaldenSV 110, perfluoropolyether)	16.6	T-piece	9 min 15 sec	56 ml

RT= Residence time RV = Residence volume

The individual temperatures of the different temperature zones in the KRAIC (labelled in Figure 5.10) are detailed in Table 5.2. The three tubing coils were insulated but not actively heated thus achieving a smooth cooling gradient which was monitored using temperature probes. As shown in Figure 5.11, the temperature along the crystalliser varied from 40 °C to 19.6 °C.

Table 5.2 - Temperature zones in the KRAIC and the temperatures used in the experiment.

Temperature zone	Description	Temperature (°C)
1a	Feed vessel	40
1b	Feed vessel	Room temperature
2a, 2b	Tubing jacket from feed to pump	40
3a, 3b	Tubing jacket from pump to mixer bath	40
4	Mixer bath	40
5	Coil 1	30
6	Coil 2	24
7	Coil 3	22

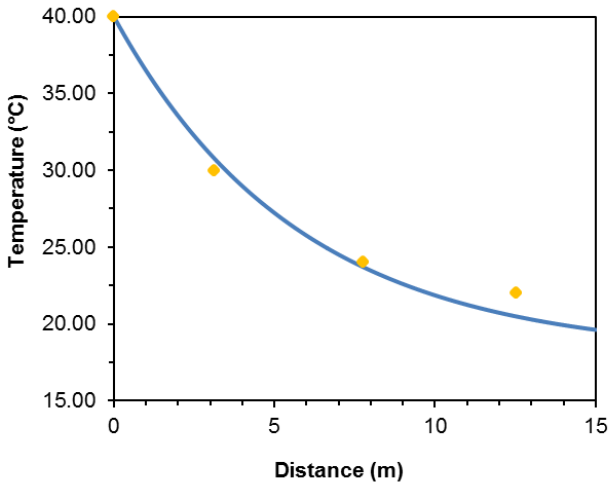

Figure 5.11 - The calculated temperature gradient over the length of the crystalliser using experimentally observed temperatures.[176]

The carrier fluid was recovered prior to filtration (as described in Section 5.1.2) and a neutral solvent (water from an ice bath) pumped into the end piece to continue transporting the product solution into the filtration stage. Solid product from each residence time was isolated using vacuum filtration, allowing for measurement of solid recovery and homogeneity of the crystallisation rate within the experiment (Table 5.3).

Table 5.3 - Solid recovery for each residence time in the crystallisation of SA from water in the KRAIC with no additive present.

% Yield							
RT1	**RT2**	**RT3**	**RT4**	**RT5**	**RT6**	**RT7**	**RT8**
2.2	2.7	2.9	3.3	3.5	3.6	3.8	4.4

The crystallisation of SA in the presence of Pluronic P123 (PP123) in the KRAIC followed the same experimental procedure as above with the exception that the feed solution also contained 0.5% PP123 (0.0007 g ml^{-1}). Due to reasons discussed below, accurate calculations of solid recovery are not reported for these experiments. The crystallisation of SA in the present of polypropylene glycol 4000 (PPG4000) again followed the same procedure but with 0.17% PPG4000 (0.0002 g ml^{-1}) present in the feed solution. Table 5.4 shows the solid recovery for the experiment.

Table 5.4 - Solid recovery for each residence time in the crystallisation of SA from water in the KRAIC with PPG4000 present.

% Yield		
RT1	**RT2**	**RT3**
0.5	1.1	1.0

Crystal shape and size distribution was monitored visually using optical microscopy. Microscope images were captured using a Nikon Coolpix P5100 camera attachment to a Brunel Microscopes microscope and a Leica DM1000 microscope equipped with an Infinity 2 microscopy camera at 4x magnification.

The solid form of the product was monitored using PXRD, for which further experimental information can be found in Chapter 3.

5.1.3.2 Crystallisation of succinic acid with no additive present

In repeated experiments in the optimised design of the KRAIC, SA crystals were consistently observed mixing inside the solution segments in the top of the second coil within 7 minutes of starting the experiment. This consistency of the nucleation point within the KRAIC, in the absence of seeding, may be a result of the sterile environment inside the platform. The solutions are filtered prior to entering the system and use of liquid segmented flow prevents exposure of the SA solution to any imperfections on the internal walls of the reactor, which can be a site of nucleation.

With no additive present the crystalliser was successfully operated for 1.5 hours with no encrustation observed within the platform. An average yield of 0.24 g (2%) was collected for each residence time. However, the masses observed range from 0.16 g – 0.32 g throughout the duration of the experiment. This variation between residence times may be attributed to a gradual decrease in the segment size during the experiment. This may have resulted in an increased mixing efficiency which may have led to an increased number of nucleation and growth events. It is clear that the solid recovery requires optimisation and in future experiments temperature control could be implemented within the coils to lower the temperature and increase the solid yield. A different neutral solvent could also be identified to eliminate the possibility of dissolution of the precipitate following recovery of the carrier fluid. The solid form of the product of each residence time was investigated using PXRD. The PXRD pattern from each residence time shows peaks corresponding to both the α-SA and β-SA polymorphs, as shown in Figure 5.12.

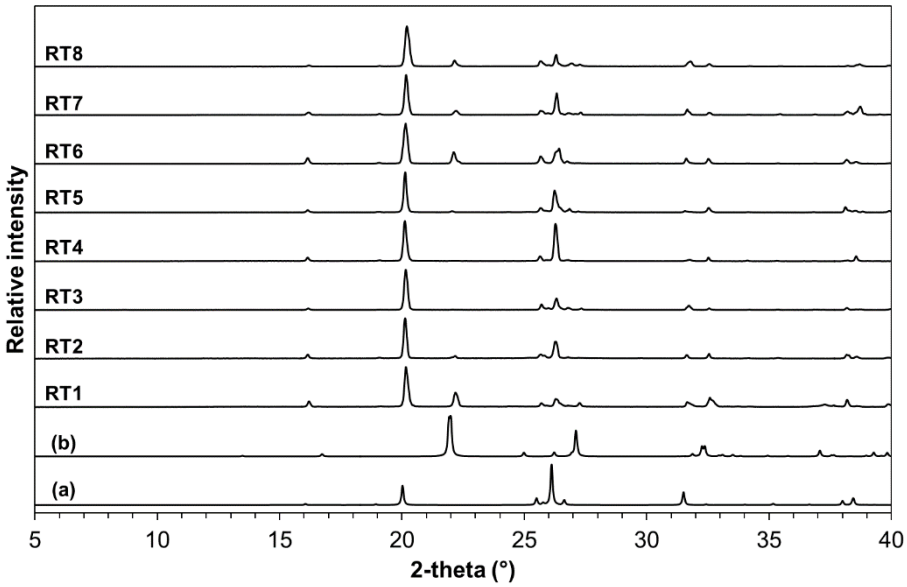

Figure 5.12 - PXRD patterns of (a) β-SA (SUCACB02), (b) α-SA (SUCACB07) and patterns from each RT in the KRAIC experiment with no additive present.

This correlates with the findings presented above from previous development experiments in the KRAIC with liquid segmentation. Preferred orientation effects can be observed in the patterns due to the sample preparation. The crystals were not ground to monodisperse sizes in order to avoid conversion of the polymorphs through grinding (discussed in Chapter 4).

Figure 5.13 shows the morphology of the crystals produced in the experiment. As noted in previous development experiments, two types of morphology are observed: plate-like crystals of inconsistent sizes and fine, striated plate-like crystals. This finding correlates with the identification of a combination of α-SA and β-SA in the samples taken during the experiment.

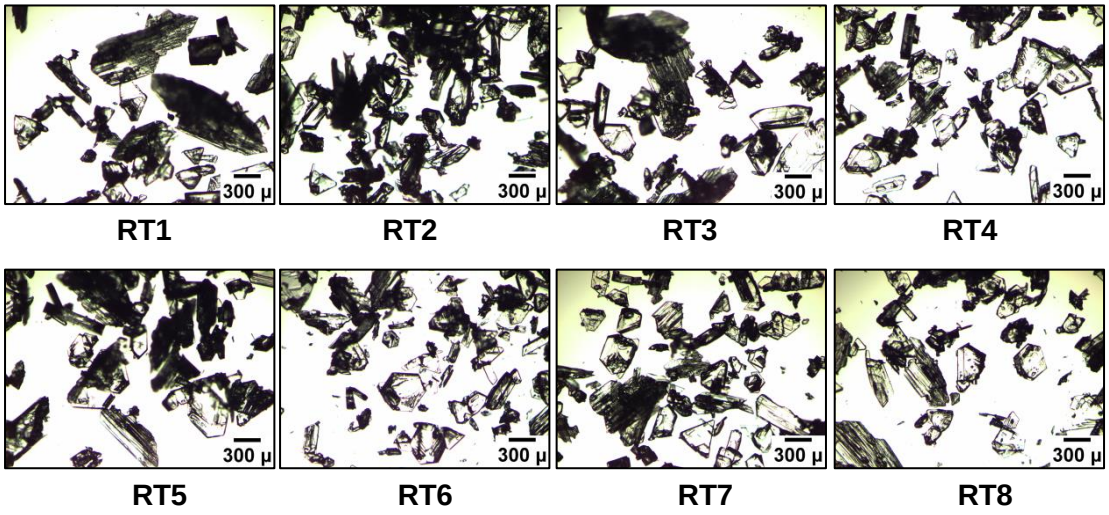

Figure 5.13 - Microscope images of the crystal morphology of SA produced in the optimised design of the KRAIC with no additive present.

5.1.3.3 Crystallisation of succinic acid in the presence of polymer additives

Additional experiments were also carried out in the presence of polymer additives with the aim of reproducing in the KRAIC the results observed in the batch environment. Firstly, experiments were carried out with 0.5% Pluronic P123 (PP123) present in the feed solution. Needle-like crystals were produced in the presence of the additive, modified from the plates, as observed in the batch environment under these conditions (Figure 5.14). Production of the more favourable block-like crystals would require lower starting concentrations of SA and therefore, operation at lower temperatures. Conditions which nucleated at room temperature, producing needle-like crystals, were tested as a starting point to obtain the correct conditions to observe a morphology change in this platform.

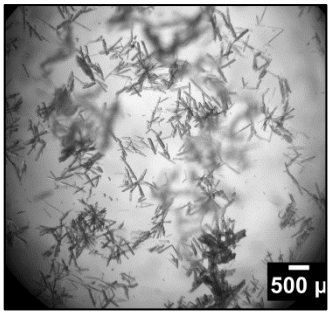

Figure 5.14 - Microscope image of SA crystals produced in the presence of PP123 in the KRIAC.

Despite the observed morphology change, showing the initial success in transferring the additive effect to a continuous crystallisation environment, the surfactant properties of the polymer enabled the polymer to act as an emulsifier of the water and carrier fluid and consequently disrupted the segmentation. Interestingly, in the presence of the polymer, only pure β-SA was produced with no α-SA present in the solid product, unlike experiments with no polymer present discussed above. This may be as a result of the disruption of the segmentation and subsequent contact with the crystalliser walls. PXRD patterns showing these findings are presented in Figure 5.15.

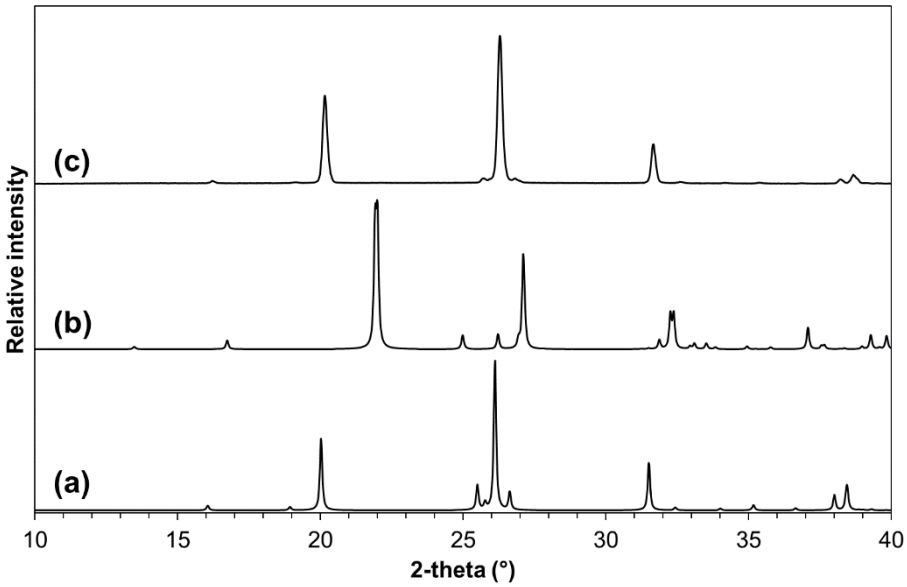

Figure 5.15 - PXRD patterns of (a) β-SA (SUCACB02), (b) α-SA (SUCACB07) and (c) SA sample from the KRAIC run in the presence of PP123.

As a result of the incompatibility of the carrier fluid and the water containing PP123, experiments were also carried out with polypropylene glycol 4000 (PPG4000) present in solution. In the batch experiments, the presence of PPG4000 displayed a similar effect to PP123, producing block-like crystals of SA in a broader range of concentrations. The block-like crystals could be produced in the case of PPG4000 additive with small

quantities of polymer present and therefore a concentration of 0.17 % was used for the experiment in the KRAIC. However, unlike in the batch environment the block-like morphology was not reproduced. Instead, plate-like crystals with well-defined edges were observed in addition to fine plate-like crystals with striated edges (Figure 5.16).

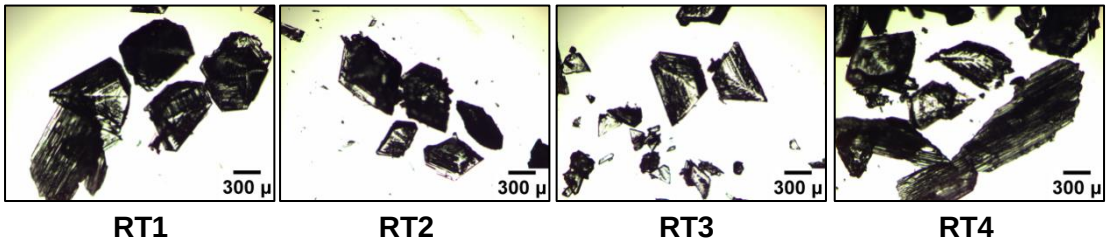

Figure 5.16 - Microscope images of crystals produced in the KRAIC in the presence of PPG4000.

This lack of production of the block-like crystals may be as a result of the gentler mixing conditions in the KRAIC in comparison to the batch environment and therefore a higher concentration of the additive may be required to produce a comparable effect on the crystal morphology of SA. The solid recovery was also lower than with no additive present with very limited crystallisation observed within the slugs. This may be due to the polymer imparting an inhibiting effect on nucleation under these conditions. However, the presence of the PPG4000 polymer in this case did not disrupt the segmentation and therefore future work could be directed towards optimisation of this experiment with a higher starting concentration of both SA and the PPG polymer. PXRD analysis of the samples from each residence time showed that both α-SA and β-SA were present in the samples (Figure 5.17).

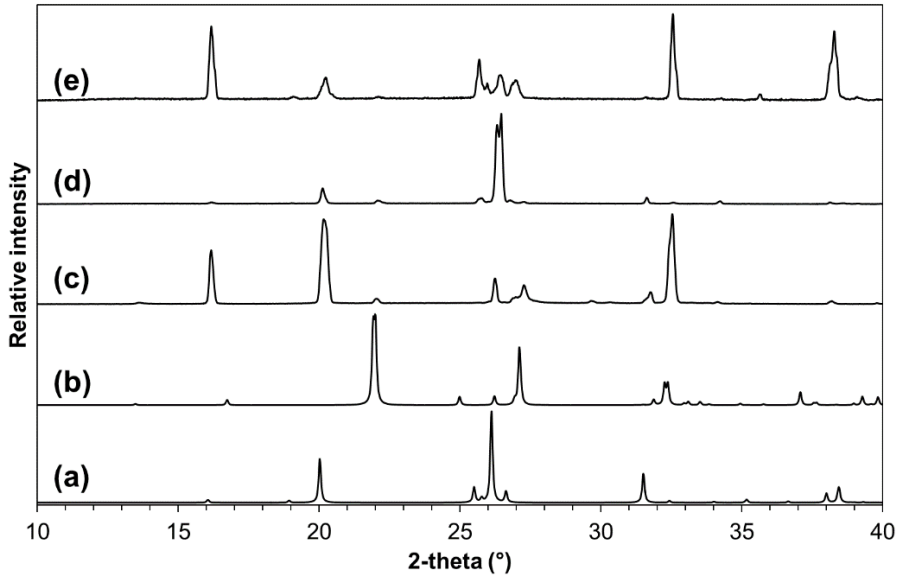

Figure 5.17 - PXRD patterns of (a) β-SA (SUCACB02), (b) α-SA (SUCACB07) and samples obtained from the KRAIC experiment with PPG4000 present in: (c) RT1, (d) RT2 and (e) RT3.

This finding, in the situation where segmentation has not been disrupted, correlates with the reasoning that α-SA may form in solution in the absence of a solid interface discussed in Section 5.1.2.

5.2 Crystallisation in the Continuous Oscillatory Baffled Crystalliser

5.2.1 Introduction and aims

The Continuous Oscillatory Baffled Crystalliser (COBC) is a marketed platform developed by NiTech Solutions.[80] It operates at larger scale than the KRAIC (g h^{-1}) and is a glass, tubular crystalliser with jacketed straights comprising small cells separated by equally spaced orifice baffles (Figure 5.18).

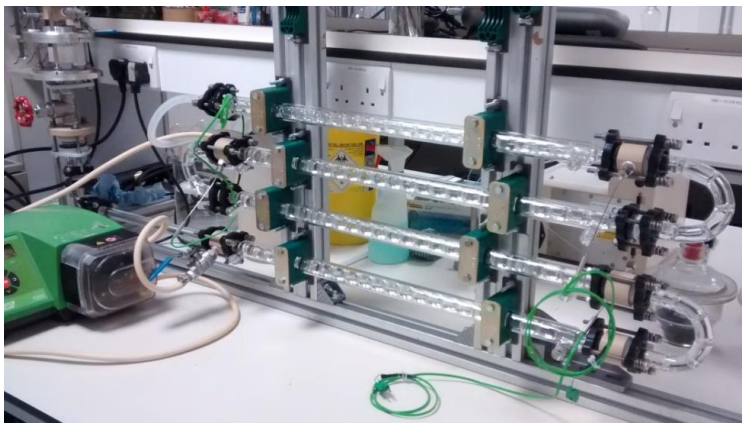

Figure 5.18 - The DN15 Continuous Oscillatory Baffled Crystalliser (COBC) used in this study.

The solution is pumped into the crystalliser with oscillatory motion superimposed on the net flow, and the interaction of the flow with the baffles generates eddy currents enabling good mixing conditions in each cell (Figure 5.19).[178] As in many flow platforms, the high surface area to volume ratio also allows for excellent heat transfer throughout the system, an advantage over stirred tank reactors in providing precise control over temperature. Through the combination of net flow from the peristaltic pump and the oscillation, the platform is designed to operate in plug flow; which describes the situation in which the same residence time is achieved for all elements of the liquid.[179] In theory, this is beneficial since under these conditions every particle experiences the same conditions, thus producing consistent and uniform particles with narrow particle size distributions.[5]

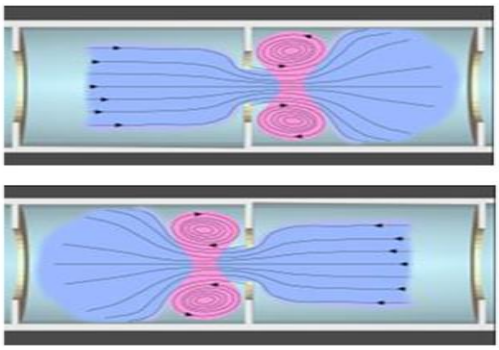

Figure 5.19 - Schematic showing the eddy currents generated by the mixing conditions in the COBC.[80]

The oscillatory flow in the COBC can be described by three dimensionless numbers: the oscillatory Reynolds number (Re_o), the Strouhal number (St) and the net flow Reynolds number (Re_n). The intensity of the oscillation in the COBC is governed by the oscillatory Reynolds number,[178-180] the ratio of the tube diameter to the oscillation amplitude is described by the Strouhal number, thus describing the propagation of eddies through the baffles, and the net flow Reynolds number describes the oscillatory mixing under flow.[5,179,181] These parameters are described by the following equations:

$$\boldsymbol{Re_o} = \frac{2\pi f x_o \rho d}{\mu}$$

$$\boldsymbol{St} = \frac{d}{4\pi x_o}$$

$$\boldsymbol{Re_n} = \frac{\rho u d}{\mu}$$

Where f = frequency (Hz), x_o = centre to peak amplitude (m), ρ = density (kg m^{-3}), d = internal tube diameter (m), μ = fluid viscosity (kg m^{-1} s^{-1}) and u = mean velocity (ms^{-1}).

The calculation of Re_o and Re_n allows for the determination of the velocity ratio, φ, which relates the oscillatory velocity and net flow velocity through the following equation:

$$\boldsymbol{\varphi} = \frac{Re_o}{Re_n}$$

The velocity ratio should be greater than one, with the velocity of oscillation higher than the velocity of net flow through the crystalliser for effective mixing.[179] To achieve plug flow, it is recommended that oscillatory flow proceeds with $Re_o \geq 100$, $St \leq 0.5$, $Re_n \geq 50$ and the velocity ratio should remain in the range of 2-10.[179-181]

Several studies of crystallisation under continuous oscillatory flow have recently been reported. Briggs *et al.* demonstrated the successful seeded continuous cooling crystallisation of L-glutamic acid in a COBC in which control over polymorphic form was achieved.[181] Continuous crystallisation of a model API was reported and a residence time of 12 minutes was used compared to a 9 hour and 40 minutes batch crystallisation.[5] Multi-component materials have also successfully been produced in the continuous oscillatory environment such as the crystallisation and scale-up of α-lipoic acid:nicotinamide co-crystal.[178] However, there are currently no reports of the combined use of polymer additives to control crystal morphology whilst operating in a continuous oscillatory environment. Therefore, the aim of this study was to investigate the transfer of the additive-mediated morphology change of SA crystals when crystallised from water (reported in Chapter 4) achieved in a batch environment, to the continuous environment under oscillatory flow.

5.2.2 Experimental information

In this work the DN15 COBC was used in a vertical set-up comprising four jacketed glass straights and three unjacketed glass bends (Figure 5.20). The set-up has a working volume of 612 ml and the glass tubes have an internal diameter of 15 mm. The inside temperature of the glass straights was controlled using four circulating baths *via* jackets (one per straight) and the solution temperature was monitored during the crystallisation using *in situ* thermocouples located at the end of the first three straights. The solution was pumped into the system *via* a peristaltic pump and the oscillation was provided through use of a PTFE bellow driven by a motor.

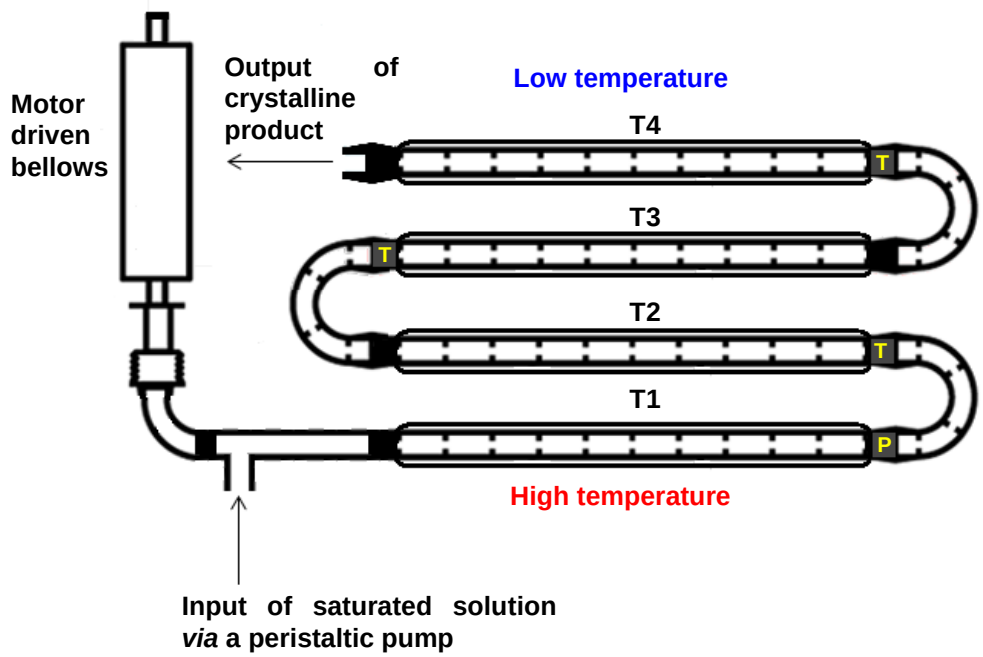

Figure 5.20 - Schematic of the 4-straight COBC set-up. Grey areas indicate the location of ports for monitoring the solution (T = thermocouple port and P = pressure gauze).

For all experiments SA, purchased from Sigma Aldrich, was used at an initial concentration of 0.09 g ml^{-1} (T_{sat} = 30 °C) and deionised water was used as the crystallisation solvent. The contents of the feed vessel were heated to 35 °C to ensure complete dissolution of the SA. In the experiments containing additives (Pluronic P123 and polypropylene glycol 4000), the polymer was dissolved in a small aliquot of the feed solvent and was added to the remaining solution containing SA in a 3 L round-bottomed flask and left to dissolve. The temperature was controlled using a Drysyn® former with a thermocouple submerged in the solution, mixing within the feed vessel was facilitated using magnetic bottom stirring or overhead stirring for experiments with large feed volumes.

Prior to all experiments, the COBC was primed with deionised water at 35 °C (temperature of the feed vessel) to remove all air bubbles from the system. The inlet tube was then transferred to the feed vessel with minimal disturbance to the system by temporarily pausing the peristaltic pump and oscillator. Upon reaching the end of the COBC, product from each residence time was collected and separated from the solution *via* vacuum filtration using a Buchner flask and funnel. The crystal morphology of the product was examined under an optical microscope (a Leica DM1000 microscope equipped with an Infinity 2 microscopy camera at 4x magnification) and the solid form characterised using PXRD.

5.2.2.1 Pump calibration for different oscillation conditions

The solution flow rate was calibrated to 50 ml min^{-1} resulting in an initial mean residence time of 12 min 14 s. Prior to experiments with different oscillation conditions to those used previously, the flow rate was recalibrated as shown in Table 5.5.

Table 5.5 - Pump calibration for different oscillation conditions in the COBC.

1Hz and 10mm			
Time	Volume	rpm	Flow rate
5mins	254ml	4.2	50.8ml/min
5mins	250ml	4.1	50ml/min
5mins	250ml	4.1	50ml/min
5mins	250ml	4.1	50ml/min
Residence time = 12 min 14 sec			

2Hz and 10mm			
Time	Volume	rpm	Flow rate
1 min	52ml	4.1	52ml/min
1 min	52ml	4.1	52ml/min
Residence time = 11 min 46 sec			

2Hz and 25mm			
Time	**Volume**	**rpm**	**Flow rate**
1 min	50ml	4.1	50ml/min
1 min	50ml	4.1	50ml/min
Residence time = 12 min 14 sec			

Table 5.6 summarises the experimental information and solid recovery for all of the COBC experiments.

Table 5.6 - Summary of experimental information for all COBC experiments carried out.

Exp No.	Polymer Conc.	Flow rate (ml min^{-1})	Oscillation		Re_o	Re_n	St	Temperature (°C)					No. of residence times operated for	% Yield					
			Frequency (Hz)	Amplitude (mm)				Feed	T1	T2	T3	T4		RT1	RT2	RT3	RT4	RT5	RT6
No polymer																			
NP(1)	N/A	50	1	10	530	79	0.24	35	30	23	17	10	2	3.5	10.6*				
NP(2)	N/A	50	1	10				35	25	15	8	12	2	10.8	3.1**				
NP(3)	N/A	52	2	10				35	25	15	8	12	2	0.7	6.6				
PP123 as polymer additive																			
PP123(1)	0.17%	52	2	10	1059	83	0.24	35	25	15	8	12	5	0.2	8.7	17.5	9.9	13.3	
PP123(2)	0.17%	52	2	10				35	25	15	10	8	3	0.0	7.1	4.8			
PP123(3)	0.17%	50	2	25				35	25	15	12	10	5	0.0	12.5	19.9	15.5	15	
PP123(4)	0.13%	50	2	25				35	25	15	12	10	5	0.0	9.2	22.3	24.6	18.4	
PP123(5)	0.13%	50	2	25				35	25	18	12	10	4	0.0	11.2	28.2	27.2		
PP123(6)	0.13%	50	2	25				35	25	23	12	10	4	0.0	7.3	25.2	26.1		
PPG4000 as polymer additive																			
PPG(1)	0.13%	50	2	25	2647	79	0.1	35	25	18	12	10	4	0.0	15.3	21.5	19.8		
PPG(2)	0.10%	50	2	25				35	25	18	12	10	4	0.0	17.6	21.5	21.83		
PPG(3)	0.10%	50	2	25				35	25	18	12	10	6	0.0	18.1	24.6	19.8	12.5	5.2**

*Incomplete residence time due to early termination of experiment
**Low yield due to problems with sedimentation.

5.2.3 Experiments with no additive

Although the focus of this work involved achieving the additive-mediated morphology in the continuous environment, initial COBC experiments were carried out with no additive present in solution to gain initial understanding of the system and its morphology under flow conditions.

NP(1): T1 = 30 °C, T2 = 23 °C, T3 = 17 °C, T4 = 10 °C, oscillation 1 Hz 10 mm

From batch experiments at 350 ml scale, it was expected that the solution would nucleate between 16-17 °C and the cooling profile was therefore designed accordingly. In the first experiment (NP(1)), back-mixing of air from the outlet into the top (fourth) straight led to the presence of large air bubbles in the fourth straight resulting in a large volume decrease for the solution. After 20 minutes, crystallisation was observed in the top straight (10 °C), indicating that the nucleation temperature may be lower in the COBC than in the batch environment. However, not long after crystals were observed in the fourth straight, encrustation on the inside of the glass walls was evident. This was exacerbated by the presence of air in the system. Issues with encrustation and the formation of a blockage on the end piece (which has a smaller aperture than the glass tubes) led to the premature termination of the experiment during the second residence time RT2 (Figure 5.21).

Figure 5.21 - Encrustation on the walls of the crystalliser (left) and on the end piece (right) in experiment NP(1).

Figure 5.22 shows microscope images of the crystal morphology of the product of RT1-2. The crystals are non-uniform in size and shape; this may be expected given the encrustation and possibility of attrition between the particles. The crystals are also smaller than those produced in the batch experiments, possibly due to the fact that nucleation occurred in the final straight allowing limited time for growth.

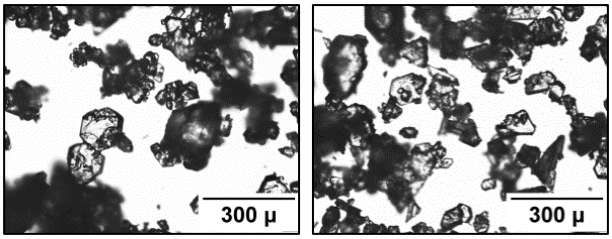

Figure 5.22 - Microscope images showing the crystal morphology of product from RT1-2 for experiment NP(1).

NP(2): T1 = 25 °C, T2 = 15 °C, T3 = 8 °C, T4 = 12 °C, oscillation 1 Hz 10 mm

In the second experiment (NP(2)) with no additive present, the previous appearance of air bubbles in the fourth straight was prevented by improved sealing of thermocouple connections and priming the exit tube with water. The temperature profile was also altered based on knowledge gained from the first experiment. The aim was to encourage nucleation to occur earlier by lowering the temperature of the third straight and to prevent further nucleation on the walls of the crystalliser by increasing the temperature of the fourth straight. At the beginning of RT1, crystals were observed in the third straight in suspension and on the crystalliser walls. At the end of RT1 crystals were also evident in the second straight and sedimentation was evident between the third bend and the fourth straight as well as at the beginning of bends two and three suggesting that the mixing conditions were not sufficient to suspend the crystals and flow against gravity through the bends (Figure 5.23). The unjacketed poly ether ether ketone (PEEK) thermocouple joints and metal thermocouple may be a site for nucleation. The experiment was terminated after two residence times due to the sedimentation issues.

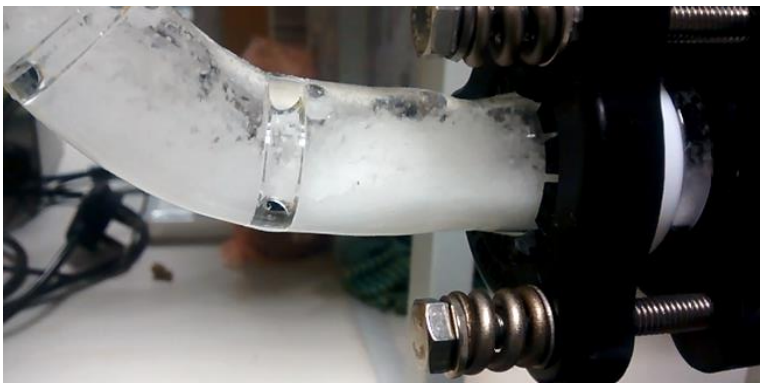

Figure 5.23 - Sedimentation at the end of the second straight in experiment NP(2).

Figure 5.24 shows the crystal morphology from this experiment. As observed in the previous experiment, the crystals appear non-uniform in shape and size with several

diamond-shaped plates evident in the second residence time; in Chapter 4 it was shown that such plates are produced from SA crystallisation from water.

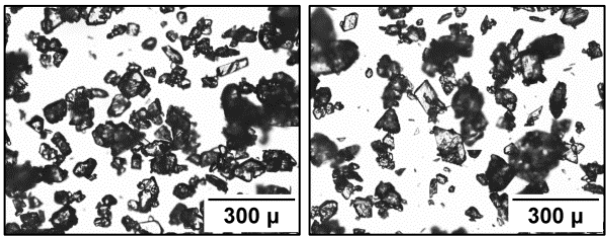

Figure 5.24 - Microscope images showing the crystal morphology of product from RT1 and RT2 for experiment NP(2).

NP(3): T1 = 25 °C, T2 = 15 °C, T3 = 8 °C, T4 = 12 °C, oscillation 2 Hz 10 mm

As a result of the sedimentation issues experienced previously, the oscillation conditions were altered in the third experiment (NP(3)) but the temperature profile was retained. The residence time was re-determined as a result of this change in conditions (Table 5.5). As reported in the previous experiment, crystals were observed in the third straight in suspension but also on the crystalliser walls; however, this occurred slightly later than in the previous experiment, in the middle of RT1 (Figure 5.25). At the end of RT1, sedimentation was observed in the same sites as in the previous experiment and in addition was observed on the outlet tube. The encrustation observed in the third straight worsened with time yet no encrustation was observed in the final straight, indicating that the higher temperature was effective in preventing nucleation on the walls of the crystalliser. At the beginning of RT2 crystals were observed in the second straight, suggesting that back-mixing of crystals may be occurring. However, by the end of RT2 the quantity of crystals in the final straight had decreased with respect to RT1. It is presumed that sedimentation and reduced suspension capability through the vertical bends led to this reduction in crystals reaching the final straight. This continued sedimentation led to the termination of the experiment at the end of RT2.

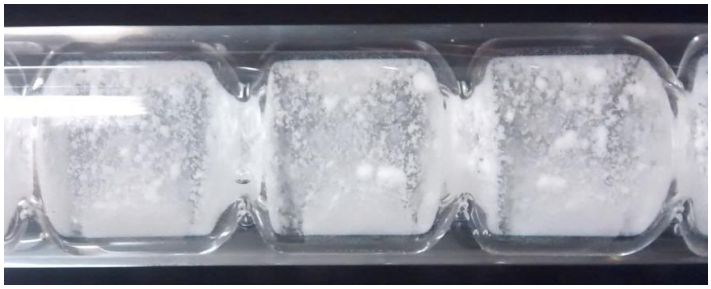

Figure 5.25 - Encrustation on the third straight in experiment NP(3).

Figure 5.26 shows the crystal morphology from the experiment. The crystals have a similar appearance to those from experiment NP(2).

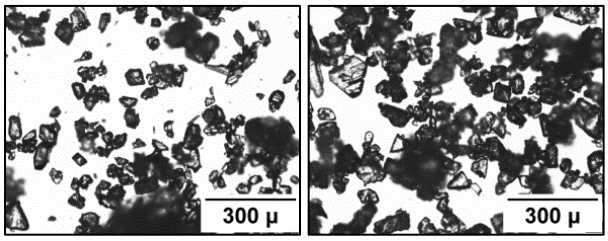

Figure 5.26 - Microscope images showing the crystal morphology of product from RT1 and RT2 in experiment NP(3).

5.2.4 Experiments with PP123 additive

PP123(1): T1 = 25 °C, T2 = 15 °C, T3 = 8 °C, T4 = 12 °C, oscillation 2 Hz 10 mm, 0.17% PP123

For experiments with the PP123 additive present, the temperature profile and oscillation conditions used for the experiments with no additive were initially selected as a starting point. Initial additive concentrations were selected based on the conditions required to produce the desirable block-like crystals observed in the batch crystallisations and therefore a starting concentration of 0.17% was used. In the first experiment (PP123(1)), a longer induction time for crystallisation was evident and crystals were not observed until 25 minutes after the experiment commenced (i.e. at the beginning of RT2); this was approximately 8 minutes later than the experiments with no additive present. However, the crystals were initially observed in the same location, in the third straight. It was also evident that in the presence of the polymer, crystals were nucleating on the walls of the crystalliser at a slower rate, suggesting that the polymer may be creating a more viscous environment, enhancing suspension (Figure 5.27). Several minutes after the first observation of crystals in the third straight, crystals were also observed to be present in the second straight. However, encrustation was only occurring on the walls of the third straight suggesting that the presence of the crystals in this location may be as a result of back-mixing of suspended solids rather than nucleation in the second straight.

Figure 5.27 - Encrustation on the third straight in experiment PP123(1).

At the beginning of RT3 sedimentation was observed in the system in several locations: the exit piece, exit tube and at the second and third thermocouple ports. As with the encrustation, the sedimentation was not as severe as for the experiments with no additive present, suggesting that the crystals are suspended more effectively in the presence of the additive. After five residence times the experiment was terminated as the feed solution had been expended. The sedimented material within the COBC was also collected for analysis of the crystal morphology. Figure 5.28 shows the crystal morphology produced in each residence time in this experiment.

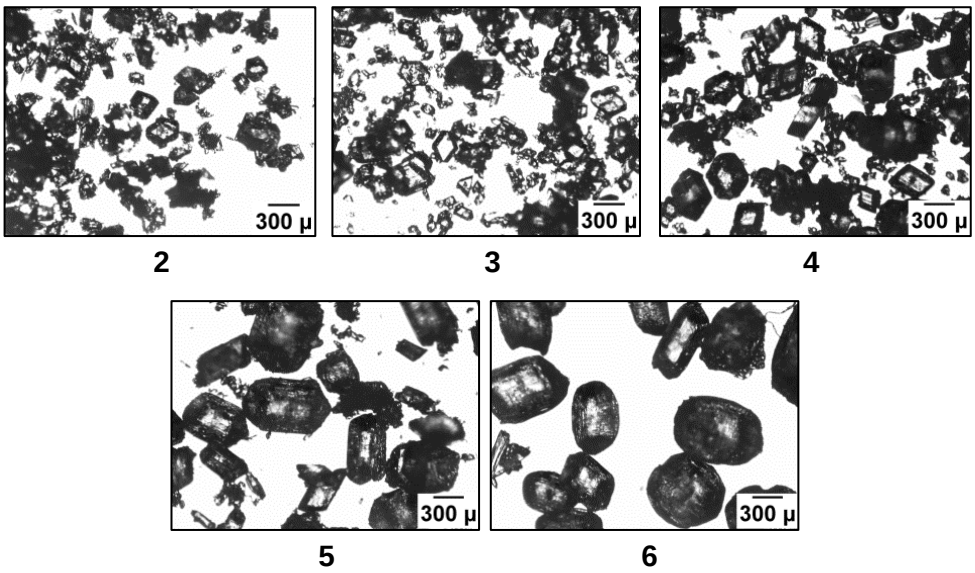

Figure 5.28 - Microscope images showing the crystal morphology of product from RT2-5 and sedimented material (6) for PP123(1).

Firstly, it can be concluded that the crystals are larger in the presence of the PP123 additive in comparison to the case when no additive is present. As observed in the batch experiments, block-like crystals are evident in the samples, showing the additive effect. However, they are not uniform in size and are accompanied by smaller fine crystals, especially in the first three residence times. As the experiment progresses the crystals

became larger and the block-like crystals are replaced with more rod-like crystals. There is also evidence of partial dissolution of the particles as they reach the higher temperature final straight, which is most clearly shown in the images of SA from RT5 and the remaining contents of the crystalliser (6) in Figure 5.28, in which the crystals have more rounded edges. The presence of block and rod crystals shows that the additive morphology effect has been successfully reproduced in the continuous crystallisation environment in the COBC.

PP123(2): T1 = 25 °C, T2 = 15 °C, T3 = 10 °C, T4 = 8 °C, oscillation 2 Hz 10 mm, 0.17% PP123

In the second experiment with the PP123 additive (PP123(2)), the cooling profile was altered to remove the heating step in the final straight to prevent dissolution of the particles. The temperature of the final straight was thus lowered to 8 °C and that of the other straights changed accordingly to maintain a linear cooling profile (see Table 5.6). Within 20 minutes of commencing the experiment (end of RT2), crystals were observed in the third straight and in the fourth straight several minutes afterwards. Five minutes after the first crystals were reported, sedimentation was observed near the exit piece, exit tube and near the third thermocouple port. A small quantity of encrustation was observed on the walls of the third straight but this was not as severe as in experiments with no additive present. At the end of the second residence time sedimentation was observed prior to the final bend and crystals were beginning to emerge into the second straight through back-mixing. The experiment was then terminated due to these sedimentation issues. The experiment was more successful with the temperature profile used in PP123(1). Removal of the heating step in the final straight, as implemented in PP123(2), led to more nucleation, more crystals and as a result, more sedimentation. The crystal morphology shown in the microscope images in Figure 5.29 demonstrates that block-like crystals (i.e. with favourably modified morphology) were produced in the residence times for which the system was operated.

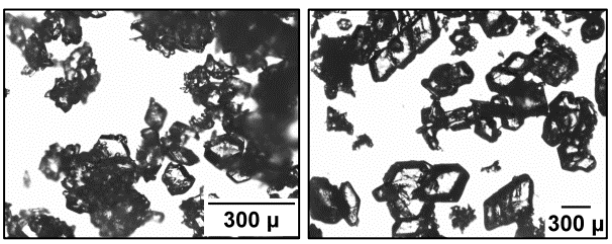

Figure 5.29 - Microscope images showing the crystal morphology of product from RT2-3 for experiment PP123(2).

PP123(3): T1 = 25 °C, T2 = 15 °C, T3 = 12 °C, T4 = 10 °C, oscillation 2 Hz 25 mm, 0.17% PP123

In the third experiment with additive (PP123(3)), the aim was to achieve the improved morphology (block-like crystals) whilst improving the mixing conditions to prevent sedimentation. In comparison to the previous experiment, the final temperature was raised and the amplitude of the oscillation was also increased. This was intended to suspend the crystals more effectively and mitigate the problems experienced with sedimentation. As the oscillation conditions were altered, the residence time was re-determined (Table 5.5). After 26 minutes, small crystals were observed in the outlet tube and subsequently in the final straight. Three minutes later crystals were observed in the third straight suggesting that enhanced back-mixing may be occurring due to the increased amplitude of oscillation. However, this amplitude was required to suspend the particles more effectively. The experiment was run for five residence times. Sedimentation in this experiment was not as severe as observed previously and crystals were able to flow through the bends more readily. Evidence of encrustation was also more limited than previously observed. However, upon inspection of the resulting crystal morphology from each residence time it can be concluded that the morphology is very inconsistent and non-uniform. There is also limited evidence of the block-like crystals and instead, the crystals become increasingly elongated over the residence times (Figure 5.30).

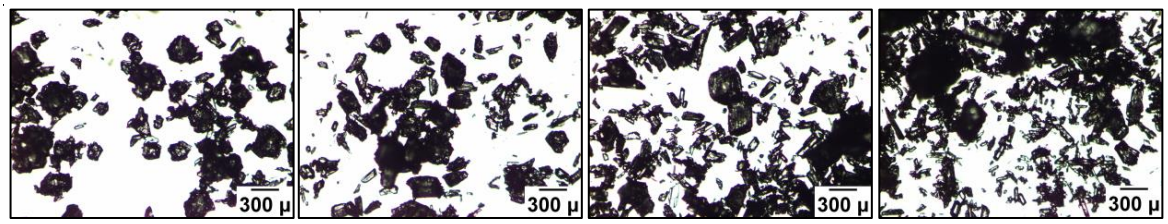

Figure 5.30 - Microscope images showing the crystal morphology of product from RT2-5 for experiment PP123(3).

A number of observations, explanations and possibilities can be noted from the crystal morphology resulting from this experiment:

- Upon increasing the amplitude of oscillation, the sedimentation was significantly reduced and the crystals were able to flow through the bends more readily. Improved mixing may result in a larger quantity of additive interacting with the crystal surface and producing a more enhanced effect with respect to experiments PP123(1/2). Batch experiments in an STR showed that, with consistent mixing

conditions but with increased levels of polymer additive, the morphology became more elongated. Therefore, it may be that, due to the enhanced mixing conditions produced, a lower concentration of additive is required to have the same effect in the continuous environment with these oscillation conditions. **Next step:** Lower the quantity of additive;

- Back-mixing of crystals into the previous, higher temperature straights results in such crystals acting as seeds and inducing crystal growth at this higher temperature. Batch experiments with PP123 in an STR showed that the morphology change is dependent on the crystallisation temperature: at high temperatures more elongated crystals are produced. **Next step:** Improve the mixing conditions to prevent back-mixing or increase the temperature of the second straight to dissolve back-propagated crystals. If the crystals still do not dissolve a more enhanced effect can be expected due to the crystallisation occurring at higher temperature and thus generating more elongated morphologies;
- Filtration issues (such as caking) and continual washing of precipitate with effluent during a residence time may result in changes to the morphology. **Next step:** Collect a small sample of product from each residence time for more representative inspection of the morphology.

For all subsequent PP123 experiments SA solutions containing a reduced quantity of polymer (0.13%) were used. The filtration procedure was also changed to investigate the effect of continual washing of the filtrate with effluent. The product of each RT was collected in a large Buchner funnel in the normal procedure, however 30 seconds before the end of each residence time the collection vessel was changed to another, smaller Buchner funnel to observe the morphology of a small sample. This filtration procedure was implemented for all experiments that follow.

PP123(4): T1 = 25 °C, T2 = 15 °C, T3 = 8 °C, T4 = 12 °C, oscillation 2 Hz 25 mm, 0.13% PP123

In the fourth experiment with PP123 present (PP123(4); with the reduced quantity of polymer additive), the same temperature profile and oscillation conditions as employed in PP123(3) were used. After 25 minutes, small crystals were observed in the outlet tube and subsequently observed in the final straight; this correlates with the previous experiment. During the third residence time crystals were also observed in the second straight suggesting that back-mixing may be occurring. The severity of sedimentation and

encrustation was similar to those observed in the previous experiment. The experiment was run for five residence times. The crystals produced from this experiment had a more desirable morphology than those observed previously. As anticipated, decreasing the quantity of polymer present in solution was effective in producing the desired block-like morphology in initial residence times, with crystals from RT2 and RT3 being uniformly block-like (Figure 5.31). However, the crystals produced in subsequent residence times were less uniform – the morphology was still predominantly blocks, but rod-like and needle-like fines were also now evident. This change in crystal morphology over residence times could be due to the back-mixing of crystals from straight three to straight two. Batch crystallisations in an STR have shown that the additive effect is dependent on the crystallisation temperature; in later residence times the back propagation of seed crystals, from straight three to straight two, would result in such crystals growing at a higher temperature than in prior residence times.

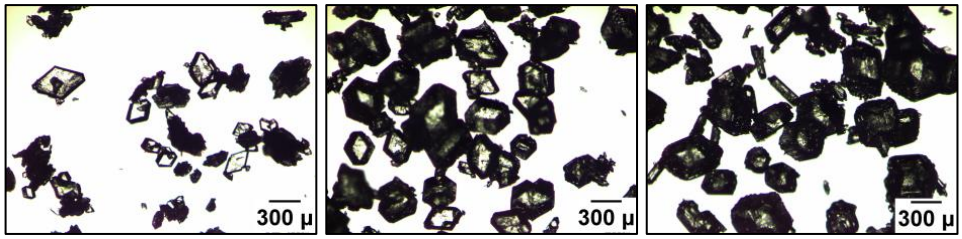

Figure 5.31 - Microscope images showing the crystal morphology of a small sample of product from RT2-4 for experiment PP123(4).

The crystal morphology from the bulk residence time samples is shown in Figure 5.32. The crystal shape produced is similar to those obtained from the small sample, however there are more fines present and the crystal surface appears more irregular. The presence of the polymer in solution may encourage adhesion of the smaller particles to the larger ones as the effluent washes over the precipitate. From this point forward morphology analysis will be reported for determinations carried out from the small samples which are less likely to be affected by filtration issues.

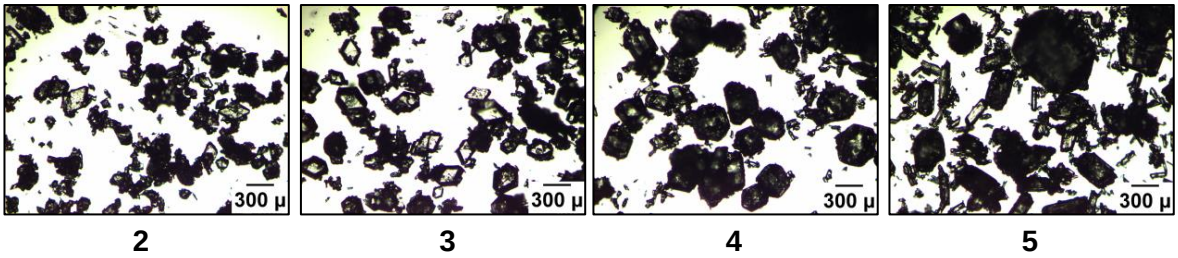

Figure 5.32 - Microscope images showing the crystal morphology of the bulk sample of product from RT2-5 for experiment PP123(4).

PP123(5): T1 = 25 °C, T2 = 18 °C, T3 = 12 °C, T4 = 10 °C, oscillation 2 Hz 10 mm, 0.13% PP123

In experiment PP123(5), the temperature profile was altered with the aim of limiting the production of needle-like crystals by alleviating the effect of the back-mixing of crystals into the second straight. The temperature of the second straight was increased by 3 °C to promote dissolution of any seed crystals which may appear within the straight by back propagation. As reported in the previous two experiments, crystals were observed in the fourth and third straight after around 27 minutes of the start of the experiment and several minutes later crystals were observed in the second straight. Crystals near the second bend were observed descending to the second straight due to gravity; this helped facilitate the back-mixing. This suggests that increasing the temperature of the second straight by 3 °C was not effective in dissolving the crystals. However, it was noted that crystals never back-mix into the first straight from the second straight, as it is likely that the temperature of the first straight is high enough for the crystals to dissolve. Sedimentation was also observed in the same sites as previously in this experiment. The experiment was terminated at the end of RT4. The crystal morphology produced was block-like for the first residence time and increasingly rod-like for the residence times that followed. This supports the theory that the back-propagated crystals are seeding the higher temperature straights and growing in the presence of the additive into different morphologies (Figure 5.33).

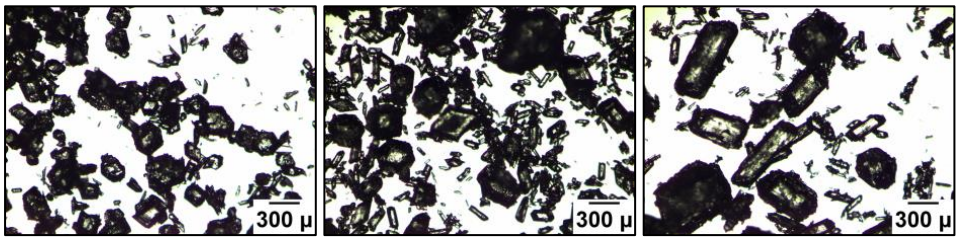

Figure 5.33 - Microscope images showing the crystal morphology of product from RT2-4 for experiment PP123(5).

PP123(6): T1 = 25 °C, T2 = 23 °C, T3 = 12 °C, T4 = 10 °C, oscillation 2 Hz 10 mm, 0.13% PP123

In the sixth experiment (PP123(6)) the jacket temperature of the second straight was increased further, by 5 °C to 23 °C, with the aim of preventing the back-mixing by dissolving the back-mixed particles or to observe the morphology produced if back-mixing did occur. After 25 minutes, crystals were observed in the exit tube and subsequently in the final straight. Several minutes later crystals were observed in the third straight and

had reached the second straight by the end of the RT2. There were however, more particles in the bend at the end of the second straight than in the second straight which suggest partial dissolution of crystals upon reaching the second straight was occurring. Furthermore, throughout the experiment there was no encrustation observed on the walls of the second straight suggesting that no secondary nucleation was occurring. There were also fewer crystals in the third straight, especially at the beginning where the two temperature zones met (23 °C and 12 °C). This is to be expected as this is a large change in temperature and at this point at the beginning of the third straight the temperature is likely to be higher than 12 °C where it meets the warm solution emerging from straight 2. There was also more encrustation to the third straight which is also expected as rapid crystallisation is likely at this large temperature jump due to a sudden change in solubility. The experiment was terminated at the end of RT4. The crystal morphologies produced from this experiment are shown in Figure 5.34. The microscope images suggest that the block-like crystals were produced for longer than in the previous experiment, persisting into RT4 unlike in previous experiments in which rod-like crystals were produced by this residence time. This suggests that the higher temperature of the second straight was effective in suppressing the effect of the back-mixing on the crystal morphology. However, the block-like crystals are accompanied by small needle-like crystals which may have resulted from the crystals that continued to back-mix into the second straight without dissolution.

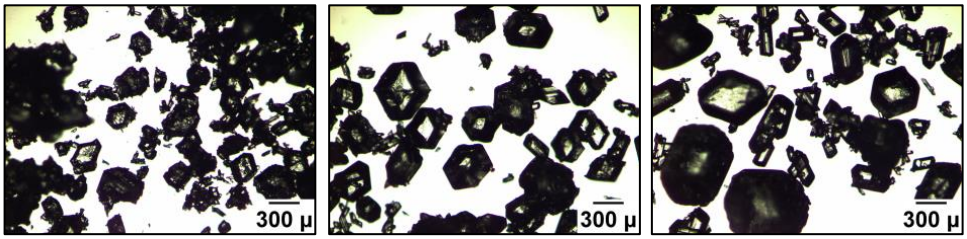

Figure 5.34 - Microscope images showing the crystal morphology of samples from RT2-4 for experiment PP123(6).

5.2.5 Experiments with PPG4000 additive

Although the morphology modification effect has been demonstrated on the COBC runs, and the incremental evolution of the experimental parameters tending towards producing the block-like crystals more reliably, there were still problems with inconsistent crystal morphology over the course of an experiment with PP123 additive. Further experiments were therefore carried out using PPG4000 as an additive. It was previously observed in batch experiments that, using PPG4000, the crystal morphology was less dependent on

crystallisation temperature and the more desirable block-like crystals could be accessed over a broader range of conditions and temperatures rather than needles (Chapter 4).

The temperature profile used for experiment PP123(5) was selected for the experiments with PPG4000. In the batch experiments, the presence of 0.17% PPG4000 produced block-like crystals, however in the COBC experiments with PP123, lower concentrations of the additive (0.13%) were still effective in producing the desired block-like crystals. Therefore, a starting concentration of 0.13% PPG4000 was selected for these experiments. PPG4000 is poorly soluble in water so use of a lower concentration is more desirable.

PPG(1): T1 = 25 °C, T2 = 18 °C, T3 = 12 °C, T4 = 10 °C, oscillation 2 Hz 10 mm, 0.13% PPG4000

In the first experiment with PPG4000 as an additive (PPG(1)), crystals were observed in the final straight after 25 minutes and in the third straight two minutes later. During the second residence time encrustation was observed on the end piece as well as in all straights except the first. There was also evidence for crystals back-mixing into the second straight. At the end of RT4, the experiment was terminated. It was evident that, with the PPG4000 additive, the encrustation is worse in comparison to when the PP123 additive is present in solution (Figure 5.35).

Figure 5.35 - Encrustation in experiment PPG(1).

However, in terms of crystal morphology, block-like crystals were produced more consistently over the course of the experiment (Figure 5.36). The obtained crystals did appear to increase in size over the experiment which may be as a result of the encrustation or back-mixing.

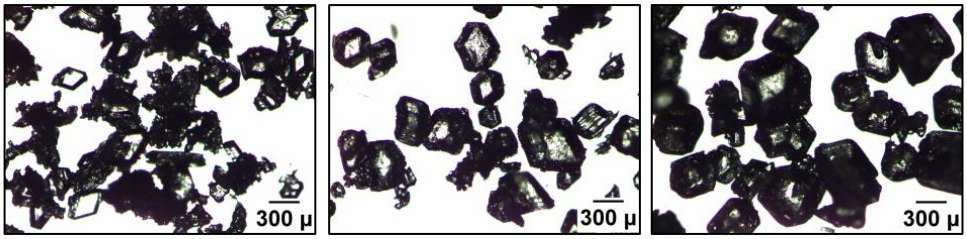

Figure 5.36 - Microscope images showing the crystal morphology of samples from RT2-4 for experiment PPG(1).

PPG(2): T1 = 25 °C, T2 = 18 °C, T3 = 12 °C, T4 = 10 °C, oscillation 2 Hz 10 mm, 0.10% PPG4000

As block-like crystals were produced in the previous experiment, the concentration of PPG was further reduced to 0.1% for the second experiment (PPG(2)). After 24 minutes, crystals were observed in the final straight and in the third straight a minute later. By RT2 fouling was again evident on the end piece and crystals were also present in the second straight. In RT3, larger crystals were observed encrusting on all straights except the first one. The lower concentration of additive had no effect on the severity of encrustation. At the end of RT4 the experiment was terminated. Images of the crystal morphology produced in this experiment are shown in Figure 5.37. A lower concentration of polymer was still effective in producing the block-like crystals, however once again they increased in size over the residence times.

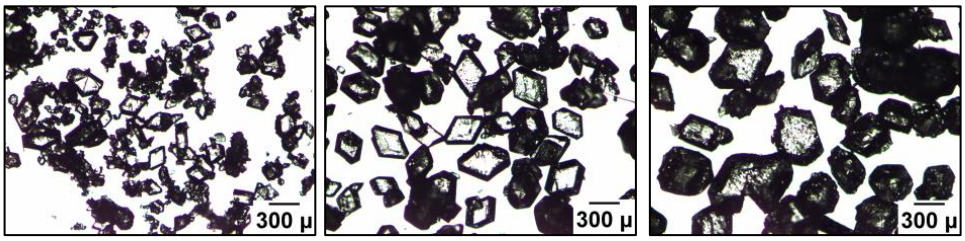

Figure 5.37 - Microscope images showing the crystal morphology of samples from RT2-4 for experiment PPG(2).

PPG(3): T1 = 25 °C, T2 = 18 °C, T3 = 12 °C, T4 = 10 °C, oscillation 2 Hz 10 mm, 0.10% PPG4000

In the third experiment (PPG(3)), a larger quantity of feed solution was prepared with the aim of operating the crystalliser for a longer period of time. Due to the larger volume of solution, overhead stirring was used to mix the feed solution at a rate of 600 rpm. After 26 minutes crystals were observed in the final straight, followed by crystals appearing in the

third straight after several minutes. Again by RT2, crystals had back-mixed into the second straight and encrustation was observed on all straights except the first one. In RT5 there was evidence of sedimentation at the end of the second straight where large particles could not suspend themselves against gravity through the bends. During the final residence time (RT6) the yield decreased significantly, likely to be due to the sedimentation at the end of the second straight. Almost all of the crystals in the system were either sedimented or encrusted on the walls of the crystalliser and as a result the experiment was terminated at the end of the sixth residence time. The crystal morphology of the product is shown in Figure 5.38 where it can be observed that only the favourable block-like crystals were produced in all residence times. However, as the experiment progresses the surface of the crystals produced is less faceted suggesting that the crystals may have grown at higher supersaturation or temperature.

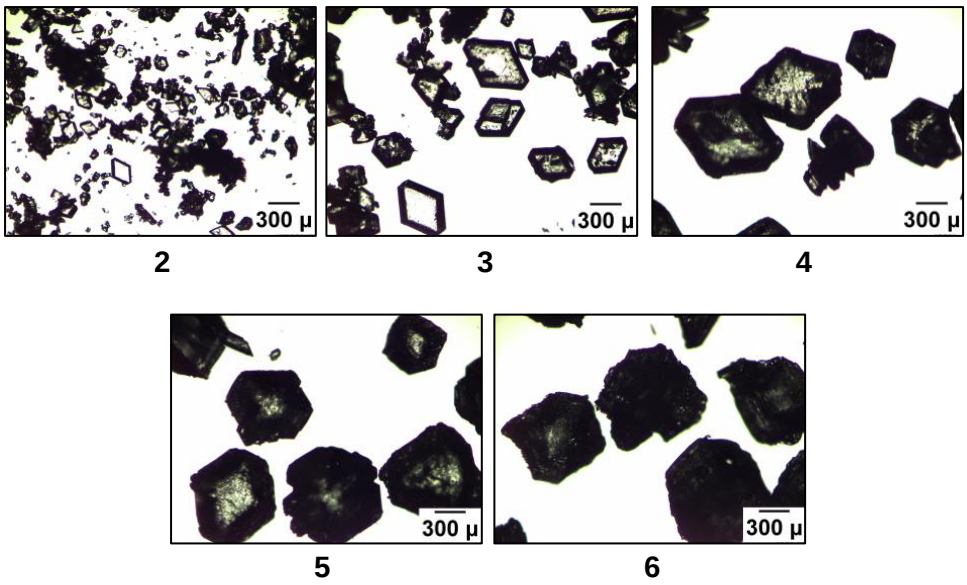

Figure 5.38 - Microscope images showing the crystal morphology of samples from RT2-6 for experiment PPG(6), and the persistence of the block-like morphology.

The production of block-like crystals shows the success not only of transferring the polymer-additive morphology effect from batch to continuous, but a step forward in optimising the continuous crystallisation runs in the COBC to maximise the production of the favourable block-like morphology in the presence of polymer additive.

5.2.6 Solid form analysis

In all of the COBC experiments PXRD analysis was carried out on samples collected from each residence time. As observed in the batch environment, the presence of the polymer had no effect on the solid form of the product, which remained as the β-polymorph in all

cases. Figure 5.39 shows PXRD patterns of samples produced in the COBC in the presence of the different concentrations of additive used.

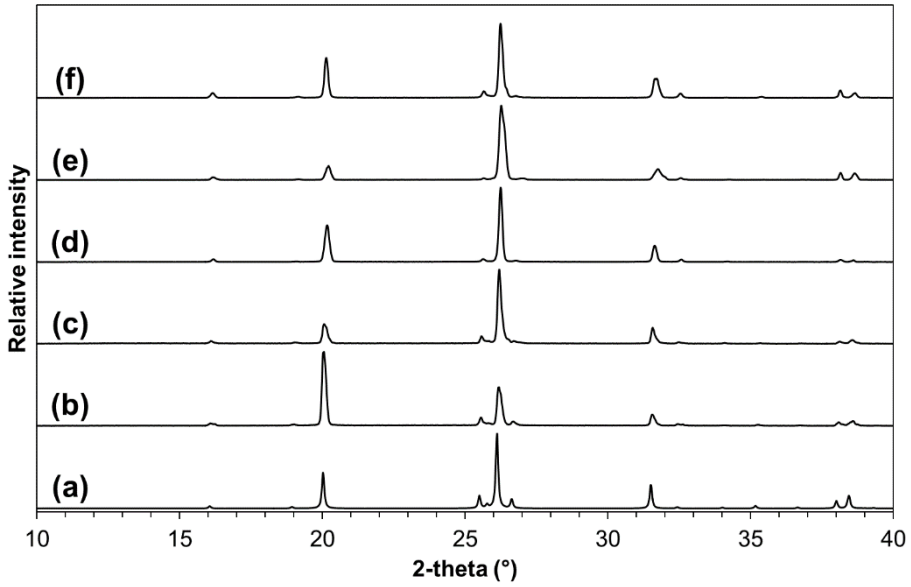

Figure 5.39 - (a) Calculated PXRD pattern of β-SA (SUCACB02) and PXRD patterns of SA produced in the COBC in the presence of (a) no polymer, (b) 0.17% PP123, (c) 0.13% PP123, (d) 0.13% PPG4000 and (e) 0.10% PPG4000.

5.3 Conclusions

5.3.1 Crystallisation in segmented flow

The SA system has been used to aid the development and evaluation of a mesoscale segmented flow reactor. Initial experiments used air segmentation, however this resulted in significant fouling to the body of the reactor. In subsequent experiments liquid segmentation was employed which eliminated encrustation on the reactor walls. However, significant fouling was observed on the mixer piece and inside the feed tubes. This was overcome by implementing improved temperature control through development of a water bath for the mixer piece and jackets for the feed tubes. Expulsion of the crystals from the outlet of the crystalliser proved problematic, but this was mitigated by the implementation of an end piece at the outlet of the crystalliser designed to propel the crystals into the filtration unit. A system designed to separate the carrier fluid from the solution prior to filtration was also implemented in the experiments, which prevented problems with adhesion of the filter paper to the filter funnel, caking of precipitate and enabled effective recovery of the carrier fluid.

Such developments of the platform enabled effective operation of the crystalliser with the target SA system for over an hour without any observation of encrustation. Recovery of the carrier fluid prior to filtration was achieved and this also helped to overcome filtration issues. Furthermore, the unique environment for crystal nucleation and growth provided by the liquid segmentation enabled the unexpected production of α-SA (as part of a mixture of both α- and β-polymorphs of SA) which may be the result of crystallisation occurring in the absence of a solid interface.

Additional experiments were also carried out with the aim of achieving, under continuous crystallisation conditions in the KRAIC platform, the polymer additive-mediated morphology changes observed in the batch environment. These were successful in the case of the PP123 polymer; however despite the low concentrations of the polymer added to the solution, issues with incompatibility of the polymer with the carrier fluid were experienced, resulting in disruption of the segmentation and poor control over the crystallisation. This resulted in testing of the PPG polymer for an additive effect in crystallisations carried out in the KRAIC. Although the presence of this polymer in solution did not disrupt the segmentation in the system, the presence of the additive did not produce the optimised morphology of SA observed in the batch environment and instead large, plate-like crystals were produced. It was theorised that the mixing in the KRAIC platform is gentler than in the batch environment and future steps towards achieving the additive-mediated morphology of SA in the KRAIC should encompass use of higher concentrations of the additive in the feed solution. Furthermore, it is clear that the solid recovery, in experiments both with and without polymer additive present, requires significant optimisation and this will form the theme of future experiments within the KRAIC.

5.3.2 Crystallisation in the COBC

Significant steps towards the aim of reproducing in the continuous environment the additive-mediated morphology changes produced in the batch environment, were achieved to a greater extent in the COBC platform. SA crystals of block-like morphology were successfully produced in the presence of both the PP123 and the PPG polymers in the continuous environment of the COBC.

However, in all experiments fouling and sedimentation remained a large barrier to the successful operation of the COBC and despite making changes to the mixing and temperature conditions; these problems could not be mitigated. The mixing conditions were not sufficient to enable suspension of the particles, with back-mixing of crystals

evident in the system. Although the optimised morphology of SA was produced in initial residence times, these challenges were reflected in the morphology and size of the resultant crystals in later residence times in which production of the favourable block-like morphology was not sustained. This was especially true in crystallisations carried out in the presence of the PP123 polymer in which the shape of the SA crystals produced is more dependent on the temperature of crystallisation than with PPG. Interestingly, although the presence of the PP123 resulted in less severe encrustation, the crystals back-mixing into previous, higher temperature straights acted as seeds inducing crystal growth at higher temperatures resulting in inconsistent morphologies over residence times. The use of PPG as an alternative additive was selected in attempt to overcome this issue, due to the morphology change in the presence of this additive being less dependent on crystallisation temperature. This was effective and the crystals were of block-like morphology for multiple residence times. However, encrustation and sedimentation remained an issue affecting the prolonged running of the platform in all experiments. Unlike in crystallisations in the KRAIC, where the segmentation ensures the sample solution does not encounter a solid interface (at the walls of the crystalliser), solid produced from the COBC both with and without a polymer additive present in solution was found to be pure β-SA.

Encrustation leads to loss of control of the crystallisation and, as noted by McGlone *et al.*, encrustation is one of the biggest challenges associated with continuous crystallisation.[179] Briggs *et al.* reported that encrustation issues experienced in unseeded crystallisations of L-glutamic acid in the COBC were overcome with the implementation of seeding and operation was possible for at least 10 hours.[181] Thus, the application of seeding methods to the crystallisation of SA in the COBC may enable problems with encrustation and fouling to be overcome and more uniform crystals to be produced.

The work presented in this Chapter represents the first example of a polymer-additive mediated morphology effect being implemented in continuous crystallisation in the fine chemicals and pharmaceuticals area. It shows the potential for successful continuous crystallisation of complex multi-component preparations, and also demonstrates the importance of optimising batch conditions prior to transferring these to continuous; in this case the basic parameters for the batch experiments represented a viable start point for optimising the continuous crystallisation runs.

Chapter 6

Investigating the effect of additives on the crystal morphology of isoniazid

6.1 Introduction and aims

The aim of this work was to investigate the effect of a range of additives (structurally similar, sized matched and polymer) on the crystal morphology of a pharmaceutical compound through small scale screening experiments using different crystallisation methods. Identified morphology changes in the presence of additives could then be rationalised theoretically based on the intermolecular interactions present on the surface of the crystal faces, as implemented in the case of SA in Chapter 4.

Isoniazid (Figure 6.1; IZN) is an active pharmaceutical ingredient (API) used in the treatment of tuberculosis.

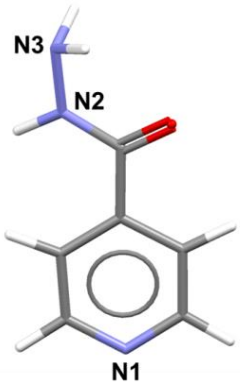

Figure 6.1 - The structure of isoniazid with the nitrogen atoms labelled (from INICAC03).[182]

There is currently only one reported polymorphic form of IZN, which crystallises in the orthorhombic space group $P2_12_12_1$ with an asymmetric unit containing one IZN molecule. The crystal structure[182] consists of herringbone chains of molecules connected through intermolecular N3-H···N1 hydrogen bonds between a hydrogen atom on the amine group on one IZN molecule and the nitrogen atom on the pyridine ring (N1) of another IZN molecule with an N3···N1 distance of 3.0403(3) Å. The chains interact with one another through intermolecular N2-H···N3 hydrogen bonds between the amide N-H bond and the nitrogen atom of the amine group (N3) (N2···N3 distance of 2.9147(2) Å). These interactions result in the formation of nets of molecules with the orientation of the IZN molecule alternating between chains due to the presence of a 2-fold screw axis (Figure 6.2, left). The nets stack along the *a* axis through bridging N3-H···N1 hydrogen bonds between the terminal amine group and the nitrogen atom on the pyridine ring with an N3···N1 distance of 3.1442(3) Å (Figure 6.2, right).

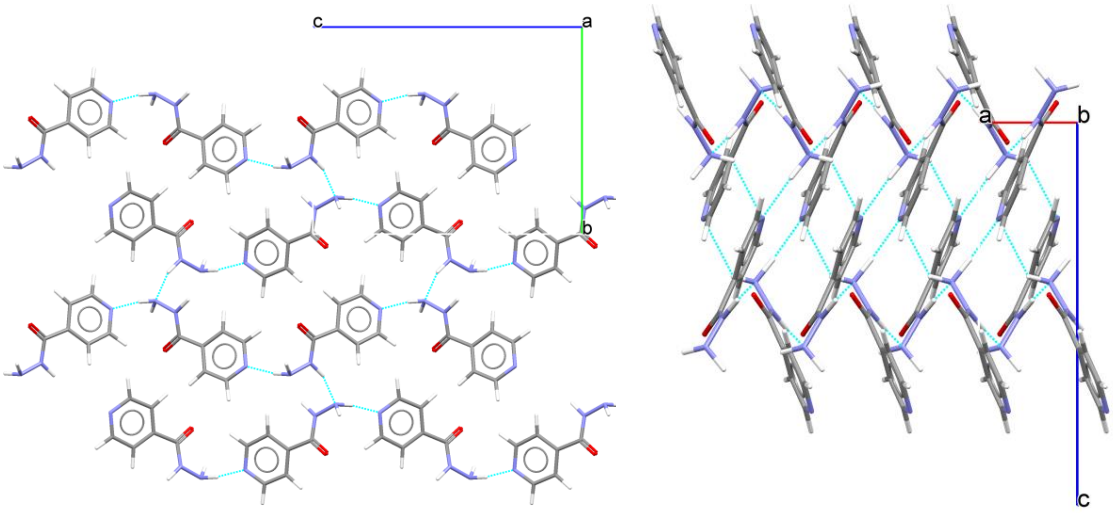

Figure 6.2 - Crystal packing in the only reported polymorphic form of IZN (from INICAC03)[182]: (left) hydrogen bonded nets of IZN molecules viewed down the crystallographic *a* axis, and (right) infinite hydrogen bonds running along the *a* axis viewed down the *b* axis.

IZN crystallises in a needle or plate-like habit from many organic solvents[145,183] and most multi-component molecular complexes of IZN are also reported to crystallise in a needle-like habit.[145,184-186] As these morphologies tend to be unfavourable for pharmaceutical materials processing, this makes it a suitable compound for this work targeting the use of additives to modify morphology. This experimentally observed shape of IZN crystals agrees well with the BFDH-predicted elongated morphology shown in Figure 6.3.

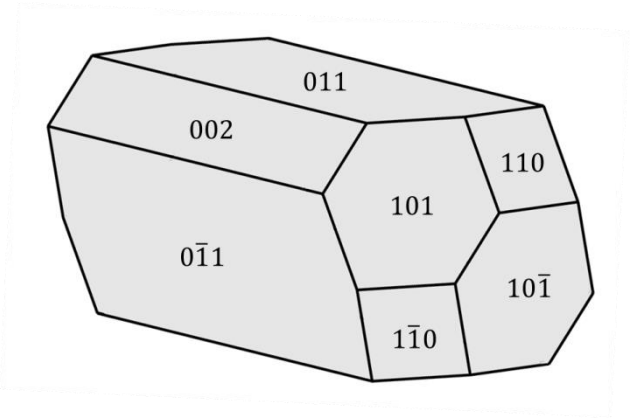

Figure 6.3 - Predicted morphology of IZN (INICAC03)[182] using the BFDH tool in Mercury.[141]

In the predicted morphology there are four fast growing faces which intercept the direction of the crystallographic *a* axis ($(101), (10\bar{1}), (110)$ and $(1\bar{1}0)$). This suggests that the bridging N3-H···N1 interactions between the IZN molecules, involving the amine group and pyridine nitrogen atom and running along the crystallographic *a* axis, are the dominant interactions in the crystal structure. An additive may be successful in slowing down crystal growth in this direction and thus altering the overall morphology by intercepting and interrupting the assembly of the structure *via* these favourable hydrogen bonds. The N3-H···N1 interaction between the N3-H bond of the terminal amine group and the nitrogen atom of the pyridine ring, formed in the direction of the crystallographic *c* axis, is intercepted by the slow growing faces and an additive that interrupts that interaction may result in crystals with increased elongation.

6.1.1 Selection of additives

There are several structurally similar molecules to IZN that are also Generally Recognized As Safe (GRAS) compounds, making them ideal candidates for employment as additives; these include nicotinic acid and nicotinamide. In addition, other compounds of similar size to IZN that contain hydrogen bond donor and acceptor groups were used in this study to provide a strong synthon set. The additives used in this work are shown in Figure 6.4.

Structurally similar additives

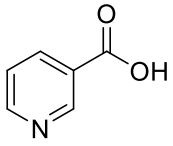

Nicotinic acid

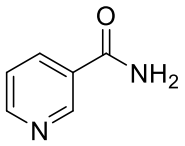

Nicotinamide

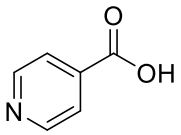

Isonicotinic acid

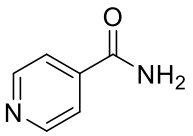

Isonicotinamide

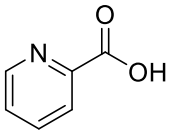

2-picolinic acid

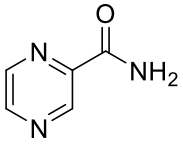

Pyrazine carboxamide

Sized matched additives

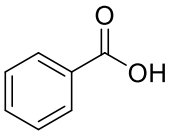

Benzoic acid

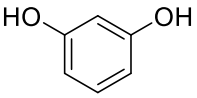

Resorcinol

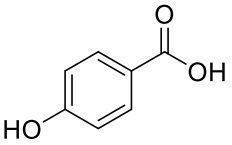

4-hydroxybenzoic acid

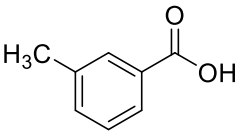

3-methylbenzoic acid

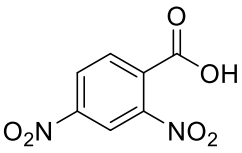

2,4-dinitrobenzoic acid

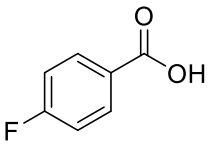

4-fluorobenzoic acid

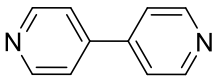

4,4'-bipyridyl

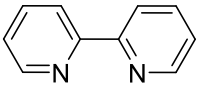

2,2'-bipyridyl

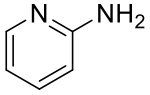

2-aminopyridine

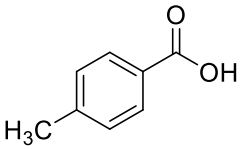

4-methylbenzoic acid

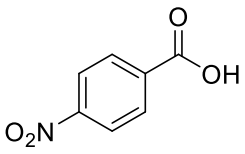

4-nitrobenzoic acid

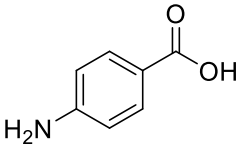

4-aminobenzoic acid

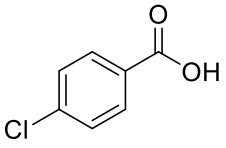

4-chlorobenzoic acid

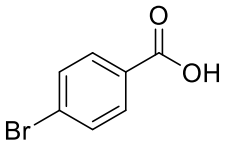

4-bromobenzoic acid

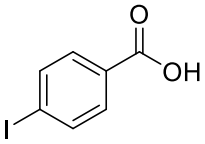

4-iodobenzoic acid

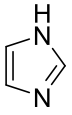

Imidazole

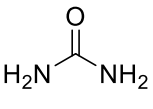

Urea

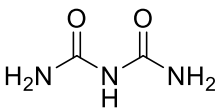

Biuret

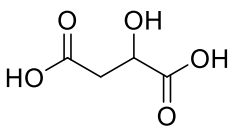

Malic acid

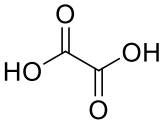

Oxalic acid

Figure 6.4 - Molecular structures of structurally similar and size-matched additives used for morphology studies of IZN.

Several polymers were also investigated for an additive effect, as investigated for succinic acid in Chapter 4, and their molecular structures are shown in Figure 6.5.

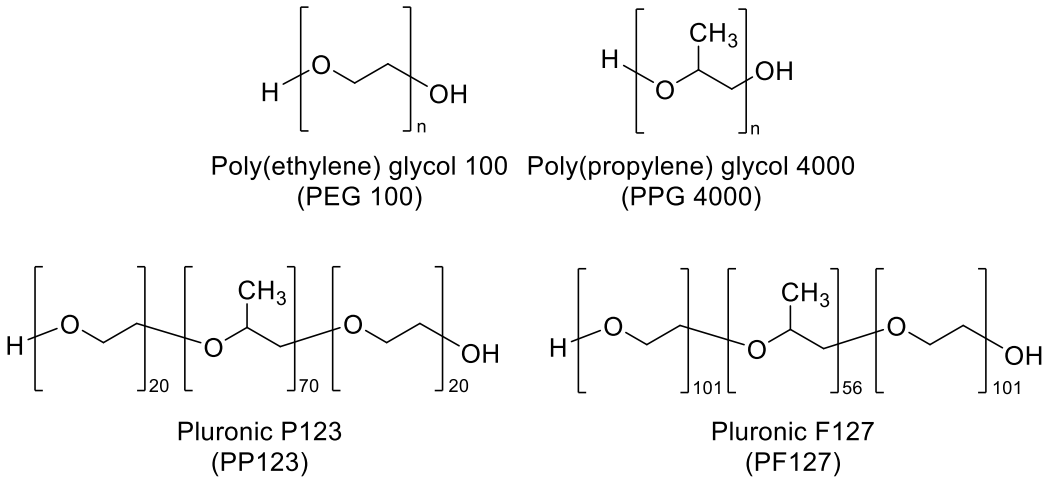

Figure 6.5 - Molecular structure of polymer additives used.

Crystallisations were carried out using a variety of methods including evaporative crystallisation and cooling crystallisation at different scales.

6.2 Experimental information

All compounds used were obtained from commercial sources and used without further purification.

6.2.1 Solubility determination

Solubility measurements of IZN from ethanol and water were carried out using the Technobis Crystallization Systems Crystalline at 3 ml scale and the Technobis Crystallization Systems Crystal16 at 1 ml scale, respectively. Vials containing the chosen solvent and different concentrations of IZN were heated from 20 °C to 70 °C at a heating rate of 0.5 °C min^{-1} using magnetic bottom stirring at 400 rpm. The data were analysed using CrystalClear software.[133]

6.2.2 Evaporative crystallisation

Evaporative crystallisations were prepared by dissolving small quantities of IZN (0.0137 g) and the additive compound in the minimum amount of solvent in 7 ml vials. Holes were pierced in the lids allowing for slow evaporation of the solvent at room temperature. Solvents used included water, ethanol, methanol, isopropanol/water (1:1).

IZN to additive molar (for size-matched) or mass (for polymer) ratios investigated were 1:1, 10:1 and 100:1.

6.2.3 Cooling crystallisation

All cooling crystallisations were carried out using the Cambridge Reactor Design Polar Bear Plus crystalliser. For crystallisations from ethanol, an IZN concentration 0.025 g ml^{-1} (T_{sat} = 42 °C) was used with a linear cooling profile of 75 °C to 5 °C with a cooling rate of 0.5 °C min^{-1} implemented. Mixing was induced using magnetic bottom stirring. A stirring rate of 400 rpm was used in initial experiments, however, at this stirring speed the resulting crystals were extremely small, forming a microcrystalline powder that was difficult to analyse. Stirring rates of 150 and 200 rpm were then tested. At 150 rpm the crystals produced were larger but less uniform in shape suggesting that the mixing was not sufficient at this speed. At 200 rpm the crystals were larger than at 400 rpm and more uniform, balancing good mixing with ease of observation of morphology changes; this stirring rate was thus chosen for comparison of the crystal morphology in the presence of additives. Crystallisations from water were prepared in a concentration of 0.2 g ml^{-1} (T_{sat} = 35 °C) of IZN and a linear cooling profile of 60 °C to 5 °C with a cooling rate of 0.5 °C min^{-1} used. Mixing was induced using magnetic bottom stirring at 400 rpm, which produced appropriate crystals in this case. 1 ml and 5 ml scale crystallisations were carried out in 1.5 ml and 20 ml glass vials, respectively. Crystallisations were prepared with an IZN to additive molar (for size-matched) or mass (for polymer) ratio of 10:1. 10 ml scale crystallisations were carried out in 20 ml glass vials and overhead stirring was implemented using a magnetically controlled overhead stirrer from Technobis Crystallization Systems. In parallel to the crystallisations in the presence of additives, a control crystallisation containing no additive was prepared for all crystallisation conditions for comparison of the resulting crystal morphology. At the end of the crystallisation, visual analysis of the crystal morphology was carried out using optical microscopy.

6.2.4 Single crystal structures

Several of the evaporative crystallisations prepared in a 1:1 molar ratio resulted in the formation of multi-component molecular complexes and single crystal structures were determined. All of the structures were solved by direct methods using SHELXS-2013[137] and refined using SHELXL-2013[138] within the WinGX[139,140] program. Crystallographic data for each complex are shown in Table 6.1.

Table 6.1 - Crystallographic information for IZN crystal structures.

	1	2	3
Code	IZN^{2+} OA^{2-}	IZN RES	IZN^{+} $24DNBA^{-}$
Formula	$(C_6H_9N_3O)^{2+}$ $(C_2O_4)^{2-}$	$(C_6H_7N_3O)$ $(C_6H_6O_2)$	$(C_6H_8N_3O)^{+}$ $(C_7H_3N_2O_6)^{-}$
M / g mol^{-1}	227.18	247.25	349.27
T (K), radiation	150, Mo K_α	150, Mo K_α	150, Mo K_α
Space Group	$P2_1/c$	$P2_1/c$	P b c a
a (Å)	7.4160(10)	5.0740(2)	6.9781(2)
b (Å)	18.621(2)	15.9115(9)	15.1035(5)
c (Å)	6.8475(9)	14.7309(6)	27.6939(9)
α (^{o})	90	90	90
β (^{o})	109.404(16)	96.926(4)	90
γ (^{o})	90	90	90
Volume ($Å^3$)	891.9(2)	1180.62(10)	2918.76(16)
Z	4	4	8
ρ_{cal}/ Mg cm^{-3}	1.692	1.391	1.590
μ/mm^{-1}	0.143	0.102	0.132
θ range/°	3.339-25.677	3.785-25.672	3.299–26.369
Completeness	99.8	99.8	96.2 %
Refln. Collected	3473	7053	19973
Independent	1688	2241	2815
Refln (obs.*I*>2σ(*I*))	1418	1782	2240
Rint	0.032	0.029	0.042
Parameters	181	215	270
GooF	1.086	1.042	1.047
R_1 (obs)	0.044	0.041	0.036
R_1 (all)	0.054	0.057	0.051
wR_2 (all)	0.099	0.090	0.088
$\rho_{max,min}$/e $Å^{-3}$	0.209,-0.290	0.175,-0.197	0.195,-0.274

Preparation of single crystals

(1) Isoniazid oxalic acid (1:1) (IZN^{2+} OA^{2-})

Equimolar quantities of IZN (0.014 g) and OA (0.009 g) were combined and dissolved in water. Slow evaporation produced rod-like crystals. Data were collected using the Rigaku Oxford Diffraction SuperNova diffractometer with Mo-K_α radiation (λ=0.71073 Å) at 150 K.

(2) Isoniazid resorcinol (1:1) (IZN RES)

A molecular complex of IZN (0.014 g) with RES (0.012 g) was produced from an equimolar solution of the two components left to evaporate from water. Data were collected using the Rigaku Oxford Diffraction Xcalibur diffractometer with Mo-K_α radiation (λ=0.71073 Å) at 150 K.

(3) Isoniazid 2,4-dinitrobenzoic acid (1:1) (IZN^+ $24DNBA^-$)

A molecular salt of IZN (0.014 g) with 24DNBA (0.024 g) was produced when equimolar quantities were dissolved in water and left to crystallise by evaporation. Data were collected using the Rigaku Oxford Diffraction Gemini Ultra A CCD diffractometer with Mo-K_α radiation (λ=0.71073 Å) at 150 K.

6.2.5 Analytical methods

Microscope images of crystals from evaporative crystallisations and 1 ml scale cooling crystallisations were taken on a Nikon Coolpix P5100 camera through a Brunel Microscopes microscope. Microscope images of crystals from 10 ml scale crystallisations were taken using a Leica DM1000 microscope equipped with an Infinity 2 microscopy camera at 4x magnification.

Scanning Electron Microscopy (SEM) images were obtained using a JEOL SEM6480LV SEM in which samples were coated with chrome using a Quoron QT Chrome Coater with a film thickness of 20 nm.

Face indexing was carried out using a Rigaku Oxford Diffraction (formerly Agilent Technologies) Xcalibur diffractometer with Mo-K_α (λ=0.71073 Å) radiation. Unit cell screenings were carried out at 150 K where the temperature was controlled using an Oxford Cryosystems Cryostream. Face indexing was then carried out using the CrysAlisPro 171.37.33 software.[134] Analysis of the crystal structure and morphology of IZN and use of the BFDH morphology tool was carried out using Mercury 3.5.[141]

Experimental information for the PXRD, DSC and NMR measurements undertaken are detailed in Chapter 3.

6.3 Characterisation of IZN starting material

Figure 6.6 shows the PXRD pattern of the only reported polymorph of IZN calculated from single crystal XRD data alongside the measured pattern of the IZN obtained from Sigma Aldrich. A good match between the peaks in each pattern is observed, confirming the starting material as the known polymorph of IZN.

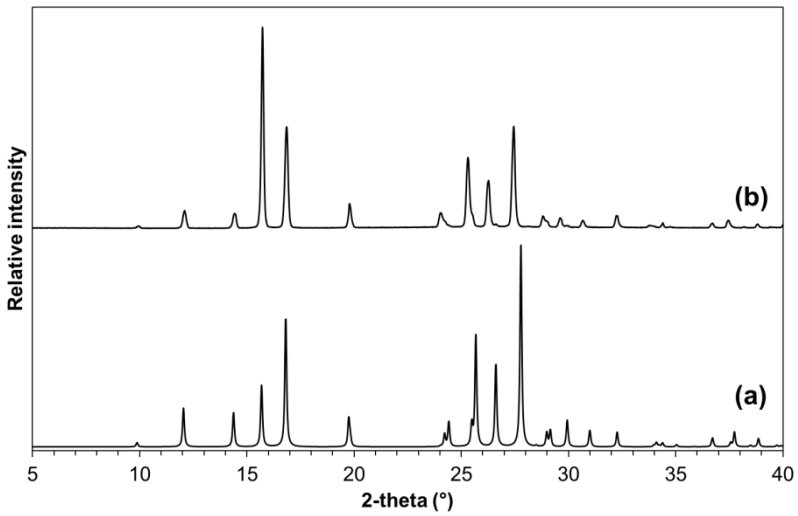

Figure 6.6 - PXRD patterns of IZN: (a) calculated from the structure of the only reported polymorph (CSD ref. code = INICAC) and (b) IZN starting material.

The material obtained from Sigma Aldrich was also characterised using DSC, showing a sharp endothermic peak at 171 °C representing its melting point (Figure 6.7).

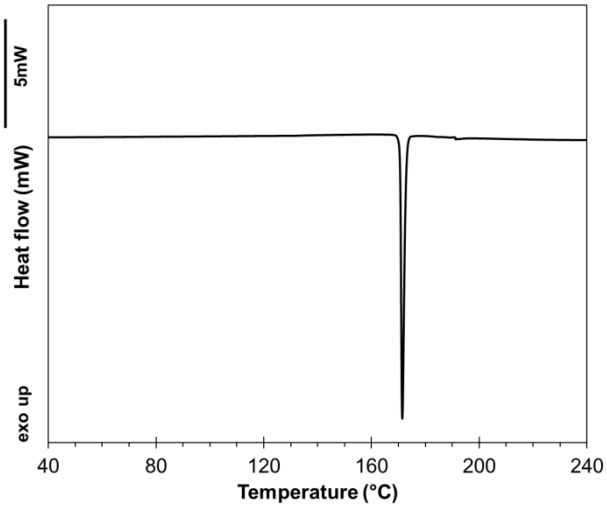

Figure 6.7 - DSC trace of IZN obtained from Sigma Aldrich.

The solubility of IZN in water and in ethanol was determined with respect to temperature using turbidometric techniques described in Section 6.2.1; the solubility curves are shown in Figure 6.8.

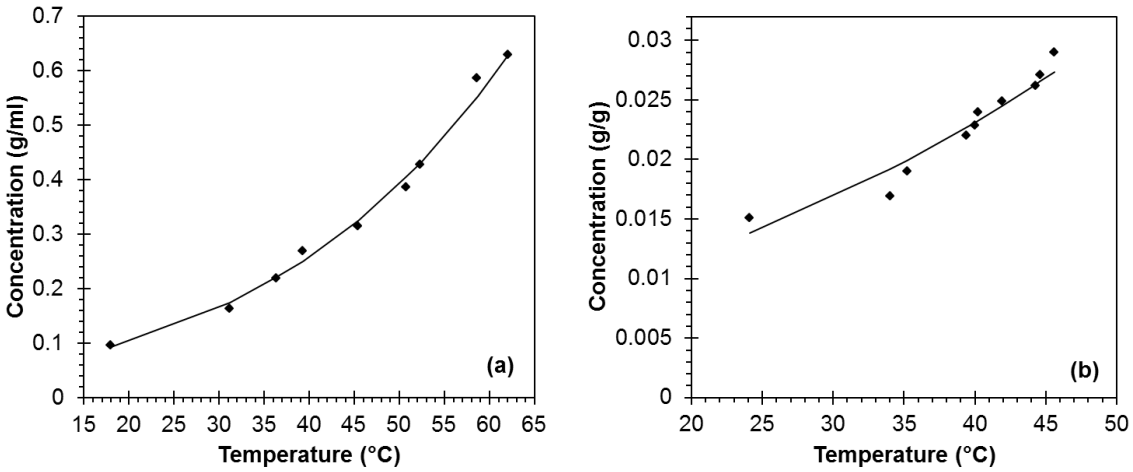

Figure 6.8 - Solubility curves of IZN in (a) water and (b) ethanol with lines of fit based on a Van't Hoff functional form as a guide to the eye.

The morphology of the raw material is shown in Figure 6.9. The crystals are of needle-like morphology in a mixture of lengths and thicknesses.

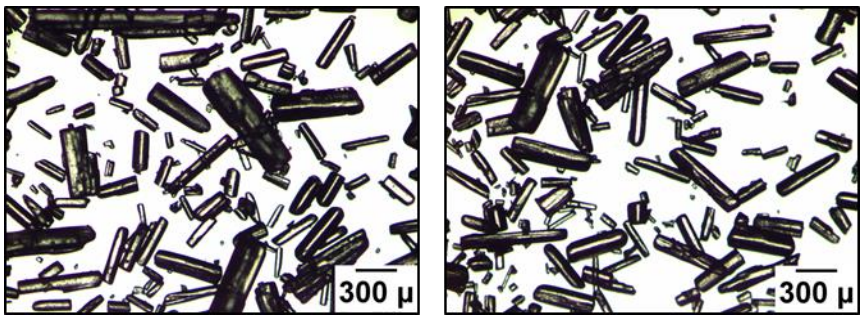

Figure 6.9 - Microscope images of the crystal morphology of IZN obtained from Sigma Aldrich.

6.4 Effect of solvent on crystal morphology of IZN

It is common for crystallisation from different solvents to produce different crystal morphologies as a result of different face-specific interactions of the solvent molecules with the growing crystal surface.[32,66] The crystallisation of IZN from a number of solvents in cooling and evaporative crystallisation was therefore carried out and the resulting crystal morphologies analysed using optical microscopy.

6.4.1 Crystallisation from ethanol

In evaporative crystallisation of IZN from ethanol, elongated plate-like crystals are produced, the size and shape of which varied significantly, as shown in Figure 6.10. This may be as a result of lack of agitation in the solution in evaporative crystallisation resulting in a non-homogeneous solution and poor mass transfer.

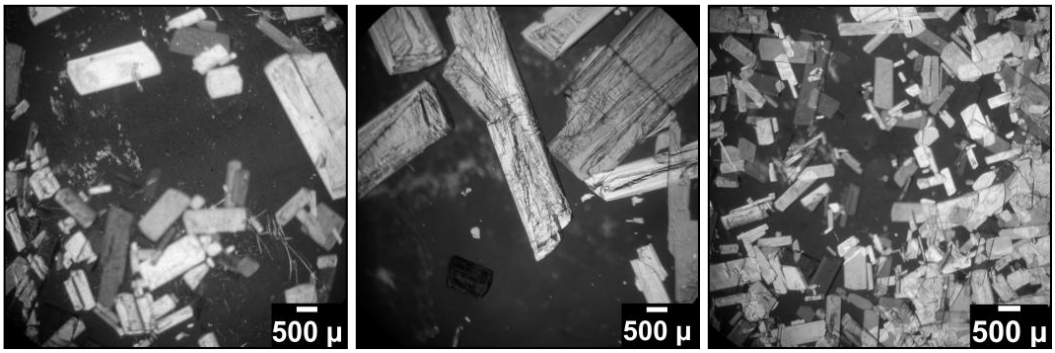

Figure 6.10 - Microscope images of IZN crystals produced from ethanol in an evaporative crystallisation.

In cooling crystallisation from ethanol, with magnetic bottom stirring at 1 ml scale, small plate-like crystals were consistently produced, as shown in Figure 6.11. The rough edges observed on some of the crystals suggest that crystal breakage may have occurred from the abrasive action of the stirring bar. The surfaces of the crystals are also rounded suggesting that they may have been produced at high supersaturation. In contrast, when overhead stirring was implemented at 10 ml scale, more uniform plate-like crystals were produced in which the edges of the crystals are less rounded (Figure 6.11 right).

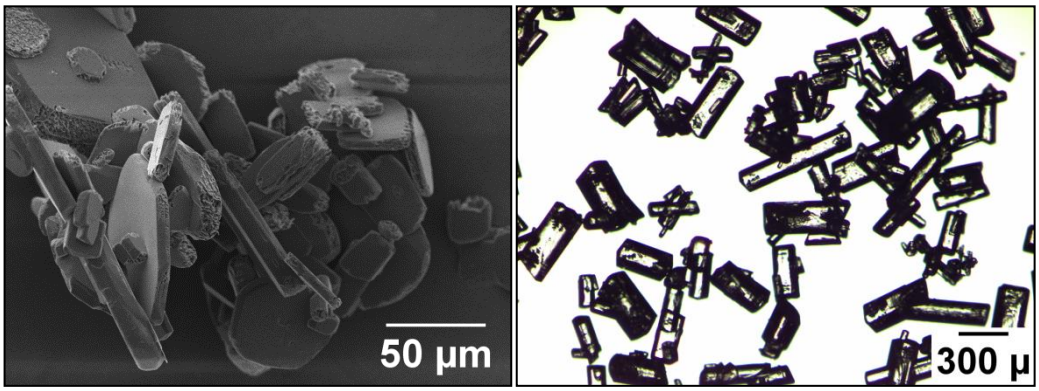

Figure 6.11 - Plate-like crystals of IZN produced from ethanol cooling crystallisations with (left) magnetic bottom stirring and (right) overhead stirring.

The large size of the crystals produced from evaporative crystallisation and cooling crystallisation with overhead stirring made it possible to undertake face indexing. In each

case the same faces were observed as dominant in the morphology. Figure 6.12 shows the indexed faces of a plate-like crystal produced from evaporative crystallisation. The (010) face is the largest and slowest growing face, while the (001), (101) and $(10\bar{1})$ faces grow more quickly relative to the (010) face which results in the plate-like shape of the crystal.

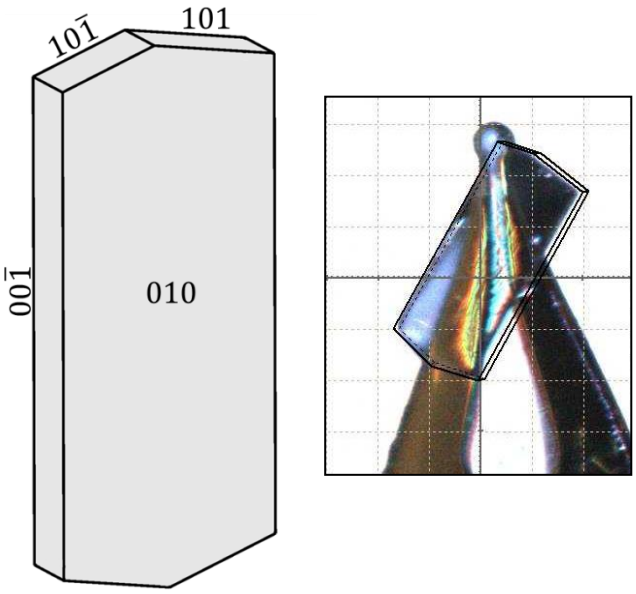

Figure 6.12 - Face indexing of plate-like crystals of IZN produced from ethanol.

In the crystal structure of IZN the (101) and $(10\bar{1})$ planes – lying parallel to the smallest and fastest growing faces – intercept the direction of stacking of the hydrogen bonded nets of IZN molecules through an infinite network of N3-H···N1 hydrogen bonds. In contrast, the (010) plane (the slowest growing face) intercepts the direction of interactions between the chains of IZN molecules and therefore the N2-H···N3 hydrogen bonds linking the amide N-H bond and the nitrogen atom of the amine group in two IZN molecules that lie adjacent to one another. These interactions, however, are not infinite in the direction perpendicular to the face (along the crystallographic *b* axis), and growth in that direction will potentially therefore be slower than in the direction of the infinite N3-H···N1 bridging interactions forming along the *a* axis. The hydroxyl groups of the solvent ethanol molecules could also interact favourably with the nitrogen atom of the amine group, interrupting the interaction between IZN molecules and further slowing down growth in the direction of the crystallographic *b* axis. The (001) plane intercepts the direction of hydrogen bonded herringbone chains of IZN molecules forming along the *c* axis. The morphology suggests that the (001) face grows faster than the (010) face but slower than the (101) and $(10\bar{1})$ faces.

Comparisons can also be made between the shape and faces present in the predicted BFDH morphology of IZN and the experimental morphology (Figure 6.13). The BFDH prediction generates an elongated morphology in which four different faces on the sides of the crystal are present ($(011), (0\bar{1}\bar{1}), (0\bar{1}1)$ and $(01\bar{1})$) which are not present in the experimental morphology. Instead, the experimental plate-like morphology features the (010) and $(0\bar{1}0)$ faces. Both morphologies share the (001), (101) and $(10\bar{1})$ faces, allowing the plate-like morphology to be superimposed on the BFDH morphology (dotted lines in Figure 6.13 left). As the BFDH model does not take into account molecular-level interactions, the difference in the experimental and predicted morphologies could be a result of the ethanol molecules interacting strongly with the (010) face, diminishing the (011) and $(0\bar{1}1)$ faces in the experimental morphology.

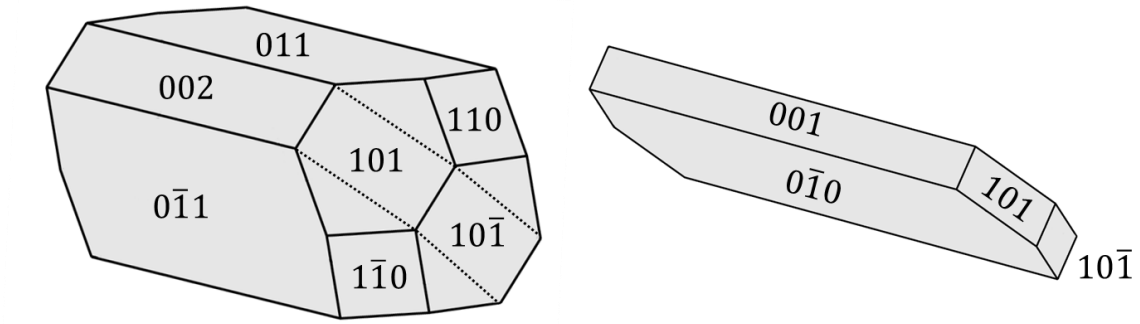

Figure 6.13 - Comparison of (left) BFDH morphology and (right) indexed faces.

6.4.2 Crystallisation from water

Unlike in the case of crystallisation from ethanol, IZN reproducibly crystallises from water in an unfavourable, fine needle-like habit in both evaporative and cooling crystallisation (Figure 6.14). Due to the fine needle-like habit produced from the crystallisations from water, accurate indexing of the crystal faces was not possible.

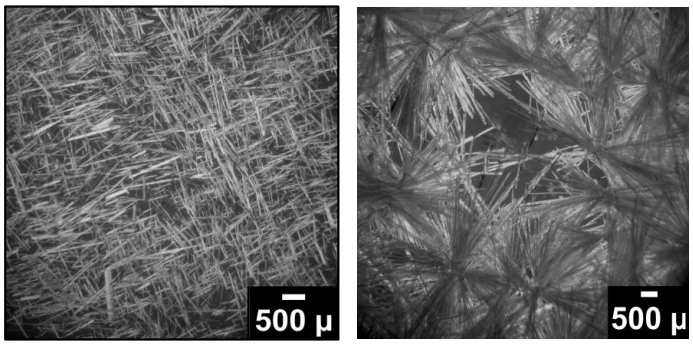

Figure 6.14 - Microscope images of IZN crystals produced from an aqueous solution in (a) cooling crystallisation and (b) evaporative crystallisation.

Crystallisation of IZN from isopropanol/water (1:1), acetonitrile and methanol was also investigated in an evaporative environment and needle-like crystals were produced in all cases.

6.5 Crystallisation of IZN in the presence of 4,4'-bipyridine

The most significant finding from the screening crystallisations of IZN with a range of additives present in solution was the modified crystal morphology produced from ethanol in the presence of 4,4'-bipyridine (44BP). The molecular structures of IZN and 44BP are shown in Figure 6.15. The molecules show structural similarity in the presence of a pyridine ring in each structure.

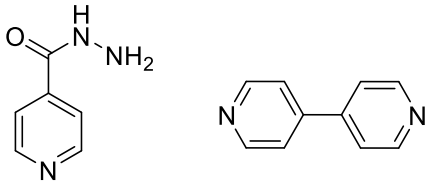

Figure 6.15 - Molecular structure of (left) isoniazid and (right) 4,4'-bipyridine.

6.5.1 Analysis of crystal morphology and solid form

Initial evaporative crystallisations of IZN from ethanol prepared in a 10:1 IZN to 44BP molar ratio resulted in the reproducible production of needle-like crystals of consistent size and shape (Figure 6.16). This presents a significant change in morphology compared to the plate-like crystals produced from ethanol with no additive present. Although needle-like crystals are largely unfavourable for processing, an understanding of the molecular level interactions inducing this change in the shape of the crystals may enable the design of future additives that may give a more desirable effect on crystal morphology.

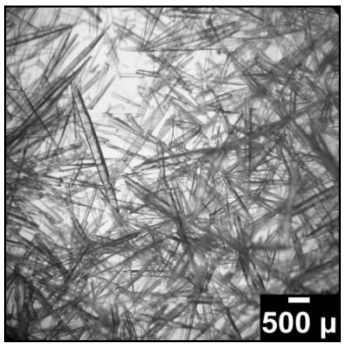

Figure 6.16 - Needle like crystals of IZN produced in the presence of 44BP in evaporative crystallisation.

Additional evaporative experiments were also prepared with an IZN to 44BP molar ratio of 20:1. These resulted in crystals with a plate-like morphology, comparable to those produced in the presence of no additive. This suggests that the 44BP additive must be present in a higher concentration to result in a significant effect on the relative growth rates of the crystal faces.

In addition to evaporative crystallisation, it was also possible to produce the needle-like crystals in a cooling environment reproducibly. At 1 ml scale with magnetic bottom stirring, needle-like crystals were observed, however they were significantly smaller than those produced by evaporative crystallisation which may be a result of the mixing conditions in the 1 ml vials. Interestingly, initial experiments carried out at 10 ml scale with overhead stirring resulted in longer needle-like crystals (Figure 6.17). The crystals appear finer than those produced by evaporative crystallisation which may be a consequence of the faster growth rates and better mixing in the cooling crystallisation experiments. This would result in the additive having a more enhanced effect on the overall crystal morphology.

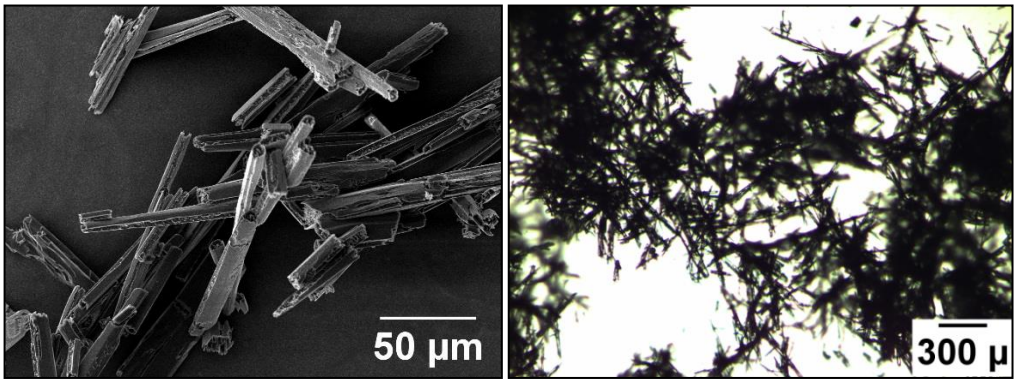

Figure 6.17 - Microscope images of IZN crystals produced in the presence of 44BP in cooling crystallisation at (left) 1 ml scale with magnetic bottom stirring, and (right) 10 ml scale with overhead stirring.

The solid form of the product of each type of crystallisation was analysed using PXRD, as shown in Figure 6.18; this shows that the presence of the additive in the crystallisation does not result in a change in the solid form of isoniazid. Furthermore, the patterns do not show any peaks corresponding to 44BP suggesting that the additive is not present in the solid product in quantities detectable by PXRD.

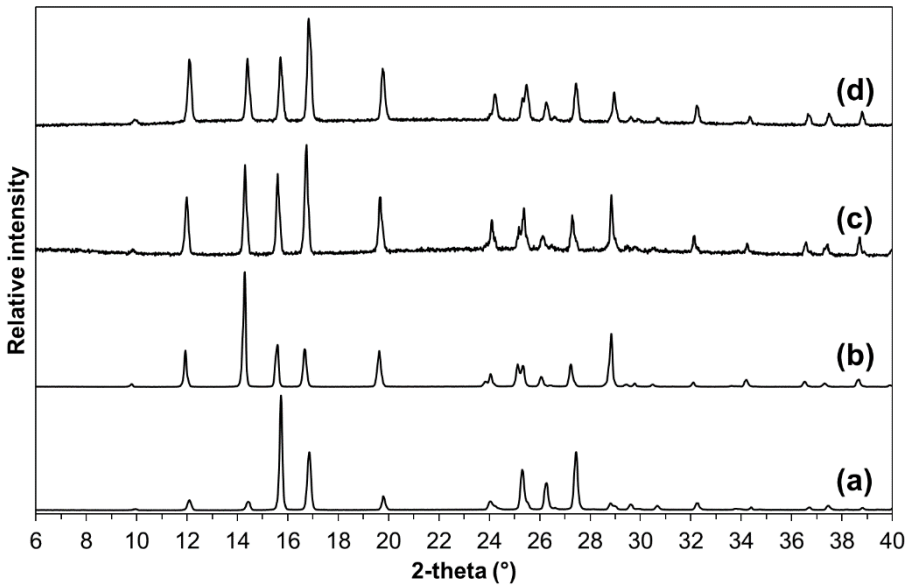

Figure 6.18 - PXRD patterns of (a) IZN starting material, IZN crystallised with 44BP present (10:1) in (b) an evaporative environment, (c) a cooling environment (1 ml scale), and (d) a cooling environment (10 ml scale).

6.5.2 Face indexing analysis

Due to the reproducible nature of the interaction of IZN crystals with the 44BP additive in crystallisation from ethanol, further investigation into the additive-induced change in morphology from plates to needles was carried out through face indexing. The aim was to identify the dominant faces in the needle-like morphology and understand the functional groups present on the surfaces of the faces that may form an interaction with the additive. Face indexing analysis was carried out on crystals from evaporative crystallisation. The small size of the crystals produced by cooling crystallisation limited the ability to perform face indexing, however, comparable needle-like morphologies were achieved in both evaporative and cooling crystallisation in the presence of 44BP, with indexed faces shown in Figure 6.19.

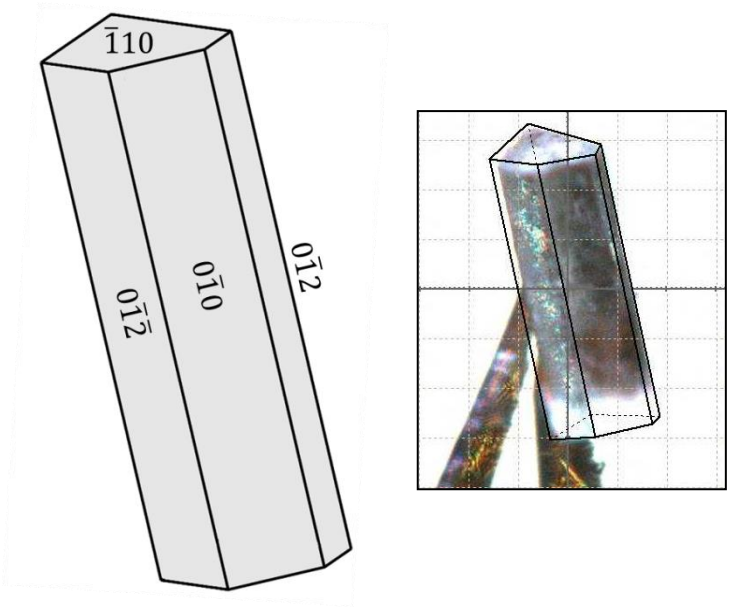

Figure 6.19 - Face indexing of needle-like crystals of IZN produced by crystallisation from ethanol in the presence of 44BP.

The fast growing end face in this crystal is the $(\bar{1}10)$ face. This face is present in the predicted BFDH morphology of IZN and makes a similar angle with the direction of the *a* axis as do the $(10\bar{1})$ and (101) faces present on the plate-like morphology of IZN produced from ethanol with no additive present. The $(0\bar{1}0)$ face is common to both plate and needle-like morphologies, but in the needle-like morphology the (010) face is diminished. The $(0\bar{1}0)$ face is accompanied by the $(0\bar{1}\bar{2})$ and $(0\bar{1}2)$ faces and their corresponding mirror faces on the side of the crystal. The change in crystal shape from plate to needle suggests that it is the growth of these side faces that is inhibited by the 44BP additive.

This can be supported by analysing the crystal structure and by identifying the functional groups that lie in the direction of the slow growing crystal faces. In the crystal structure of IZN, the IZN molecules lie at two angles. Figure 6.20 shows the view along the $(0\bar{1}2)$ plane; this plane intercepts interactions between the IZN molecules due to bridging N3-H···N1 hydrogen bonds between the amine group and the nitrogen atom on the pyridine ring.

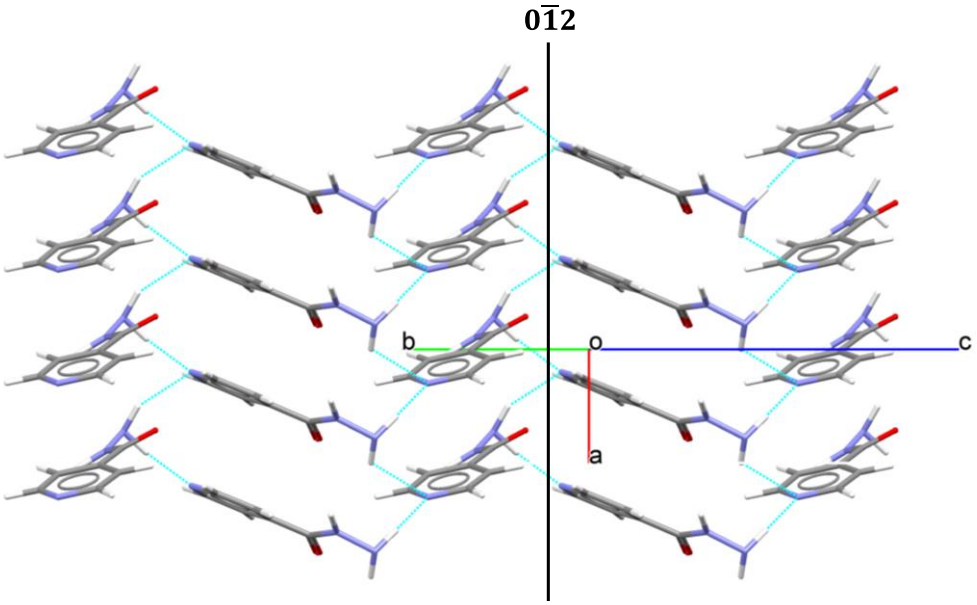

Figure 6.20 - Stacked chains of IZN molecules viewed along the $(0\bar{1}2)$ plane.

A similar observation can be made when viewing the crystal structure along the $(0\bar{1}\bar{2})$ plane in which the same interaction is intercepted between IZN molecules lying in the other orientation (Figure 6.21). These interactions can be observed more clearly when the crystal packing is viewed down the *a* axis, as shown in Figure 6.22.

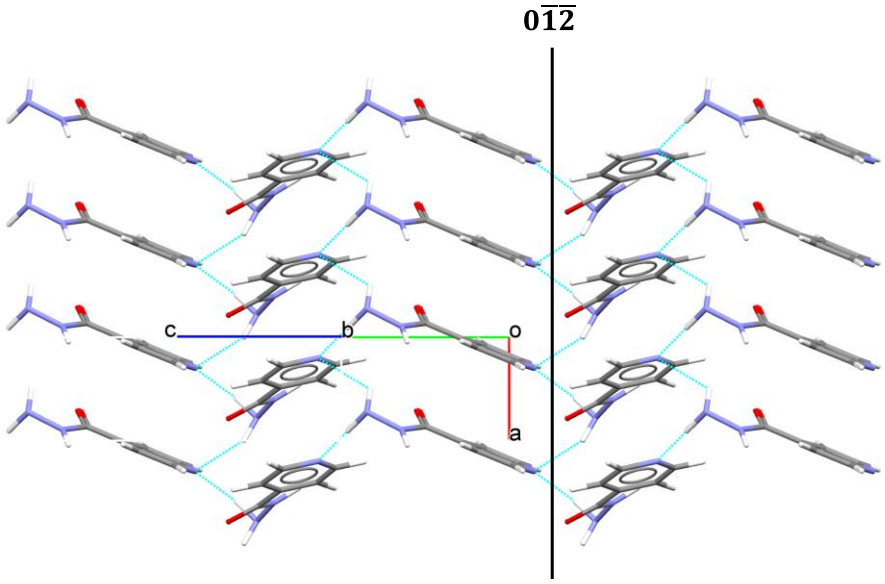

Figure 6.21 - Stacked chains of IZN molecules viewed along the $(0\bar{1}\bar{2})$ plane.

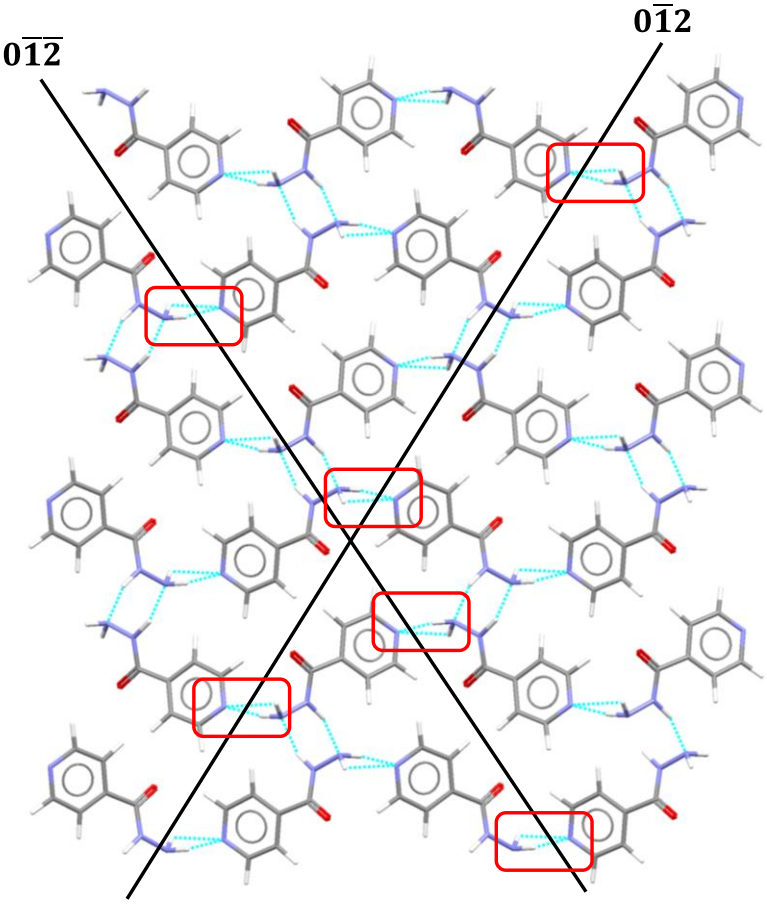

Figure 6.22 - View along the $(0\bar{1}2)$ and $(0\bar{1}\bar{2})$ planes looking down the crystallographic *a* axis with relevant interactions intersected by the planes circled in red.

The position of these planes in the crystal structure suggests that the action of the additive may proceed through the 44BP molecule, mimicking the action of the pyridine ring in the IZN molecule and interacting with the amine N3-H bond of IZN molecules. The 44BP molecule does not contain any hydrogen bond donor groups and thus may prevent the addition of further IZN molecules and hence slows down growth in the direction perpendicular to such faces.

6.5.3 ^{1}H NMR analysis

For crystallisation studies in the presence of additives it is important to maintain the solution as undersaturated with respect to the additive compound to ensure the impurity is not present in the final product. The presence of 44BP in the crystallisation product would be unfavourable due to its toxicity, which presents a disadvantage of using structurally similar additives in comparison to polymer additives – many polymers are often used as excipients in pharmaceutical formulations. ^{1}H NMR was therefore used to investigate the purity of the product (see Appendix A6.1). The results suggest that there

is no 44BP present in the product in quantities detectable by NMR, and that there is no uptake of the additive into the crystal lattice.

6.6 Crystallisation of IZN in the presence of other additives

In addition to 44BP, many other compounds were investigated for an additive effect on the crystal morphology of IZN when crystallised from ethanol and from water; these screening experiments were largely undertaken by R. Lunt and the author during the former's undergraduate MChem project at the University of Bath. Optical microscopy and SEM were used to visualise the crystal morphology produced from these trials and PXRD analysis was used to confirm the solid form of the product. With the exception of crystallisations prepared in a 1:1 molar ratio in which, in some cases, multi-component complexes were produced or unless otherwise stated, the additives had no effect on the solid form (polymorph) of the IZN product (see Appendix A6.3 for PXRD patterns). In terms of morphology of IZN, none of the polymer additives showed a morphology-modifying effect in either water or ethanol; however, several of the structurally similar and size-matched additives were found to affect the morphology of IZN and the most significant findings are presented here.

6.6.1 Evaporative crystallisation from ethanol

Evaporative crystallisations from ethanol were initially prepared in a 100:1 IZN to additive molar ratio with structurally similar additives. These crystallisations resulted in no change in crystal morphology and as a result, subsequent crystallisations were carried out in a 10:1 molar ratio, from the products of which several morphology changes were observed.

Evaporative crystallisation from ethanol in the presence of imidazole, 4-fluorobenzoic acid and 4-hydroxybenzoic acid resulted in small changes in the shape of the plate-like crystals; in some cases the crystals were more elongated than those produced without additives. However, as shown in Figure 6.23, these observations were not fully reproducible; results from repeat crystallisations gave different results in terms of crystal size and shape.

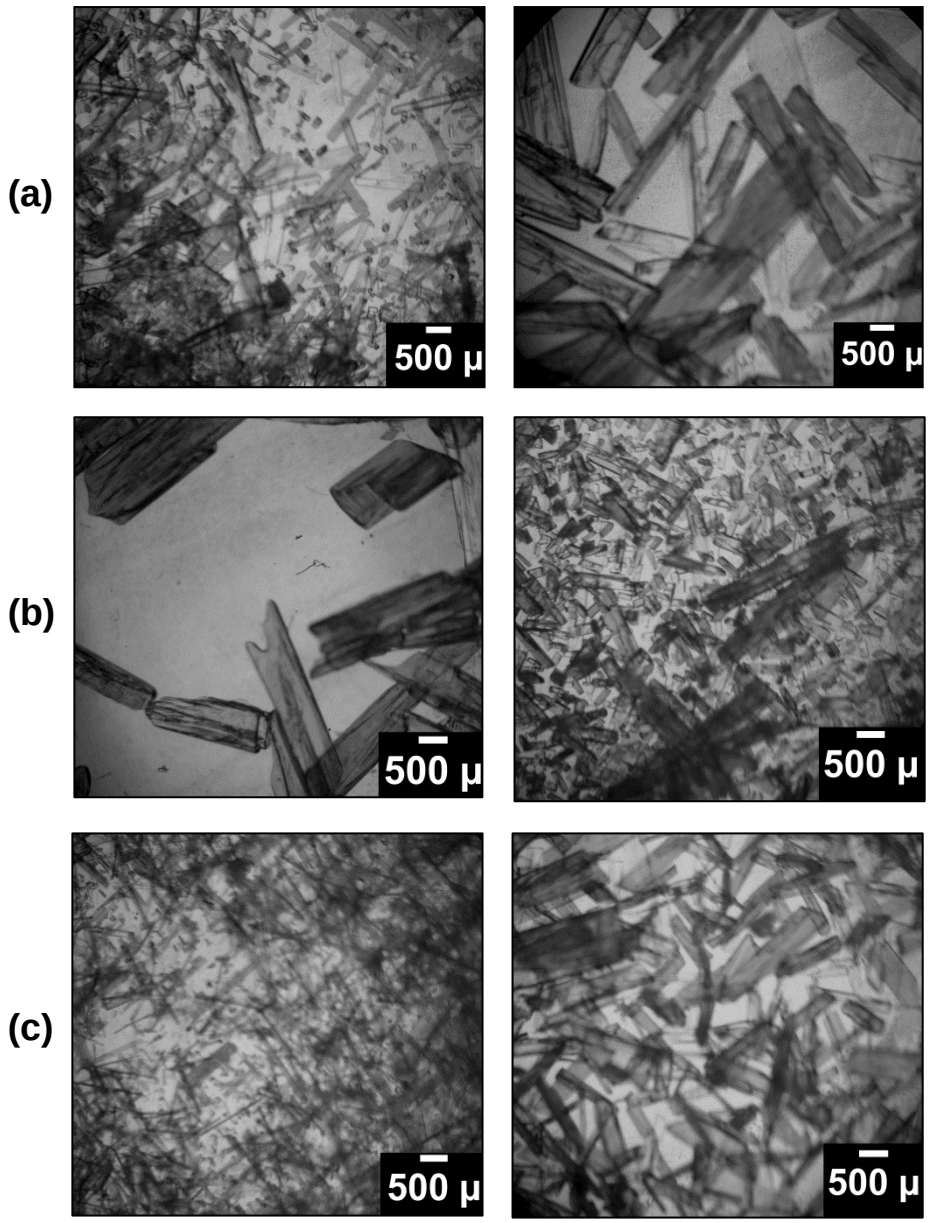

Figure 6.23 - Inconsistent morphologies of IZN produced in repeat evaporative crystallisations from ethanol in the presence of (a) imidazole, (b) 4-flurobenzoic acid and (c) 4-hydroxybenzoic acid.

The control crystallisations also resulted in variability in the size and shape of the plate-like crystals (as shown in Section 6.4.1); such inconsistencies in morphology produced in an evaporative environment may result from lack of agitation in the system and poor mass transfer.

Crystallisation in the presence of many of the other additives produced plate-like crystals of inconsistent size, similar to those produced with no additive present. However, in the presence of resorcinol and benzoic acid the plate-like crystals appeared to be broader

than in some of the crystallisations with no additive present (Figure 6.24). This morphology change was small and not fully reproducible, and this lack of consistency was also evident when a series of 4-substituted benzoic acids were used as additives (see Appendix A6.1); inconsistencies in the outcomes of repeat experiments lead to the conclusion that the morphology changes cannot definitively be attributed to the presence of the additive.

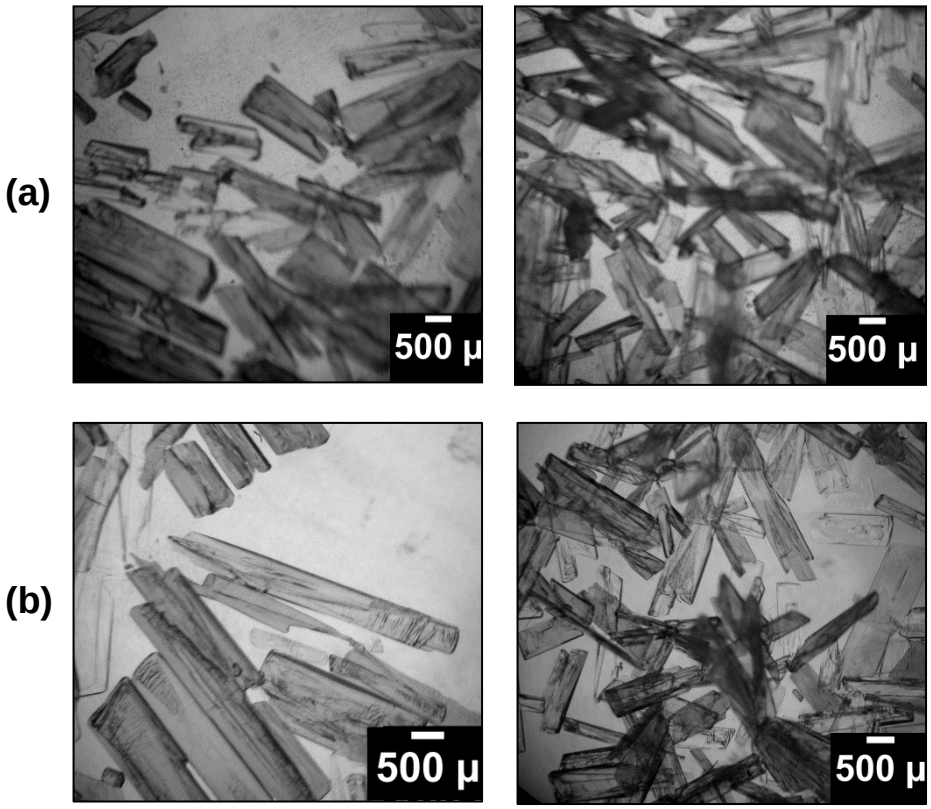

Figure 6.24 - Plate-like crystals of IZN produced in the presence of (a) resorcinol and (b) benzoic acid in an evaporative environment from ethanol. Two images are shown for each case, highlighting inconstancies.

6.6.2 Cooling crystallisation from ethanol

Cooling crystallisation of IZN was carried out in the presence of all additive compounds utilised in the evaporative experiments. Due to the small size of the crystals produced at 1 ml scale, SEM was used to observe the crystal morphology. As noted previously, the morphology of IZN produced from ethanol with no additive present in a cooling environment is plate-like and more consistent in repeat crystallisations than in the evaporative crystallisations. Therefore, more conclusive comparisons can be made with experiments carried out in the presence of an additive. This may be as a result of improved temperature control and mixing in the cooling crystallisation experimental set-up. Significant and reproducible morphology changes were observed in the presence of

some of the additives in an IZN to additive molar ratio of 10:1 in a cooling environment, including the structurally similar additives.

In the presence of isonicotinic acid and 2-picolinic acid, plate-like crystals of IZN were observed, however they are more elongated than those produced with no additive present. Figure 6.25 shows the SEM images of the crystal morphologies. The crystals produced in the presence of isonicotinic acid appear to be thinner than those produced in the presence of 2-picolinic acid. This suggests that the isonicotinic acid may be interacting with the slowest growing (010) face and inhibiting growth in the direction perpendicular to the face (the crystallographic *b* axis) by intercepting N2-H···N3 interactions. Isonicotinic acid and 2-picolinic acid differ only by the position of the nitrogen atom in the pyridine ring; positioned in the *para* and *ortho* positions, respectively. This nitrogen atom may interfere with the interactions by offering an alternative hydrogen bond acceptor. The different morphologies produced may suggest that the position of the nitrogen atom on the ring is important in facilitating an inhibiting effect of crystal growth in the direction of the crystallographic *b* axis.

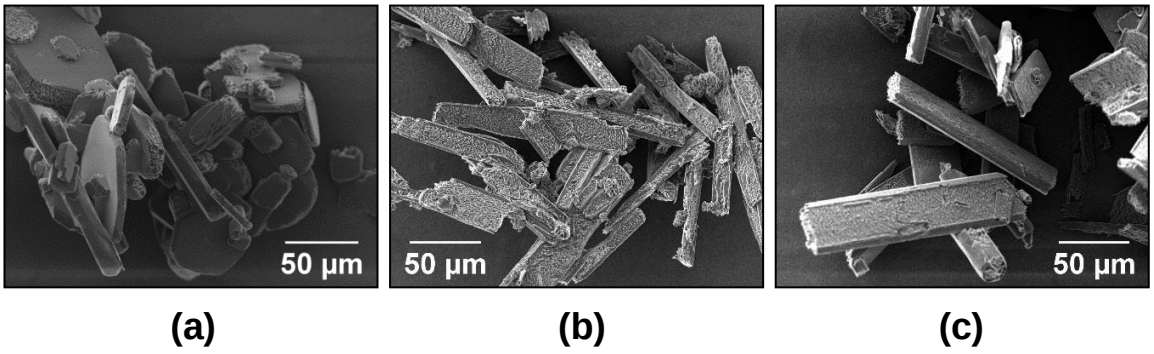

Figure 6.25 - SEM images of IZN crystals produced in the presence of (a) no additive, (b) isonicotinic acid and (c) 2-picolinic acid.

Furthermore, use of nicotinamide and isonicotinamide as additives did not have an effect on the crystal morphology of IZN. This suggests that the carboxylic acid group on the isonicotinic acid and the 2-picolinic acid molecules is also important and may interact favourably with the growing crystal of IZN. This is further supported by the observation that in some cases nicotinic acid had a similar effect on morphology, although this effect was not as reproducible as with isonicotinic acid and 2-picolinic acid. Modifications in the crystal morphology of IZN were also observed in the presence of other size-matched additives in a 10:1 molar ratio; biuret and 2,4-dinitrobenzoic acid as additives in solution consistently produced elongated plates of IZN.

Further crystallisations with those additives that produced a morphology modification effect at 1 ml scale were repeated at 10 ml scale with overhead stirring. Microscope images of the crystal morphologies produced are shown in Figure 6.26.

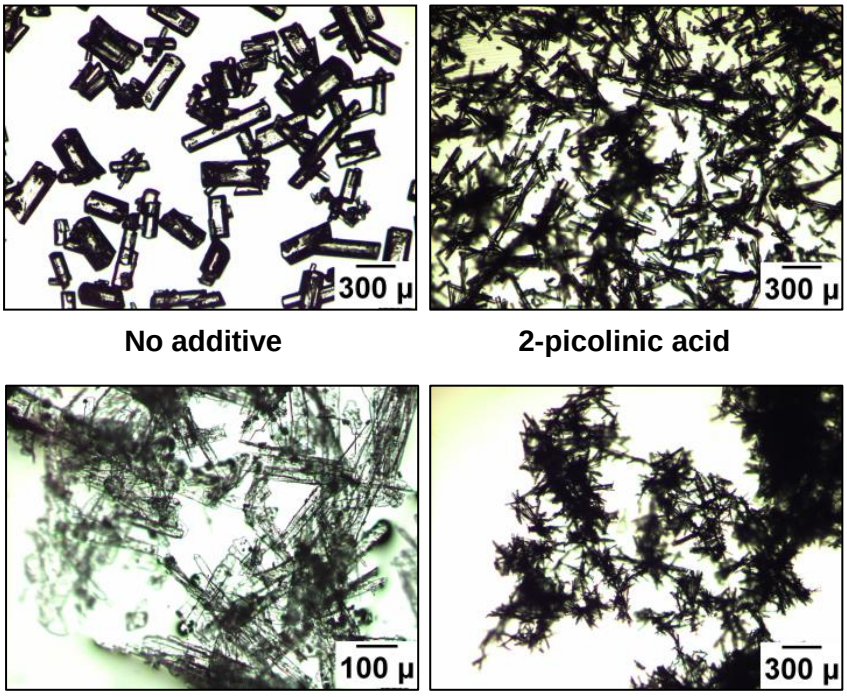

Figure 6.26 - Microscope images of IZN crystals produced at 10 ml scale in the presence of different additives in a 10:1 IZN to additive molar ratio.

At 10 ml scale the size of the crystals were larger, but comparable results to the small scale crystallisations were observed in terms of morphology. In the presence of 2-picolinic acid, elongated plates were observed whereas with isonicotinic acid present very thin plate-like crystals of IZN were produced. The presence of biuret produced needle-like crystals, finer than those observed at small scale. A control experiment was also carried out under these conditions, with no additive present, in which plate-like crystals were produced. Despite the observation of morphology changes in the presence of additives, none of the additives improved the crystal morphology of IZN (in terms of favourable particle shapes for processing) in comparison to this control crystallisation.

6.6.3 Evaporative crystallisation from water

As mentioned previously, crystallisation of IZN from water results in the formation of needle-like crystals. In parallel to the crystallisations from ethanol initial evaporative crystallisations from water focused on the use of structurally similar additives in a 100:1 IZN to additive molar ratio. The use of such additives resulted in needle-like crystals of

IZN in all cases, however, the needles varied in length in comparison to those produced in the absence of additive (Figure 6.27). For example, crystallisation of IZN in the presence of isonicotinamide resulted in shorter needles suggesting that the additive may influence the growth of the fast growing end face of the needle. Such small changes in crystal morphology were not, however, deemed significant enough to pursue for further study.

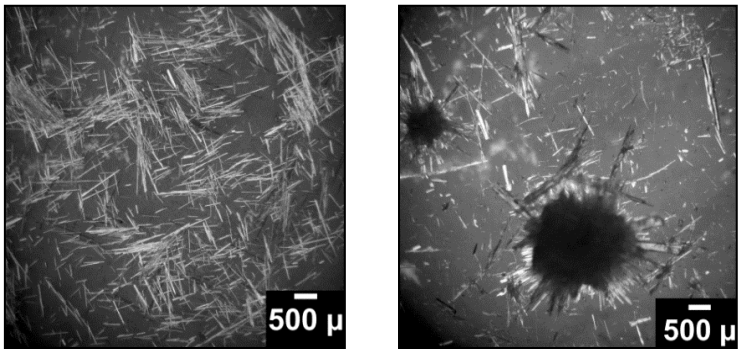

Figure 6.27 - Microscope images of crystal morphology of IZN produced through evaporation from water in the presence of (a) isonicotinic acid and (b) 2-picolinic acid.

A broader range of sized-matched additives were then investigated at a higher IZN to additive molar ratio of 10:1, in which a more significant effect of the additives on crystal morphology was observed (Figure 6.28).

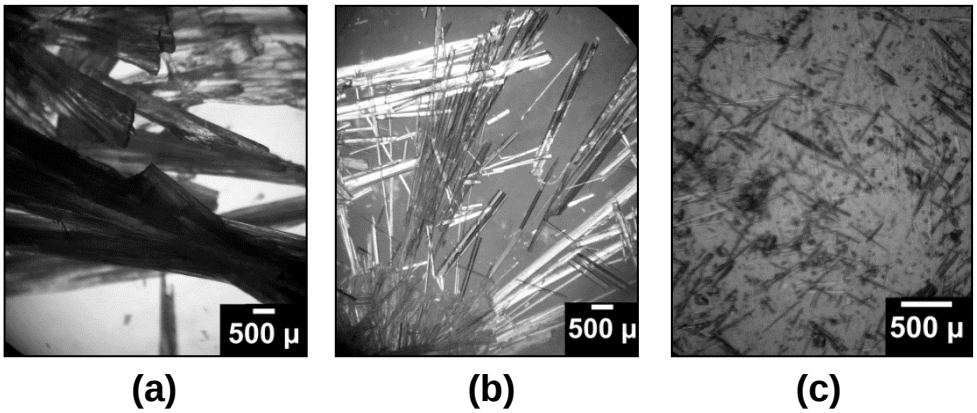

Figure 6.28 - Microscope images of IZN crystals produced in the presence of (a) resorcinol, (b) urea and (c) 4-hydroxybenzoic acid.

In the presence of resorcinol, elongated plate-like crystals were produced. In the presence of urea as an additive, the IZN crystals displayed a needle-like morphology, but these needles were broader and longer than observed in the presence of no additive, resembling a blade-like morphology. In the presence of 4-hydroxybenzoic acid a mixture

of morphologies were produced from needle-like to block-like crystals. The solid form of all products was identified as the known polymorph of IZN. A more detailed analysis of the two morphologies is presented in the next section.

6.6.4 Cooling crystallisation from water

In the cooling crystallisation experiments, stirring was implemented allowing for more uniform mass transfer than in evaporative crystallisations. All cooling crystallisations with additives present were prepared in an IZN to additive molar ratio of 10:1. None of the structurally similar additives produced a significant morphology change in a cooling environment under the conditions measured. In contrast, some of the size-matched additives induced a morphology change, but only two of these produced the effect reproducibly.

In the presence of 2,2'-bipyridyl, in some cases the product needle-like crystals displayed a larger aspect ratio; this suggests that the additive may have an inhibiting effect of growth perpendicular to the side faces of the crystals, further increasing the relative growth rate of the fast growing face. However, in other cases the needles resembled those produced from water in the presence of no additive so the effect was not considered significant. In the presence of imidazole, initially the crystals produced were broader and more plate-like needles. However, this result was not reproducible and needle-like crystals were produced upon repetition of the experiment. The morphology effect of the presence of 4-hydroxybenzoic acid and urea were each found to be reproducible; microscope images of the crystals produced in the presence of these additives are shown in Figure 6.29.

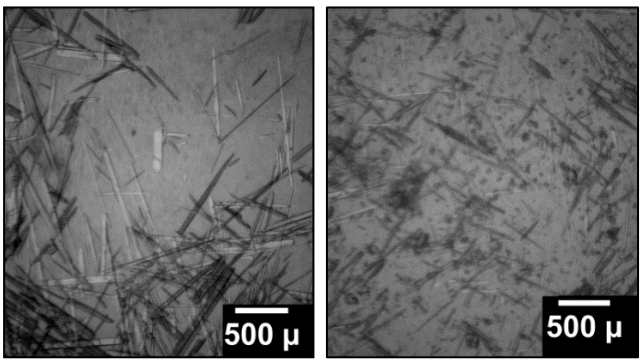

Figure 6.29 - Microscope images of IZN crystals produced from cooling crystallisation in the presence of (a) urea and (b) 4-hydroxybenzoic acid.

As observed in evaporative crystallisations from water, blade-like crystals produced in the presence of urea were observed in a cooling environment. This may imply that the additive may slow down growth of one of the slow growing side faces of the needle-like crystal. Based on the BFDH morphology prediction, this would result from interruption of N-H···N hydrogen bonding in the direction of the crystallographic *b* or *c* axes. These hydrogen bonds both involve the amine group on the IZN molecule; the urea molecule also features amine groups which may mimic the interactions of the IZN molecules.

Crystallisations carried out in the presence of 4-hydroxybenzoic acid (4HBA) resulted in a mixture of crystal morphologies with needle and block-like crystals produced, which correlates with the results from the evaporative crystallisations. Cooling crystallisation was also repeated at 5 ml scale with the same mixture of morphologies produced. A PXRD pattern of the product shows peaks corresponding to the known IZN polymorph; however, unlike in the evaporative sample, these peaks are accompanied by several less intense peaks (e.g. at ~13°, 13.5°, and 20° 2θ). Aitipamula *et al.* recently reported the structures of two concomitant polymorphs of hydrated co-crystals of IZN and 4HBA produced when the two starting materials are combined in equimolar quantities. The polymorphs show block and needle-like morphologies.[145] Figure 6.30 shows the PXRD pattern of the product from the cooling crystallisation, along with calculated patterns of the reported co-crystals.

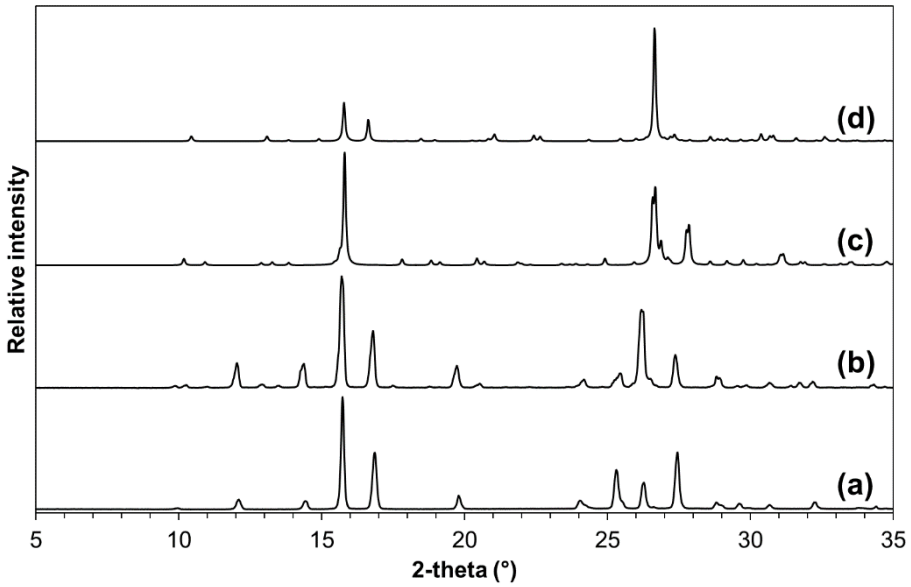

Figure 6.30 - PXRD patterns of (a) IZN starting material, (b) sample from IZN cooling crystallisation from water in the presence of 4HBA (10:1), (c) IZN 4HBA hydrate form II (BICQUB) and (d) IZN 4HBA hydrate form I (BICQUB01).

The additional low intensity peaks present in the pattern of the cooling crystallisation in this work may correspond to peaks present in the patterns of the co-crystals. The patterns of the two co-crystals are very similar and therefore it is difficult to deduce which polymorph may be present in the crystallisation product; the polymorphs are reported to form concomitantly so they may both be present in the sample. In addition, hot-stage microscopy was also used to characterise the sample and this showed the block-like crystals present in the sample turning opaque in the region of 110-125 °C. This correlates with the temperature at which water is lost in both hydrates reported in the literature.[145] The conclusion from this is that the modified morphologies observed in the presence of 10% 4HBA may be the result of co-crystal formation rather than modification of IZN morphology; isolation of pure samples of each morphology suitable for X-ray diffraction was not possible so this could not be confirmed.

6.7 Crystallisation of multi-component complexes of IZN

One drawback of using structurally similar additive compounds for control of crystal morphology as opposed to polymer additives is that when used in high concentrations, the additive compound may be incorporated into the crystal structure forming a multi-component complex such as a co-crystal, salt or solid solution instead of producing an additive effect and remaining in solution. For example, the co-crystals of 4HBA and IZN noted above.[145] Additionally, in other cases the presence of an additive in high concentrations can have an effect on the polymorphic form of the starting material.[47,48] To investigate the likelihood of these effects occurring for the chosen additives, crystallisations with IZN and the additive in equimolar quantities were thus also prepared. These experiments produced a number of molecular complexes co-crystals that have been analysed using X-ray diffraction and thermal analysis and are presented here.

6.7.1 IZN^{2+} oxalic $acid^{2-}$

Crystallisation of IZN in the presence of equimolar quantities of oxalic acid (OA) resulted in a salt form. The complex crystallises in the monoclinic space group $P2_1/c$ and the asymmetric unit consists of one doubly protonated IZN molecule and one doubly deprotonated OA molecule (Figure 6.31). One proton from the OA molecule has transferred to the terminal amine group on the IZN molecule and the other proton has transferred across a strong hydrogen bond to be located closer to the nitrogen atom on the pyridine ring. The pyridyl N^+-H bond has a $N^{\cdots}H$ distance of 1.22(4) Å and the $O^{-\cdots}H$ bond has an $O^{\cdots}H$ distance of 1.32(4) Å (Table 6.2).

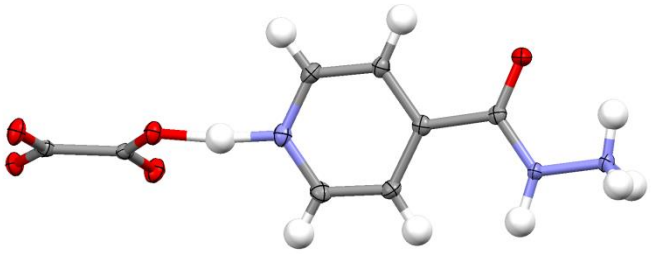

Figure 6.31 - Asymmetric unit of the IZN^{2+} OA^{2-} complex viewed down the crystallographic *c* axis.

Hydrogen bonding between the nitrogen atom on the pyridine ring of the IZN molecule and a carboxylic acid group on the co-former molecule is a common synthon in IZN structures. A Cambridge Structural Database (CSD) search of IZN structures produced 46 complexes with co-formers containing a carboxylic acid group and of those, 41 feature such an interaction. Proton transfer across this hydrogen bond is observed in six complexes. This hydrogen bond is particularly short and strong in this complex, with an O···N distance of 2.532(2) Å, which makes it an ideal candidate for temperature dependent proton transfer studies. Such studies have previously been carried out on a complex of IZN and 4-aminosalicylic acid.[187]

In the structure the molecules assemble in herringbone chains through a bifurcated hydrogen bond between the other carboxylate group of the OA molecule and the N-H amide bond of the IZN molecule. In addition, an N^{+}-H···O^{-} hydrogen bond forms between this carboxylate group and the protonated terminal amine group on the IZN molecule, linking the herringbone chains together (Figure 6.32).

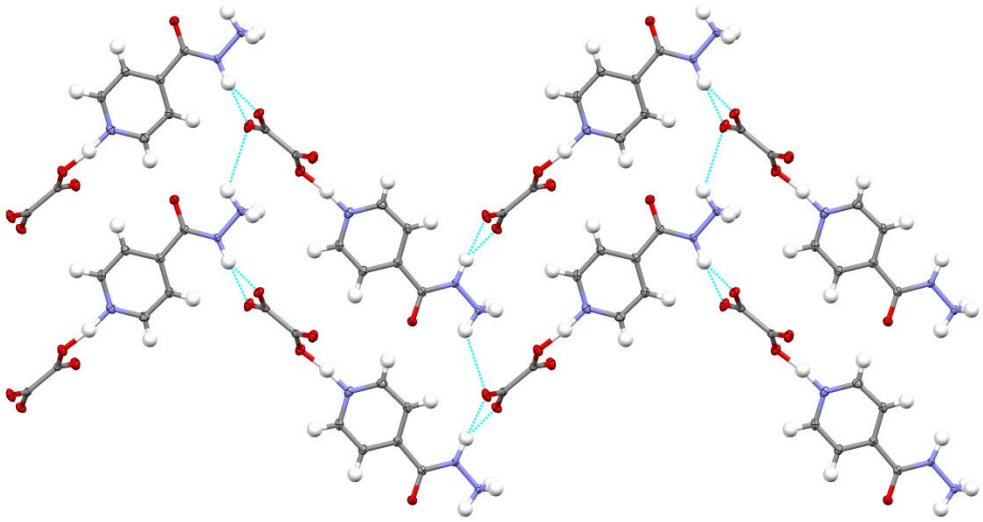

Figure 6.32 - Herringbone packing arrangement viewed down the crystallographic *c* axis.

The remaining two N^+-H groups on the terminal amine group of the IZN molecule form hydrogen bonds with C-O^- groups on the oxalic acid molecule and these interactions link the layers of herringbone chains in the third dimension, as show in Figure 6.33.

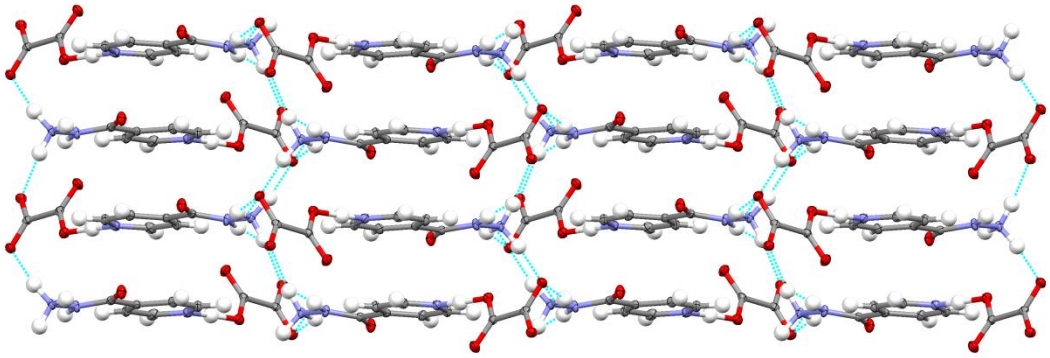

Figure 6.33 - Stacking of the layers of molecules viewed down the crystallographic *a* axis.

Table 6.2 - Hydrogen bonds in IZN^{2+} OA^{2-} (Å and °).

D-H···A	d(D-H)	d(H···A)	d(D···A)	<(DHA)
C(3)-H(1)···O(5)#1	0.94(2)	2.39(2)	3.208(2)	145.8(18)
C(6)-H(3)···O(3)#2	1.02(2)	2.34(3)	3.231(3)	145.1(18)
N(3)-H(7)···O(2)#3	0.95(2)	1.82(2)	2.768(2)	171(2)
N(3)-H(8)···O(1)#4	1.02(3)	1.77(3)	2.773(2)	168(2)
N(3)-H(6)···O(5)	0.95(3)	2.15(2)	2.664(2)	112.9(18)
N(2)-H(5)···O(1)#5	1.02(2)	2.63(2)	3.433(2)	136.1(16)
N(2)-H(5)···O(2)#5	1.02(2)	1.72(3)	2.685(2)	157(2)
N(1)-H(9)···O(4)	1.22(4)	1.32(4)	2.532(2)	171(3)
N(1)-H(9)···O(3)	1.22(4)	2.64(3)	3.535(2)	129(2)

Symmetry transformations used to generate equivalent atoms:
#1 x-1,y,z #2 x+1,y,z #3 x+1,-y+3/2,z-1/2
#4 x+1,-y+3/2,z+1/2 #5 -x,y+1/2,-z+1/2

In addition to singe crystal X-ray diffraction (scXRD), PXRD was used to determine the phase purity of the sample from evaporative crystallisation. Figure 6.34 shows the PXRD pattern of the bulk material alongside the pattern calculated from scXRD data as well as diffraction patterns for the two starting materials; this suggests that the sample has good phase purity.

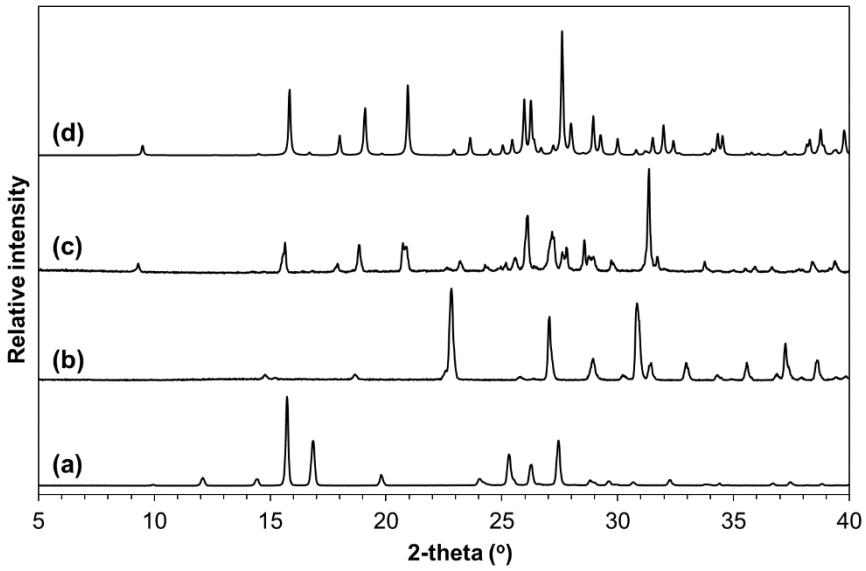

Figure 6.34 - PXRD patterns (a) IZN, (b) OA, (c) IZN^{2+} OA^{2-} measured and (d) IZN^{2+} OA^{2-} calculated.

Analysis of a single crystal product from evaporative crystallisation of IZN and OA in a 10:1 ratio was also carried out using scXRD and it was found that under these conditions the salt was not produced; the sample isolated was IZN. This suggests that the salt will not form with lower additive ratios and therefore the OA could be used as an additive to disrupt crystal growth in such lower concentrations. However, the crystallisation produced low yields and therefore bulk analysis was not possible to confirm that none of the salt form was present in the sample.

The salt form was also analysed thermally using DSC (Figure 6.35).

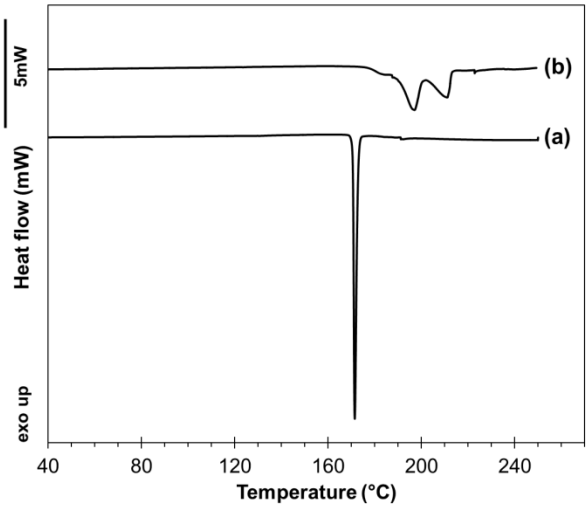

Figure 6.35 - DSC traces of (a) IZN and (b) IZN^{2+} OA^{2-}.

Two endothermic events (at 197 and 211 °C) are observed, at temperatures that are higher than the melting point of both IZN (171 °C) and OA (189.5 °C).[188] This suggests that the salt form is more thermally stable than the IZN and OA starting materials.

To investigate these events further, hot-stage microscopy was also carried out; the images are shown in Figure 6.36. Firstly, a thermosalient effect is observed around 160 °C in which the crystals appear to jump and move on the microscope slide. At around 190 °C the crystals become opaque and begin partially to melt suggesting that they may undergo a phase transition to a high temperature form. This is then followed by a full melt of the crystal between 220 and 230 °C.

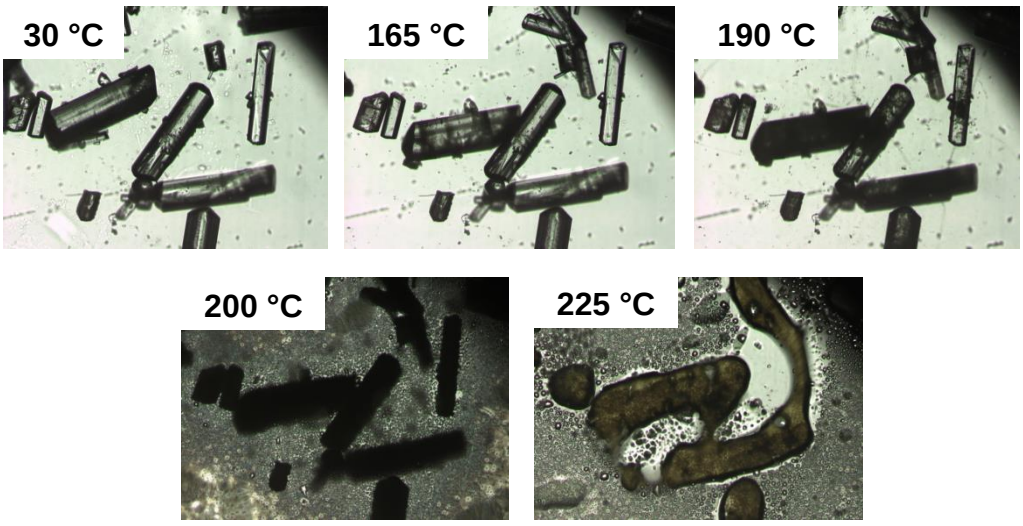

Figure 6.36 - Hot-stage microscopy images of IZN^{2+} OA^{2-} molecular complex.

6.7.2 IZN resorcinol*

An evaporative crystallisation of IZN and resorcinol (RES) combined in equimolar quantities produced a 1:1 molecular complex of the two starting materials. The structure crystallises in the monoclinic space group $P2_1/c$ and the asymmetric unit contains one molecule of IZN and one molecule of RES. The nitrogen atom on the pyridine ring of the IZN molecule forms an O-H···N hydrogen bond with one of the hydroxyl groups on the RES molecule with the rings of each molecule lying co-planar to one another. The other hydroxyl group on the RES molecule forms two interactions, each with a different IZN molecule. First, the hydroxyl group forms an O-H···N interaction with the nitrogen atom of the amine group of one IZN molecule. Secondly, the oxygen atom of the hydroxyl group on the RES molecule interacts with one of the N-H bonds of the amine group of a

* This structure was subsequently published by Swapna *et al.* during these studies.[186]

different IZN molecule in an N-H···O interaction (Figure 6.37). The IZN molecule has two other hydrogen bond donor groups which form interactions in the structure. The N-H bond of the amide group forms an N-H···O hydrogen bond with the amide carbonyl group of an IZN molecule directly below it, allowing the co-planar IZN and RES units to stack off-set to one another.

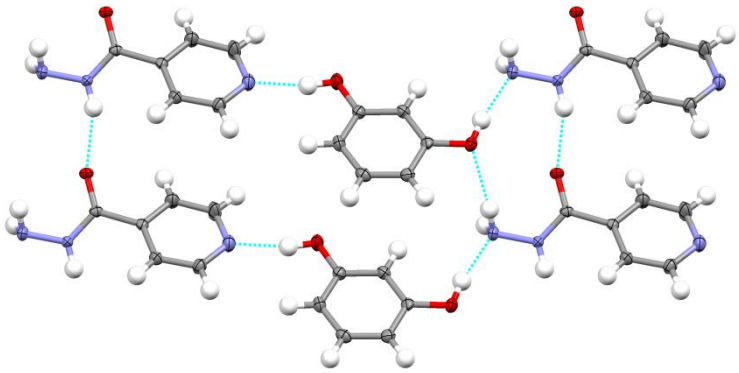

Figure 6.37 - Hydrogen bond interactions in the IZN RES complex viewed down the crystallographic *b* axis.

Secondly, the N-H bond on the amine group of the IZN molecule also forms an N-H···O hydrogen bond with the amide carbonyl group on a symmetry generated IZN molecule. The combination of these hydrogen bonds forms two-molecule deep layers of IZN and RES molecules (Figure 6.38).

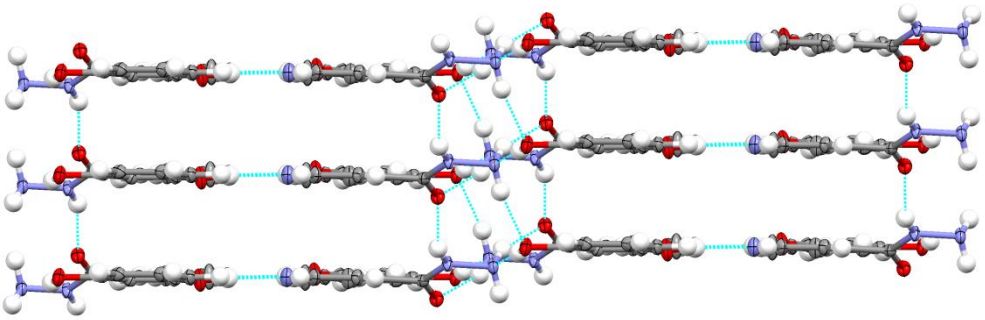

Figure 6.38 - Layers of IZN and RES molecules in the IZN RES complex.

Weak C-H···C interactions hold groups of layers together with an angle of 73.8° between the layers (Figure 6.39).

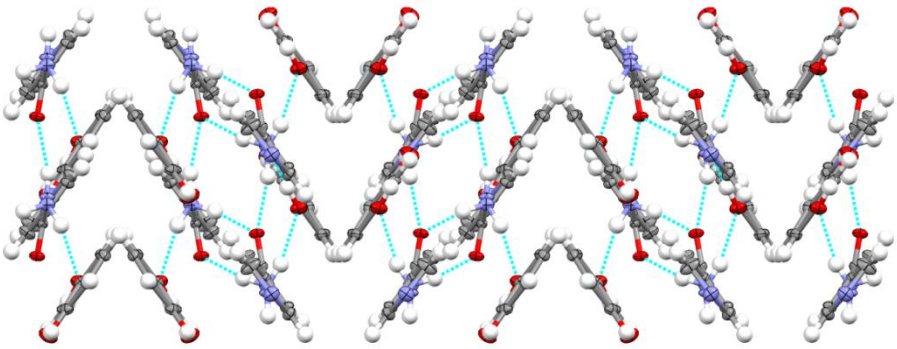

Figure 6.39 - Packing of IZN and RES molecules in the complex viewed down the crystallographic *c* axis.

Table 6.3 - Hydrogen bonds in IZN RES (Å and °).

D-H···A	d(D-H)	d(H···A)	d(D···A)	<(DHA)
C(10)-H(9)···O(2)#1	0.924(18)	2.638(18)	3.282(2)	127.4(13)
N(5)-H(13)···O(3)#2	0.932(19)	2.122(19)	3.0038(19)	157.4(15)
N(5)-H(12)···O(1)	0.91(2)	2.21(2)	3.0960(18)	162.8(17)
N(4)-H(11)···O(3)#3	0.865(18)	2.109(19)	2.9205(17)	156.1(16)
O(1)-H(1)···N(5)#4	0.92(2)	1.94(2)	2.8438(18)	169.9(19)
O(2)-H(3)···N(3)#5	0.92(2)	1.86(2)	2.7669(17)	168(2)

Symmetry transformations used to generate equivalent atoms:
#1 -x,-y+1,-z+1 #2 -x+1,-y+1,-z+1 #3 x+1,y,z
#4 x-1,y,z #5 x-1,y,z-1

PXRD analysis of the bulk material from the evaporative crystallisation was also carried out (Figure 6.40), suggesting that the complex is produced as a phase pure sample under the conditions used.

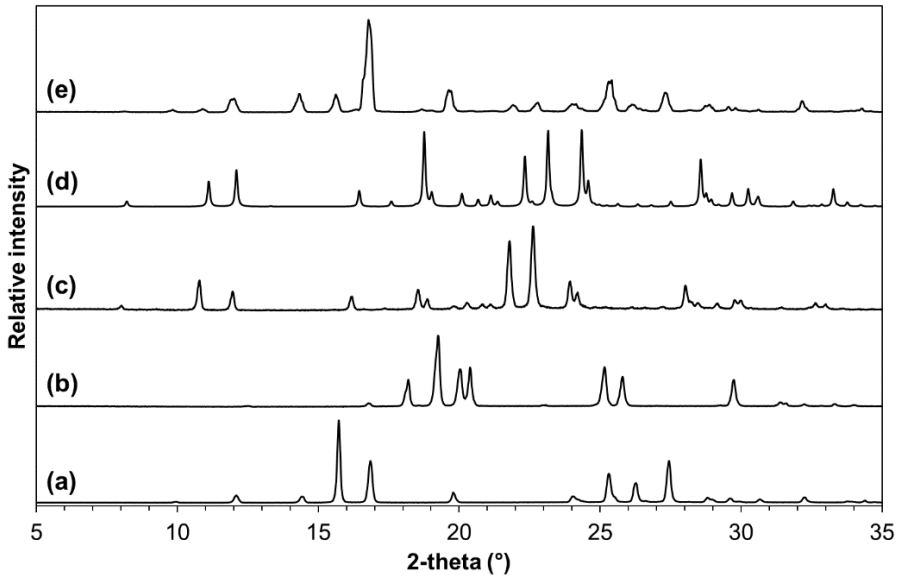

Figure 6.40 - PXRD patterns of (a) IZN, (b) RES, (c) IZN RES measured, (d) IZN RES calculated and (e) product of crystallisation of IZN and RES prepared in a 10:1 molar ratio.

PXRD analysis of the product of a crystallisation prepared with an IZN to RES ratio of 10:1 is shown in Figure 6.40e. The pattern shows peaks related to the pattern for the IZN starting material as well as several small peaks matching that of the IZN RES complex. This suggests that in this case under these conditions the complex forms in small quantities and the excess IZN crystallises as the known polymorph. Thus in evaporative crystallisation, this concentration of RES (10:1) could not be used for an additive effect without compromising the purity of the product by concomitantly producing the IZN RES complex.

The thermal properties of the bulk product were also analysed using DSC, as shown in Figure 6.41. A sharp endothermic melting event is present at 147 °C, lower than that of the IZN starting material but higher than the RES starting material. This suggests that the complex is less thermally stable than IZN but more thermally stable than RES.

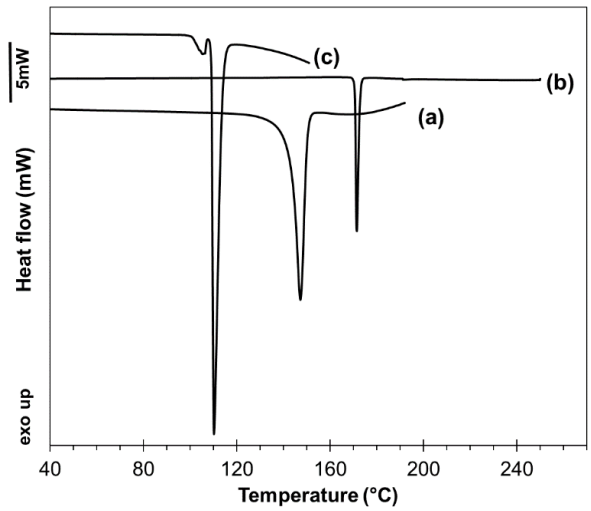

Figure 6.41 - DSC traces of (a) IZN RES, (b) IZN and (c) RES.

6.7.3 IZN^{+} 2,4-dinitrobenzoic $acid^{-}$

An equimolar combination of IZN and 2,4-dinitrobenzoic acid (24DNBA) resulted in the formation of a salt. The structure crystallises in the orthorhombic space group Pbca. Proton transfer has occurred from the carboxylic acid proton on the 24DNBA molecule to the terminal amine group on the IZN molecule.

Unlike in the complex with oxalic acid, the carboxylate group of the 24DNBA molecule does not interact with the nitrogen atom on the pyridine ring of the IZN molecule. Instead, a hydrogen bonded dimer forms between the two molecules through two N-H···O hydrogen bonds. The oxygen atoms in the carboxylate group of the 24DNBA molecule

interact with the amide N-H bond of the IZN molecule and with the protonated nitrogen atom of the terminal amine group of the IZN molecule. The latter of these two hydrogen bonds is relatively short and strong with a N···O distance of 2.5819(17) Å. The nitrogen atom of the pyridine ring on the IZN molecule instead forms an N-H···N hydrogen bond with an N-H bond on the terminal amine of another IZN molecule. The third N-H bond on the amine group on the IZN molecule forms an N-H···O hydrogen bond with the amide carbonyl group of another IZN molecule. These interactions allow the molecules to assemble in a two dimensional hydrogen bonded chain of IZN molecules flanked by 24DNBA molecules on either side (Figure 6.42).

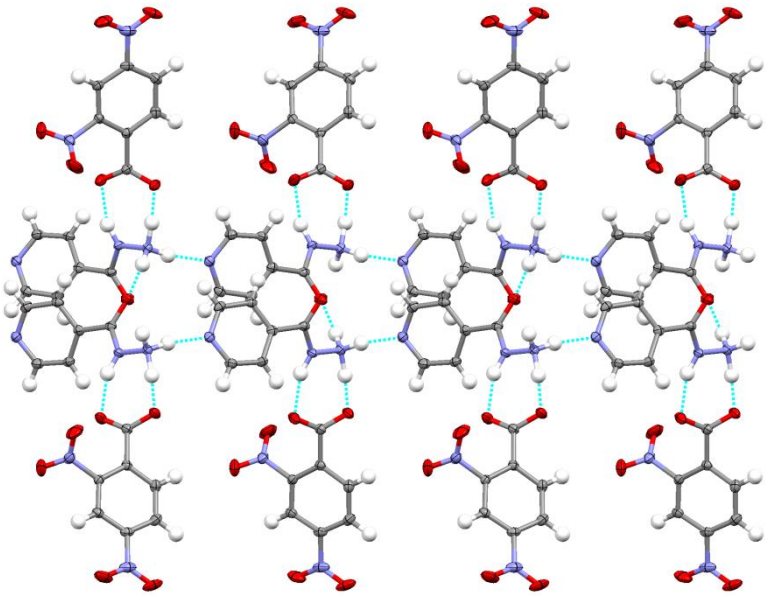

Figure 6.42 - Hydrogen bonding in the IZN^{+} $24DNBA^{-}$ complex viewed down the crystallographic *a* axis.

The hydrogen bonded sheets stack off-set to one another as shown in Figure 6.43 where the 24DNBA molecules overlay in the middle of the image.

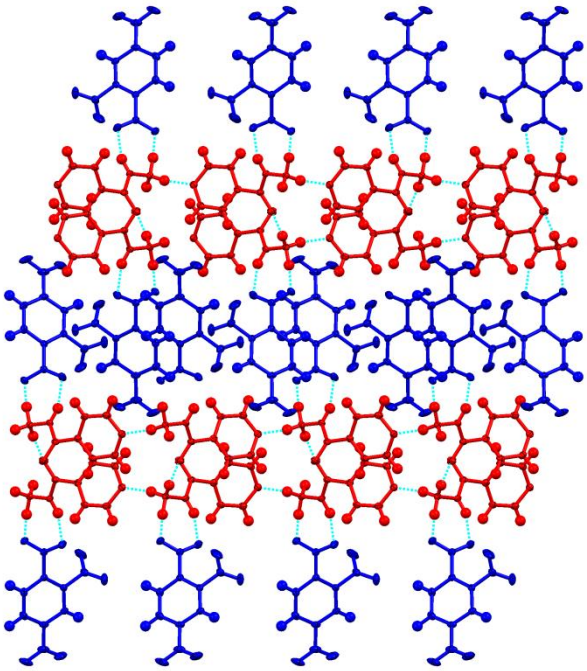

Figure 6.43 - Overall packing arrangement viewed down the crystallographic *a* axis. Colour coding shows the molecules of IZN in red and 24DNBA in blue and highlights the way in which they overlay.

Table 6.4 - Hydrogen bonds in IZN^{+} $24DNBA^{-}$ (Å and °).

D-H···A	d(D-H)	d(H···A)	d(D···A)	<(DHA)
C(1)-H(10)···O(5)#1	0.963(18)	2.612(18)	3.352(2)	133.8(13)
C(7)-H(1)···O(2)#2	0.962(17)	2.372(17)	3.3159(19)	166.7(14)
N(2)-H(7)···O(2)#3	0.928(18)	1.910(18)	2.7769(17)	154.5(16)
C(4)-H(8)···O(6)#4	0.955(18)	2.424(17)	3.044(2)	122.4(13)
N(3)-H(6)···O(1)#5	0.91(2)	1.93(2)	2.8406(17)	173.8(17)
N(3)-H(4)···N(1)#6	0.96(2)	1.84(2)	2.7925(19)	170.7(17)
N(3)-H(5)···O(2)#3	1.07(2)	2.618(19)	3.2237(17)	115.5(13)
N(3)-H(5)···O(3)#3	1.07(2)	1.52(2)	2.5819(17)	172.8(17)

Symmetry transformations used to generate equivalent atoms:
#1 -x+1,-y+1,-z+1 #2 x+1/2,-y+3/2,-z+1 #3 -x,y-1/2,-z+1/2
#4 -x+1,y-1/2,-z+1/2 #5 x-1/2,y,-z+1/2 #6 -x+1/2,y+1/2,z

As for the other complexes, PXRD analysis was carried out to analyse the purity of the bulk product from the evaporative crystallisation. The PXRD patterns are shown in Figure 6.44, there is a significant match between the peaks in the measured and calculated patterns suggesting that the bulk product exhibits phase purity; however, the measured pattern is somewhat noisy.

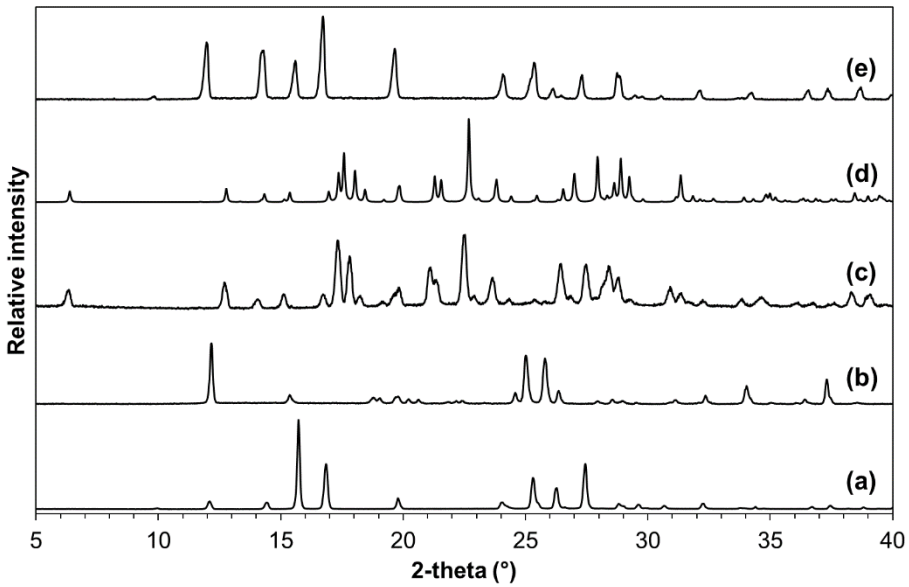

Figure 6.44 - PXRD patterns of (a) IZN, (b) 24DNBA, (c) IZN^+ $24DNBA^-$ measured (d) IZN^+ $24DNBA^-$ calculated and (e) from a 10:1 IZN:24DNBA staring material molar ratio.

PXRD analysis was also carried out for a sample prepared in a 10:1 IZN to 24DNBA ratio; the peaks in the resulting pattern match those for IZN, suggesting that the salt is not produced under these conditions with this concentration of 24DNBA.

DSC analysis on the complex shows a broad endothermic peak at 145 °C representing the melting point of the complex (Figure 6.45). However, the onset for this peak is at the much lower temperature of 120 °C suggesting that the sample may not be pure. The melting point is also lower than those of the IZN and 24DNBA starting materials suggesting that the salt form is less thermally stable than the starting materials.

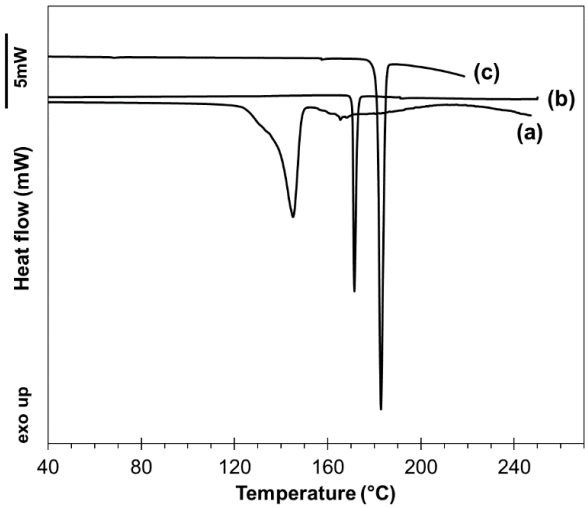

Figure 6.45 - DSC traces of (a) IZN^+ $24DNBA^-$, (b) IZN and (c) 24DNBA.

6.8 Conclusions

The crystal morphology of the API isoniazid (IZN) produced from different solvents and in the presence of different ratios of a range of additive compounds has been investigated in a batch environment. The additives were categorised into structurally similar, size-matched and polymer additives. Some of the structurally similar compounds used are also Generally Recognised as Safe (GRAS) compounds.

IZN was found to crystallise in a plate-like morphology from ethanol and in a needle-like morphology from water, both of which are undesirable morphologies for the downstream processing of a pharmaceutical ingredient. The modification of the crystal morphology of IZN using additives was difficult to achieve, with limited success using structurally similar GRAS additives. Some of the size-matched additives did show an effect on crystal morphology, however problems with reproducibility were encountered in many of the experiments, especially those using evaporative crystallisation. The lack of active mixing, resulting in poor mass transfer in evaporative crystallisation, may be a reason for this variability in crystal shape. Cooling crystallisation showed more reproducible results with some of the additives inducing morphology changes in crystallisations from ethanol. None of the polymer additives used displayed an effect on crystal morphology of IZN. In contrast to crystallisations of SA in the presence of very low concentrations of polymer additives presented in Chapter 4, higher concentrations of structurally similar and size-matched additives are required in order to induce an effect on the shape of the crystals.

One of the most reproducible findings in this work was the crystallisation of IZN in the presence of 4,4'-bipyridyl (44BP) in which elongated crystals were produced from both evaporative and cooling crystallisation from ethanol. This presented a large change in crystal morphology from the plate-like crystals produced in the presence of no additive; its favourability was demonstrated by the reproducible nature of the morphology change. Face indexing was carried out to compare the most dominant faces present in the plate-like morphology produced from ethanol with no additives and the elongated morphology produced with 44BP present in solution. It was found that in the presence of the 44BP additive, the slow growing faces change and it is suggested that the $(0\bar{1}\bar{2})$ and $(0\bar{1}2)$ faces in the elongated crystals are those with which the additive may be interacting.

Identification of the functional groups present on the surface of the slow growing faces of the elongated crystals allowed a possible mechanism to be constructed. The action of the 44BP additive may proceed through the molecule mimicking the interaction of the

pyridine ring of the IZN molecule with the amine N-H bond of the IZN molecules. The 44BP molecule does not feature any hydrogen bond donor groups and as a result, prevents the addition of further IZN molecules interacting with the growing face whilst the molecule is occupying the site. Many of the structurally similar additive molecules used feature a pyridine ring, but in contrast to 44BP they also contain a hydrogen bond donor group in the form of an acid or amide group. This difference could have been a factor in the limited success of the structurally similar compounds suggesting that they are “too” structurally similar to IZN to have an effect and do not inhibit the addition of further IZN molecules interacting with the crystal surface. This study has emphasised that the design of additives for growth inhibition still largely relies on trial-and-error methods.[39] However, gaining an understanding of the molecular level interactions enabling this change in shape may aid the design of future additives for a more desirable effect on the crystal morphology of IZN.

Additives were also added to crystallisations of IZN in equimolar quantities and some of these crystallisations produced multi-component complexes of the two starting materials rather than an additive effect on the morphology of the starting material. These experiments confirm that additives must be used in low enough concentrations to prevent compromising the purity of the product by producing mixed component systems. The potential for complex formation must be considered when attempting to induce morphology change using size-matched additives.

Chapter 7

Molecular complexes of piroxicam

Solubility measurements made by the author and presented in this chapter were included in part in the following journal article:

L. H. Thomas, A. R. Klapwijk, C. Wales and C. C. Wilson, Intermolecular hydrogen transfer and solubility tuning in multi-component molecular crystals of the API piroxicam. *CrystEngComm*, 2014, 16 (26), 5924 – 5932.

7.1 Introduction and aims

Piroxicam (PX) is a non-steroidal anti-inflammatory drug (NSAID) used for the treatment of inflammatory diseases, relieving the symptoms of rheumatoid arthritis and osteoarthritis.[189] It is well reported in the literature that PX exists in different ionisation states in the solid state. Figure 7.1a shows the non-ionised tautomer of PX (PXN) in which the conformation is locked by an O-H···O intramolecular hydrogen bond. Intramolecular hydrogen transfer of the hydroxyl hydrogen atom to the nitrogen atom on the pyridine ring results in the formation of the zwitterionic tautomer of PX (PXZ) (Figure 7.1b), which is accompanied by a significant change in the conformation of the molecule about the amide bond, maximising the number and strength of charge assisted intramolecular N-H···O hydrogen bonds.[190] Charged forms of PX may also exist where intermolecular proton transfer has occurred (Figure 7.1c and d). In the case of the protonated PX molecule (PX^+), where both nitrogen atoms are protonated, the conformation of the PX molecule is the same as the neutral PX which is governed by an O-H···O intramolecular hydrogen bond. The opposite is true for the deprotonated PX molecule (PX^-), in which a single N-H···O intramolecular hydrogen bond is present and the conformation resembles that of PXZ with the exception of the rotation of the pyridine ring.

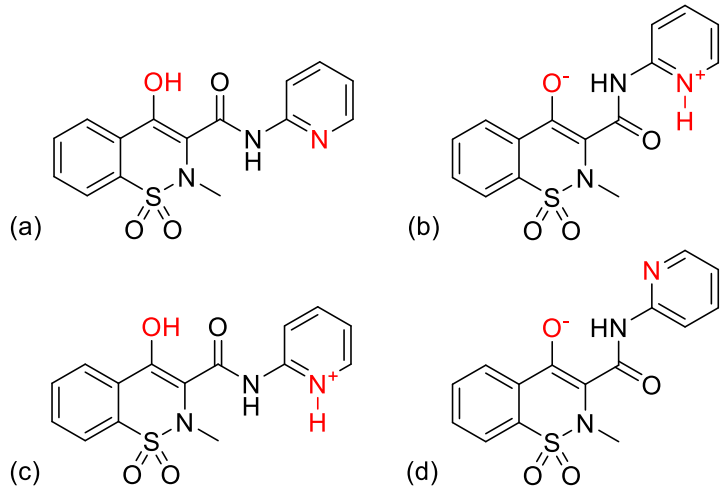

Figure 7.1 - The different possible configurations of the piroxicam molecule with the sites relevant to the tautomerism and proton transfer in each case shown in red.[190]

The tautomeric form and conformation of PX may also be distinguished based on the colour of the material whereby PX present in its non-ionised form is characteristically white and PX present in its zwitterionic form is yellow in colour.[191]

As for many active pharmaceutical ingredients (APIs), PX is polymorphic – the ability for the same molecule to occupy different packing arrangements in the solid state. There are currently four fully structurally-characterised polymorphic forms reported; PX exists in its non-ionised state in forms I, II and III. The structure of form IV has recently been published by Thomas *et al.* and adopts an unusual mixed ionic state, featuring five PX molecules in the asymmetric unit, four of which are present as the non-ionised tautomer and one in the zwitterionic state.[48] A new multi-component ("templated" crystallisation) route to producing single crystals of form III, previously solved only from PXRD data,[192] was also reported. Furthermore, PXRD data of other new PX forms were recently published by Nyström *et al.* in an electrospray study[193] and Lavrič *et al.* as part of a study on PX polymorphs using ^{14}N nuclear quadrupole resonance analysis and a range of other, non-crystallographic, analytical techniques.[194] A purely zwitterionic polymorph of PX remains unreported, although this tautomer has been observed in form IV (coexistent with the neutral form), the monohydrated form[195] and other solvated forms, and in molecular complexes.

PX is known for possessing low aqueous solubility at physiological pH.[191] Poor aqueous solubility can impact the bioavailability of an active pharmaceutical ingredient and so new crystalline forms may be desirable for access to improved properties. There are thus

many previously reported co-crystals and salts of PX, a large proportion of which include co-formers containing the carboxylic acid functionality such as substituted benzoic acids[196,197] and dicarboxylic acids.[191] Molecular complexes of PX with *N*-heterocycles and haloanilic acids have also recently been reported,[190] as well as an extensive screening of the effect of co-former and crystallisation conditions on the formation of multi-component molecular complexes of PX.[198] The study also reports several solid forms from crystallisations with trimesic acid (TA), also used in this study; however, as it was part of an extensive screening investigation, full structural characterisation of these PX TA complexes was not reported. There are also several solvates of PX reported, including with *p*-dioxane,[191] acetic and isobutyric acid[199] as well as with methanol.[48] The driving force for the tautomeric form adopted in the solid state is unclear and it has been suggested that the pK_a of the co-former may affect the outcome. Wales *et al*. grouped co-formers based on their pK_a value and found that the co-formers with the lowest or highest pK_a values resulted in complexes with the zwitterionic tautomer of PX.[197] The rare phenomenon of tautomeric polymorphism has also been observed in molecular complexes of PX. Examples include the multi-component complexes of PX with 4-hydroxybenzoic acid[191] as well as with 2-, 3- and 4-fluorobenzoic acid.[197] Such examples present an exception to observations and predictions based on pK_a.

7.1.1 Structural targets and design strategy

This work aims to produce layered solid-state molecular systems of PX in which molecular disorder is present; in particular, the approach adopted targets situations where a whole molecule or part of a molecule in a structure adopts different orientations in different unit cells, with the potential to create void spaces in the structure. Such structural attributes may introduce desired properties such as compressibility through slippage of the layers, or the enhanced solubility often observed in disordered molecular materials. Symmetrical, planar co-former molecules were selected for use in multi-component crystallisation with this target in mind. Some of the resulting complexes also have interesting thermal properties which will be presented. Figure 7.2 shows the molecular structure of the co-formers used in this study. Although use of GRAS compounds was desirable in this work, some non-GRAS compounds were also used to provide a strong synthon set.

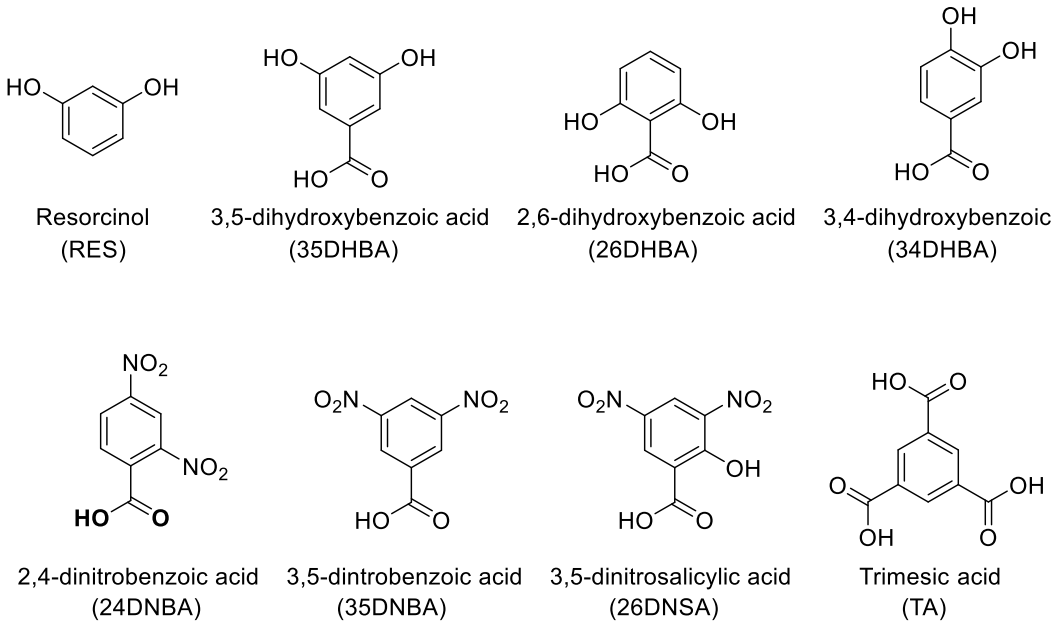

Figure 7.2 - Molecular structure of each co-former used.

7.2 Experimental information

All of the compounds and solvents used were obtained from commercial sources and used without further purification.

7.2.1 Preparation of single crystals and structural information

All single crystals suitable for X-ray diffraction were produced using evaporative crystallisation with the exception of the crystal used to determine the structure of the piroxicam trimesic acid complex, which was accessed *via* a phase transition (see below). A small quantity of each component was dissolved in a solvent and left to evaporate slowly at room temperature, on temperature controlled hot plates or in the refrigerator. Crystallisations were prepared for a range of solvents, temperatures and starting material stoichiometries. Data were collected using three laboratory Rigaku Oxford Diffraction diffractometers: the Gemini A Ultra, Supernova and Xcalibur. In addition, synchrotron radiation was used in the determination of one of the structures. A detailed description of the preparation of single crystals and the data collection method used for each complex is outlined below. All of the structures were solved by direct methods using SHELXS-2013[137] and refined using SHELXL-2013[138] within the WinGX[139,140] program. Crystallographic data are shown in Table 7.1.

(1) Piroxicam trimesic acid acetone (1:1:1) (PXZ TA ACT)

PX (0.020 g) and TA (0.013 g) were combined in a 1:1 molar ratio and dissolved in acetone. Slow evaporation at room temperature yielded yellow plate-like crystals. Data were collected using the Rigaku Oxford Diffraction SuperNova diffractometer with Mo K_α radiation at 100 K.

(2) Piroxicam trimesic acid acetonitrile (1:1:1) (PXZ TA ACN)

PX (0.020 g) and TA (0.013 g) were combined in a 1:1 molar ratio and dissolved in acetonitrile. Slow evaporation at room temperature yielded yellow elongated plate-like crystals. Data were collected using the Rigaku Oxford Diffraction Gemini Ultra A CCD diffractometer with Mo K_α radiation at 100K. Dynamic disorder of the methyl group on the acetonitrile molecule in this structure could not be resolved and therefore the hydrogen atoms were placed in an idealised position based on a riding model.

(3) Piroxicam trimesic acid (1:1) (PXN TA)

Attempts to obtain the desolvated form at ambient conditions were unsuccessful and this complex could only be obtained by desolvation of either solvate (**1**) or (**2**). A reasonable structural model of the desolvated form was obtained by slow heating of the solvated single crystals to 140 °C using a Mettler Toledo FP82 temperature controllable stage, cooling to room temperature and transferring a crystal to a Rigaku Oxford Diffraction SuperNova diffractometer and collecting the data at 100 K. These small and weakly scattering crystals gave a twinned diffraction pattern which may have been caused by splitting of the crystal during the phase transition or when subject to the cryostream. As a result, data of higher quality were collected using synchrotron radiation at the Advanced Light Source, Berkeley, USA, where *in-situ* heating could be carried out. A single crystal of PXZ TA ATN was mounted at room temperature and the temperature was ramped at 360 K hr^{-1} to 390 K followed by a further ramp to 420 K at 120 K hr^{-1}. The sample was then cooled to room temperature, but this led to loss of crystallinity of the sample. A cluster of crystals were then mounted at room temperature and these were heated to 390 K at 360 K hr^{-1} then to 420 K at 120 K hr^{-1}. A single crystal was selected from the cluster of crystals and re-mounted at room temperature. The crystal was then cooled to 100 K *in-situ* and a full data collection carried out at 2 second exposure time. An incident radiation of wavelength 0.9538 Å (13 keV) was used.

(4) Piroxicam 3,5-dihydroxybenzoic acid (1:1) (PXZ 35DHBA)

PX (0.021 g) and 35DHBA (0.010 g) were combined in a 1:1 molar ratio and dissolved in acetonitrile. Slow evaporation at 30 °C yielded yellow plate-like crystals. Data were collected using the Rigaku Oxford Diffraction Gemini Ultra A CCD diffractometer with Mo K_α radiation at 100 K.

(5) Piroxicam resorcinol (1:1) (PXZ RES)

PX (0.021 g) and RES (0.014 g) were combined in a 1:2 molar ratio and dissolved in a mixed solvent of acetonitrile and methanol in a 1:1 v/v ratio. Slow evaporation of solvent at 50 °C yielded yellow block crystals within a multi-phase sample. Data were collected using the Rigaku Oxford Diffraction Gemini Ultra A CCD diffractometer with Mo K_α radiation at 100 K.

(6) Piroxicam 3,4-dihydroxybenzoic acid acetonitrile (2:1:2) (PXZ 34DHBA ACN)

PX (0.020 g) and 34DHBA (0.009 g) were combined in a 1:1 molar ratio and dissolved in acetonitrile. Slow evaporation at room temperature yielded yellow plate-like crystals. Data were collected using the Rigaku Oxford Diffraction Xcalibur diffractometer with Mo K_α radiation at 150 K. All hydrogen atoms on the 3,4-dihydroxybenzoic acid molecule were placed in an idealised position based on a riding model.

(7) Piroxicam 3,5-dinitrobenozic acid (1:1) (PXN 35DNBA)

PX (0.025 g) and 35DNBA (0.032 g) were combined in a 1:2 molar ratio and dissolved in a mixture of methanol and acetonitrile (1:1 v/v). Slow evaporation at 40 °C yielded colourless plate-like crystals. Data were collected using the Rigaku Oxford Diffraction SuperNova diffractometer with Cu K_α radiation at 150 K. The hydrogen atoms of the methyl group on the PX molecule were placed in an idealised position based on a riding model.

(8) Piroxicam 3,5-dinitrosalicylic acid (1:1) (PX^+ $35DNSA^-$)

PX (0.021 g) and 35DNSA (0.014 g) were combined in a 1:1 molar ratio and dissolved in a mixture of methanol and acetonitrile (1:1 v/v mixture). Slow evaporation at room temperature yielded colourless prism crystals. Data were collected using the Rigaku Oxford Diffraction Xcalibur diffractometer with Mo K_α radiation at 150 K. An aromatic hydrogen atom on the PX molecule was placed in an idealised position based on a riding model.

(9) Piroxicam 2,4-dinitrobenzoic acid acetonitrile (1:1:1) (PX^+ $24DNBA^-$ ACN)

PX (0.020 g) and 24DNBA (0.026 g) were combined in a 1:2 molar ratio and dissolved in acetonitrile. Slow evaporation at room temperature yielded colourless plate-like crystals. Data were collected using the Rigaku Oxford Diffraction Xcalibur diffractometer with Mo K_α radiation at 150 K.

(10) Piroxicam 2,6-dihydroxybenzoic acid (1:1) (PX^+ $26DHBA^-$)

PX (0.020 g) and 26DHBA (0.009 g) were combined in a 1:1 molar ratio and dissolved in a 1:1 mixture of acetonitrile and methanol. Slow evaporation at 50 °C yielded colourless block-like crystals. Data were collected using the Rigaku Oxford Diffraction SuperNova diffractometer with Cu K_α radiation at 150 K. In the refinement of this crystal structure, additional electron density was observed in a site that would occupy a disordered sulphur atom, however modelling of this low level of disorder was not possible and as a result the nearby methyl hydrogen atoms on the PX molecule were placed in an idealised position based on a riding model.

Table 7.1 - Crystallographic data for PX molecular complexes. (For structure 6 formula is displayed as the formula of the asymmetric unit (1:½:1)).

	1	2	3	4	5	6	7	8	9	10
Code	PXZ TA ACT	PXZ TA ACN	PXN TA	PXZ 35DHBA	PXZ RES	PXZ 34DHBA ACN	PXN 35DNBA	PX^+ $35DNSA^-$	PX^+ $24DNBA^-$ ACN	PX^+ $26DHBA^-$
Formula	$(C_{15}H_{13}N_3O_4S_1)$ $(C_9H_6O_6)$ $(C_3H_6O_1)$	$(C_{15}H_{13}N_3O_4S_1)$ $(C_9H_6O_6)$ $(C_2H_3N_1)$	$(C_{15}H_{13}N_3O_4S_1)$ $(C_9H_6O_6)$	$(C_{15}H_{13}N_3O_4S_1)$ $(C_7H_6O_4)$	$(C_{15}H_{13}N_3O_4S_1)$ $(C_6H_6O_2)$	$(C_{15}H_{13}N_3O_4S_1)$ $(C_{3.5}H_3O_2)$ $(C_2H_3N_1)$	$(C_{15}H_{13}N_3O_4S_1)$ $(C_7H_4O_6N_2)$	$(C_{15}H_{14}N_3O_4S_1)^+$ $(C_7H_3O_7N_2)^-$	$(C_{15}H_{14}N_3O_4S_1)^+$ $(C_7H_3O_6N_2)^-$ $(C_2H_3N_1)$	$(C_{15}H_{14}N_3O_4S_1)^+$ $(C_7H_5O_4)^-$
M / g mol^{-1}	599.56	582.53	541.48	485.46	441.46	449.46	543.47	559.46	584.52	485.46
T (K), radiation	100, Mo Kα	100, Mo Kα	100, λ 0.9538	100, Mo Kα	100, Mo Kα	150, Mo Kα	150, Cu Kα	150, Mo Kα	150, Mo Kα	150, Cu Kα
Space Group	$P\bar{1}$	$P\bar{1}$	$P\bar{1}$	$P\bar{1}$	$P\bar{1}$	$P\bar{1}$	$P2_1/n$	$P\bar{1}$	$P\bar{1}$	$P2_1/n$
a (Å)	9.0646(5)	9.3683(4)	9.3590(19)	7.0479(2)	6.6762(3)	7.1470(4)	6.8053(5)	9.5770(5)	6.9668(4)	15.1189(3)
b (Å)	9.9522(5)	10.0228(4)	11.184(2)	11.7553(5)	11.9985(5)	9.1033(6)	22.5979(13)	9.7461(6)	13.0247(11)	6.83600(10)
c (Å)	15.1176(10)	14.6673(6)	11.811(2)	13.3003(5)	12.7345(7)	16.4368(12)	14.6305(11)	12.6681(6)	14.7179(9)	21.5103(4)
α (°)	94.481(5)	104.190(4)	87.54(3)	92.212(3)	86.123(4)	77.813(6)	90	81.441(5)	74.731(6)	90
β (°)	105.869(5)	99.078(4)	69.79(3)	93.190(3)	79.714(4)	81.110(5)	97.638(7)	74.536(4)	80.328(5)	104.826(2)
γ (°)	90.114(4)	97.587(4)	85.46(3)	106.217(3)	77.022(4)	83.186(5)	90	85.779(5)	75.802(6)	90
Volume ($Å^3$)	1307.43(13)	1297.33(10)	1156.4(5)	1054.76(7)	977.65(8)	1028.64(12)	2230.0(3)	1126.21(11)	1241.35(16)	2149.14(7)
Z	2	2	2	2	2	2	4	2	2	4
ρ_{cal}/ Mg cm^{-3}	1.523	1.491	1.555	1.529	1.500	1.451	1.619	1.650	1.564	1.500
μ/mm^{-1}	0.195	0.192	0.453	0.212	0.213	0.205	1.949	0.222	0.204	1.845
θ range/°	3.57-25.68	2.80-25.68	2.45-35.56	3.17-25.68	3.18-26.23	3.32-25.68	3.91-70.06	3.37-25.68	3.50-25.68	4.12-70.06
Completeness	99.7 %	99.9 %	99.9 %	99.9 %	99.6 %	99.8 %	99.8 %	99.8 %	99.7 %	99.8 %
Refln. Collected	10358	15394	11675	16673	6857	7900	11084	8163	9440	8209
Independent	4952	4924	4385	4006	3916	3894	4225	4272	4700	4058
Refln (obs.I>2σ(I))	3999	4236	2875	3523	3262	2888	3290	3569	3789	3787
Rint	0.041	0.027	0.054	0.027	0.026	0.030	0.055	0.021	0.025	0.024
Parameters	479	447	419	383	356	386	399	416	450	372
GooF	1.062	1.034	1.026	1.045	1.051	1.032	1.116	1.040	1.043	1.101
R_1 (obs)	0.048	0.034	0.052	0.030	0.038	0.050	0.078	0.043	0.043	0.057
R_1 (all)	0.065	0.041	0.096	0.036	0.050	0.075	0.100	0.053	0.059	0.060
wR_2 (all)	0.102	0.089	0.118	0.079	0.099	0.1138	0.204	0.104	0.098	0.159
$\rho_{max,min}$/e $Å^{-3}$	0.277, -0.454	0.343, -0.445	0.282, -0.388	0.354, -0.425	0.350, -0.437	0.241, -0.348	1.316, -0.662	0.578, -0.402	0.367, -0.416	1.561, -0.550

7.2.2 Other preparation methods of PX TA complexes

Experiments using other crystallisation methods such as grinding, solution mediated (slurrying) and cooling were carried out in attempt to prepare multi-component complexes of PX and TA in the larger quantities required for subsequent heating and vapour diffusion experiments.

7.2.2.1 Grinding

Dry and liquid assisted grinding experiments were carried out manually using a mortar and pestle. In the case of liquid assisted grinding, several drops of solvent were added during grinding. In each experiment the starting materials were combined in an equimolar quantity and ground together for a defined period of time; Table 7.2 outlines all other experimental information.

Table 7.2 - Experimental conditions for grinding experiments of PX and TA.

Mass of PX (g)	Mass of TA (g)	Solvent	Vol. of solvent	Time grinding (mins)
0.010	0.006	Acetone	2 drops	10
0.010	0.006	Acetonitrile	2 drops	10
0.010	0.060	-	-	5
0.010	0.064	-	-	10

7.2.2.2 Rapid cooling crystallisation

Initial cooling crystallisations were carried out using a rapid cooling method. In each experiment the starting materials were combined in equimolar quantities and dissolved in the specified solvent to produce a saturated solution. The vial was then transferred to an ice bath to facilitate rapid cooling of the solution and subsequent crystallisation. Table 7.3 summarises the experimental conditions used.

Table 7.3 - Experimental conditions for rapid cooling experiments of PX and TA.

Mass of PX (g)	Mass of TA (g)	Ratio	Solvent*	Vol. of solvent (ml)
0.040	0.026	1:1	Acetone	5
0.040	0.026	1:1	Acetonitrile/ methanol	5

*in the case of mixed solvents, 1:1 v/v mixtures were used.

7.2.2.3 Controlled cooling crystallisation

After rapid cooling experiments, small-scale controlled, cooling crystallisations were carried out in 20 ml vials using the Cambridge Reactor Design Polar Bear Plus

crystalliser. A linear cooling profile of 50°C to 5°C at 0.5 °C min^{-1} was used employing magnetic bottom stirring at a stirring speed of 350 rpm.

Table 7.4 - Experimental conditions for controlled cooling experiments of PX and TA.

Mass of PX (g)	Mass of TA (g)	Ratio	Solvent*	Vol. of solvent (ml)
0.08	0.050	1:1	Acetone	10
0.08	0.050	1:1	Acetonitrile/ methanol	10
0.04	0.014	2:1	Acetonitrile/ methanol	5
0.04	0.050	1:2	Acetonitrile/ methanol	5

*in the case of mixed solvents, 1:1 v/v mixtures were used unless otherwise specified.

7.2.2.4 Solution mediated (slurrying)

Equimolar quantities of PX and TA were weighed into 20 ml vials and a specified quantity of solvent was added. The slurries were stirred using magnetic bottom stirring (150 rpm) at a constant temperature of 20 °C maintained using the Cambridge Reactor Design Polar Bear Plus. The product was filtered and the solid form characterised using PXRD. Table 7.5 summarises the conditions used for each experiment.

Table 7.5 - Experimental conditions for slurrying experiments of PX and TA.

Mass of PX (g)	Mass of TA (g)	Solvent*	Vol. of solvent (ml)	Time stirring (hours)
0.150	0.095	Acetone	2	1
0.150	0.095	Acetone	2	4.5
0.150	0.095	Acetone	4	14
0.150	0.095	Acetonitrile	2	1
0.150	0.095	Acetonitrile	2	4.5
0.150	0.095	Acetonitrile/ methanol	2	1
0.150	0.095	Acetonitrile/ methanol	2	4.5

*in the case of mixed solvents, 1:1 v/v mixtures were used.

7.2.3 Vapour diffusion experiments

Vapour diffusion experiments were carried out by placing a small quantity (~25 mg) of the crystalline powder in a vial which was then placed in a larger vial containing 1 ml of the chosen solvent. The larger vial was sealed with a lid as well as paraffin film allowing for slow diffusion of the solvent into the smaller vial at ambient conditions whilst preventing

vapour escaping from the vessel (Figure 7.3). PXRD, DSC and FTIR were used to confirm the solid form of the material following vapour diffusion.

Figure 7.3 - Experimental set-up for vapour diffusion experiments.

7.2.4 Analytical methods

Experimental information for analytical techniques used exclusively in the work in this chapter is outlined below. Experimental information for techniques relevant to other chapters is outlined in Chapter 3.

7.2.4.1 Variable temperature powder X-ray diffraction (VT-PXRD)

VT-PXRD was carried out at the I11 beamline at Diamond Light Source. A sample of PXZ TA ACT was heated to 140 °C at a rate of 360 K hr^{-1} and a PXRD pattern recorded at 1 °C intervals until the desolvation transition at which point the temperature was held at 140 °C.

7.2.4.2 Variable temperature Raman spectroscopy

A Renishaw inVia Raman Microscope along with a Mettler Toledo FP82 hot stage was used for the variable temperature Raman spectroscopy measurements. Samples were heated at a rate of 10 °C min^{-1} and spectra were taken every 10 °C from room temperature to 150 °C.

7.2.4.3 Solubility measurements

Solubility measurements of PX in ethanol and methanol were carried out using the Technobis Crystallization Systems Crystal16 at 1 ml scale. Vials containing different concentrations of PX were heated between temperatures of 5 °C and 75 °C using a

heating/cooling rate of 0.5 °C min^{-1}, with magnetic bottom stirring at 800 rpm employed. The data were analysed using CrystalClear software.[133]

7.3 Characterisation of PX starting material

Figure 7.4 shows an experimental PXRD pattern of the PX starting material, compared with calculated patterns of PX polymorphs and its monohydrate from the Cambridge Structural Database (CSD). The starting material is seen to be PX form I.

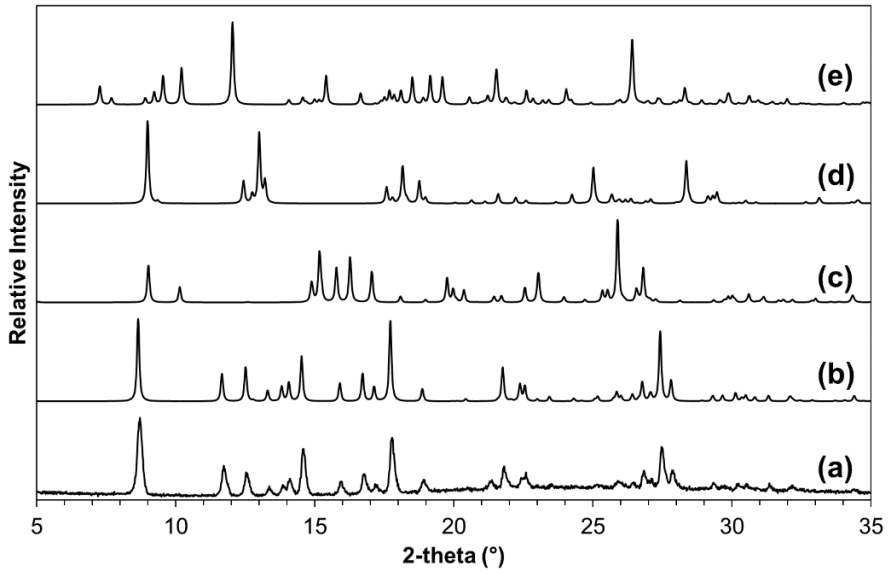

Figure 7.4 - PXRD patterns of PX: (a) raw material, (b) PX form I (BIYSEH04), (c) PX form II (BIYSEH06), (d) PX form III (BIYSEH07) and (e) PX monohydrate (CIDYAP01).

The solubility of PX was measured turbidometrically using the Technobis Crystallization Systems Crystal16 platform in two solvents: methanol and ethanol (Figure 7.5).[190]

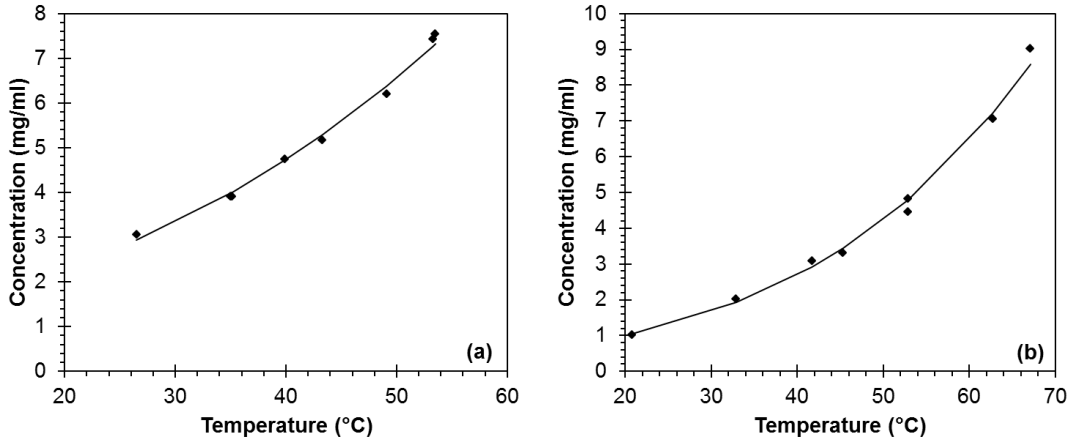

Figure 7.5 - Solubility curves of PX in (a) methanol and (b) ethanol with lines of fit based on a Van't Hoff functional form as a guide to the eye.

7.4 Solvates of a multi-component system of piroxicam with trimesic acid

Two solvates of a molecular complex of PX and TA with acetone and with acetonitrile as well as the desolvated form were produced. The structural results are complemented with thermal and spectroscopic analysis.

7.4.1 Structural comparison of solvates

Both PX-TA solvate co-crystals crystallise in the triclinic space group $P\bar{1}$ with the asymmetric unit containing one molecule each of PX, TA and acetone or acetonitrile. Intramolecular proton transfer from the hydroxyl group to the nitrogen atom of the pyridine ring on the PX molecule means that PX is present in its zwitterionic form in both solvates. The deprotonated oxygen atom forms an intramolecular electrostatic interaction with the nearby protonated nitrogen atom. Furthermore, the protonated nitrogen atom on the pyridine ring forms an electrostatic interaction with the carbonyl oxygen atom alongside it. These intramolecular interactions lock the conformation of the molecule.

In both solvates the PX molecules form a co-planar hydrogen bonded dimer unit held together by two N^{+}-H···O charge assisted hydrogen bonds. A TA molecule lies on either side of the PX dimer interacting through a charge assisted O-H···O^{-} hydrogen bond from the hydroxyl group on the TA molecule to the deprotonated hydroxyl group on the zwitterionic PX molecule. There is also a weak C-H···O interaction between the carbonyl oxygen atom on the carboxylic acid group of the TA molecule and the hydrogen atom on the pyridine ring of the PX molecule. These interactions allow the molecules to arrange themselves in a four molecule tetrameric hydrogen bonded unit, a common synthon present in zwitterionic PX complexes,[190,191,197] as well as in complexes of the related API tenoxicam.[200] In both solvates this synthon is planar with the exception of the methyl and sulfonyl groups of the PX molecules (and a slight rotation of the benzene ring on PX). Another common synthon, the carboxylic acid dimer, can be found in both structures linking one-dimensional zig-zag chains of TA molecules.

Although the two solvates both contain these common synthons they are not isostructural. In the acetone solvate, chains of TA molecules are disrupted by the formation of an O-H···O hydrogen bond between a carboxylic acid hydroxyl group on the TA molecule and the carbonyl oxygen atom on the acetone molecule (Figure 7.6). This hydrogen bond forms in preference to a carboxylic acid dimer between the two TA molecules, limiting the prospective chain to two TA molecules.

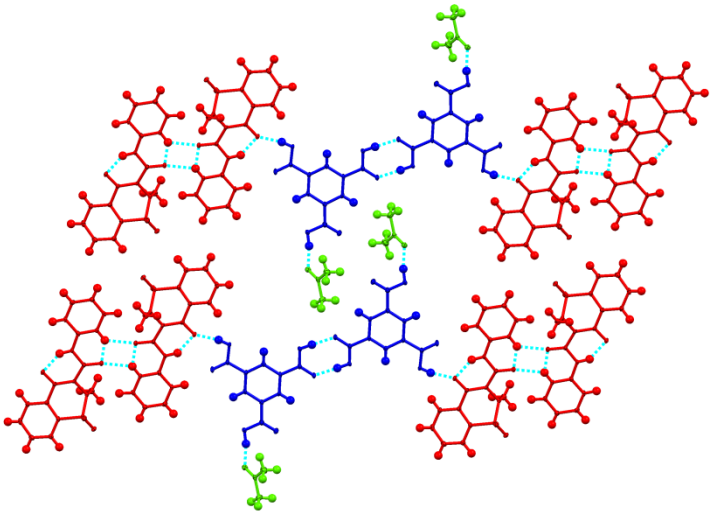

Figure 7.6 - Hydrogen bonded layers of molecules in the PXZ TA ACT solvate viewed down the crystallographic *b* axis. Colour coding shows the molecules of PXZ in red, TA in blue and acetone in green.

As a result of this interaction the methyl groups of the acetone molecule project out of the layers forming weak C-H···O bifurcated interactions with the nearby oxygen atom of the sulfonyl group on the PX molecule in the next layer. The layers stack offset to one another to allow space for the projecting methyl and sulfonyl groups and the acetone molecules (Figure 7.7). The acetone molecules therefore sit in pockets within the structure and do not form obvious connected channels.

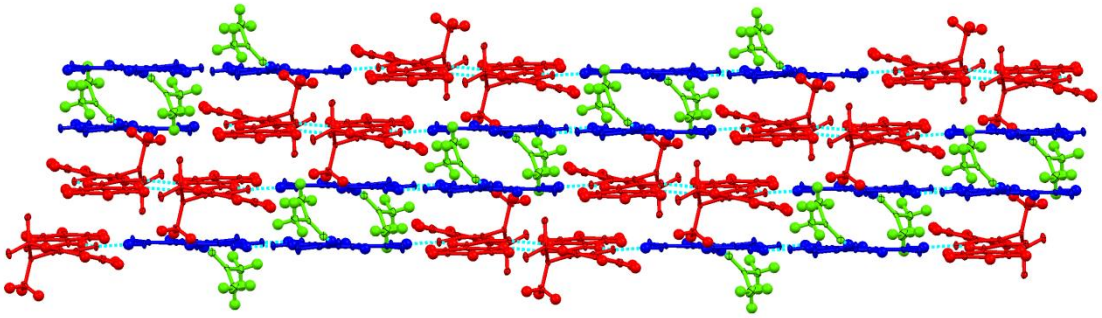

Figure 7.7 - Packing arrangement of the molecules in PXZ TA ACT viewed down the crystallographic *c* axis.

In contrast, in the acetonitrile solvate the molecules arrange themselves in a two-dimensional hydrogen bonded ribbon with the TA molecules forming infinite zig-zag chains which are linked to one another by hydrogen bonds to PX dimers. Unlike in the acetone solvate, the acetonitrile molecules do not form hydrogen bonds in the structure.

The acetonitrile molecules sit free in the void space created by the zig-zag arrangement of TA molecules (Figure 7.8).

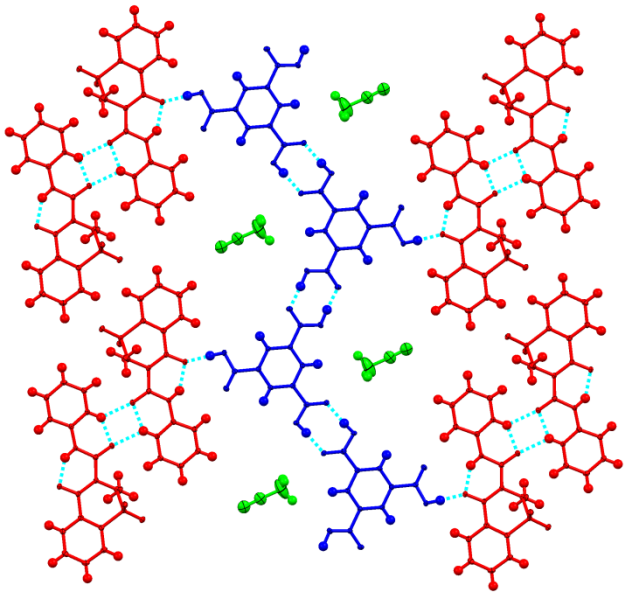

Figure 7.8 - Hydrogen bonded ribbons of molecules in PXZ TA ACN. Colour coding shows the molecules of PXZ in red, TA in blue and acetonitrile in green.

These ribbons make up infinite layers held together by weak interactions within the structure. As in the acetone solvate, offset stacking of these layers means that the gaps within the layers containing the solvent molecule form discrete pores instead of open channels (Figure 7.9). As well as hosting a solvent molecule, the pores accommodate the methyl and sulfonyl groups that lie out of the plane. The layers of tetrameric units have an interlayer distance of between 3.0 and 3.2 Å and are held together by weak interactions. Achieving layered forms was one of the aims of these co-crystallisation experiments – these weak interactions between the layers may encourage slippage and subsequently improve the compaction and solubility properties of the bulk material.

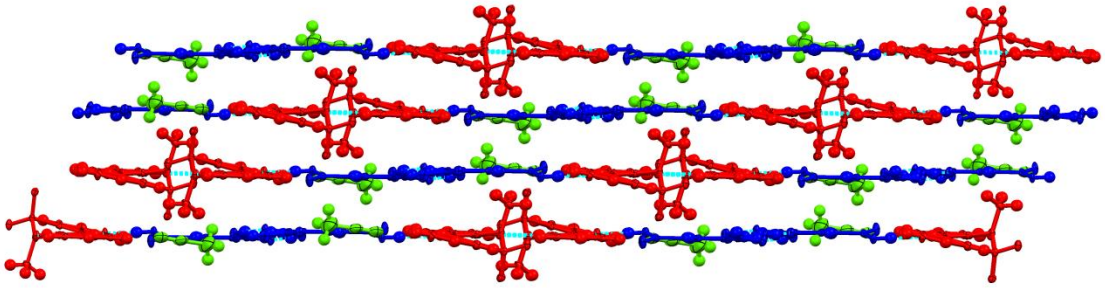

Figure 7.9 - Ribbons of molecules assembled in offset layers in PXZ TA ACN.

Table 7.6 - Hydrogen bonds in PXZ TA ACT (Å and °).

D-H···A	d(D-H)	d(H···A)	d(D···A)	<(DHA)
C(24)-H(6)···O(5)#1	0.91(3)	2.27(2)	3.143(3)	161.6(18)
C(14)-H(1)···O(9)#2	0.95(2)	2.50(2)	3.432(3)	168.9(17)
N(2)-H(5)···O(10)	0.91(3)	1.82(3)	2.623(2)	146(2)
N(1)-H(10)···O(11)	0.94(3)	1.84(3)	2.595(2)	136(3)
N(1)-H(10)···O(11)#3	0.94(3)	2.19(3)	2.875(3)	130(2)
C(27)-H(9)···O(11)#3	0.98(3)	2.53(2)	3.095(3)	116.5(16)
C(27)-H(9)···N(3)#3	0.98(3)	2.35(3)	3.311(3)	169.0(17)
O(4)-H(17)···O(10)#4	0.83(4)	1.75(4)	2.571(2)	169(3)
C(3)-H(18)···O(8)#5	0.96(2)	2.64(2)	3.522(3)	153.9(18)
O(3)-H(24)···O(2)#6	0.91(3)	1.73(3)	2.636(2)	177(3)
O(6)-H(25)···O(1)#7	0.97(3)	1.67(3)	2.641(2)	172(3)

Symmetry transformations used to generate equivalent atoms:
#1 x+1,y,z #2 -x,-y,-z+1 #3 -x,-y,-z+2 #4 x-1,y,z
#5 x,y+1,z #6 -x+1,-y+1,-z+2 #7 x,y,z+1

Table 7.7 - Hydrogen bonds in PXZ TA ACN (Å and °).

D-H···A	d(D-H)	d(H···A)	d(D···A)	<(DHA)
C(2)-H(1)···O(4)#1	0.961(19)	2.547(19)	3.0989(19)	116.6(14)
C(14)-H(9)···N(3)#2	0.933(18)	2.418(18)	3.343(2)	170.9(14)
C(14)-H(9)···O(2)#2	0.933(18)	2.591(16)	3.1341(19)	117.6(12)
C(11)-H(6)···O(5)#3	0.967(19)	2.258(19)	3.2006(19)	164.5(15)
N(2)-H(5)···O(1)	0.89(2)	1.82(2)	2.5792(17)	143.1(18)
N(1)-H(10)···O(2)	0.92(2)	1.91(2)	2.6206(16)	132.7(17)
N(1)-H(10)···O(2)#2	0.92(2)	2.17(2)	2.8852(17)	134.2(17)
O(6)-H(14)···O(1)#3	0.90(2)	1.64(2)	2.5378(15)	177(2)
O(7)-H(18)···O(8)#4	0.91(3)	1.72(3)	2.6246(15)	176(2)
O(10)-H(16)···O(9)#5	1.05(4)	1.54(3)	2.5878(15)	177(3)

Symmetry transformations used to generate equivalent atoms:
#1 -x,-y+1,-z+1 #2 -x+1,-y+2,-z+2 #3 -x,-y+2,-z+2
#4 -x+1,-y+2,-z+1 #5 -x+2,-y+3,-z+2

7.4.2 PXRD analysis of evaporative crystallisation

Figure 7.10 shows the PXRD patterns calculated from the single crystal XRD structure of each solvate and the corresponding measured pattern from the bulk material produced from evaporative crystallisation. In both cases, a good match between the two patterns is observed showing that the single crystal selected from the product of evaporative crystallisation is representative of the bulk material.

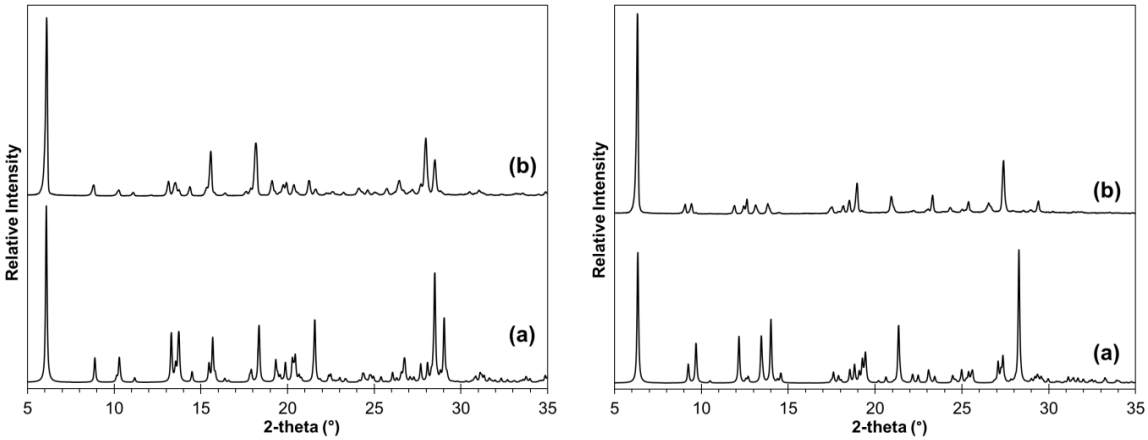

Figure 7.10 - PXRD patterns of (left) PXZ TA ACT and (right) PXZ TA ACN: (a) calculated from single crystal data and (b) measured from bulk product of evaporative crystallisation.

7.4.3 Transfer to other methods of crystallisation

Although the products of evaporative crystallisation showed phase purity, in order to produce the solvates of PX and TA in larger quantities for thorough investigations into their thermal behaviour, alternative methods of crystallisation for their production such as grinding, cooling and slurrying were tested.

7.4.3.1 Liquid assisted grinding using a mortar and pestle

Manual grinding in the presence of several drops of solvent was carried out in an attempt to produce the two solvates of PX previously produced by evaporative crystallisation. Figure 7.11 shows the PXRD patterns of the products of LAG with acetone (c) and with acetonitrile (d).

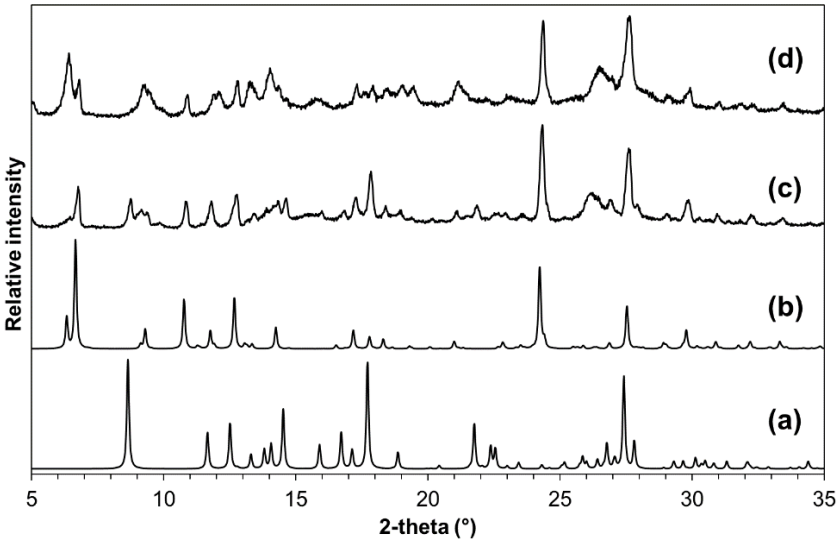

Figure 7.11 - PXRD patterns of (a) PX form I (BIYSEH04), (b) TA (BTCOAC), (c) product of LAG with acetone for 10 minutes and (d) product of LAG with acetonitrile for 10 minutes.

It can be concluded that LAG was unsuccessful as a method of producing both of the solvates and instead produced a physical mixture of the starting materials with broad diffraction peaks.

7.4.3.2 Cooling crystallisation

Cooling crystallisation was also investigated as a method to produce the complexes. Initial studies investigated rapid cooling crystallisation and this was followed by controlled cooling experiments. All samples obtained from these experiments were analysed using PXRD.

Figure 7.12 shows the PXRD patterns of the rapid and controlled cooling experiments with PX and TA in acetone. Both patterns match well with the reference pattern for the acetone solvate showing that the solvate can be prepared by cooling crystallisation at two different cooling rates, indicating its favourable formation.

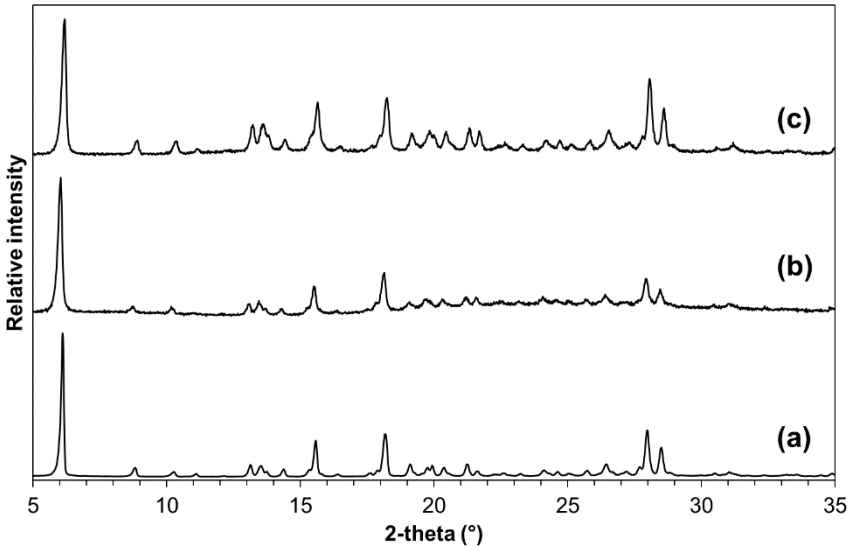

Figure 7.12 - PXRD patterns of (a) PXZ TA ACT reference, (b) rapid cooling of PX and TA (1:1) in acetone and (c) controlled cooling of PX and TA (1:1) in acetone.

Production of the acetonitrile solvate through cooling crystallisation was more challenging, these experiments producing poor quality PXRD patterns, as shown in Figure 7.13. There is evidence from the patterns that the solvate may have formed, however there are additional broad peaks that may result from residual starting materials or another solid form. Altering the ratio of the starting materials had little effect on the outcome; the resulting patterns (e), (f) and (g) correspond well with one another.

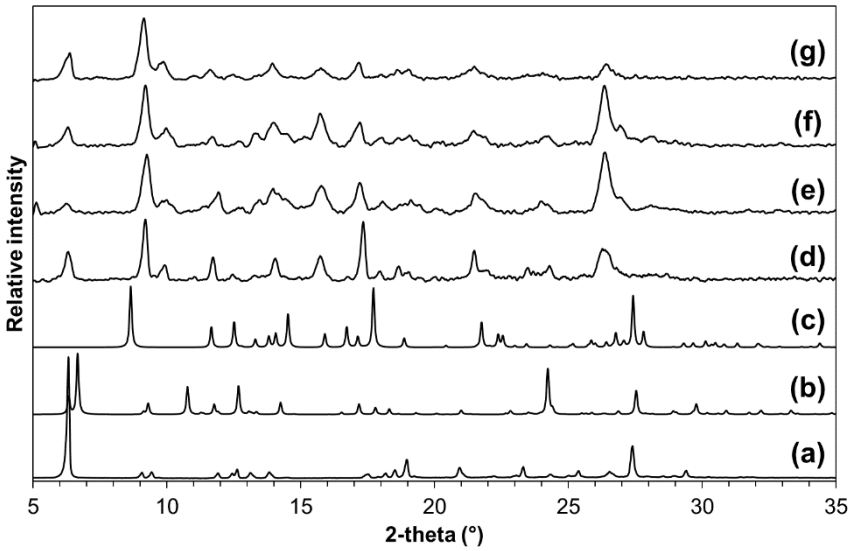

Figure 7.13 - PXRD patterns of (a) PXZ TA ACN reference, (b) TA (BTCOAC), (c) PX form I (BIYSEH04), (d) PX and TA (1:1) rapid cooling in acetonitrile, and controlled cooling in acetonitrile of: (e) PX and TA (1:1), (f) PX and TA (1:2) and (g) PX and TA (2:1).

7.4.3.3 Solution mediated (slurrying)

Crystallisation of multi-component materials can sometimes be facilitated by slurrying the two starting materials in a chosen solvent for a given amount of time. This method of crystallisation was more successful than the method of grinding or cooling for the production of the PXTA solvates. However, some optimisation of the conditions was required. Initially the starting materials were stirred in 2 ml of the solvent used for the evaporative crystallisations (acetone for the acetone solvate and acetonitrile/methanol mixture for the acetonitrile solvate) for one hour. The stirring time and quantity of solvent used was adjusted to produce the solvated materials.

Figure 7.14 shows the PXRD patterns produced from the slurrying experiments of PX and TA in acetone. After one hour of stirring the starting materials in acetone the solvated complex was produced, however more complete conversion was achieved after slurrying for a longer period of time (14 hours) in a larger quantity of solvent.

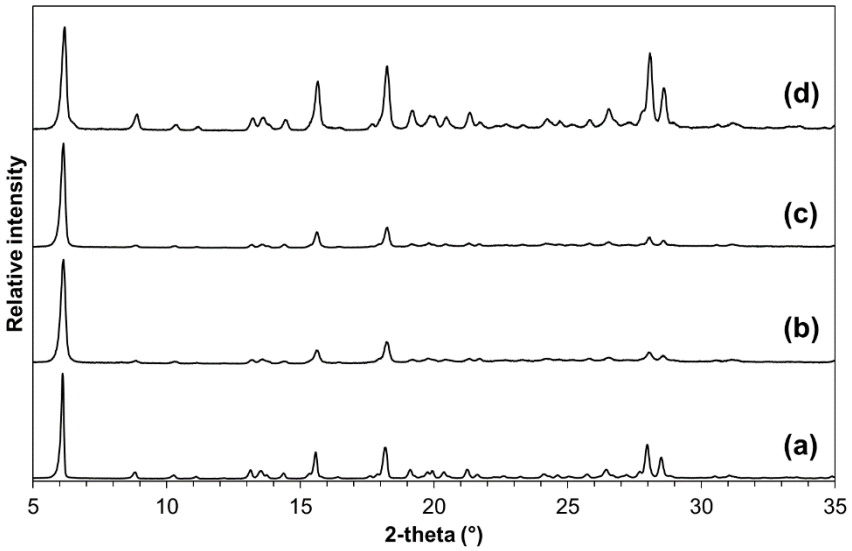

Figure 7.14 - PXRD patterns of products from slurrying experiments of PX and TA in acetone: (a) PXZ TA ACT reference from evaporative experiments, (b) slurrying for 1 hour, (c) slurrying for 4.5 hours and (d) slurrying for 14 hours.

For the acetonitrile solvate, slurrying was initially carried out in the crystallisation solvent used for evaporative crystallisations (1:1 mixture of acetonitrile and methanol). As shown in Figure 7.15, complete conversion to the solvate was achieved after one hour; however stirring for 4.5 hours produced a PXRD pattern with sharper peaks indicating more complete conversion and improved crystallinity.

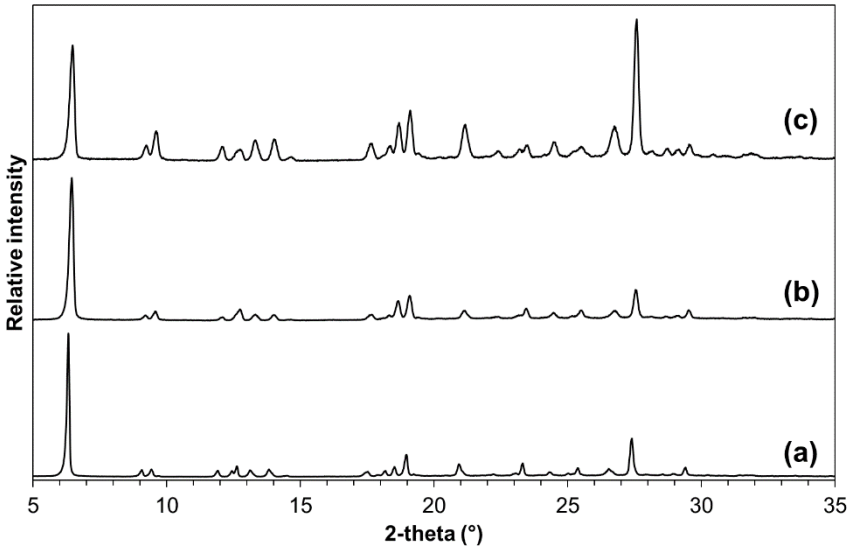

Figure 7.15 - PXRD patterns of products from slurrying experiments of PX and TA in acetonitrile:methanol (1:1) mixture (a) PXTA ACN reference from evaporative experiments, (b) slurrying for 1 hour and (c) slurrying for 4.5 hours.

In the evaporative and cooling crystallisations a solvent mixture of acetonitrile and methanol was required to facilitate the dissolution of the TA which showed poor solubility in acetonitrile. However, this means that the product could also potentially contain a methanol solvate of the two materials isostructural to the acetonitrile solvate. As slurrying does not require all of the starting materials to be completely dissolved in the slurrying solvent at once, additional experiments were carried out in pure acetonitrile. PXRD patterns from these experiments are shown in Figure 7.16. The patterns show that the desired acetonitrile solvate was successfully produced after one hour of slurrying. However, there is evidence of residual starting materials, with extra peaks corresponding to those in the patterns of the starting materials. Upon slurrying for a longer period of time, phase pure material was produced. This finding was beneficial for further analysis of the solvate as it provided pure PXZ TA ACN solvate and eliminated the possibility of the presence of an isostructural methanol solvate in the sample.

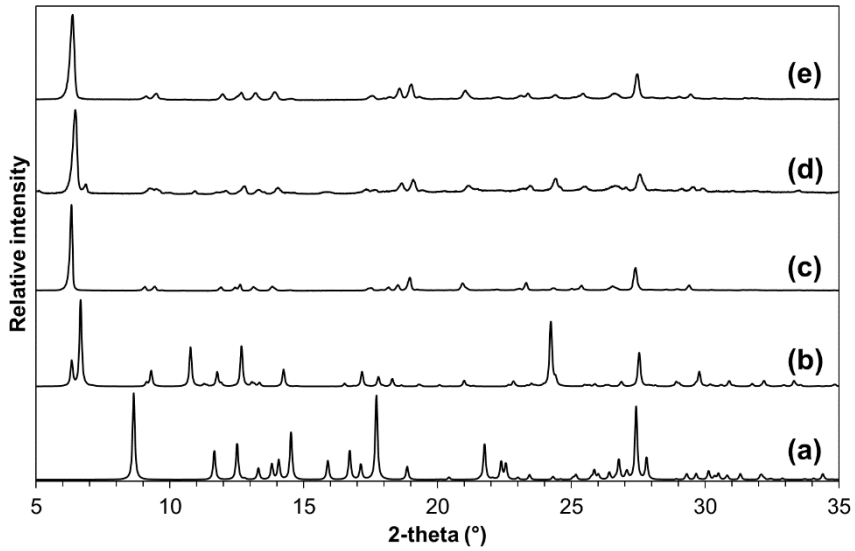

Figure 7.16 - PXRD patterns of slurrying experiments of PX and TA in acetonitrile: (a) PX form I (BIYSEH04), (b) TA (BTCOAC), (c) PXTA ACN reference from evaporative experiments, (d) slurrying for 1 hour and (e) slurrying for 4.5 hours.

7.4.4 Thermal Analysis

The thermal properties of both solvates were analysed using three complementary techniques, hot-stage microscopy (HSM), differential scanning calorimetry (DSC) and thermogravimetric analysis (TGA). HSM allowed for a visual representation of the thermal events. DSC and TGA heating profiles for each solvate are shown in Figure 7.17a and b.

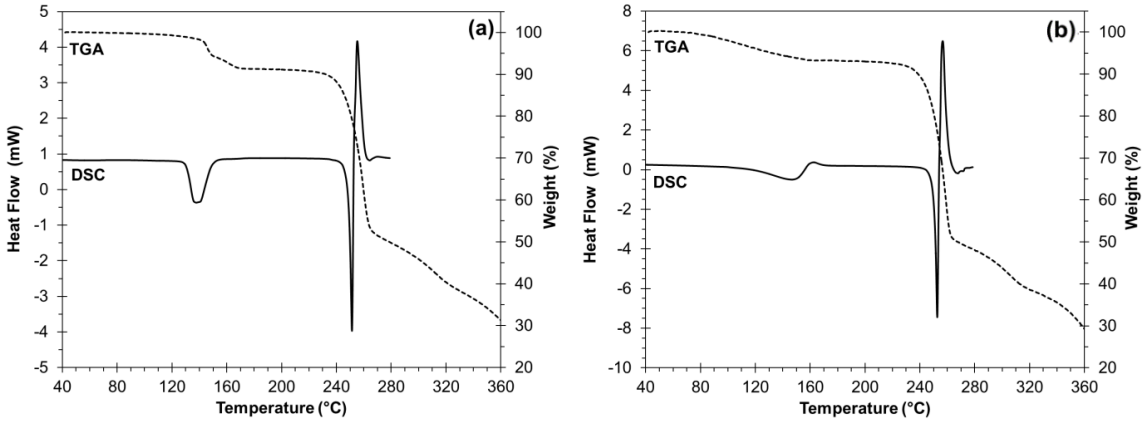

Figure 7.17 - DSC (exotherm up) and TGA traces of (a) PXZ TA ACT and (b) PXZ TA ACN.

A broad endothermic event is common to the DSC trace of each solvate indicating the loss of solvent from the complexes. It is worth noting that this temperature is much higher than the boiling points of the solvents which is typical when the solvent molecule is bound within the crystal lattice.[130] This solvent loss occurs in the range of 125-150 °C for the acetone solvate and appears to occur more gradually for the acetonitrile solvate (110-160 °C). These slight differences may be related to the different hydrogen bonding and subtleties of the situation of the solvent molecules within a very similar packing in the two solvate structures. Desolvation of the acetonitrile solvent is also followed by a small exothermic event which may represent a solid-solid phase transition. The results from the DSC correlate with those observed in the TGA patterns with a loss in mass of 8.70 % at 170 °C corresponding to one solvent molecule per asymmetric unit for acetone (theoretical = 9.69 %) and a loss in mass of 6.80 % at 160 °C corresponding to one solvent molecule per asymmetric unit for acetonitrile (theoretical = 7.05 %). Upon further heating a sharp endothermic event is observed with an onset temperature of 240 °C representing melting of the desolvated form, which is followed by an exothermic event at 255 °C, characteristic of a recrystallisation event. Following loss of the solvent molecule in the TGA, a second mass loss of 40 % for the acetone solvate and 42 % for the acetonitrile solvate occurs between 230°C and 270°C which correlates to the loss of one TA molecule per asymmetric unit (36.1%). This is immediately followed by the decomposition of PX and therefore the experimental mass loss is slightly more than the theoretical value due to the overlap of the mass loss and decomposition events. The events after the desolvation event are common to the DSC and TGA profiles of both solvates at the same temperature suggesting that upon loss of the solvent from the structure both complexes form the same desolvated form.

HSM images correlate with the events seen in the DSC and TGA traces (Figure 7.18 and Figure 7.19). However, for both solvates, the onset of desolvation is observed at a higher temperature than in the DSC traces: at 138 °C and 165 °C for the acetone solvate and the acetonitrile solvate, respectively.

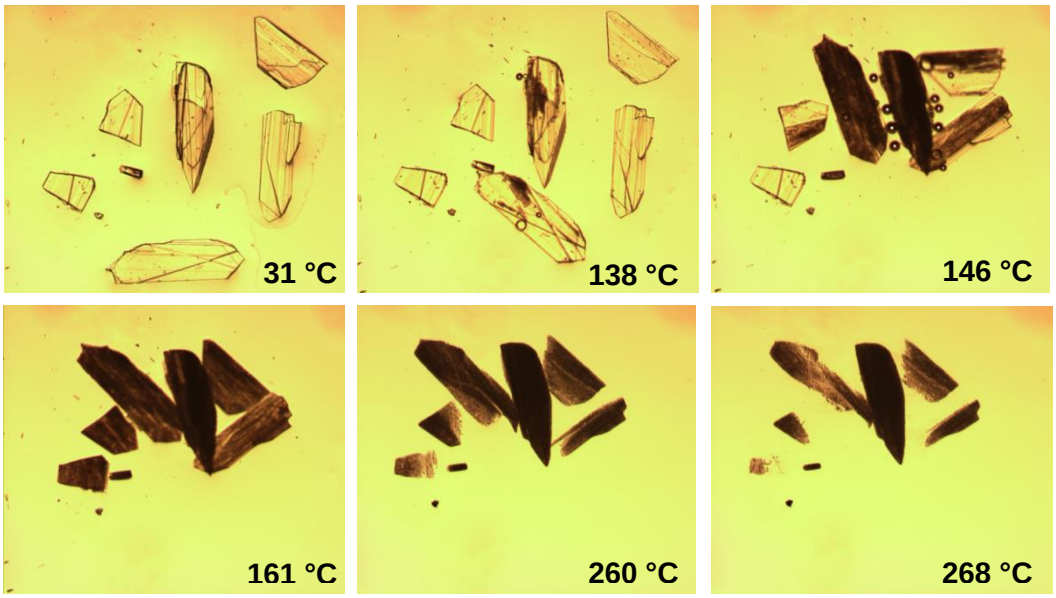

Figure 7.18 – HSM images of PXZ TA ACT solvate.

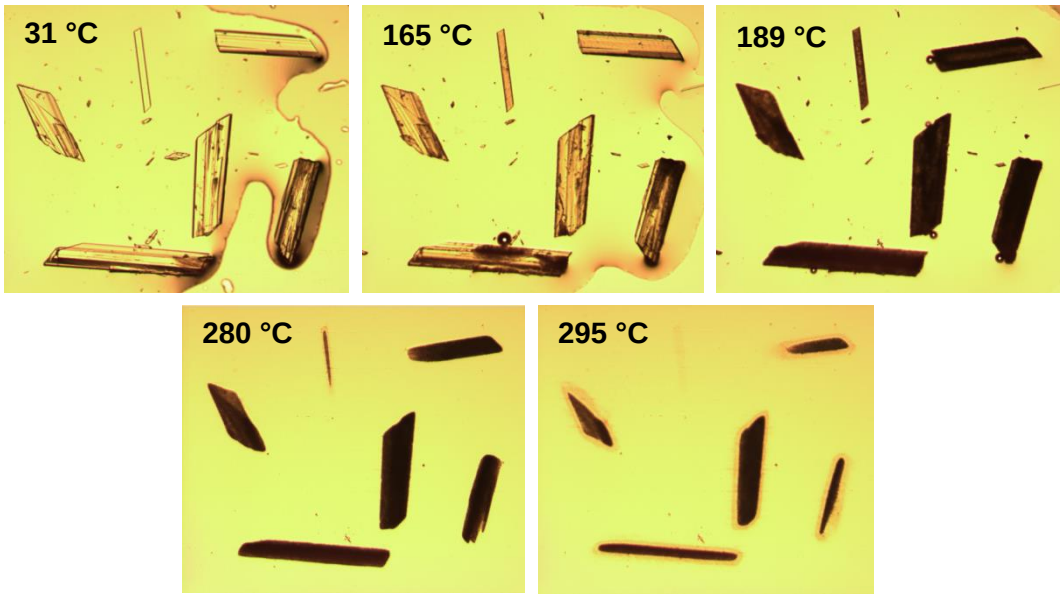

Figure 7.19 - HSM images of PXZ TA ACN solvate.

Bubbles of solvent are released in parallel to the crystals becoming opaque as the transition occurs across the crystals. This loss of transparency is common in stoichiometric solvates as the solvate forms multiple small crystallites of the desolvated form whilst maintaining its original shape.[201] Desolvation is then followed by melting and

recrystallisation which also occurs at a higher temperature than in the DSC traces. The recrystallisation event is observed clearly in the HSM image of a larger crystal of the acetonitrile solvate shown in Figure 7.20. Differences in the temperatures at which the thermal events occur in the DSC and the HSM may be a result of the nature of the sample and the different sample environments in the two techniques. The microcrystalline powder is confined in a sample pan for the DSC measurements whereas in HSM the single crystal is open to the environment.

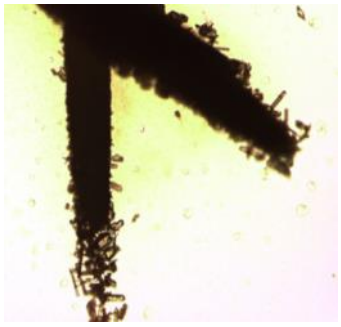

Figure 7.20 - HSM image capturing a recrystallisation event in crystals of the PXZ TA ACN complex.

It was possible to isolate the desolvated form of both solvates and a number of observations can be made about this desolvated phase. Firstly, DSC and TGA profiles of the desolvated form (Figure 7.21 a and b) no longer show evidence of a solvent loss event, suggesting that all of the solvent has been lost. The melting and recrystallisation events around 250 °C previously observed in the DSC for the solvated material are also present in the traces for the desolvated form.

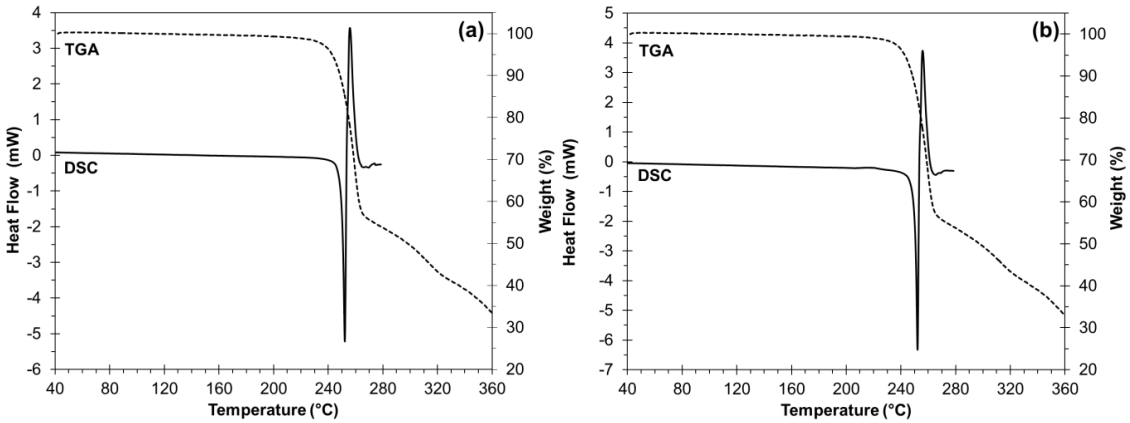

Figure 7.21 - DSC (exotherm up) and TGA traces after heating (a) PXZ TA ACT and (b) PXZ TA ACN.

Secondly, upon loss of the solvent from the complexes, crystallinity is maintained and unique diffraction peaks in the PXRD pattern suggest that the molecules rearrange to form a new crystal structure (Figure 7.22c). In addition, both solvates form the same desolvated form, producing the same PXRD pattern. Finally, upon heating a powder of each solvate, it is evident visually that the colour of the powder changes from yellow to white. As noted above, it is well reported in the literature[191,198] that the tautomeric form of PX present can be deduced from the colour of the material; the crystalline powder or single crystal is reported as yellow when the zwitterionic form is present and white (or colourless for single crystals) for the non-ionised form. The observed colour change suggests that upon desolvation there may be a change in the tautomeric form of the PX molecule in the complex. This would result in a large conformational change within the solid state, significantly altering the packing arrangement of the molecules.

Crystalline powders of the stable, desolvated form can be resolvated with either solvent (acetone, acetonitrile) by exposing the powder to solvent vapour at ambient conditions. The high volatility of acetone means that the vapour diffusion process occurred more quickly for this solvent than for acetonitrile using the same volume of solvent; after 24 hours colour change from white to yellow had occurred, resulting from acetone uptake into the structure. In the acetonitrile case, solvent induced conversion occurred more slowly; seven days were required for the transition to occur. TGA analysis of the resolvated samples (Figure 7.23 a and b) also shows that the same quantity of solvent is reabsorbed by the material with a mass loss of 9.70 % at 150 °C for the acetone solvate (theoretical = 9.69 %) and a mass loss of 6.73 % at 160 °C for the acetonitrile solvate (theoretical = 7.05 %). The DSC traces also show a broad endothermic event representing this solvent loss. This thermal event occurs between 100-150 °C for the acetone solvate, a lower onset temperature than the initial solvate which can also be noted from the desolvation temperature in the TGA. This may be a result of some loss of crystallinity of the substance following the phase transitions. For the acetonitrile solvate, desolvation occurs in the same temperature range as before, between 110-160 °C. The melting and recrystallisation events following desolvation in the DSC occur at the same temperature (onset: 140 °C) for each resolvated complex as observed previously. Upon resolvation, there is a clear colour change with the colour of the powder reverting from white back to yellow and the crystal structure returns back to its original form (Figure 7.22d and Figure 7.24). The possibility of resolvation is surprising since the solvent molecules do not sit in channels in either crystal structure, instead being positioned in discrete pockets within the structure. Furthermore, the acetone molecules in the acetone solvate are involved in the hydrogen bonding of the crystal structure. This

suggests that the mechanism of desolvation may be driven by a change in tautomeric form upon heating which allows for the solvent molecules trapped in these discrete pores to escape. Alternatively, the loss of the solvent molecules may allow freedom for the molecules to rearrange within the structure.

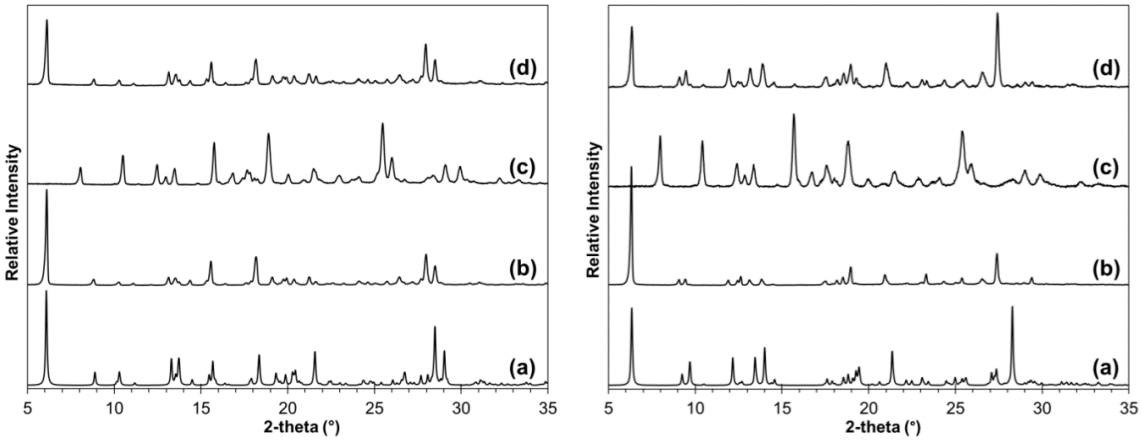

Figure 7.22 - PXRD patterns of (left) PXZ TA ACT and (right) PXZ TA ACN: (a) calculated from single crystal data, (b) measured from bulk product of evaporative crystallisation, (c) after heating sample b and (d) after vapour diffusion of sample c.

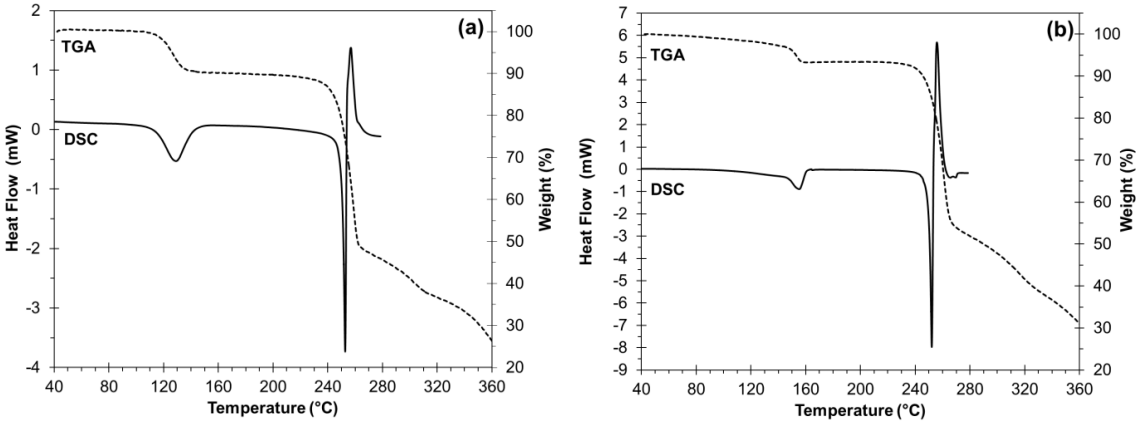

Figure 7.23 - DSC (exotherm up) and TGA traces of the desolvated form after vapour diffusion with (a) acetone and (b) acetonitrile.

Figure 7.24 - Photographs showing colour change of co-crystal upon heating and vapour diffusion.

Transitions between tautomeric forms within the solid state have been observed previously. For example, tautomeric polymorphs of the complex of PX with 2-fluorobenzoic acid were reported and it was shown that a transition from the zwitterionic form to the non-ionised form occurred upon heating,[197] however this was not reported as reversible. Based on the literature on tautomeric polymorphs of PX, attempts were made to prepare the desolvated form at ambient conditions using evaporative crystallisation; it has previously been reported that a small alteration in crystallisation conditions such as temperature[197] or solvent[191] may promote preferential growth of a tautomeric polymorph. However, these attempts were unsuccessful, yielding crystals of either starting materials or a solvate. The solvates were also placed under vacuum in search of a more gentle method of desolvation than heating; this was unsuccessful and heating was required in order for the solvent mediated transition to occur.

Dry grinding was also investigated as a possible route to the desolvated form of PX TA. Figure 7.25 shows the resulting PXRD patterns after dry grinding the two starting materials for 5 minutes (Figure 7.25d) and for 10 minutes (Figure 7.25e).

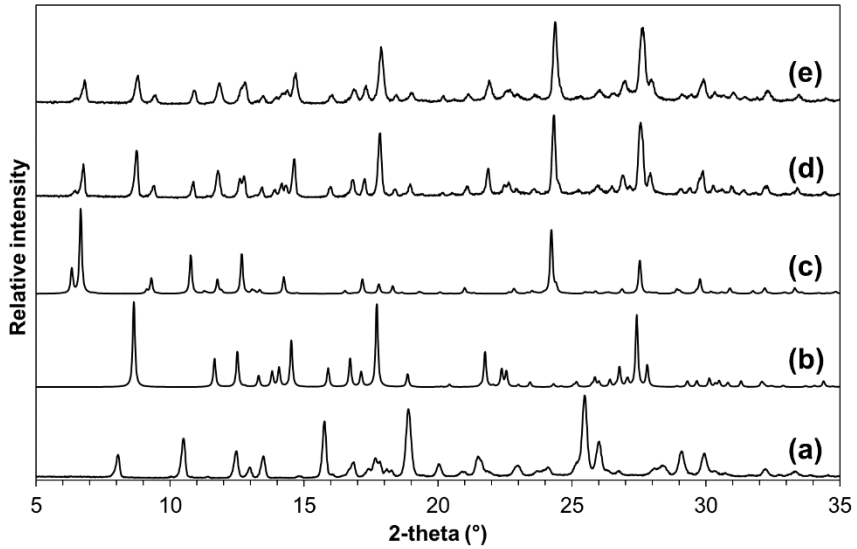

Figure 7.25 - PXRD patterns: (a) heated form of PXTA reference, (b) PX form I (BIYSEH04), (c) TA (BTCOAC), (d) product of dry grinding for 5 minutes and (e) product of dry grinding for 10 minutes.

The PXRD patterns show that dry grinding of the two starting materials for up to 10 minutes results in a physical mixture of PX and TA starting materials. After 10 minutes a slight broadening of the peaks (Figure 7.25e) suggests that prolonged grinding may result in increased amorphous content in the samples.

7.4.5 Structural analysis of desolvated form

The crystal structure of the desolvated form remains in the triclinic space group $P\bar{1}$ and confirms the loss of the solvent with the asymmetric unit containing one PX molecule and one TA molecule. The structure also confirms that a tautomeric transition has occurred upon desolvation, with the PX molecule now present in its non-ionised form. As a result of this change in ionisation state, the PX molecule has undergone a significant conformational rearrangement in the solid state. Intramolecular proton transfer on the PX molecule has occurred from the hydrogen atom bonded to the nitrogen atom of the pyridine ring to the oxygen atom to form a hydroxyl group. This allows for the formation of an O-H···O intramolecular hydrogen bond locking the conformation of the PX molecule.

As the PX molecule is no longer in its zwitterionic form and the conformation of the molecule is different, the PX molecules no longer assemble in dimers linked by charge assisted hydrogen bonds. Instead, one PX molecule sits between chains of TA molecules. Two hydrogen bonds link the PX molecule to a TA molecule *via* one of its carboxylic acid groups. An O-H···N hydrogen bond of length 2.582(3) Å forms between the O-H group on the TA molecule and the pyridine nitrogen atom on the PX molecule. Alongside this is an N-H···O hydrogen bond of length 3.064(3) Å between the carbonyl oxygen atom on the TA molecule and the N-H group on the PX molecule. As observed in the acetonitrile solvate, the two other carboxylic acid groups on the TA molecule form hydrogen bond dimers with other TA molecules forming a sheet of infinite herringbone chains of TA molecules flanked by PX molecules (Figure 7.26).

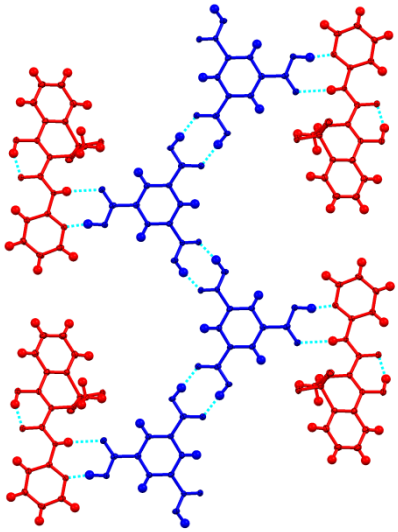

Figure 7.26 - Sheets of molecules in the PXN TA complex made up of an infinite herringbone chain of TA molecules flanked by PXN molecules. Colour coding shows the molecules of PXN in red and TA in blue.

Interestingly, whereas in both solvates all the TA molecules are co-planar in the crystal structure, in the desolvated form there is a change in the torsion angles of one of the carboxylic acid groups on the TA molecule. This results in the TA molecules in the chain lying parallel but not in the same plane. Furthermore, due to the position of the groups involved in the hydrogen bonds formed between the PX and TA molecules and the change in the conformation of the PX molecules, the PX and TA molecules do not lie in the same plane. The structure is therefore, no longer layered.

As the PX molecules do not form hydrogen bonded dimers in the non-ionised conformation, the sheets interlock in a zip-like nature (Figure 7.27). This occurs through weak interactions including a C-H···O interaction with a C···O distance of 3.445(4) Å between a hydrogen atom of the methyl group on the PX molecule and a C=O bond on the PX molecule in the next sheet. The overall packing arrangement of the structure is built up through offset stacking of the sheets of molecules, as shown in Figure 7.28.

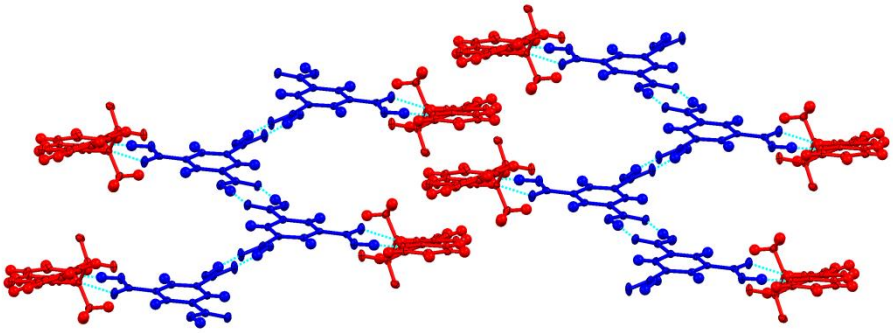

Figure 7.27 - Interlocking of hydrogen bonded sheets through weak interactions in the PXN TA complex.

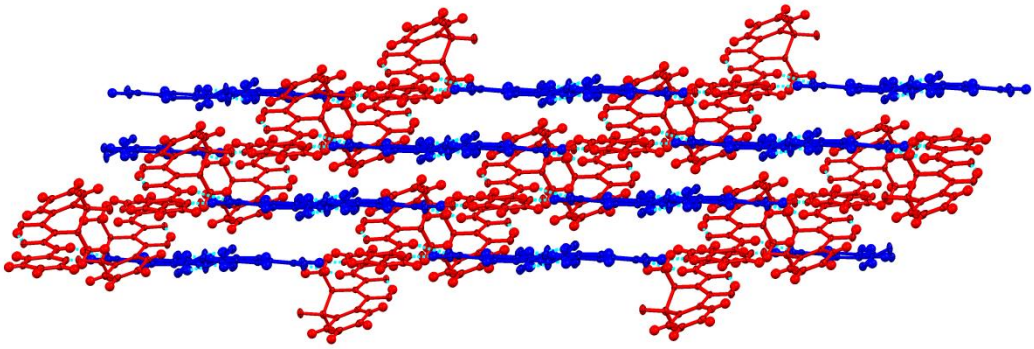

Figure 7.28 - Overall packing arrangement of molecules in the PXN TA complex.

Table 7.8 - Hydrogen bonds in PXN TA (Å and °).

D-H···A	d(D-H)	d(H···A)	d(D···A)	<(DHA)
C(13)-H(10)···O(10)	0.95(3)	2.20(3)	2.808(4)	121(2)
N(2)-H(19)···O(1)#1	0.85(3)	2.26(3)	3.064(3)	159(3)
O(2)-H(1)···N(3)#2	1.06(4)	1.53(4)	2.582(3)	169(4)
O(3)-H(3)···O(4)#3	0.91(4)	1.73(4)	2.637(3)	176(3)
O(9)-H(11)···O(10)	0.94(5)	1.65(5)	2.525(3)	152(4)
O(5)-H(5)···O(6)#4	0.99(4)	1.63(4)	2.615(3)	173(4)

Symmetry transformations used to generate equivalent atoms:
#1 x+1,y,z #2 x-1,y,z #3 -x,-y+1,-z+1 #4 -x,-y+2,-z

A good match of the powder pattern predicted from the single crystal structure to the measured PXRD pattern was observed (Figure 7.29).

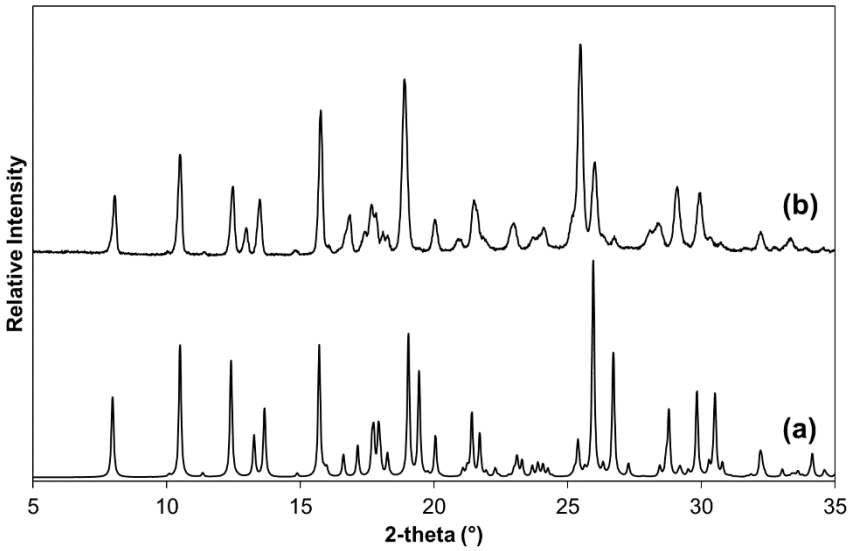

Figure 7.29 - PXRD patterns of PXN TA (a) calculated and (b) experimental.

7.4.6 Other analytical techniques

Several other techniques were also implemented to characterise the tautomeric transition in the PX-TA solvates including variable-temperature powder X-ray diffraction, variable-temperature Raman spectroscopy and FTIR spectroscopy.

7.4.6.1 Variable-temperature powder X-ray diffraction

VT-PXRD was carried out for the acetone solvate in order to observe the desolvation event. Figure 7.30 shows the patterns at the transition point. It is evident that the onset of the transition occurs at 137.5 °C; the peak at 5.5° 2θ begins to appear at this temperature, which correlates well with the DSC, TGA and HSM results.

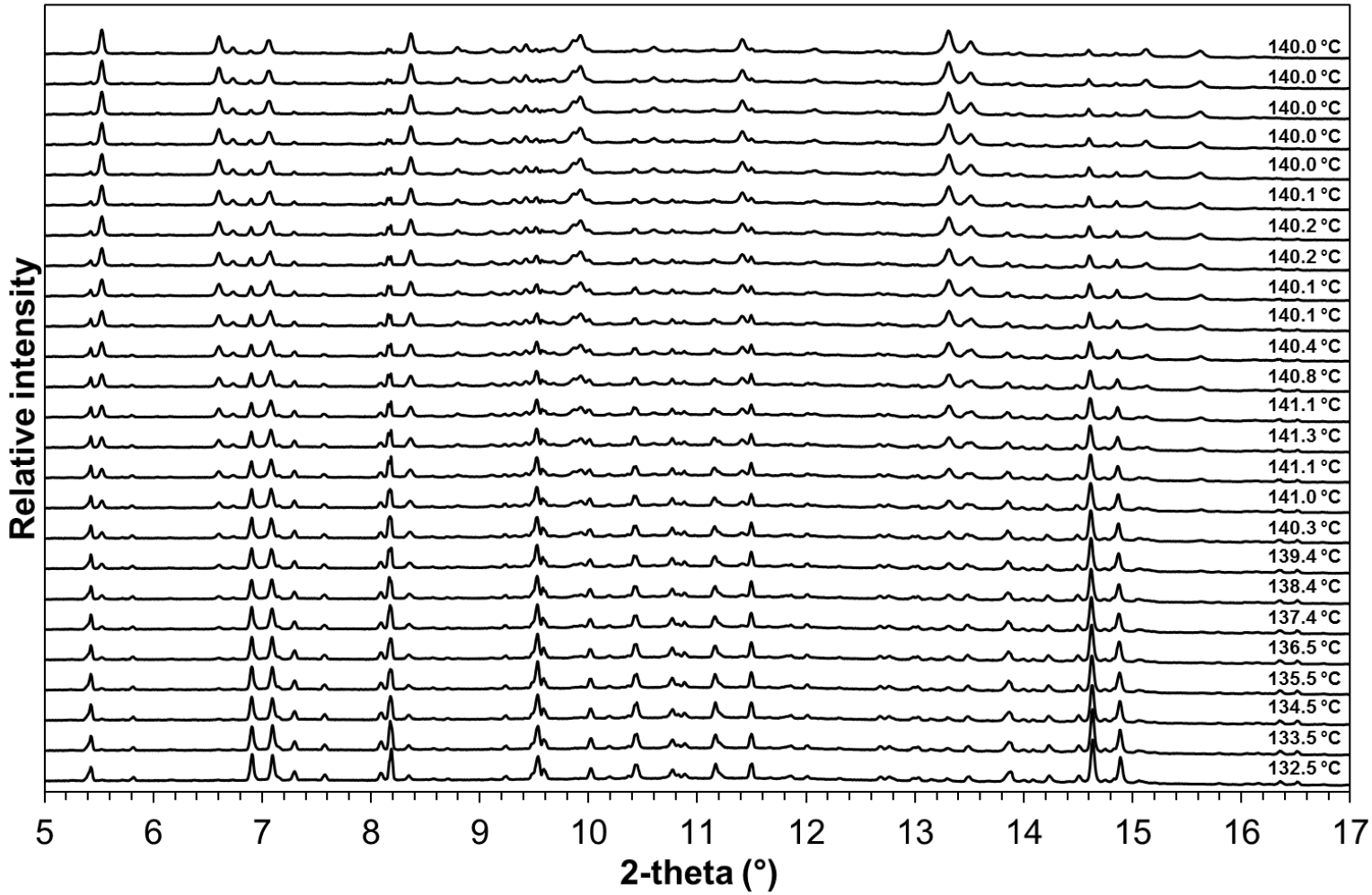

Figure 7.30 - VT-PXRD patterns of PXZ TA ACT.

7.4.6.2 Variable temperature Raman spectroscopy

Different solid forms of PX can be identified using Raman spectroscopy[191,202-204] and it was therefore possible to monitor the desolvation and tautomeric transition by monitoring the Raman signal whilst heating a powder of each solvate (Figure 7.31).

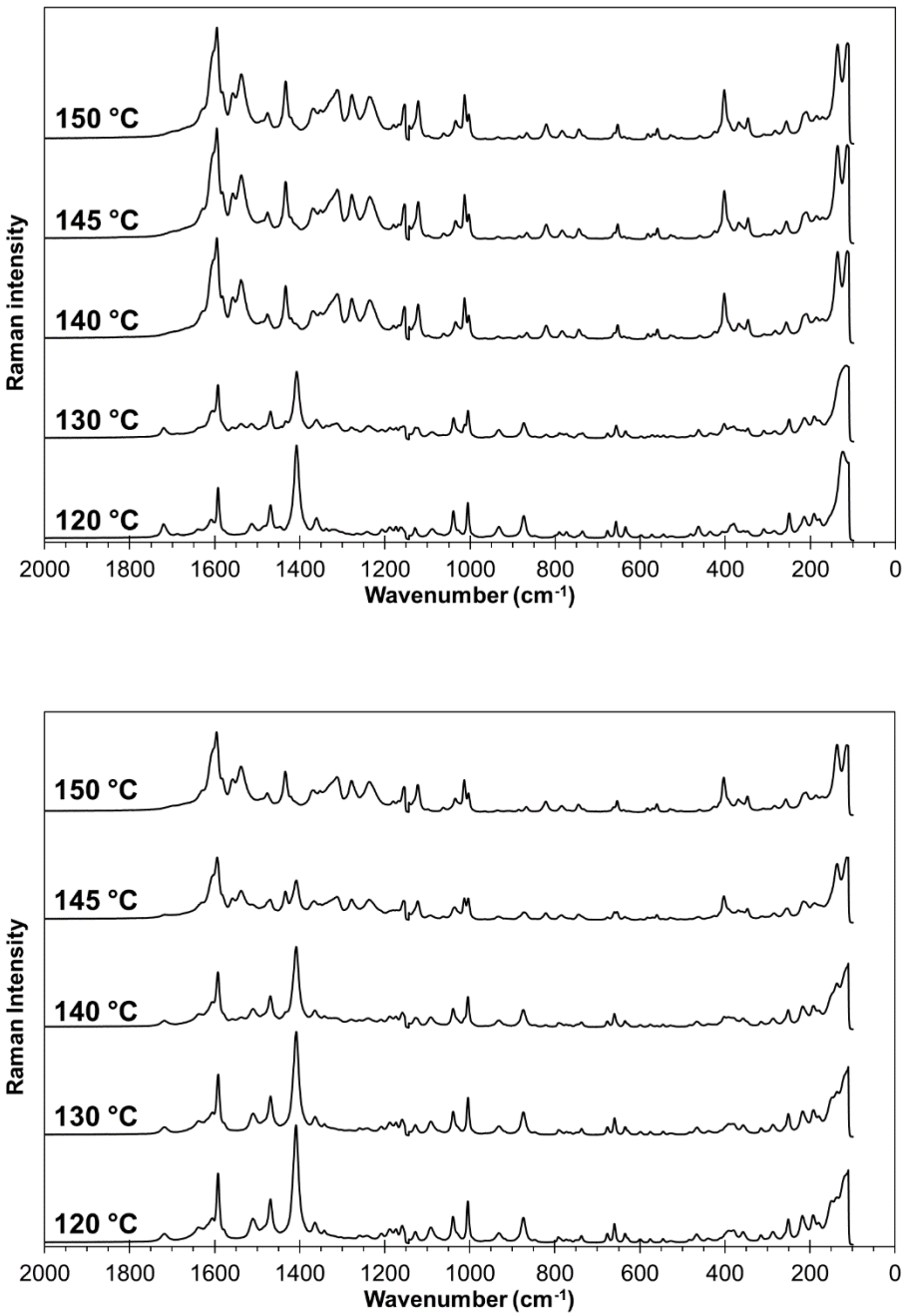

Figure 7.31 - Raman spectra of (top) PXZ TA ACT and (bottom) PXZ TA ACN at different temperatures.

The zwitterionic tautomer can be identified by the presence of Raman bands at ~1410 cm^{-1} and ~1470 cm^{-1} which are present in the Raman signal for both solvates at room temperature. Upon increasing the temperature, the Raman signal changes; in the

acetone solvate the intensity of this peak decreases at 130 °C and by 140 °C these indicative peaks are no longer present and a new Raman spectrum is produced. As observed in the thermal analysis, the transition occurs later for the acetonitrile solvate and the peaks at 1410 cm^{-1} and 1470 cm^{-1} decrease in intensity at 140 °C; by 150 °C the Raman spectrum of the desolvated form is observed. For the acetonitrile solvate the Raman spectrum at 145 °C shows peaks representing both the solvate and the desolvate.

7.4.6.3 Fourier transform infra-red spectroscopy

FTIR spectra of each solvate were collected before and after heating, as well as after vapour diffusion experiments (Figure 7.32).

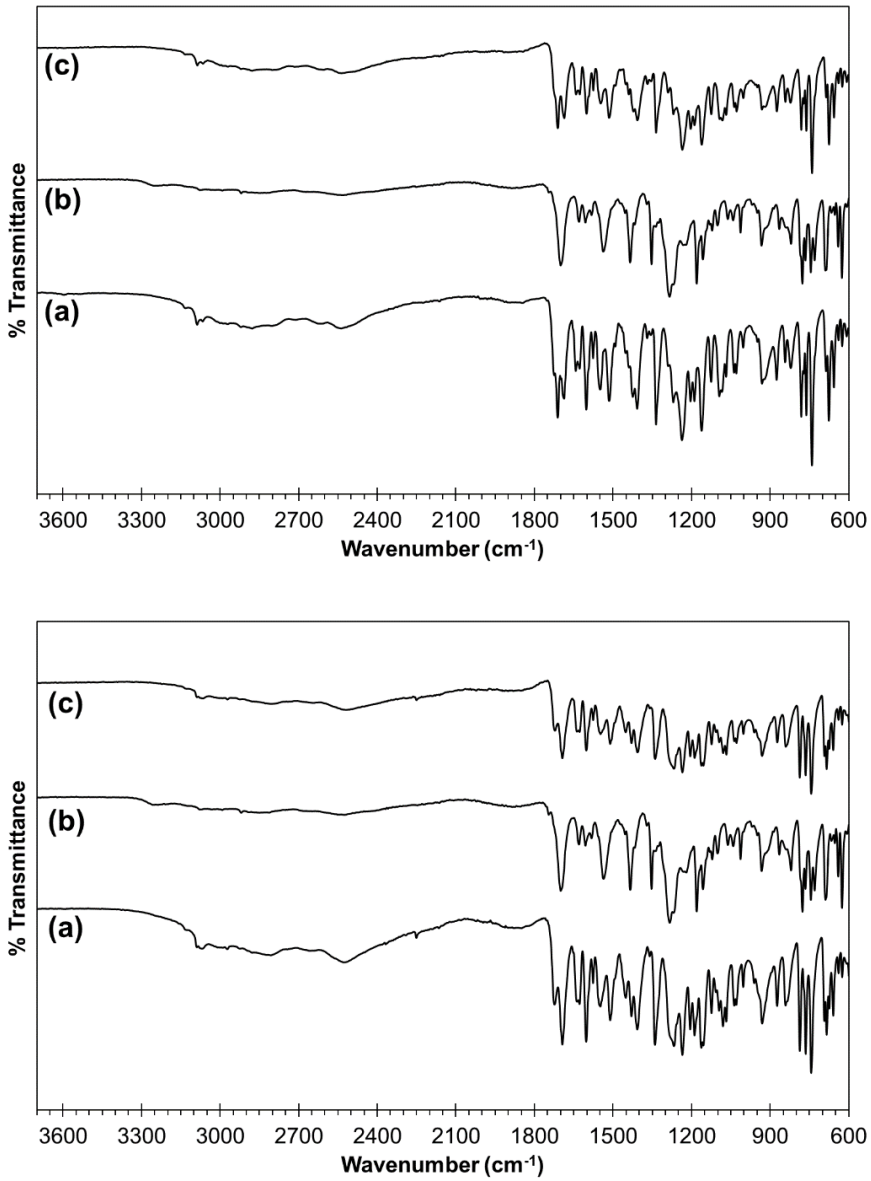

Figure 7.32 - FTIR spectra of (a) solvate, (b) solvate heated and (c) vapour diffusion of sample of (top) PXZ TA ACT and (bottom) PXZ TA ACN.

The spectra support the PXRD data showing that both solvates return to their original form after vapour diffusion experiments; they also confirm that both solvates form the same desolvated form upon heating.

7.5 Structural comparison with other molecular complexes of PX

In this study ten multi-component molecular complexes were produced (including those with TA); PX is present in its zwitterionic form (PXZ) in five of the complexes. In this form, the formation of two intramolecular hydrogen bonds locks the conformation of the molecule. Two of the remaining complexes feature PX in its non-ionised form (PXN). In the final three complexes, intermolecular proton transfer from the carboxylic acid group of the co-former molecule to the nitrogen atom on the pyridine ring of the PX molecule results in the formation of a salt with a protonated PX molecule (PX^+); one of these salts is solvated with acetonitrile. The protonated PX^+ has only previously been observed in the solid state in complexes with strong acids: chloranilic acid and bromanilic acid.[190] In both the PX^+ and the PXN complexes an O-H···O intramolecular hydrogen bond is present allowing the PX molecule to adopt a different conformation to that found in the PXZ complexes. None of the complexes feature the deprotonated PX^-.

7.5.1 PXZ complexes

As observed in the solvated structures of PX with TA (Section 7.4.1), in all of the remaining complexes containing PX in its zwitterionic form, the PXZ molecules self-assemble in hydrogen bonded dimers. Such dimers form through two charge assisted N^+-H···O hydrogen bonds between the protonated pyridinal nitrogen atom and the carbonyl oxygen atom. In each complex, a co-former molecule lies on either side of the PX dimers interacting through a charge assisted O-H···O^- hydrogen bond to the deprotonated hydroxyl group on the zwitterionic PX molecule. This makes up a four molecule tetrameric hydrogen bonded unit comprising two PX molecules forming a dimer in the centre[197] (Figure 7.33).

However, although each PXZ complex contains this unit, the overall packing arrangement of the tetrameric units in each complex differs as a result of the position of the different hydrogen bond donor and acceptor groups in each co-former molecule.

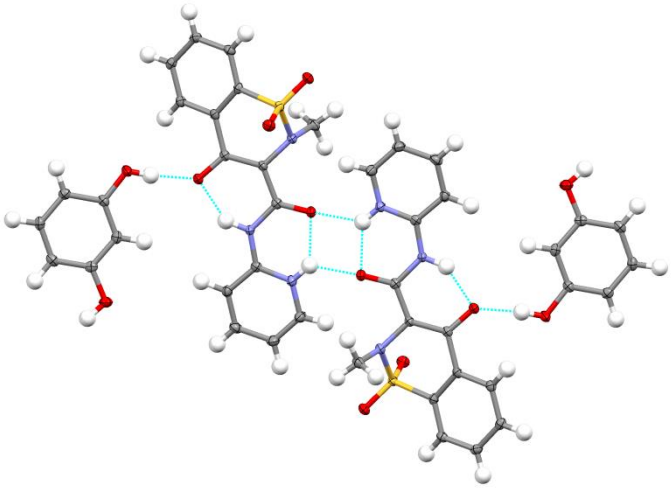

Figure 7.33 - Four molecule tetrameric hydrogen bonded unit in the PXZ RES complex.

As observed in the complexes with TA, in the 35DHBA complex, the units assemble in AABB chains with the tetrameric units interacting through carboxylic acid dimers between the two 35DHBA molecules (Figure 7.34).

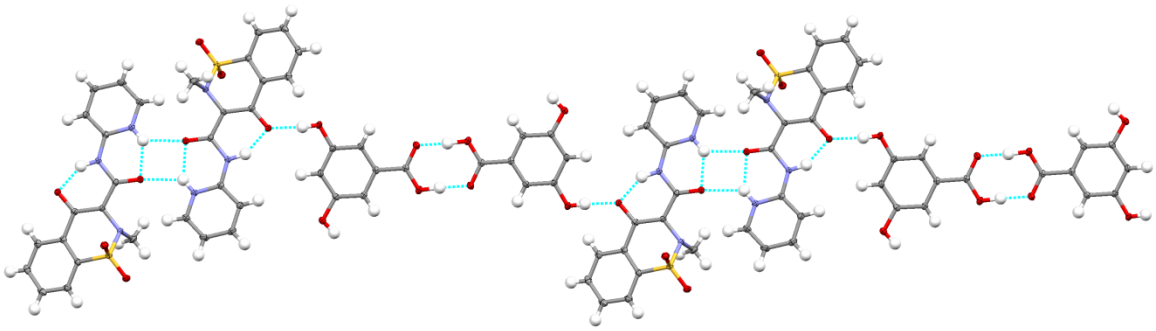

Figure 7.34 - AABB chains of PXZ and 35DHBA molecules in the PXZ 35DHBA complex.

However, unlike the TA complexes, the dimers lie above and below the plane of the PX dimer. The infinite chains stack in offset layers with the remaining hydrogen bonding donor hydroxyl group on the 35DHBA molecule interacting with the S=O group on the PX molecule in the layer above with an O···O distance of 2.8407(15) Å (Figure 7.35).

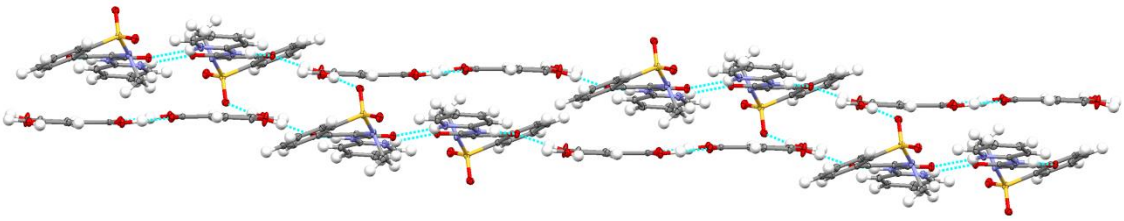

Figure 7.35 - Layers of PXZ 35DHBA chains viewed down the crystallographic *b* axis.

Table 7.9 - Hydrogen bonds in PXZ 35DHBA (Å and °).

D-H···A	d(D-H)	d(H···A)	d(D···A)	<(DHA)
C(21)-H(15)···O(2)	0.921(17)	2.597(16)	3.2789(17)	131.3(12)
C(14)-H(9)···O(3)#1	0.942(18)	2.602(18)	3.1268(18)	115.6(13)
C(14)-H(9)···N(3)#1	0.942(18)	2.546(18)	3.4496(19)	161.0(14)
N(2)-H(5)···O(4)	0.91(2)	1.72(2)	2.5516(15)	148.9(18)
C(22)-H(11)···O(5)#1	1.016(19)	2.544(19)	3.5302(19)	163.5(14)
N(1)-H(10)···O(3)	0.87(2)	1.95(2)	2.6443(16)	135.3(17)
N(1)-H(10)···O(3)#1	0.87(2)	2.188(19)	2.8531(16)	132.9(16)
O(8)-H(18)···O(4)#2	0.87(2)	1.77(2)	2.6343(14)	174(2)
O(7)-H(14)···O(2)	0.85(2)	2.00(2)	2.8407(15)	172.4(19)
O(6)-H(16)···O(5)#3	1.04(3)	1.56(4)	2.5938(14)	177(3)

Symmetry transformations used to generate equivalent atoms:
#1 -x+1,-y+1,-z+2 #2 -x+1,-y+1,-z+1 #3 -x,-y+1,-z+2

Resorcinol is the structural analogue of 35DHBA without the carboxylic acid group. Therefore, the four molecule tetrameric units do not form chains in the same way as in PXZ 35DHBA as there is no hydrogen bond dimer present in the 1-position. However, the hydroxyl groups on the resorcinol molecule interact in the same way as observed in the 35DHBA structure. The tetrameric units therefore overlay and interlock through O-H···O hydrogen bond interactions with the S=O groups on the PX molecules, as observed in the 35DHBA complex with a similar O···O distance of 2.8397(18) Å (Figure 7.36).

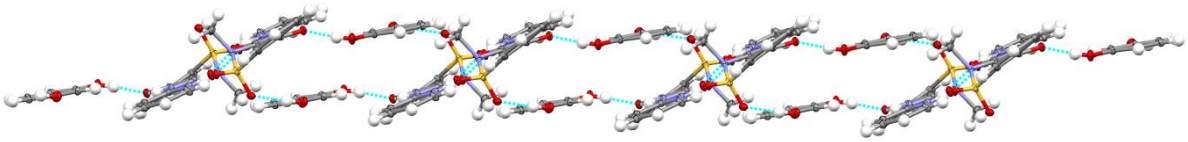

Figure 7.36 - Hydrogen bonded chains of PXZ RES molecules.

As shown in Figure 7.37, the chains stack through offset π-stacking interactions which are present between the overlapping aromatic rings of PX molecules at an inter-planar distance of ~3.2 Å.

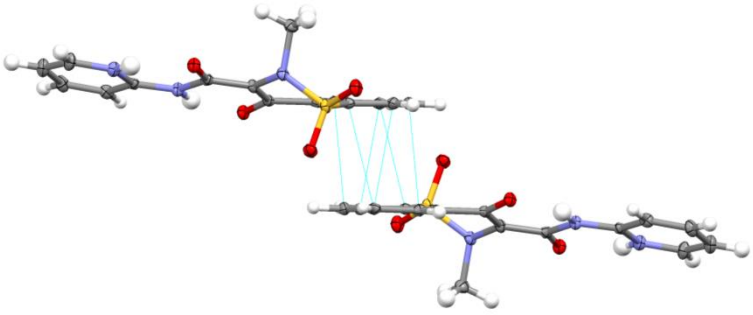

Figure 7.37 - Offset π-stacking interactions between PX molecules in the PXZ RES complex.

Table 7.10 - Hydrogen bonds in PXZ RES (Å and °).

D-H···A	d(D-H)	d(H···A)	d(D···A)	<(DHA)
C(8)-H(3)···O(1)#1	0.941(19)	2.558(19)	3.131(2)	119.6(14)
N(2)-H(15)···O(6)	0.89(2)	1.92(2)	2.6122(18)	133(2)
N(2)-H(15)···O(6)#2	0.89(2)	2.19(2)	2.8643(19)	132.9(19)
C(19)-H(10)···N(3)#2	0.91(2)	2.50(2)	3.342(2)	152.6(18)
N(1)-H(14)···O(5)	0.92(2)	1.78(2)	2.5839(18)	144.2(19)
C(21)-H(9)···O(6)	0.99(2)	2.63(2)	3.180(2)	115.4(15)
O(2)-H(19)···O(3)	0.88(3)	1.96(3)	2.8397(18)	175(2)
C(21)-H(7)···O(4)#3	0.97(2)	2.44(2)	3.346(2)	153.8(18)
O(1)-H(18)···O(5)#4	0.87(3)	1.80(3)	2.6679(18)	172(2)

Symmetry transformations used to generate equivalent atoms:
#1 x,y-1,z #2 -x,-y+1,-z #3 -x,-y,-z #4 -x,-y+1,-z+1

In the complex of PX with 34DHBA, the 34DHBA molecule lies on an inversion centre, with a resulting 50:50 ratio of the occupancies in each symmetry dependent orientation (Figure 7.38). As a result of this disorder the asymmetric unit contains one PX molecule, half a 34DHBA molecule and one acetonitrile molecule.

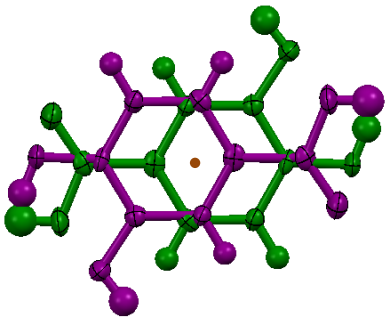

Figure 7.38 - Disorder of the 34DHBA molecule over an inversion centre in the PXZ 34DHBA complex with the two positions in green and purple overlaid.

In contrast to RES and 35DHBA, there is a hydrogen bond donor group (a hydroxyl group) on the 4-position of the benzene ring of the 34DHBA molecule. This allows for the PX dimers to interact with 34DHBA on either side of the molecule through O-H···O hydrogen bonds of almost equivalent strength (length) from the hydroxyl group and the carboxylic acid group. As observed in the TA complexes, the presence of the carbonyl group on the carboxylic acid group on the 34DHBA molecule allows for a C-H···O interaction to form, reinforcing the interaction of the PXZ and 34DHBA molecules. The other hydrogen bond dimer of the 34DHBA molecule interacts with the sulfonyl group of

the PX molecule in the layer below through an O-H···O interaction with an O···O distance of 2.871(3) Å, as observed in the previous two complexes.

The complex is solvated and each PX molecule forms a weak C-H···N interaction with a molecule of acetonitrile. Sheets of dimers of PX molecules separated by a disordered 34DHBA molecule and two acetonitrile molecules assemble in a layered arrangement with the methyl and sulfonyl groups of PX sticking out of the plane (Figure 7.39). These layers stack with the molecules offset to one another (Figure 7.40 and Figure 7.41).

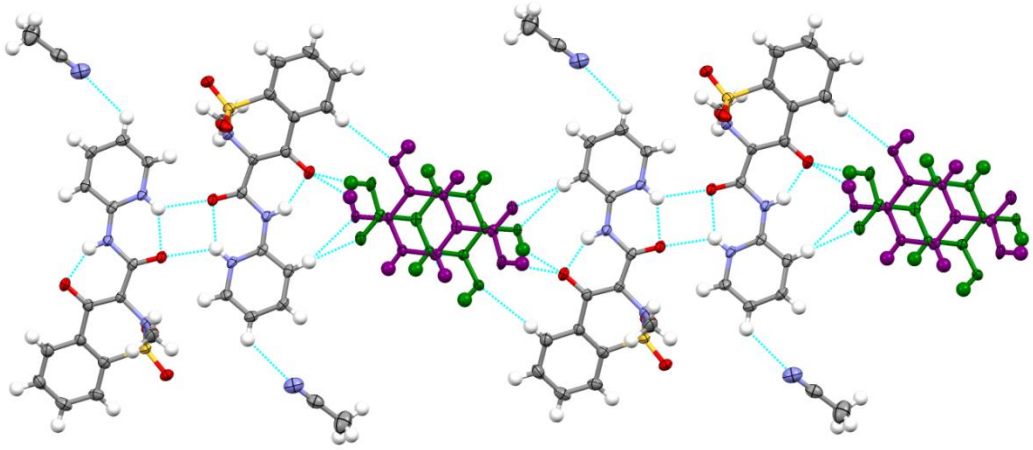

Figure 7.39 - Sheets of molecules in the PXZ 34DHBA ACN complex.

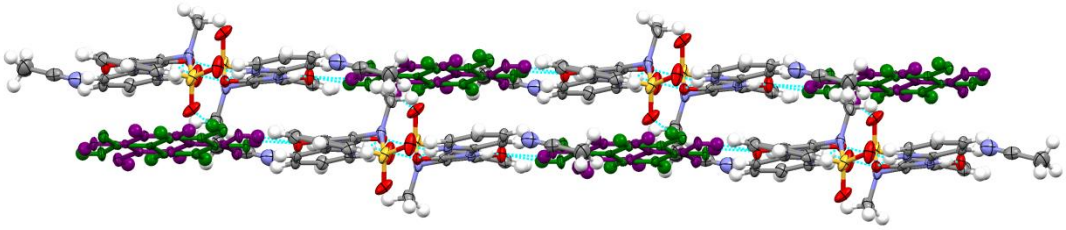

Figure 7.40 - Layers of PXZ 34DHBA ACN sheets viewed down the crystallographic *c* axis.

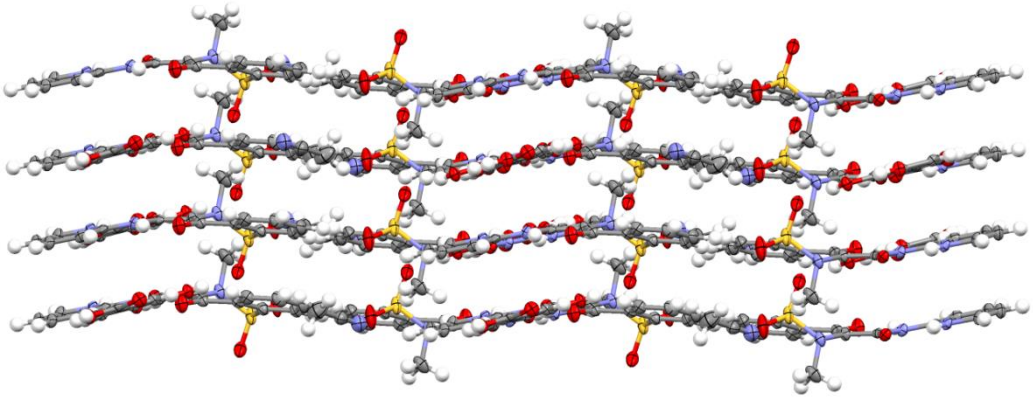

Figure 7.41 - Layers of molecules in the PXZ 34DHBA ACN complex.

Table 7.11 - Hydrogen bonds in PXZ 34DHBA ACN (Å and °).

D-H···A	d(D-H)	d(H···A)	d(D···A)	<(DHA)
O(5)-H(18)···O(6)	0.82	2.3	2.735(5)	113.4
O(5)-H(18)···O(3)#1	0.82	1.95	2.594(4)	135.3
O(6)-H(17)···O(2)	0.82	2.06	2.871(3)	172.9
O(8)-H(21)···O(3)#2	0.82	1.76	2.565(3)	165
N(2)-H(6)···O(3)	0.85(2)	1.81(2)	2.569(2)	147(2)
C(4)-H(1)···O(5)#3	0.92(2)	2.64(2)	3.523(5)	160.1(18)
C(4)-H(1)···O(7)#2	0.92(2)	2.33(2)	3.249(4)	177.4(19)
N(3)-H(5)···O(4)	0.86(2)	1.99(2)	2.657(2)	134(2)
N(3)-H(5)···O(4)#4	0.86(2)	2.25(2)	2.880(2)	130(2)
C(13)-H(10)···O(1)#5	0.94(3)	2.43(3)	3.233(3)	143(2)
C(1)-H(4)···O(4)#4	0.93(2)	2.50(2)	3.051(3)	118.3(16)
C(1)-H(4)···N(1)#4	0.93(2)	2.53(2)	3.445(3)	166.3(18)

Symmetry transformations used to generate equivalent atoms:
#1 x,y-1,z #2 -x+2,-y+2,-z #3 x,y+1,z #4 -x+1,-y+1,-z #5 -x+1,-y+1,-z+1

Of the five PXZ complexes produced, three of the structures show a layered packing arrangement with one also showing disorder in the crystal structure, two features targeted in these PX co-crystallisation investigations. All of the co-formers that produced layered crystal structures interact with the PXZ molecule *via* the carboxylic acid functional group. This allows for two interactions to form between the molecules: an O-H···O interaction and a weaker C-H···O interaction. The combination of interactions allows for the molecules to lie in the same plane and form a layered arrangement. In the structures that did not produce a layered packing arrangement, on the other hand, the co-former molecule interacts with the PX molecule through a hydroxyl group which only forms one interaction.

7.5.2 PXN complexes

PX is present in its neutral form in the complex with 35DNBA as well as in the desolvated complex with TA (previously discussed in Section 7.4.5). In both complexes PX interacts with the carboxylic acid group of the respective co-former molecule through two hydrogen bonds (Figure 7.42). The first of these is between the hydroxyl group on the co-former molecule and the deprotonated nitrogen atom of the pyridine ring on the PX molecule. In the 35DNBA structure this hydrogen bond is short and strong (2.521(5) Å) indicating that proton transfer could be possible across this hydrogen bond (for example in the complex with 24DNBA in Section 7.5.3). The second intermolecular hydrogen bond common to both structures is an N-H···O hydrogen bond between the carbonyl group of the carboxylic acid group on the co-former molecule and the protonated nitrogen atom on the PX molecule.

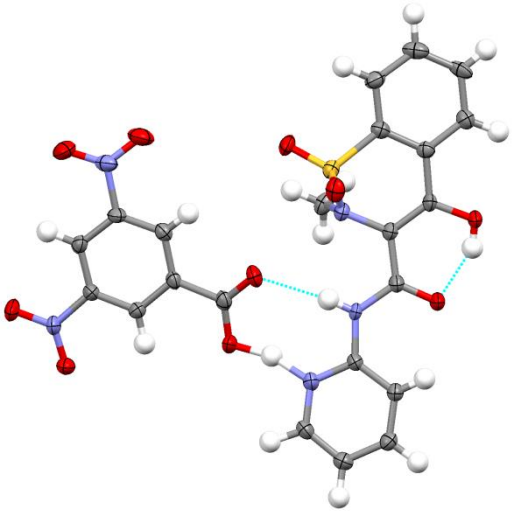

Figure 7.42 - Hydrogen bonding in the asymmetric unit of the PXN 35DNBA complex viewed down the crystallographic *a* axis.

Unlike the desolvated crystal structure of PXN with TA, in the structure with PXN and 35DNBA the molecules self-assemble in one-dimensional ABAB hydrogen bonded chains (Figure 7.43). Whereas in the TA molecule the presence of additional carboxylic acid groups on the co-former molecule allows for dimers to form between the TA molecules, the nitro groups on the 35DNBA molecule cannot form this interaction. Instead, one of the nitro groups on the 35DNBA molecule interacts favourably with the hydroxyl group on the PX molecule creating a bifurcated hydrogen bond.

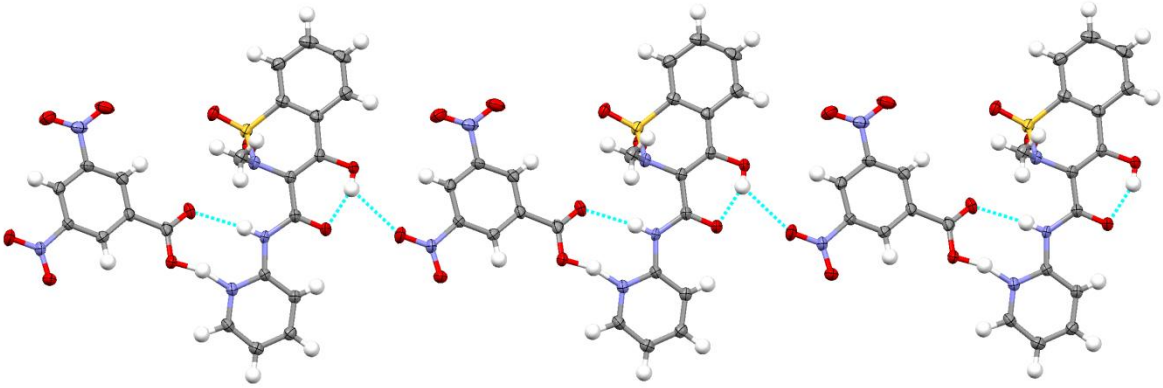

Figure 7.43 - Hydrogen bonded chains in the PXN 35DNBA complex viewed down the crystallographic *a* axis.

Weak interactions link the ABAB chains of PX and 35DNBA molecules to form sheets made up of PXN and 35DNBA molecules (Figure 7.44). These interactions comprise hydrophobic C-H···H-C interactions as well as a C-H···O interaction between two PX molecules involving a C-H group on the pyridine ring and the S=O group.

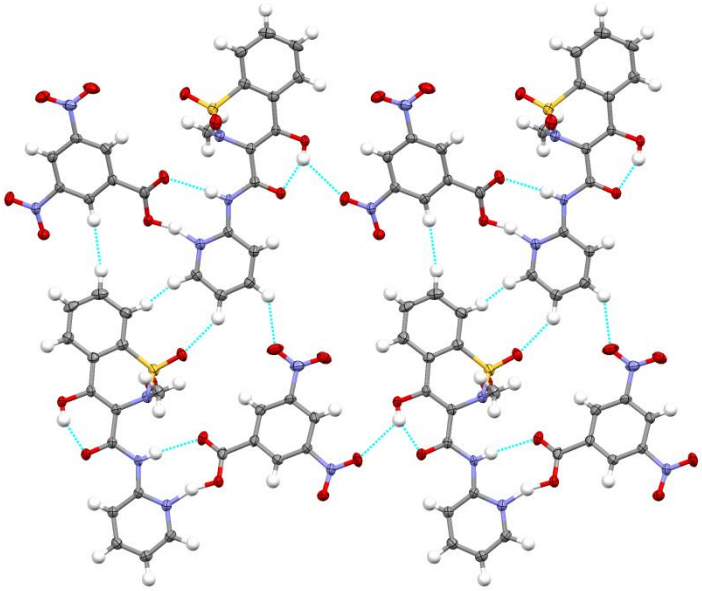

Figure 7.44 - Sheets of PXN and 35DNBA viewed down the crystallographic *a* axis.

The hydrogen bonded sheets stack through further weak interactions to form layers of molecules (Figure 7.45).

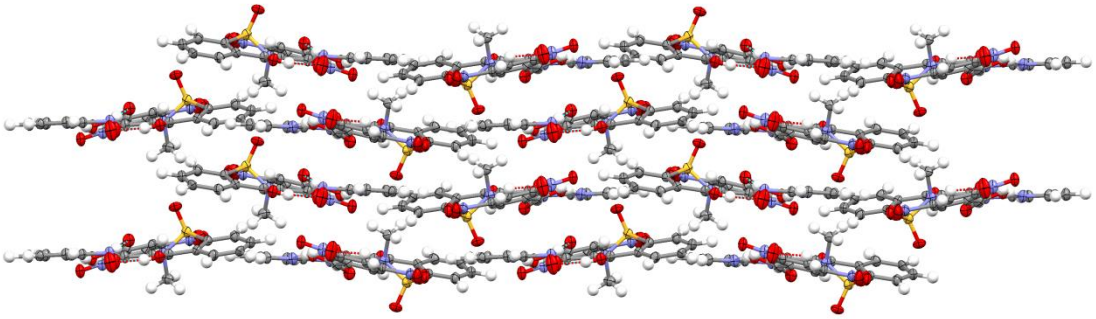

Figure 7.45 - Layers of PZN 35DNBA sheets viewed down the crystallographic *c* axis.

Table 7.12 - Hydrogen bonds in PX 35DNBA (Å and °).

D-H···A	d(D-H)	d(H···A)	d(D···A)	<(DHA)
C(11)-H(6)···O(4)	0.90(5)	2.20(5)	2.770(6)	121(4)
N(2)-H(11)···O(5)	0.83(5)	2.15(5)	2.973(5)	171(4)
C(13)-H(8)···O(2)#1	1.00(5)	2.53(5)	3.328(6)	136(3)
O(6)-H(10)···N(2)	1.22(8)	2.68(8)	3.665(5)	138(5)
O(6)-H(10)···N(3)	1.22(8)	1.34(8)	2.521(5)	161(7)
N(3)-H(10)···O(5)	1.34(8)	2.41(8)	3.342(5)	124(5)
O(3)-H(5)···O(4)	0.82(7)	1.77(7)	2.524(4)	152(7)
O(3)-H(5)···O(8)#2	0.82(7)	2.48(7)	3.041(5)	127(6)
C(15)-H(15C)···O(1)#3	0.96	2.61	3.077(5)	110.6

Symmetry transformations used to generate equivalent atoms:
#1 -x+1/2,y-1/2,-z+1/2 #2 x,y,z-1 #3 x-1,y,z

7.5.3 PX^+ complexes

In each of the three PX^+ complexes, the co-former molecule interacts with a PX molecule through three N-H···O hydrogen bonds between the deprotonated carboxylate group on the co-former molecule and the protonated nitrogen atoms of the PX molecule. In each complex, one of the oxygen atoms in the carboxylate group forms a bifurcated hydrogen bond, forming an interaction with both N-H bonds which is also observed in the PX^+ complexes reported by Thomas *et al.*[190] In the 35DNSA complex, the groups lie offset to one another which results in the weakest of the three hydrogen bonds in the other two complexes being the strongest in this complex. In the complex with 24DNBA, this unit also includes an acetonitrile molecule which forms weak interactions with the two components through C-H···O and C-H···N interactions. In two of the complexes (with 35DNSA and 26DHBA) hydroxyl groups are present on the benzene ring position adjacent to the carboxylate group. In each case the deprotonation results in the formation of an intramolecular O-H···O^- hydrogen bond between the hydroxyl group and the carboxylate oxygen atom on the co-former molecule. This intramolecular interaction is stronger in the complex with 35DNSA, with an O···O distance of 2.466(3) Å, compared to the two intramolecular interactions in the complex with 26DHBA complex, which have O···O distances of 2.589(3) Å and 2.525(3) Å. Figure 7.46 shows the described interactions in the asymmetric units of each PX^+ complex.

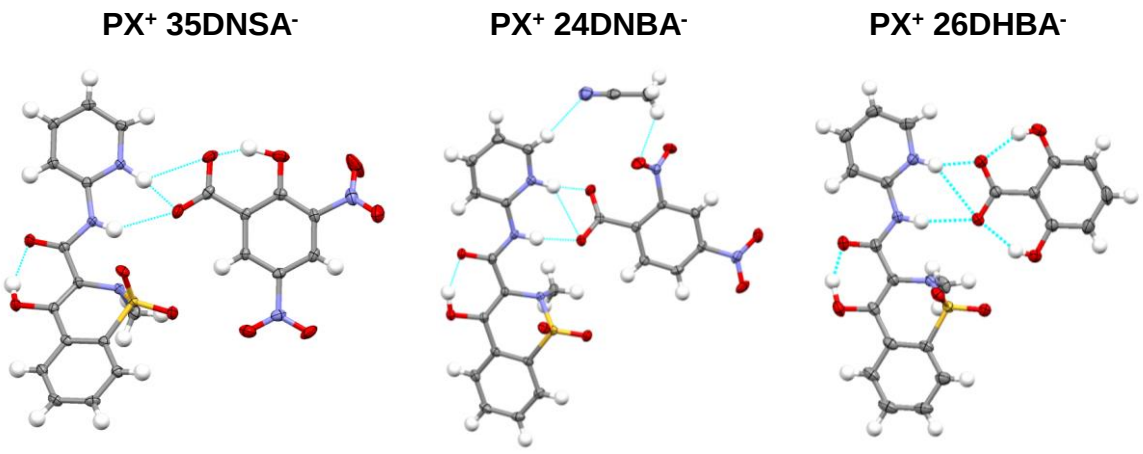

Figure 7.46 - Hydrogen bonding interactions in the asymmetric units of each PX^+ complex.

The zero-dimensional hydrogen bonded units of PX and the co-former molecule interact with each other through weak interactions in each complex, but in different arrangements. First, in the complex with 35DNSA, the molecules interact in an AABB arrangement with the units inverting in orientation to allow them to stack favourably, as shown in Figure 7.47. This arrangement is supported by a C-H···O interaction from the 35DNSA

molecule with the S=O group of the PX molecule with a distance of 3.522(3) Å. The PX molecules interact through two weak C-H···O interactions, each with a distance of 3.417(3) Å. Figure 7.48 shows this packing arrangement from the side view.

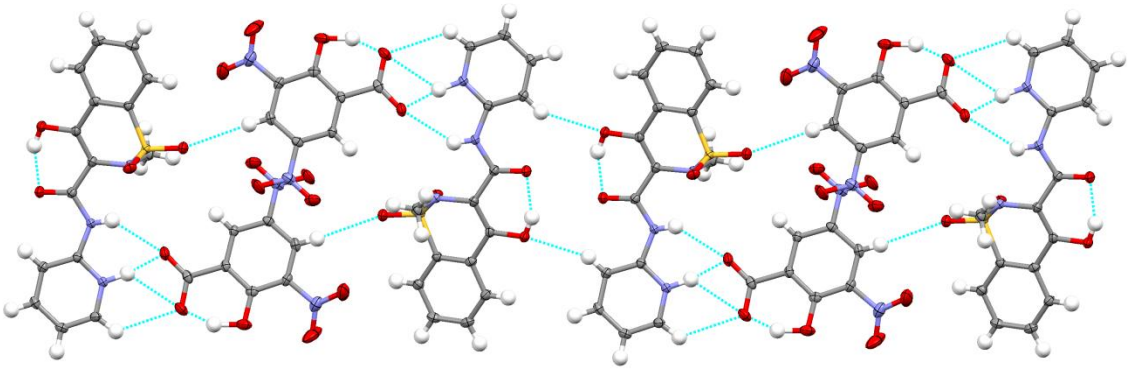

Figure 7.47 - Hydrogen bonding interactions in the PX^{+} $35DNSA^{-}$ complex.

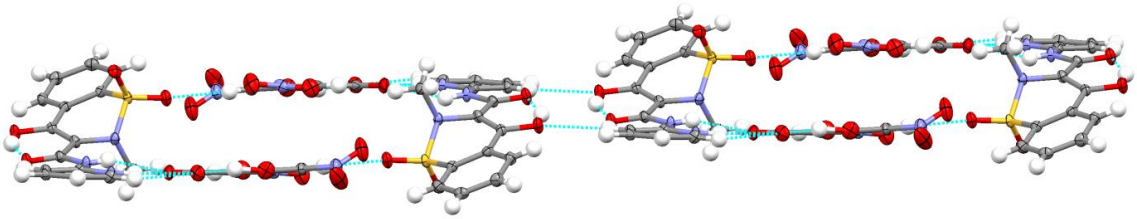

Figure 7.48 - Hydrogen bonding interactions in the PX^{+} $35DNSA^{-}$ complex shown from the side view.

Table 7.13 - Hydrogen bonds in PX^{+} $35DNSA^{-}$ (Å and °).

D-H···A	d(D-H)	d(H···A)	d(D···A)	<(DHA)
C(14)-H(9)···O(3)#1	0.95(2)	2.45(2)	3.196(2)	135.0(19)
C(14)-H(9)···O(6)	0.95(2)	2.64(3)	3.283(3)	125.4(18)
C(11)-H(6)···O(2)#2	0.92(2)	2.56(3)	3.417(3)	155(2)
C(11)-H(6)···O(1)	0.92(2)	2.32(2)	2.876(3)	118.4(19)
C(13)-H(8)···O(9)#3	0.94(2)	2.47(3)	3.105(3)	124.6(19)
N(1)-H(11)···N(2)	0.82(3)	2.26(2)	2.717(3)	116(2)
N(1)-H(11)···O(5)	0.82(3)	2.39(3)	3.052(3)	138(2)
C(16)-H(12)···O(7)#4	0.97(3)	2.54(3)	3.476(3)	162(2)
O(2)-H(5)···O(1)	0.84(3)	1.82(3)	2.588(2)	153(3)
N(5)-H(10)···O(5)	0.99(3)	1.63(3)	2.608(2)	172(3)
N(5)-H(10)···O(6)	0.99(3)	2.47(3)	3.161(3)	126(2)
O(11)-H(15)···O(6)	1.15(4)	1.39(4)	2.466(3)	152(4)

Symmetry transformations used to generate equivalent atoms:
#1 -x+1,-y+1,-z #2 -x+1,-y+1,-z+1 #3 x+1,y+1,z #4 -x,-y+1,-z

Unlike the 35DNSA complex, in the solvated complex of PX with 24DNBA the molecules arrange themselves in ABAB chains, as shown in Figure 7.49. The presence of an

inversion centre allows the chains to invert and interlock forming a zip-like ribbon lined with acetonitrile molecules.

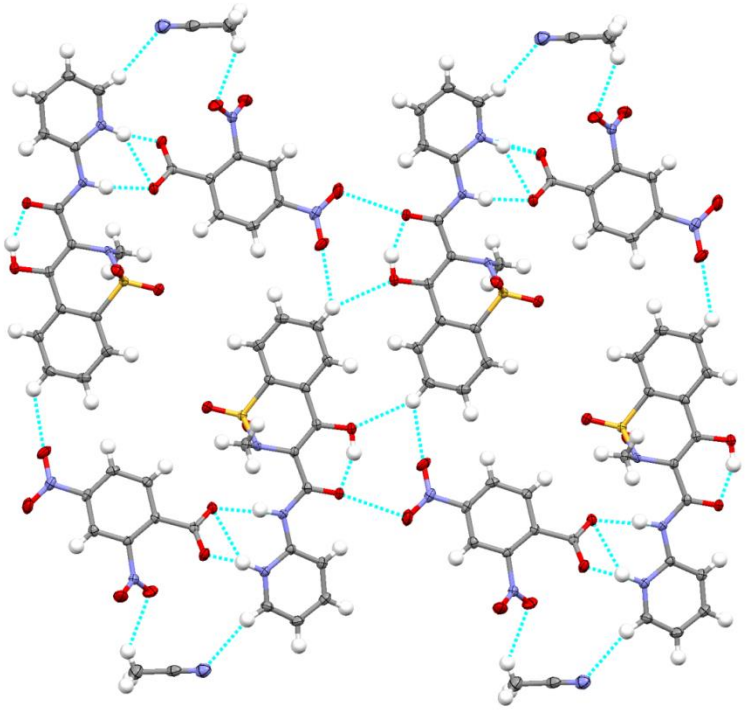

Figure 7.49 - Hydrogen bonding interactions in the PX^{+} $24DNBA^{-}$ ACN complex viewed down the crystallographic *a* axis.

The overall packing arrangement of molecules in the PX^{+} $24DNBA^{-}$ ACN complex is shown in Figure 7.50. The acetonitrile molecules sit in discrete pores within the structure.

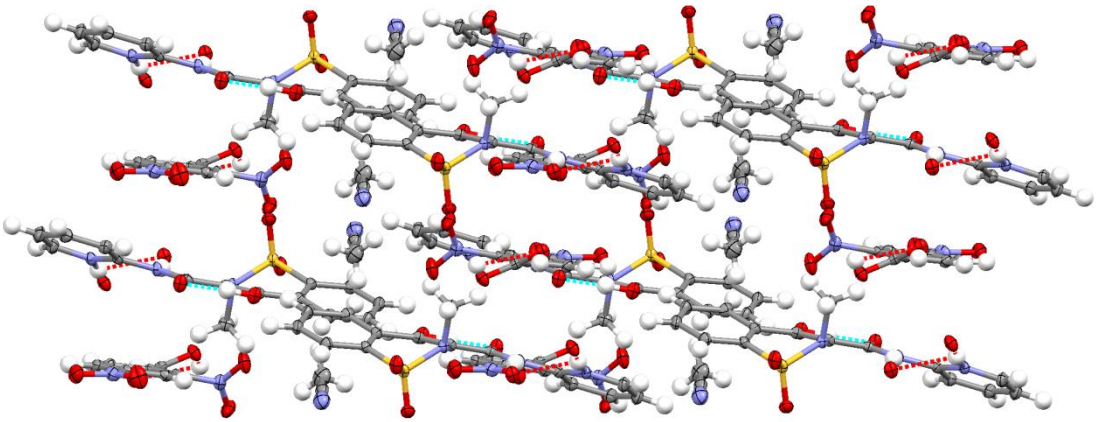

Figure 7.50 - Packing arrangement of molecules in the PX^{+} $24DNBA^{-}$ ACN complex viewed down the crystallographic *c* axis.

Table 7.14 - Hydrogen bonds in PX^+ $24DNBA^-$ ACN (Å and °).

D-H···A	d(D-H)	d(H···A)	d(D···A)	<(DHA)
C(12)-H(5)···O(1)	0.92(2)	2.23(2)	2.800(3)	119.2(16)
C(9)-H(11)···O(9)#1	0.99(2)	2.47(2)	3.395(3)	155.1(17)
C(19)-H(13)···O(3)#2	0.88(3)	2.54(3)	3.376(3)	158.1(19)
N(2)-H(9)···O(5)	0.90(3)	1.83(3)	2.713(2)	169(2)
O(2)-H(19)···O(1)	0.93(3)	1.66(3)	2.530(2)	154(3)
N(1)-H(20)···O(6)	1.02(3)	1.63(3)	2.638(2)	171(3)
N(1)-H(20)···O(5)	1.02(3)	2.48(3)	3.153(2)	122.8(19)
C(23)-H(16)···O(7)#2	0.86(4)	2.57(4)	3.257(4)	138(3)

Symmetry transformations used to generate equivalent atoms:
#1 -x+1,-y+2,-z+2 #2 -x,-y+2,-z+2

In contrast to the previous structures which are both in the triclinic space group, $P\bar{1}$, the complex of PX with 26DHBA is in the monoclinic space group, $P2_1/n$. In this structure the unit cell contains four PX^+ $26DHBA^-$ units and they assemble in ABAB chains which interlock with the chains below through weak interactions to form a ribbon of molecules (Figure 7.51). In contrast to the previous two structures the units are not inverted due to the inversion centre being in a different position. The ribbons of molecules stack in layers, as shown in Figure 7.52.

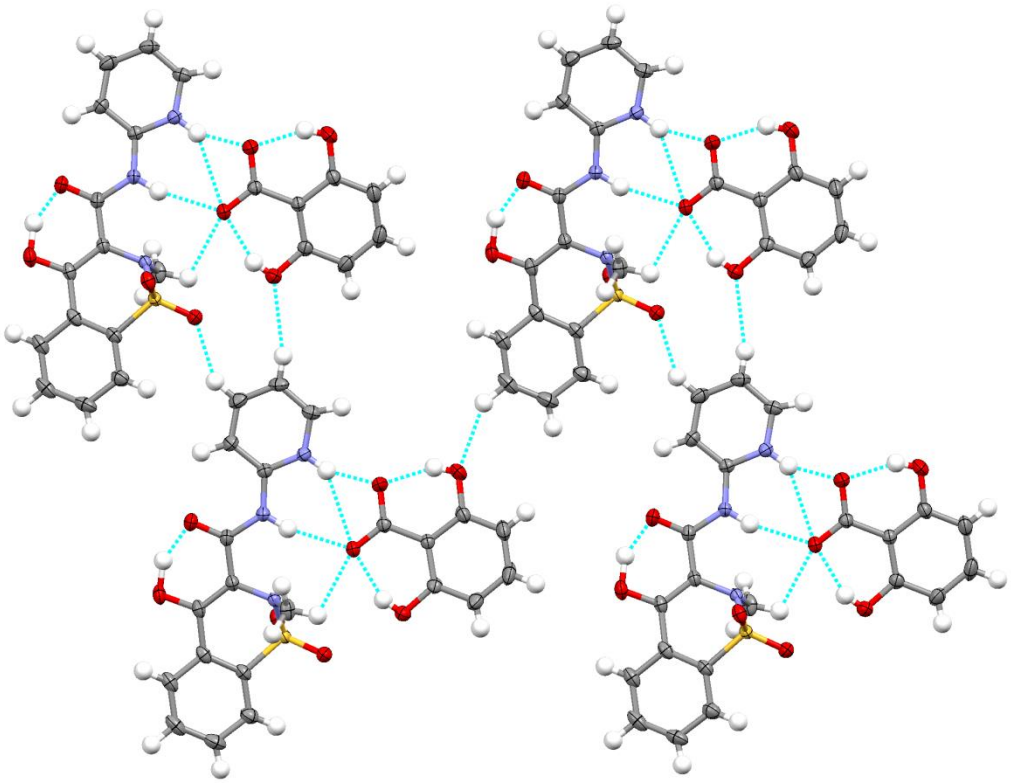

Figure 7.51 - Hydrogen bonding interactions in the PX^+ $26DHBA^-$ complex viewed down the crystallographic *b* axis.

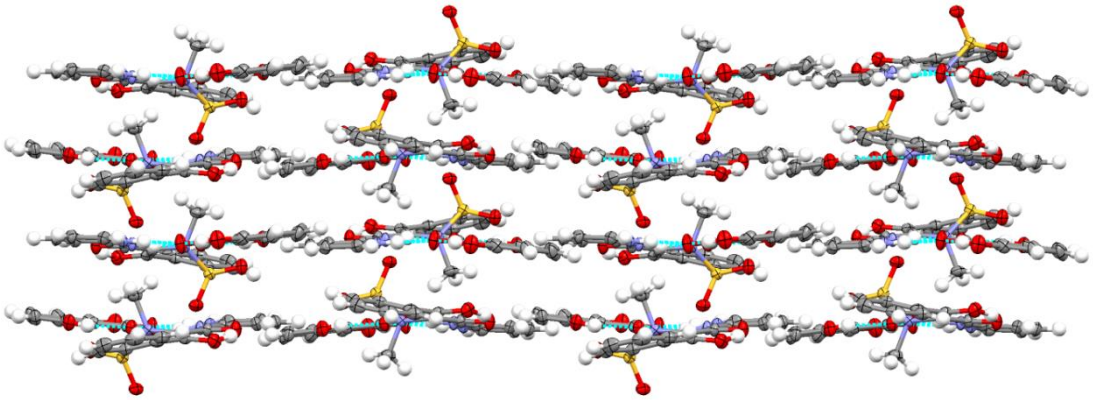

Figure 7.52 - Packing arrangement of molecules in the PX^+ $26DHBA^-$ complex viewed down the crystallographic *a* axis.

Interestingly, a complex of PX with the related co-former 2,5-dihydroxybenzoic acid in which PXN is present was recently reported[196] in which proton transfer has not occurred and the length of the hydrogen bond is 2.659(3) Å. This is to be expected since 26DHBA is a stronger acid with a lower pK_a (1.22) compared to 25DHBA with a pK_a of 2.97.

Table 7.15 - Hydrogen bonds in PX^+ $26DHBA^-$ (Å and °).

D-H···A	d(D-H)	d(H···A)	d(D···A)	<(DHA)
C(14)-H(8)···O(3)#1	0.98(3)	2.51(3)	3.435(3)	158(2)
N(2)-H(10)···O(5)	0.91(3)	2.17(3)	3.060(3)	166(3)
C(11)-H(5)···O(2)	0.97(3)	2.25(3)	2.806(3)	115(2)
N(3)-H(9)···O(5)	0.88(3)	2.63(3)	3.384(3)	144(3)
N(3)-H(9)···O(6)	0.88(3)	1.75(3)	2.591(3)	159(3)
C(13)-H(7)···O(8)#2	0.91(3)	2.59(3)	3.452(3)	159(3)
O(8)-H(15)···O(5)	0.76(4)	1.88(4)	2.589(3)	155(4)
O(7)-H(11)···O(6)	0.78(4)	1.81(4)	2.525(3)	151(4)
O(1)-H(19)···O(2)	1.09(5)	1.53(5)	2.552(3)	152(4)

Symmetry transformations used to generate equivalent atoms:
#1 -x+3/2,y+1/2,-z+1/2 #2 x+1/2,-y+1/2,z+1/2

Of the three PX^+ complexes discussed here, one shows a layered arrangement of molecules in the crystal structure, which was one of the original structural motivations (along with the production of disordered solid forms) of this study of PX complexes.

7.6 pK_a analysis of PX structures

In a recent study of complexes of PX with benzoic acids by Wales *et al.*[197] a trend between the pK_a of the co-former molecule and the tautomeric form adopted by the PX molecule was identified. The relationship indicates that of the substituted benzoic acid co-

formers used, those with the lowest and highest pK_a values produced complexes in which the PX molecule is present in its zwitterionic form. Those compounds with pK_a values in the middle region featured a non-ionised PX molecule. Table 7.16 show pK_a values for PX and the co-formers used in this study, as well as a relevant complex from the literature.[196] The new structures presented here support the findings by Wales *et al.* in that the pK_a values of the complexes featuring a neutral PX molecule lie in the middle region of the pK_a values of all of the co-former molecules and are of a similar value (~3) to those reported previously. However, in these complexes the pK_a value of co-formers which resulted in complexes with a zwitterionic PX molecule lies above those of the complexes with the neutral PX tautomer only. Salt forms of PX complexes were not discussed previously; however, the co-formers which formed salts in this work have the lowest pK_a values, as expected based on the ΔpK_a rule. The ΔpK_a value for all of the salt forms reported in this work lies in the intermediate region of the salt-co-crystal continuum, between 0 and 3, where it is difficult to predict whether a salt or co-crystal will form. For the TA system the value is closer to the region where a neutral complex is likely to form which correlates with the experimental outcome. The ΔpK_a value for all of the other co-crystal forms lies below 0 which correlates with the region where a co-crystal is expected to form in the salt-co-crystal continuum.

Table 7.16 - pK_{a1} (base) value for PX, pK_{a1} (acid) values for co-former molecules used and the ΔpK_a value comparing the two values.

	pK_{a1} (base) (predicted)[205]	**pK_{a1} (base) (measured)**			
PX	2.4 ± 0.4	2.25[206]			
Co-former	**pK_{a1} (acid) (predicted)[205]**	**pK_{a1} (acid) (measured)**	**PX**	**Form**	**ΔpK_a**
TA	3.0 ± 0.8	2.13[207]	PXN	Co-crystal	0.12
35DNBA	2.7 ± 0.9	2.82[207]	PXN	Co-crystal	−0.57
25DHBA	*3.0 ± 0.4*	*2.97[208]*	*PXN*	*Co-crystal*	*−0.72*
35DNSA	1.4 ± 0.4	0.70[209]	PX^+	Salt	1.55
26DHBA	1.8 ± 0.4	1.22[207]	PX^+	Salt	1.03
24DNBA	1.4 ± 0.4	1.43[208]	PX^+	Salt	0.82
TA	3.0 ± 0.8	2.13[207]	PXZ	Co-crystal	0.12
35DHBA	4.2 ± 0.4	4.04[208]	PXZ	Co-crystal	−1.79
34DHBA	4.4 ± 0.4	4.48[208]	PXZ	Co-crystal	−2.20
RES	9.6 ± 0.4	9.32[208]	PXZ	Co-crystal	−7.07

*italicised structures are from the literature.[196]

7.7 Thermal analysis of complexes

PXRD and thermal analysis of the product of evaporative crystallisations were carried out for all complexes to further confirm the presence of a new complex, determine the phase purity of the product and to investigate its thermal properties. Complexes that display interesting thermal behaviour are presented here.

7.7.1 Thermal analysis of disordered PXZ 34DHBA ACN complex

The complex of PXZ 34DHBA ACN shows interesting thermal behaviour with multiple endothermic and exothermic events observed in the DSC and HSM images. Figure 7.53 shows the HSM images in which the crystals become opaque upon desolvation of the acetonitrile from the complex with an onset temperature of 125 °C. This desolvation event is also present in the DSC trace (Figure 7.54) in which a broad endothermic event, characteristic of a solvent loss event, is observed at 120 - 130 °C. The desolvation event in the DSC is followed by an endothermic event characteristic of a melt at around 155 °C and an exothermic recrystallisation event at 163 °C. Recrystallisation can be observed in the HSM images where at 160 °C small crystallites are observed on the sides of the crystal (circled in red). In both thermal techniques this is followed by melting at 178 °C.

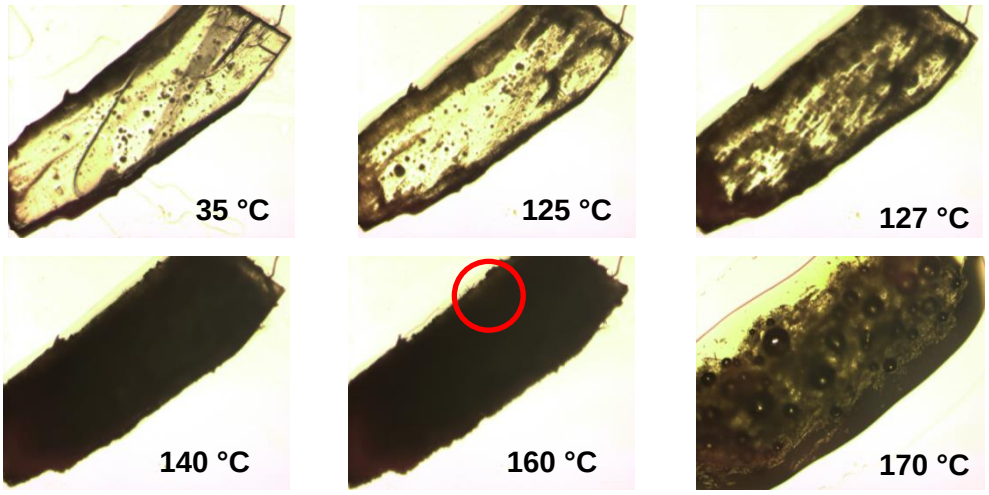

Figure 7.53 - HSM images showing thermal events of the PXZ 34DHBA ACN complex. Recrystallisation of small crystallites on the side of the crystal are circled in red.

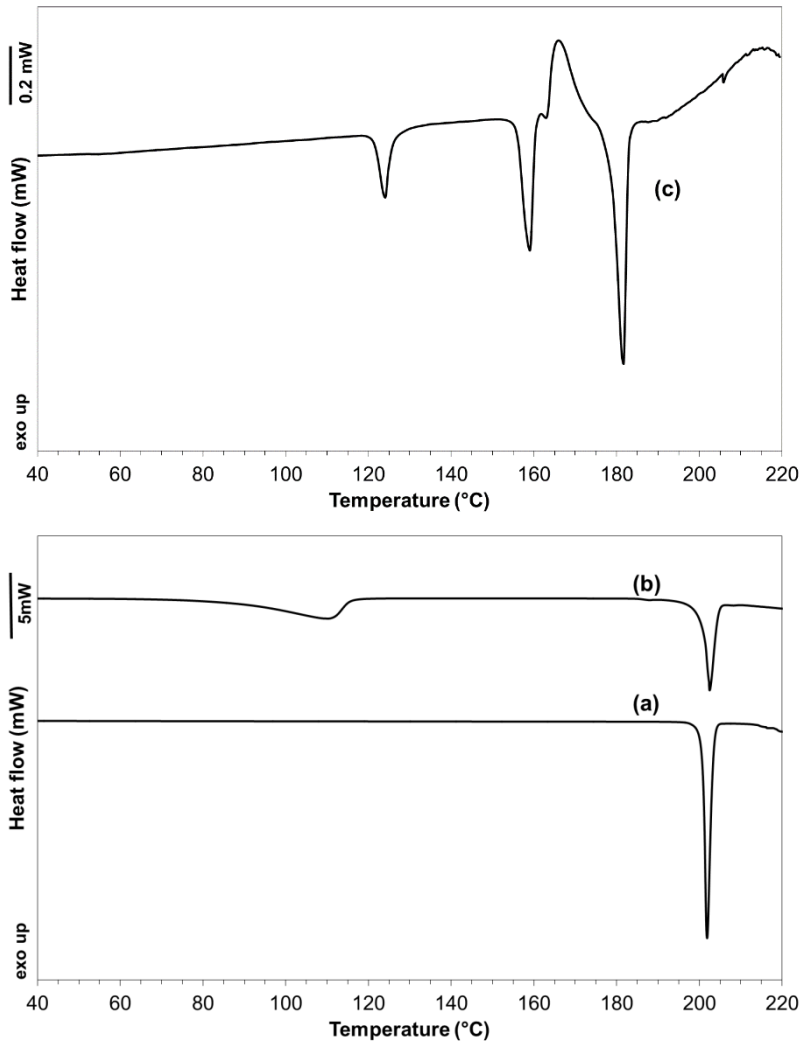

Figure 7.54 - DSC traces of (a) PX, (b) 34DHBA and (c) PXZ 34DHBA ACN complex.

As PX is present in its zwitterionic form in this solvated complex, similar experiments were carried out as those with the TA system (Section 7.4.4) to observe whether desolvation results in colour change of the complex. A microcrystalline powder of the bulk product of evaporative crystallisation was heated past the temperature of desolvation (140 °C) at 1 °C min^{-1}. However, unlike the PX TA solvates, heating did not result in a change in colour and the powder remained yellow. Figure 7.55 shows the PXRD pattern of the heated form and is presented with the pattern of the solvated form. New diffraction peaks in the pattern suggest upon desolvation the complex does form a different solid form, however the lack of colour change suggests the PX molecule remains in its zwitterionic form in this case. Extra peaks present in the measured pattern for the solvated form, that are not present in the calculated pattern, correlate with those in the pattern for the desolvated form which suggests that there may be non-solvated material present in the sample from evaporative crystallisation. This is most obvious in the peaks

at low angle values. For example, only one peak at 5.5° 2θ is present in the calculated pattern whereas in both measured patterns an additional peak is observed at around 6.1° 2θ which is more intense in the pattern for the desolvated form. The peak at 5.5° 2θ is more intense in the measured pattern for the solvated form.

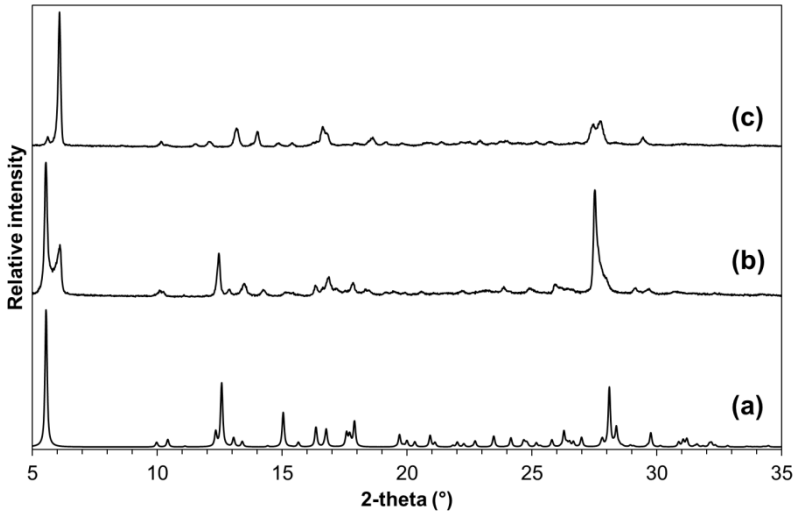

Figure 7.55 - PXRD patterns of (a) PX 34DHBA ACN and (b) PX 34DHBA ACN after heating to 140 °C.

7.7.2 Thermal analysis of PX^{+} $35DNSA^{-}$ complex

Figure 7.56 shows the PXRD pattern of the bulk material from the evaporative crystallisation of PX and 35DNSA along with the calculated pattern from the crystal structure of the complex. A good match is observed between the two patterns suggesting that the single crystal selected is representative of the bulk material.

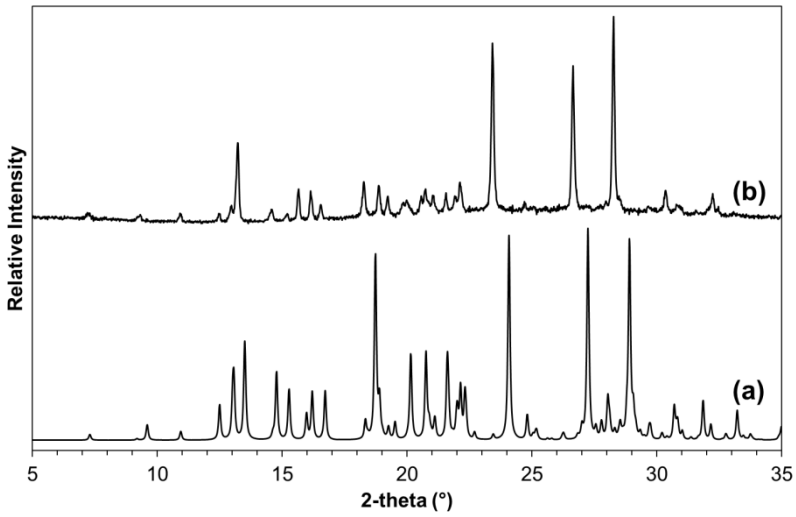

Figure 7.56 - PXRD patterns of (a) PX^{+} $35DNSA^{-}$ calculated and (b) PX^{+} $35DNSA^{-}$ bulk material measured.

Figure 7.57 shows the DSC trace of the product of the evaporative crystallisation of PX^+ $35DNSA^-$. The complex melts at 235 °C which is followed by an exothermic peak. This suggests that upon melting the complex recrystallises into another high temperature form which appears visually to be non-crystalline and resembles an oil type form (Figure 7.58).

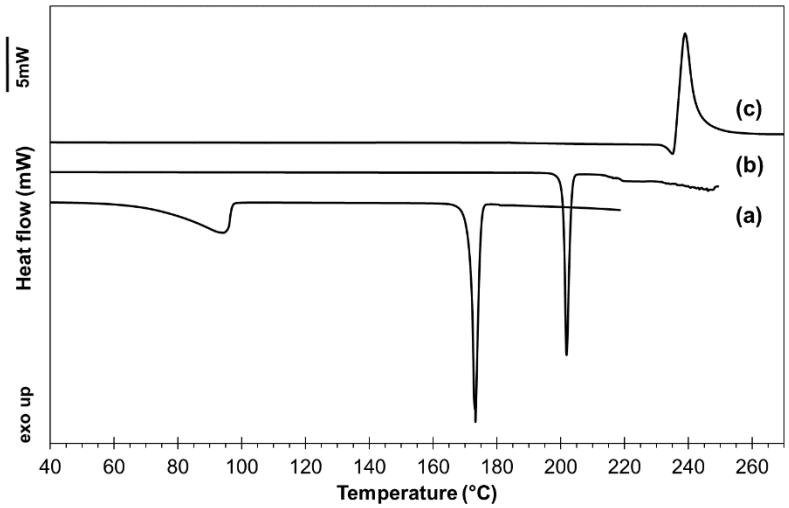

Figure 7.57 - DSC traces (a) 35DNSA, (b) PX and (c) PX^+ $35DNSA^-$ complex.

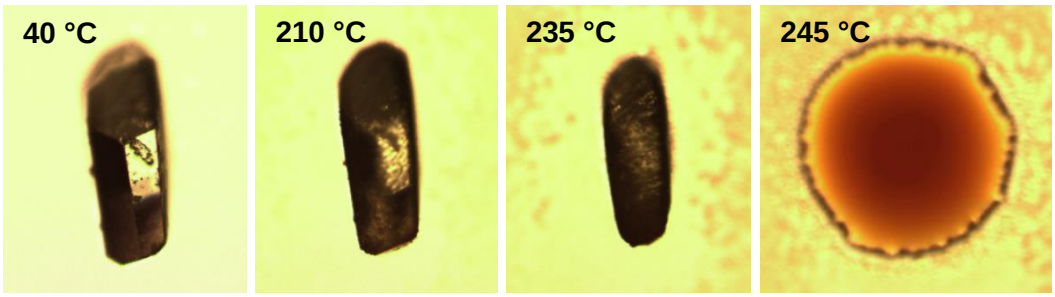

Figure 7.58 - HSM images of PX^+ $35DNSA^-$ complex.

7.7.3 Thermal analysis of PX^+ $24DNBA^-$ ACN complex

Figure 7.59 displays the PXRD pattern for the bulk product material from the evaporative crystallisation of PX and 24DNBA, along with the calculated pattern from the crystal structure of the solvated complex. The measured pattern is of poor quality and therefore it is difficult to draw a firm conclusion, however the peaks visible in the pattern demonstrate a good positional match with the stronger peaks in the calculated pattern for the PX^+ $24DNBA^-$ ACN complex.

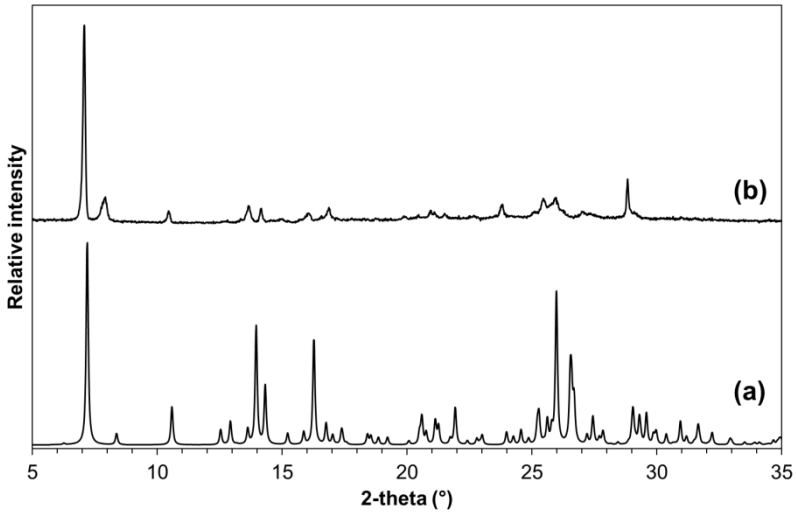

Figure 7.59 - PXRD patterns of (a) PX^+ $24DNBA^-$ ACN calculated and (b) PX^+ $24DNBA^-$ ACN bulk material measured.

Figure 7.60 shows the DSC trace of the solvated complex of PX^+ $24DNBA^-$. The DSC shows that the acetonitrile solvent is lost from the structure between 85-110 °C. This is followed by melting of the desolvated form, at a lower temperature than those of the two starting materials.

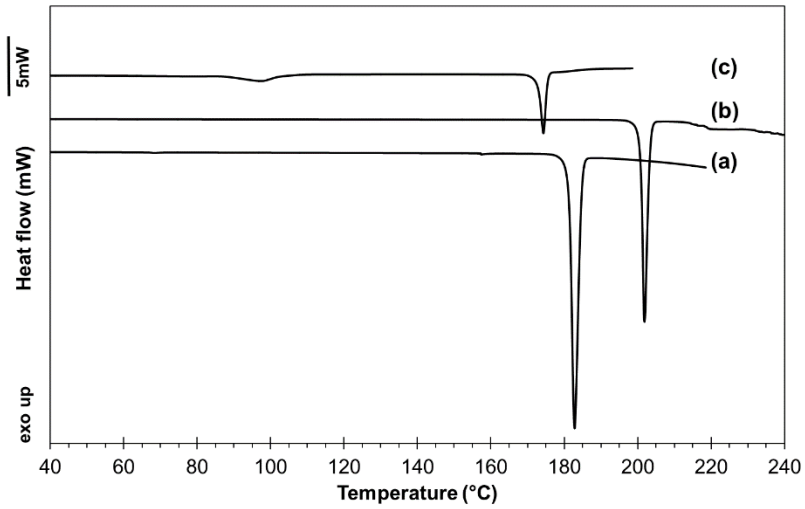

Figure 7.60 - DSC traces of (a) 24DNBA, (b) PX and (c) PX^+ $24DNBA^-$ ACN complex.

7.8 Conclusions

Ten multi-component molecular complexes of PX with planar co-former molecules have been presented with respect to their ionisation state and common synthons in their crystal structures have been identified. Moreover, in five of these complexes layered

architectures are present, and in one of the structures disorder is evident. Layering and disorder were the targets of this study towards the optimisation of properties through improved designed structural attributes. In all of the PX complexes which show a layered packing arrangement, the co-former molecule interacts with the PX molecule through its carboxylic acid group, in which two interactions are formed, encouraging the formation of the layered structure.

The structures have also been analysed with respect to their pK_a values and comparisons made with the ΔpK_a rule. It was found that the pK_a values of the co-formers support the findings of Wales *et al.*,[197] in that the co-formers which produced complexes containing PXN have pK_a values in the middle region of all of the co-formers used in the work. However, the pK_a value of all the co-formers which resulted in complexes containing PXZ is higher than those of co-formers producing PXN complexes. As expected, given the ΔpK_a rule, the co-formers which resulted in salt forms have the lowest pKa values and their resulting complexes have ΔpK_a values in the intermediate region of the salt-co-crystal continuum. With the exception of PX TA, the ΔpK_a value of all of the co-crystal forms reported in this work lie in the co-crystal region of the salt-co-crystal continuum.

Through this materials discovery study a multi-component molecular complex of PX and TA with particularly interesting structural and thermal behaviour was identified; the findings on which are summarised in Figure 7.61.

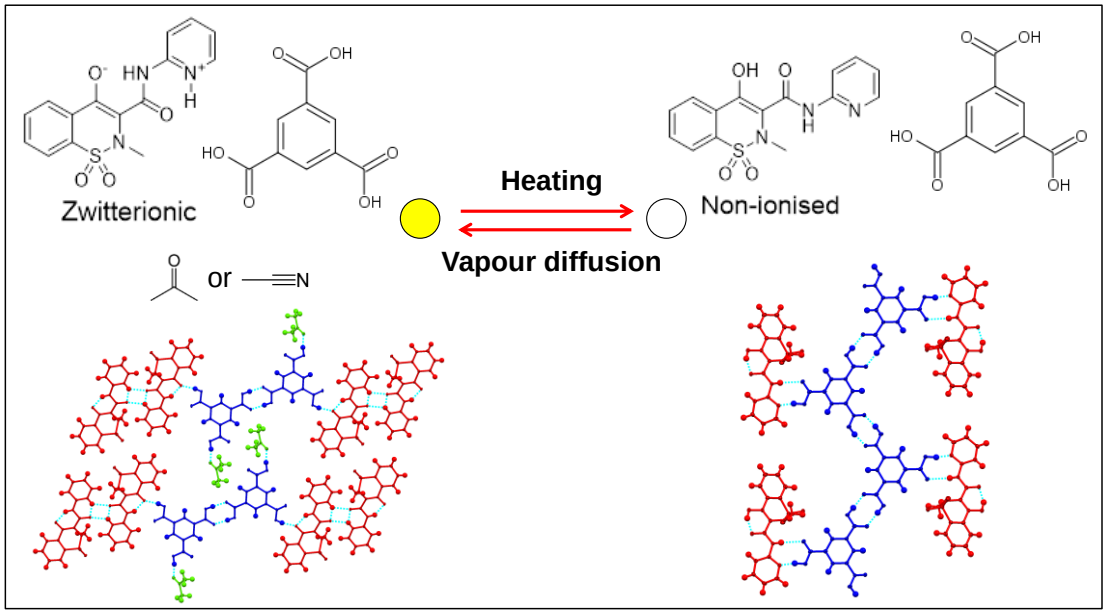

Figure 7.61 - Summary of findings on the solvates of a PX TA co-crystal.

Two solvated PX TA co-crystals were identified and their preparation using different crystallisation methods was investigated. Solution mediated (slurrying) methods were found to be an effective method of producing the solvates in larger quantities. The solvates show a layered packing arrangement that, upon desolvation by heating, undergoes significant structural rearrangement in the solid state to a non-layered structure featuring PXN. The tautomeric transition is further demonstrated by the change in colour of the material upon desolvation from yellow to white. The transition was also identified as reversible (to a fully crystalline, resolvated form) when the desolvated form is exposed to solvent vapours at ambient conditions. Multiple solid-state analytical methods were employed to study the transition upon desolvation including thermal analysis and spectroscopic methods.

Chapter 8

Disorder levels in 5-chlorouracil

8.1 Introduction and aims

As noted in Chapter 1, the presence of disorder can affect the solid-state properties of molecular materials, which was investigated for planar co-crystalline molecular complexes of piroxicam in Chapter 7. Here, disorder is investigated in a single component molecular material. 5-chlorouracil (5CL) is a planar molecule analogous to the anti-cancer agent 5-fluorouracil. Like several other 5-substituted uracils, 5CL has been found to exhibit orientational disorder across the long axis of the molecule in its crystal structure, whereby the molecule can lie in two distinct orientations.[120,210] These correspond to a 180° rotation about the Cl1-C1-C2-O2 axis where O1 can take the position of H3 and *vice versa* (Figure 8.1).

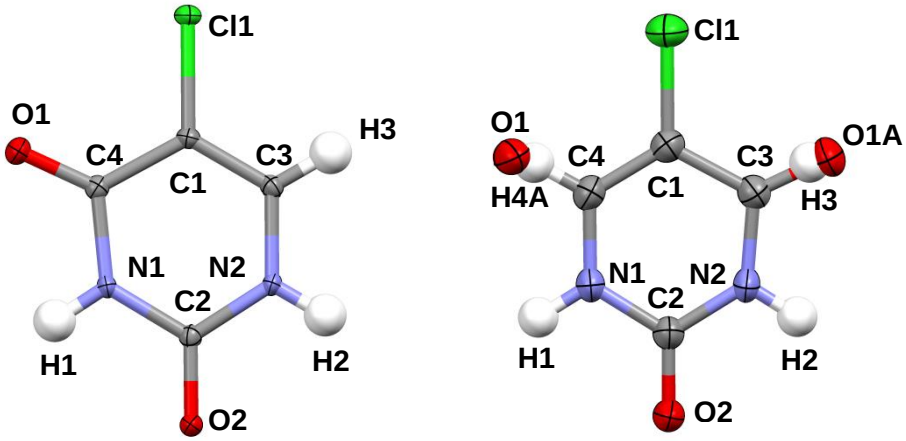

Figure 8.1 - The structure of 5-chlorouracil with the atoms labelled for (left) an ordered model and (right) a disordered model. Only the atoms for which the type of species is different in the disordered configuration are labelled as disordered, for clarity.

A simple CSD search for 5CL yields two structures (Table 8.1). The first structure shows disorder, the occupancies of the sites of which are unclear,[210,211] while the second structure, a lower temperature determination, shows disorder for all the non-hydrogen atoms modelled over two sites corresponding to the two orientations with a site occupancy ratio of 85:15.[210]

Table 8.1 - Structures of 5CL from a CSD search.

CSD Code	CLURAC10[211]	CLURAC11[210]
a	8.450(6)	8.439(1)
b	6.842(3)	6.841(1)
c	11.072(16)	9.368(1)
α	90	90
β	123.53(19)	104.20(1)
γ	90	90
V	533.607	524.327
Space group	$P2_1/c$	$P2_1/n$
Temp (K)	283-303	150
Disorder	One oxygen atom is disordered	The molecule is disordered over two sites with occupancies 0.85:0.15

In the $P2_1/n$ model, the symmetry of the molecule allows for a similar packing arrangement to be present in the reported structures of 5CL regardless of the presence of the disorder. N-H···O hydrogen bonds form $R_2^2(8)$ dimers with O2 being a hydrogen bond acceptor to two NH groups in bifurcated hydrogen bonds with lengths of 2.779(2) Å and 2.811(2) Å, respectively. There is also a weak C-H···O hydrogen bond between O1 and the hydrogen atom H3 on the adjacent molecule. These interactions form a planar ribbon arrangement of molecules with the chlorine atoms pointing in opposite directions. Cl1 forms a Cl···O contact with the O1 atom on the adjacent ribbon of molecules with a bond distance of 3.183(1) Å. These interactions link the ribbons of molecules together in a co-planar arrangement (Figure 8.2).

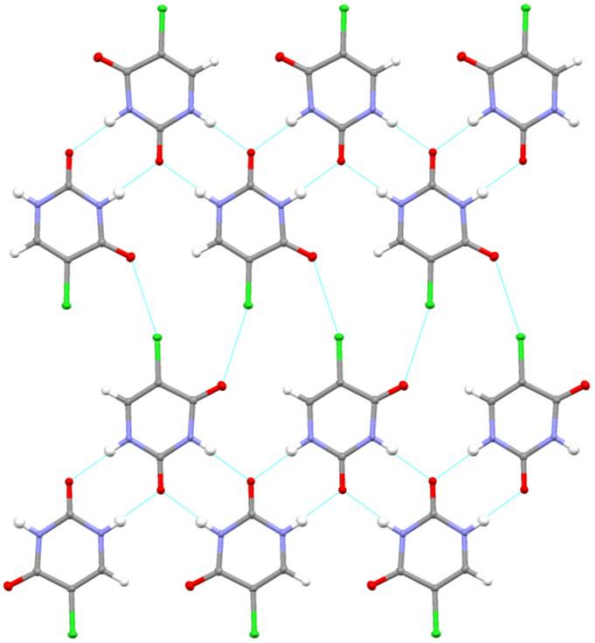

Figure 8.2 - Molecular ribbons forming sheets of 5CL molecules.

As the disorder results in the possibility of the molecules being positioned in one of two orientations throughout the crystal structure, the implication for the pattern of hydrogen bonding within this packing arrangement is significant. The orientations of the molecules can be described in relation to one another.[210]

Within each ribbon the molecules can be arranged in two ways that can be described as polar and non-polar (Figure 8.3). When classified as polar all of the C4=O1 carbonyl groups point in the same direction within a ribbon. When non-polar, alternate C4=O1 carbonyls point in opposite directions within a ribbon.

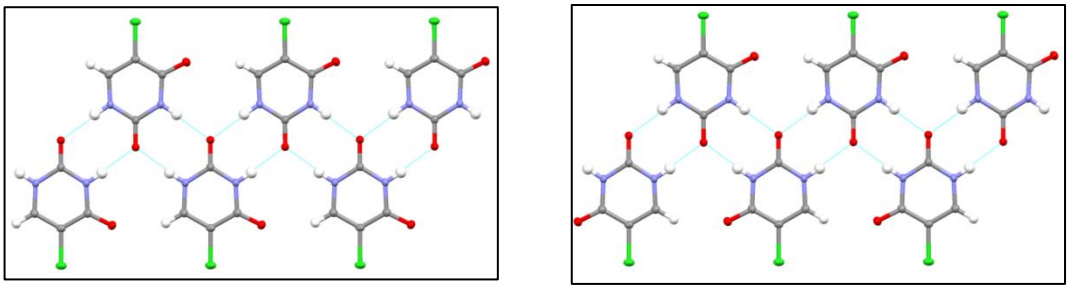

Polar arrangement Non-polar arrangement

Figure 8.3 - Polar and non-polar hydrogen bonding arrangement in ribbons of 5CL.

As discussed above, adjacent ribbons are held together by Cl···O interactions. The combination of ribbons of different orientation can be classified as parallel or anti-parallel.

This leads to four possible types of hydrogen bonding arrangements within each sheet (Figure 8.4).

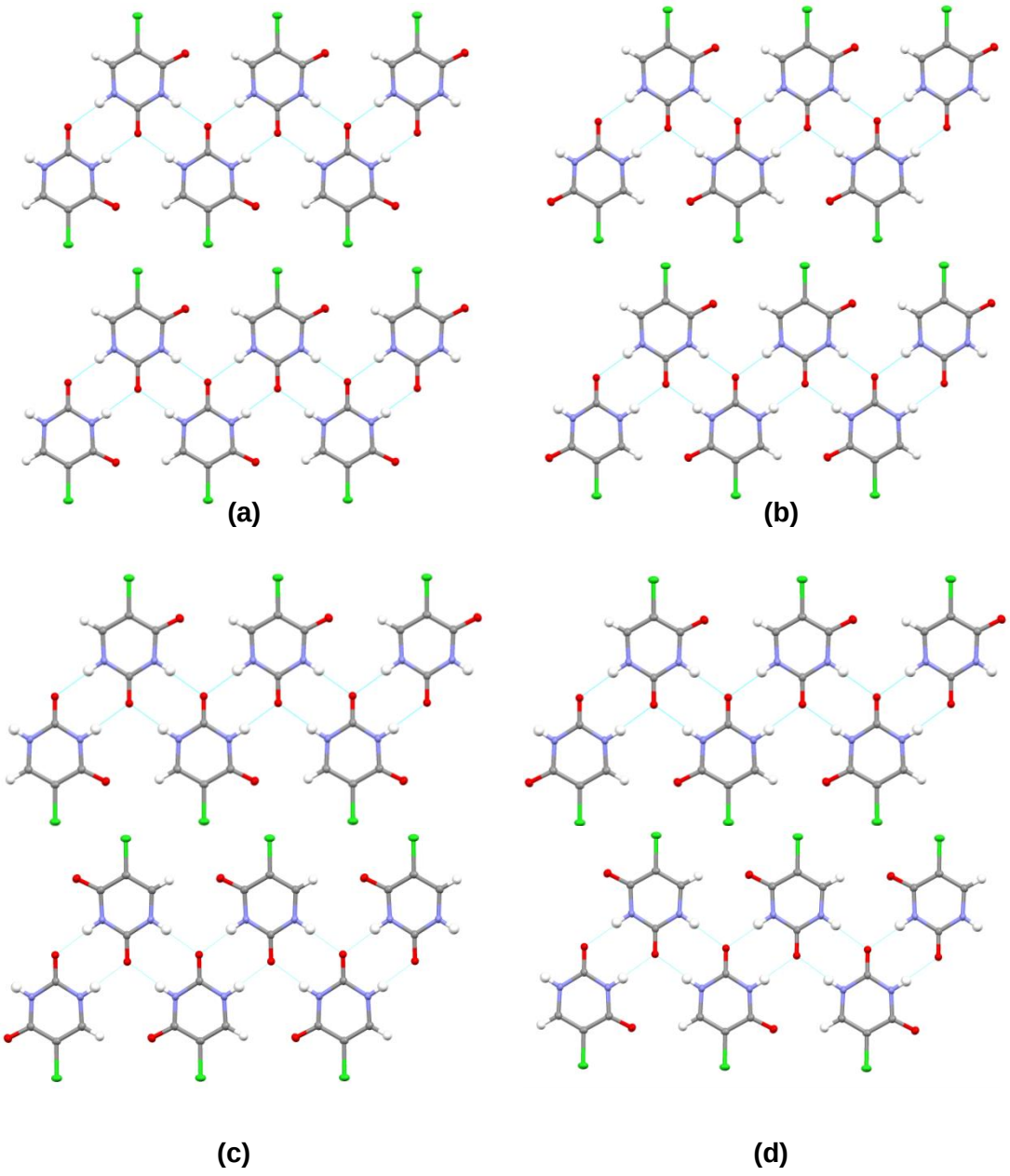

Figure 8.4 - Hydrogen bonding in 5CL sheets (a) polar parallel, (b) non-polar parallel, (c) polar anti-parallel and (c) non-polar anti-parallel

When looking at the overall packing of the molecules, the sheets of co-planar ribbons pack in layers along the (1 0 -3) planes (Figure 8.5).

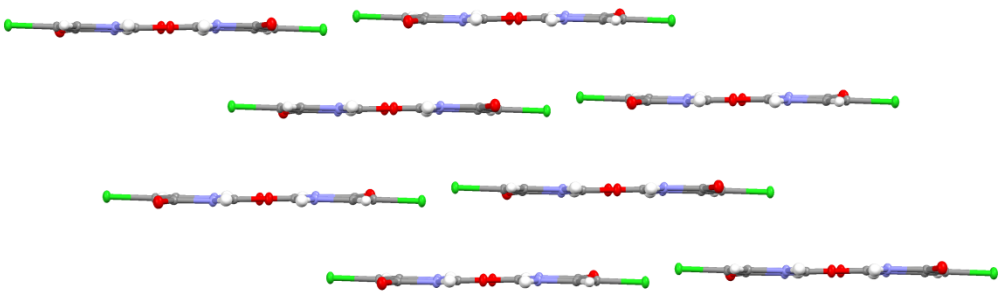

Figure 8.5 - Molecular packing of 5CL in layers viewing down the crystallographic *b* axis.

The orientational disorder in 5CL is similar to the disorder present in 5-ethynyluracil (eniluracil). Copley *et al.* suggested that the disorder in eniluracil could be directly related to the crystallisation conditions of that related material.[120] As noted above, the presence of such disorder in the structure may affect the bulk properties of the substance. For this disorder to be exploitable as a solid-state characteristic, its presence needs to be understood effectively (and ideally able to be designed into the formation of the crystalline solid form). It has also been noted that variation in samples due to disorder resulting from different growth conditions can also be readily confused with polymorphism, offering another rationale for attempting to control its presence during crystallisation.[120,212]

In order to probe the possible effect of the growth conditions on the level of disorder in 5CL, small scale crystallisation experiments were performed. Evaporative crystallisation methods at controlled temperatures, along with controlled cooling methods, were used to produce single crystals and the disorder present was characterised using single crystal X-ray diffraction. An overview of the initial crystal structures produced using these methods is presented, followed by subsequent systematic investigations towards the aim of establishing further understanding of the disorder in the 5CL system. This understanding would aid further studies into controlling this potentially important parameter for solid-state physical property optimisation.

8.2 Experimental information

8.2.1 Preparation of single crystals and structural information

Single crystal X-ray diffraction data were collected using two laboratory diffractometers: the Rigaku Oxford Diffraction Gemini Ultra A diffractometer and the Rigaku R-AXIS/RAPID diffractometer. All of the structures were solved by direct methods using SHELXS-2013[137] and refined using SHELXL-2013[138] within the WinGX[139,140] program.

Structure 1 - Ordered

10 mg of 5CL was dissolved in the minimum amount of water and crystallisation was facilitated through evaporation at 30 °C. A suitable single crystal was selected and data were collected at 100 K using a Rigaku Oxford Diffraction Gemini Ultra A CCD diffractometer with Mo-K_α radiation. Atom H3 was constrained in an idealised position based on a riding model.

Structure 2 – 94(1):6(1) occupancy ratio

Crystals were grown through controlled cooling using the Cambridge Reactor Design Polar Bear Plus. 3.8 mg of 5CL was dissolved in 1 ml of water in a 1.5 ml vial and subject to a cooling profile of 60 °C to 5 °C at 0.01 °C min^{-1}. Data were collected at 298 K using a Rigaku Oxford Diffraction Gemini Ultra A CCD diffractometer with Mo-K_α radiation. Disordered hydrogen atoms were constrained in an idealised position based on a riding model.

Structure 3 - Disorder of equal (50:50) occupancy

Crystals were grown through controlled cooling using the ReactArray Microvate. 10 mg of 5CL was weighed into the 2.5 ml vials and filled with a mixed solvent of acetonitrile and water in a 1:2 ratio. The temperature was then ramped to 80 °C at 5 °C min^{-1} and held for 2 hours to ensure complete dissolution. The lids of the vials were removed to allow for evaporation during the cooling phase. The temperature was then lowered to 40 °C at a rate of 0.1 °C min^{-1}. At the end of the experiment the temperature was held at 40 °C prior to the selection of a suitable crystal for diffraction. Data were collected at 100 K using the Rigaku R-AXIS-RAPID diffractometer with Mo-K_α radiation. The disordered hydrogen atom was constrained in an idealised position based on a riding model.

Structure 4 – 62(1):38(1) occupancy ratio

Crystals were grown from a cooling environment using the ReactArray Microvate. 10 mg of 5CL was weighed into the 2.5 ml vials and filled with a mixed solvent of ethanol and water in a 1:2 ratio. The temperature was then ramped to 80 °C at 5 °C min^{-1} and held for 2 hours to ensure complete dissolution. The lids of the vials were removed to allow for evaporation to occur during the cooling phase. The temperature was then lowered to 40 °C at a rate of 0.1 °C min^{-1}. At the end of the experiment the temperature was held at 40 °C until a crystal was selected for diffraction. Data were collected at 100 K using the Rigaku R-AXIS RAPID diffractometer with Mo-K_α radiation. All hydrogen atoms were constrained in idealised positions based on a riding model.

Variable-temperature study (298 and 100 K): Structures 5 and 6

A second crystal was selected from the same crystallisation experiment as Structure 3. A data collection was carried out at 298 K (Structure 5) and immediately followed by another data collection at 100 K (Structure 6) on this second single crystal. Data were collected using the Rigaku Oxford Diffraction Gemini Ultra A CCD diffractometer with Mo-K_α radiation. For both Structures 5 and 6a all hydrogen atoms were constrained in idealised positions based on a riding model. For Structure 6b only the disordered hydrogen atom was constrained in an idealised position based on a riding model.

Further crystallographic information for structures collected in this study is shown in Table 8.2. Some of the structures were refined in two crystallographic models; crystallographic information is labelled a and b in such cases.

Table 8.2 - Crystallographic information for 5CL structures from crystals obtained from different experiments.

	1	**2**	**3**	**4**	**5**	**6a**	**6b**
Disorder occupancy	1.0	0.937(4)	0.5	0.621(11)	0.607(7)	0.588(9)	0.5
Formula	$C_4H_3N_2O_2Cl$	$C_4H_3N_2O_2Cl$	$C_4H_3N_2O_2Cl$	$C_4H_3N_2O_2Cl$	$C_4H_3N_2O_2Cl$	$C_4H_3N_2O_2Cl$	$C_4H_3N_2O_2Cl$
M / g mol^{-1}	146.53	146.53	146.53	146.53	146.53	146.53	146.53
T (K), radiation	100, Mo K_α	298, Mo K_α	100, Mo K_α	100, Mo K_α	298, Mo K_α	100, Mo K_α	100, Mo K_α
Space Group	$P2_1/n$	$P2_1/n$	$P2_1/m$	$P2_1/n$	$P2_1/n$	$P2_1/n$	$P2_1/m$
a (Å)	8.4270(4)	8.4617(11)	5.4557(4)	8.454(3)	8.4601(4)	8.4215(5)	5.4612(3)
b (Å)	6.8330(3)	6.8455(11)	6.8341(5)	6.811(3)	6.8382(3)	6.8350(3)	6.8392(3)
c (Å)	9.3072(6)	9.5264(13)	7.0245(7)	9.316(4)	9.5306(6)	9.3290(5)	7.0136(4)
α (°)	90	90	90	90	90	90	90
β (°)	104.203(5)	104.432(13)	95.950(7)	104.547(1)	104.537(6)	104.312(6)	95.971(5)
γ (°)	90	90	90	90	90	90	90
Volume ($Å^3$)	519.54(5)	534.40(14)	260.50(2)	519.2(1)	533.71(5)	520.32(5)	260.54(2)
Z	4	4	2	4	4	4	2
ρ_{cal}/ Mg cm^{-3}	1.873	1.821	1.868	1.875	1.824	1.871	1.868
μ/mm^{-1}	0.639	0.621	0.637	0.639	0.622	0.638	0.637
θ range/°	2.924-28.907	2.884-25.014	3.76-27.48	3.75-25.01	2.882-25.013	2.920-25.022	2.920-25.027
Completeness	99.9 %	100 %	99.8 %	99.9 %	100 %	100 %	100 %
Refln. Collected	4542	2381	3469	5057	3887	3738	1943
Independent	1261	939	642	912	937	918	507
Refln (obs.I>2σ(I))	1146	592	572	778	701	777	483
R_{int}	0.0179	0.0406	0.0244	0.0277	0.0246	0.0226	0.0195
Parameters	90	94	56	56	86	71	56
GooF	1.058	1.005	1.137	1.363	1.308	1.386	1.164
R_1 (obs)	0.028	0.044	0.026	0.110	0.069	0.085	0.023
R_1 (all)	0.031	0.081	0.030	0.124	0.091	0.099	0.025
wR_2 (all)	0.081	0.086	0.073	0.242	0.146	0.173	0.065
$\rho_{max,min}$/e $Å^{-3}$	0.528, -0.206	0.225,-0.221	0.342, -0.061	1.178,-1.395	0.558,-0.663	0.881,-1.371	0.258,-0.239

Crystals selected from the same batch: Structures 7-11

A saturated solution of 5CL (3.8 mg ml^{-1}) was prepared in a 1.5 ml glass vial and dissolved in 1.5 ml of water. All crystals (7-11) were selected from the same vial grown by cooling from 70 °C to 20 °C at 0.3 °C min^{-1} from water using the Polar Bear Plus crystalliser from Cambridge Reactor Design. All data were collected at the same temperature (298 K). Single crystal X-ray diffraction data were collected using a Rigaku Oxford Diffraction Gemini Ultra A CCD diffractometer with Mo-K_α radiation. Table 8.3 and Table 8.4 show the crystallographic information for data obtained in this study. Repeat collections were carried out (from the same crystal) for Structure 8 (labelled 8.1, 8.2 and 8.3). Some of the structures were refined in two crystallographic models; crystallographic information is labelled a and b in such cases. The hydrogen atom models used are summarised below.

Structure 7 – The disordered hydrogen atoms were constrained in idealised positions based on a riding model.

Structure 8.1 – The disordered hydrogen atoms were constrained in idealised positions based on a riding model.

Structure 8.2 – The disordered hydrogen atoms were constrained in idealised positions based on a riding model.

Structure 8.3 – The disordered hydrogen atoms were constrained in idealised positions based on a riding model.

Structure 9a – All of the hydrogen atoms were constrained in idealised positions based on a riding model.

Structure 9 – The disordered hydrogen atom was constrained in an idealised position based on a riding model.

Structure 10a – All of the hydrogen atoms were constrained in idealised positions based on a riding model.

Structure 10b – the hydrogen atoms were refined freely.

Structure 11a – All of the hydrogen atoms were constrained in idealised positions based on a riding model.

Structure 11b – The disordered hydrogen atom was constrained in idealised positions based on a riding model.

Crystallisation in the presence of Pluronic P123: Structures 12 and 13

As part of the systematic study of 5CL crystallisations under different conditions, sample crystallisations were also carried out in the presence of the polymer additive Pluronic

P123 (PP123). The primary aim of the additive experiments was morphology control of 5CL, which crystallises in a plate-like morphology in the absence of additive (see Chapter 1 for an account of the importance of morphology control in crystallisation). Cooling crystallisations of 5CL in the presence of PP123 were carried out using the Cambridge Reactor Design Polar Bear Plus at 1 ml scale. 3.8 mg of 5CL and 25 mg of PP123 were dissolved in 1 ml of water and the solution was subject to a linear cooling profile of 60 °C to 5 °C at a rate of 0.05 °C min^{-1}. Single crystal X-ray diffraction data were collected from two selected crystals (12 and 13) using a Rigaku Oxford Diffraction Gemini Ultra A CCD diffractometer with Mo-K_α radiation. Further crystallographic information is reported in Table 8.5. Both structures were refined in two crystallographic models; crystallographic information is labelled a and b for these.

Structure 12a – The disordered hydrogen atoms were constrained in idealised positions based on a riding model.
Structure 12b – The disordered hydrogen atom was constrained in an idealised position based on a riding model.
Structure 13a – All of the hydrogen atoms were constrained in idealised positions based on a riding model.
Structure 13b – The disordered hydrogen atom was constrained in an idealised position based on a riding model.

Table 8.3 - Crystallographic information for 5CL structures from crystals obtained from the same batch.

	7	**8.1**	**8.2**	**8.3**	**9a**	**9b**
Disorder occupancy	0.826(7)	0.882(4)	0.881(4)	0.886(5)	0.504(11)	0.5
Formula	$C_4H_3N_2O_2Cl$	$C_4H_3N_2O_2Cl$	$C_4H_3N_2O_2Cl$	$C_4H_3N_2O_2Cl$	$C_4H_3N_2O_2Cl$	$C_4H_3N_2O_2Cl$
M / g mol^{-1}	146.53	146.53	146.53	146.53	146.53	146.53
T (K), radiation	298, Mo K_α	298, Mo K_α	298, Mo K_α	298, Mo K_α	298, Mo K_α	298, Mo K_α
Space Group	$P2_1/n$	$P2_1/n$	$P2_1/n$	$P2_1/n$	$P2_1/n$	$P2_1/m$
a (Å)	8.4643(13)	8.4622(4)	8.4632(5)	8.4687(7)	8.4796(10)	5.5348(6)
b (Å)	6.8305(14)	6.8449(4)	6.8420(4)	6.8470(5)	6.8555(9)	6.8501(10)
c (Å)	9.510(2)	9.5244(7)	9.5159(8)	9.5314(9)	9.5279(14)	7.1131(9)
α (°)	90	90	90	90	90	90
β (°)	104.407(18)	104.359(6)	104.324(7)	104.380(9)	104.300(13)	96.969(11)
γ (°)	90	90	90	90	90	90
Volume ($Å^3$)	532.53(18)	534.45(6)	533.89(7)	535.36(8)	536.71(13)	267.69(6)
Z	4	4	4	4	4	2
ρ_{cal}/ Mg cm^{-3}	1.828	1.821	1.823	1.818	1.813	1.818
μ/mm^{-1}	0.623	0.621	0.622	0.620	0.619	0.620
θ range/°	3.714-24.997	3.706-25.002	2.887-25.016	2.883-25.022	3.702-24.984	3.709-24.983
Completeness	99.8 %	96.2 %	98.2 %	100 %	94.3 %	94.2 %
Refln. Collected	1922	1962	1861	3576	1984	1034
Independent	934	902	922	941	886	487
Refln (obs.I>2σ(I))	436	629	663	625	567	391
R_{int}	0.0922	0.0217	0.0210	0.0384	0.0387	0.0304
Parameters	94	100	100	100	86	56
GooF	1.000	1.046	1.027	1.055	1.279	1.026
R_1 (obs)	0.086	0.034	0.034	0.037	0.087	0.035
R_1 (all)	0.149	0.057	0.056	0.070	0.133	0.047
wR_2 (all)	0.298	0.086	0.086	0.091	0.232	0.082
$\rho_{max,min}$/e $Å^{-3}$	0.473,-0.599	0.242,-0.231	0.167,-0.234	0.183,-0.247	0.600,-0.725	0.172,-0.181

Table 8.4 - Crystallographic information for 5CL structures from crystals obtained from the same batch.

	10a	**10b**	**11a**	**11b**
Disorder occupancy	0.52(2)	0.5	0.517(17)	0.5
Formula	$C_4H_3N_2O_2Cl$	$C_4H_3N_2O_2Cl$	$C_4H_3N_2O_2Cl$	$C_4H_3N_2O_2Cl$
M / g mol^{-1}	146.53	146.53	146.53	146.53
T (K), radiation	298, Mo K_α	298, Mo K_α	298, Mo K_α	298, Mo K_α
Space Group	$P2_1/n$	$P2_1/m$	$P2_1/n$	$P2_1/m$
a (Å)	8.4617(6)	5.5299(4)	8.4588(5)	5.5314(3)
b (Å)	6.8432(5)	6.8396(6)	6.8443(4)	6.8435(4)
c (Å)	9.5258(7)	7.1105(5)	9.5288(7)	7.1141(4)
α (°)	90	90	90	90
β (°)	104.366(7)	96.977(7)	104.422(6)	96.967(6)
γ (°)	90	90	90	90
Volume (Å^3)	534.34(7)	266.94(4)	534.28(6)	267.31(3)
Z	4	2	4	2
ρ_{cal}/ Mg cm^{-3}	1.821	1.823	1.822	1.821
μ/mm^{-1}	0.621	0.622	0.621	0.621
θ range/°	2.885-25.010	2.886-25.012	3.706-25.017	3.711-25.001
Completeness	100 %	100 %	99.1 %	98.6 %
Refln. Collected	2433	1312	2205	1163
Independent	939	517	931	510
Refln (obs.I>2σ(I))	610	422	705	453
R_{int}	0.0349	0.0280	0.0168	0.0154
Parameters	77	60	92	56
GooF	1.217	1.102	1.260	1.084
R_1 (obs)	0.1077	0.032	0.087	0.030
R_1 (all)	0.1480	0.044	0.113	0.035
wR_2 (all)	0.230	0.082	0.196	0.073
$\rho_{max,min}$/e Å^{-3}	0.936,-0.764	0.185,-0.201	0.757,-0.841	0.226,-0.197

Table 8.5 - Crystallographic information for 5CL structures from crystals grown in the presence of a polymer additive in the same batch.

	12a	**12b**	**13a**	**13b**
Disorder occupancy	0.723(4)	0.5	0.613(8)	0.5
Formula	$C_4H_3N_2O_2Cl$	$C_4H_3N_2O_2Cl$	$C_4H_3N_2O_2Cl$	$C_4H_3N_2O_2Cl$
M / g mol^{-1}	146.53	146.53	146.53	146.53
T (K), radiation	298, Mo K_α	298, Mo K_α	298, Mo K_α	298, Mo K_α
Space Group	$P2_1/n$	$P2_1/m$	$P2_1/n$	$P2_1/m$
a (Å)	8.4920(13)	5.5132(6)	8.4627(15)	5.5159(9)
b (Å)	6.8497(11)	6.8309(9)	6.8457(9)	6.8415(9)
c (Å)	9.557(2)	7.1316(10)	9.5484(14)	7.1333(10)
α (°)	90	90	90	90
β (°)	104.719(19)	97.025(11)	104.673(17)	97.119(15)
γ (°)	90	90	90	90
Volume ($Å^3$)	537.67(17)	266.56(6)	535.13(15)	267.11(7)
Z	4	2	4	2
ρ_{cal}/ Mg cm^{-3}	1.810	1.826	1.819	1.822
μ/mm^{-1}	0.618	0.623	0.620	0.622
θ range/°	2.869-25.681	2.878-25.242	2.876-25.671	2.878-25.670
Completeness	100 %	100 %	100 %	100 %
Refln. Collected	2388	1257	2271	1204
Independent	1025	551	1020	552
Refln (obs.I>2σ(I))	615	446	735	496
R_{int}	0.0344	0.0265	0.0178	0.0147
Parameters	100	56	86	56
GooF	1.035	1.009	1.287	1.182
R_1 (obs)	0.048	0.043	0.082	0.038
R_1 (all)	0.085	0.056	0.110	0.042
wR_2 (all)	0.128	0.106	0.200	0.102
$\rho_{max,min}$/e $Å^{-3}$	0.379,-0.224	0.399,-0.233	0.527,-0.771	0.376,-0.201

8.3 Initial crystal structures

Structures determined from different crystals selected from different experiments showed variable levels of refined orientational disorder across the 5CL molecule (Table 8.2).

8.3.1 Structure 1 – Ordered

The crystal structure of 5CL that refines as an ordered model crystallises in the monoclinic space group, $P2_1/n$. The ordered nature of the crystal structure could be attributed to the slow conditions used for crystal growth (evaporation from water). Further investigation into this structure showed that a low level of disorder could be modelled with 98:2 ratio of orientations, but some parameters in this refinement were poorly determined leading to the conclusion that the structure is more accurately described by the ordered model.

8.3.2 Structure 2 – 94(1):6(1) occupancy ratio

A crystal selected from a crystallisation carried out by slow cooling (0.01 °C min^{-1}) also gave a refinement with a low level of disorder in the $P2_1/n$ model (94(1):6(1)). This finding supports the conclusion that slow conditions used for growth may enable a crystal structure with a more ordered nature whereby the molecules are allowed to assemble in the presumably lowest energy configuration.

8.3.3 Structure 3 – Disorder of equal occupancy[2]

This data collection gave a refined structure of 5CL with previously unreported unit cell dimensions and was solved in the space group, $P2_1/m$ (Table 8.2). Figure 8.6 illustrates the atoms present in the asymmetric unit with the atoms Cl1, C1, C3 and O2 lying on a mirror plane. Atoms O1 and H2 are thus disordered with equal occupancy (50:50) while atoms N1, H1 and C2 are fully occupied.

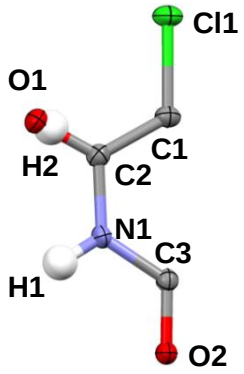

Figure 8.6 - The asymmetric unit in the $P2_1/m$ model of 5CL with the atoms labelled.

[2] This structure was subsequently reported in the CSD as a private communication (CLURAC12) after the work reported here was carried out.

In the ordered structure (Structure 1, above) the C1-C4 bond length (1.454(2) Å) is longer than that of C1=C3 (1.350(2) Å), as expected since C1=C3 is a double bond. However, in this structure with disorder of equal occupancy the comparable bond lengths are equal at 1.399(2) Å, supporting the equal occupancy disorder model.

8.3.4 Structure 4 – 62(1):38(1) occupancy ratio

This disordered structure was solved in the space group $P2_1/n$ with the two orientations refined to a final occupancy ratio of 62(1):38(1). Table 8.2 shows that the refinement of this structure resulted in relatively high values for the refinement parameters. This may indicate that the structure may require further modelling to investigate the possibility that this structure may in fact represent a 50:50 disorder situation as observed in Structure 3.

8.4 Systematic investigations

The finding of variable levels of disorder in crystals prepared by different crystallisation conditions led to more systematic investigations into a number of parameters that may affect the level of refined disorder in these 5CL structures.

8.4.1 Variable temperature X-ray diffraction study

A study was carried out to determine whether the X-ray diffraction data collection temperature affects the disorder occupancy, which may indicate solid state changes in the hydrogen bonding pattern as the temperature is lowered.

A data collection was carried out at 298 K (Structure 5), immediately followed by another data collection at 100 K (Structure 6) on the same single crystal. Both structures were solved in space group $P2_1/n$ and show orientational disorder. Structures 5 and 6a have disorder occupancies of the two orientations of 61(1)% and 59(1)%, respectively. This minor discrepancy is not significant, particularly due to the poor quality of refinement in Structure 6 in which it was not possible to refine some of the atoms anisotropically. Such high values of the refinement parameters led to attempts to resolve the structure in the $P2_1/m$ model, in which an improved refinement was obtained (6b). Attempts to solve the dataset obtained at 298 K in the $P2_1/m$ model were unsuccessful which could reflect the quality of the dataset.

The crystal used for these data collections was selected from the same crystallisation experiment as that used for the data collection of Structure 3, so it was expected that the disorder would be of equal occupancy in both cases. However, the overall refinements in the $P2_1/n$ model are not sufficiently well defined to allow proper discrimination of disorder

levels. This finding was the first indication that consistency in disorder modelling may be difficult to achieve in these experiments.

All future data collections were performed, wherever possible, at room temperature, since the physical properties that are of interest will be measured at room temperature and it is difficult to be certain that the temperature has no impact on the disorder.

8.4.2 Homogeneity of disorder occupancy from crystals from the same batch

The aim of this experiment was to investigate the homogeneity of the level of disorder in 5CL across multiple crystals selected from the same experimental set-up by carrying out full structural determinations for each crystal (Structures 7-11). Data collections were carried out for five initial crystals with repeat determinations carried out for one of the crystals (Structures 8.1, 8.2, 8.3). Table 8.3 and Table 8.4 show the crystallographic data for the collections.

All of the structures were initially solved in the $P2_1/n$ model where Structures 7 and 8 showed disorder of 83(1)% and 88(1)%, respectively. The low level of disorder across the molecule in Structure 8 allowed the data to be refined effectively in the $P2_1/n$ model. Furthermore, in repeat determinations using the same crystal, the disorder level remained constant at 88%.

In contrast, structure solution of Structures 9a, 10a and 11a in the $P2_1/n$ model produced poor refinement parameters and the occupancy level was close to equal in each of the structures (50(1)%, 52(2)% and 52(2)%). As a result, the structures were then solved in the $P2_1/m$ model (9b, 10b and 11b) in which improved refinement parameters were obtained for each structure.

These results show that there is variability in the disorder level of crystals selected from the same vial under the conditions used to produce the crystals. This may be a result of each individual crystal having different growth kinetics; the small-scale crystallisation system did not have any agitation, for example. It may also reflect the lack of definitive indications from the occupancy refinements, as noted above. This finding makes determination of the effect of the crystallisation conditions on the overall disorder level challenging and sounds a note of caution in this area; each crystal could have a different level of disorder and it is not clear that the structural refinements are able fully to discriminate the disorder levels that may be present.

8.4.3 Effect of a polymer additive on disorder

As part of the examination of the manner in which different environments may affect disorder, the use of additives were also explored. A polymer additive (PP123) was dissolved in the aqeuous crystallisation solution. Interestingly, the presence of the additive resulted in a significant change in morphology from plates to needles when compared to the control crystallisation containing 5CL alone (Figure 8.7). It is worthy of note that such a morphology modification was the primary motivation for the additive study; during the project, these findings prompted the use of PP123 additive in the morphology studies reported in Chapters 4 and 6. The unfavourable morphology resulting from additive crystallisations of 5CL (producing needle-like crystals) and the formation of very small needle-like crystals in the presence of stirring resulted in this aspect of the study not being pursued further.

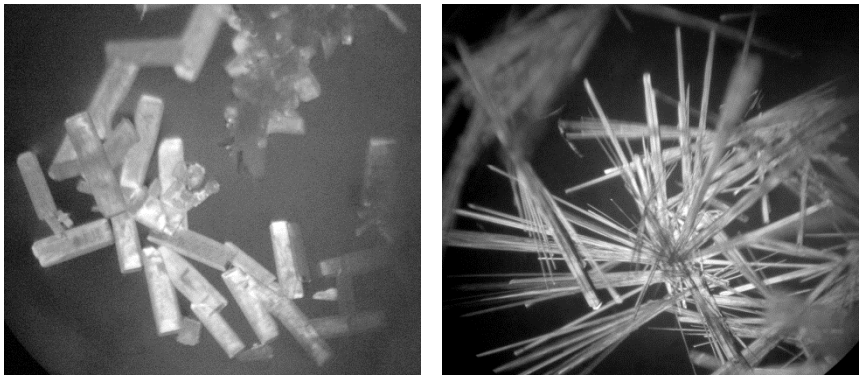

Figure 8.7 - Microscope images of 5CL crystals: (left) plate-like crystals produced in the presence of no additive and (right) needle-like crystals produced in the presence of PP123.

Data collections were also obtained for the needle-like crystals produced in the presence of the additive in order to assess the possible effect of the additive on the disorder occupancy (Table 8.5). As in the previous experiment the crystal structures were initially solved in the $P2_1/n$ model. Structure 12 gave a good refinement in the $P2_1/n$ model and produced a disorder occupancy of 72(1)%. However, the data also provided a good refinement in the $P2_1/m$ model (12b; which constrains the disorder occupancy to a 50:50 ratio). Again, another crystal selected from the same experiment produced a refinement with a different disorder occupancy (Structure 13) of 61(1)% when refined in the $P2_1/n$ model. However, these data produced a better refinement in the (50:50) $P2_1/m$ model (13b) with improved refinement parameters.

This ambiguity in space group assignment makes accurate determination of the disorder level challenging, especially when structures can give a good refinement in either model.

This suggests that the two cells are not polymorphs, and are as a result of the disorder having an impact of the assignment of the space group. Although the two choices of space group result in slightly different relative orientations of molecules in the packing, and thus different hydrogen bonding schemes in terms of local structure, the two possibilities, and the less-regular intermediates between them, are clearly very similar in terms of stabilising the overall crystal structure. In structures where there is disorder of equal occupancy or close to equal occupancy, the disorder obeys the inherent mirror symmetry in the $P2_1/m$ model more effectively (the mirror plane lies down the same axis as the orientational disorder symmetry), and therefore a good refinement can be obtained in the $P2_1/m$ model. In the structures where the disorder occupancies are more uneven, the disorder breaks the mirror symmetry so the data gives a better refinement in the $P2_1/n$ model.

8.5 Conclusions

Variations in the degree of disorder across different crystals may have implications for the physical properties of a substance. In 5CL, the molecule can lie in two orientations and a study into the different occupancies of the disorder in different crystals of 5CL has been carried out. Crystals of 5CL with different refined disorder occupancies were identified, including an ordered structure and a structure with disorder of equal occupancy of both molecular orientations. The ordered structure and a structure with a low level of disorder (94%) were both produced from samples where crystal growth was allowed to occur at slow rates. This finding may be explained by the slow rate of growth allowing for the molecules to arrange themselves in the presumably lowest energy configuration. However, following this finding, a systematic study into disorder levels of crystals selected from the same batch showed that the crystals had different levels of refined disorder.

The study therefore highlighted that the refined level of disorder may be susceptible not only to crystallisation conditions, but also to crystal choice. The findings also highlight the difficulty in accurate determination of the space group in the presence of the disorder, and hence raises a note of caution about lack of reliability of the refined disorder occupancies in the 5CL structure. In many cases reasonable structural refinements could be carried out in either $P2_1/n$ or $P2_1/m$ with some datasets accurately described by both space groups. This also illustrates the way in which disorder might be mistaken for polymorphism.

In future work it would be beneficial to carry out multiple data collections from crystals from the same experiment prepared by slow evaporation or slow cooling where it might be expected that there would be less discrepancies in the level of disorder across the batch. This could also be carried out for crystals obtained through fast evaporation or rapid cooling where uneven disorder levels may be expected. Crystals could also be produced in the presence of agitation to provide a more uniform growth environment. However, rapid crystallisation and the presence of mixing may reduce the particle size making data collection through single crystal X-ray diffraction more challenging. Therefore, identification of a bulk method of characterising the disorder may be more effective in future studies, especially in light of the fact that any beneficial physical property of such materials, such as solubility or compressibility, is likely to be manifest in polycrystalline samples.

The inconsistency in the occupancy of disorder across the range of structures collected in this work led to the truncation of the study on possible control of disorder in 5CL. However, the finding of the effect of the polymer additive on the morphology of 5CL crystals prompted further studies of this phenomenon (Chapters 4 and 6).

Chapter 9

Conclusions and future work

9.1 Conclusions

The work in this thesis presents studies towards optimising the physical and particle properties of organic solid forms, particularly with a view to producing particles suited for production in continuous crystallisation environments.

Crystal morphology is an important feature affecting the particle properties of a substance and therefore relevant to the ease of downstream processes in the fine chemicals industries. Various methods can be used to optimise the crystal morphology, one of which is the use of soluble additive compounds present in the crystallisation solution. Both polymer and structurally similar additive compounds have been shown in this work to be effective in modifying the crystal morphology of different target compounds. Their possible residual presence in the final crystalline product was also investigated.

The effect of a triblock co-polymer additive, PP123, on the crystal morphology of SA from water was studied in detail at different batch scales in the volume range of 1 ml to 350 ml. β-SA crystallises from water in a plate-like morphology in the absence of an additive. It was found that the morphology-modifying effect of the polymer was dependent on both the concentration of SA and of PP123, which were related to the supersaturation ratio of the system at nucleation. At low concentrations of SA and additive, favourable block-like crystals were produced whereas at high concentrations of SA and additive, less favourable, needle-like crystals resulted. A region of concentrations of polymer and SA was identified which favoured the desirable block-like morphology, showing that conditions can be tuned to achieve this situation. In crystallisations in the presence of the additive at both 3 ml and 350 ml scales, the supersaturation ratio at nucleation was

highest at the lowest concentration of SA and declined as the SA concentration was increased. This may explain why in crystallisations with this low supersaturation ratio the effect of the additive was enhanced as more material is available in solution for the crystals to grow. Despite the large change in crystal morphology in the presence of very small quantities of polymer additive, the solid form of the SA produced was unchanged, remaining as the β polymorph. The method of mixing was shown to be crucial in the crystal morphology produced. Experiments with magnetic bottom stirring produced very small crystals and although morphology changes were observed at 1 ml scale, at larger scales the abrasive action of the stirrer bar resulted in significant breakage of the crystals. Overhead stirring resulted in less attrition, however, the experiments carried out at 3 ml scale with overhead stirring resulted in non-uniform morphologies due to the impeller being positioned at the incorrect height for the volume used. When used at 10 ml and 350 ml scale, with the impeller at the correct height, improved mixing was achieved and more uniform particles were produced.

Indexing of the individual crystal faces for each morphology produced and analysis of the crystal structure of β-SA was carried out. This, in combination with inspection of the morphology of SA produced from additional crystallisations using the individual blocks of the triblock co-polymer as additives, allowed a mechanism of the face-specific effect of the additive to be devised. Crystals grown in the presence of the additive showed a change in their side faces (to (111) and $(1\bar{1}1)$); the change in crystal shape suggested that these were the faces whose growth may be inhibited by the additive. Analysis of the crystal structure showed that the methyl groups of the SA molecules were positioned on the surface of these faces. Furthermore, in the additional crystallisations, the hydrophobic block of the polymer (PPG4000) induced a similar effect on the crystal morphology to that induced by the triblock co-polymer. Whereas the hydrophilic PEG1000 block did not have an effect on the morphology of SA. This suggested that the additive may be interacting with the crystal surface through hydrophobic interactions (growth of the hydrophobic faces is inhibited by the hydrophobic block of the polymer). The use of PPG4000 as an additive also offered the benefit of producing block-like crystals using a broader set of crystallisation conditions, enhancing the concentration regions over which this favourable outcome is achieved.

As part of the study into the crystallisation of SA from water, other methods for optimising the crystal morphology and size were also explored in combination with the use of additives. Firstly, direct nucleation control (DNC) experiments were carried out with and without the PP123 additive present in solution; these produced large rod and plate-like

crystals, respectively. The DNC was effective in improving the size and shape uniformity of the crystals. Temperature cycling experiments were also carried out as part of collaborative work and interestingly, with no additive present, a unique shape of SA was produced. Upon reaching equilibrium, square bipyramidal shaped crystals were formed of which the (100) face observed previously was replaced with the (110) and $(1\bar{1}0)$ faces.

Another aim of this work was to achieve the implementation of an additive-mediated morphology change in a continuous platform; these investigations were carried out using the SA and polymer additive system. Two continuous crystallisation platforms were investigated: the KRAIC segmented flow crystalliser and the continuous oscillatory baffled crystalliser (COBC). Successful transfer of the additive effect was achieved in the COBC platform with the favourable block-like morphology reproduced for multiple residence times of operation. This is the first reported example of additive-induced morphology changes being designed and implemented in continuous crystallisation of small molecule systems, and represents a significant achievement towards the aims of the CMAC consortium in producing particle control in continuous crystallisation. However, significant challenges such as encrustation and sedimentation were encountered in moving this system to the continuous environment using this platform which limited the prolonged production of the desired crystals. Interestingly, in experiments with the PP123 additive present, the severity of the encrustation was less in comparison with experiments with no additive present, but back-mixing of crystals into higher temperature straights resulted in inconsistent morphologies over successive residence times. The experiments carried out in the batch environment showed that the crystal morphology produced in the presence of the PP123 polymer was dependent on the temperature of crystal growth. Back-propagated crystals therefore acted as seeds enabling crystal growth in higher temperature straights and the consequent production of elongated crystals. The production of the block-like crystals of SA for longer periods of time was achieved using the PPG4000 additive due its ability, established in the batch investigations, to produce block-like crystals at a range of temperatures (related to the saturation concentration range over which the favourable morphology change is achieved). However, problems with sedimentation and encrustation remained an issue in the experiments.

Use of the SA system in experiments in the KRAIC segmented flow crystalliser enabled significant contributions to the development of the platform, a bespoke device designed, constructed and commissioned in the group at the University of Bath. Encrustation within the tubing and mixer pieces was overcome by implementation of effective temperature control methods. Additionally, a system designed to separate the carrier fluid from the

solution prior to filtration was implemented, enabling recovery of the carrier fluid and effective filtration of the product. Initial experiments towards achieving additive induced morphology in the platform were also carried out. In these initial experiments the PP123 additive was found to be incompatible with the liquid segmentation; the surfactant properties of the polymer enabled emulsification of the two phases and significant loss of carrier fluid. In contrast, the PPG4000 additive was compatible with the set-up, however its presence in the quantities used in the initial experiments did not result in the desired block-like crystals of SA. In the KRAIC the mixing is gentler than the batch environment and therefore larger concentrations of the additive may be required to produce the same effect. Interestingly, in the experiments with liquid segmentation including those in the presence of the PPG4000 additive, the product contained a mixture of α-SA and β-SA. The appearance of the α-polymorph of SA may be a result of the absence of a solid interface in the unique environment inside the KRAIC.

Substances with structural similarity to the target compound can also be effective as additives for optimisation of crystal morphology. The structural similarity of the additive may facilitate competition for surface adsorption with the growth units of the target compound on specific faces. Such structurally similar additives formed the focus of studies into the crystal morphology of the API, isoniazid; this API adopts unfavourable morphologies in the absence of additives. The effect of a range of structurally similar and size-matched additives, some of which are GRAS compounds, were screened for a possible effect on the morphology of IZN from two solvents, water and ethanol. IZN crystallises in a needle and plate-like morphology from water and ethanol, respectively. However, the modification of the crystal morphology of IZN to more favourable morphologies using additives was difficult to achieve and unfortunately the presence of the GRAS compounds did not show a favourable effect. Several other additives were, however, found to modify the morphology of IZN and further analysis was carried out for the additive which showed the most reproducible and enhanced effect (4,4'-bipyridine, 44BP). The presence of the 44BP additive in evaporative and cooling crystallisations of IZN from ethanol resulted in elongated crystals. In comparison with the polymer additive used to modify the morphology of SA, higher concentrations of this size-matched additive were required to induce an effect on the shape of the IZN crystals. Face indexing and analysis of the crystal structure of IZN allowed a possible mechanism for the effect of the 44BP additive on crystal growth to be constructed. In the presence of the additive, the slow growing faces and those with which the additive may be interacting are $(0\bar{1}\bar{2})$ and $(0\bar{1}2)$. The inhibiting effect of the additive may proceed through the pyridine ring of the 44BP molecules mimicking the hydrogen bond interaction of the pyridine ring of the IZN

molecule with the amine N-H bond of the IZN molecules. The 44BP molecule does not possess a hydrogen bond donor group preventing further addition of IZN growth units on the crystal surface and thus slowing down crystal growth. The other additives used which feature a pyridine ring also feature a hydrogen bond donor group which may have been a factor in their limited success as morphology-modifying additives. Prior to the study, it was inherently difficult to predict which additives would alter the morphology of IZN and the work largely relied on trial-and-error methods. Although none of the additives enhanced the crystal morphology of IZN in a favourable manner in terms of solid processing, gaining an understanding of the molecular level interactions that may have resulted in changes in morphology can aid the design of future “tailor-made” additives for a more desirable effect on the crystal shape.

Due to their structural similarity one of the challenges of using such additives is the risk of their incorporation into the crystal lattice. Polymer additives are less likely to be incorporated due to their larger size but may be present on the surface of the crystals. For both studies of SA and IZN, a range of analytical techniques were used to investigate the purity of the final crystalline product. The additives were not detected in the final solid product by any of the analytical methods used suggesting that they are not present in the product or are present in quantities below the detection limit of the instruments used. For the SA system, a qualitative method involving recrystallisation was devised to determine the presence of polymer in the product and the effectiveness of washing the crystals in removing the additive. Recrystallisation of a product previously crystallised from solution containing the highest concentration of PP123 additive (rod-like crystals) resulted in block-like crystals. This suggests that a small quantity of the additive may be present on the surface of the crystals. However, slurrying of the crystals in a non-polar solvent was effective in removing the remaining additive; plate-like crystals were produced when the dry sample was recrystallised after this washing procedure.

The properties of a substance can also be affected by its structural attributes. In Chapter 7, multi-component crystallisation was used to produce novel solid forms of the API, piroxicam. The aim of the work was to induce layered or disordered solid forms using co-former molecules selected based on their planar and symmetrical nature. Ten molecular complexes were produced of which five showed layered crystal structures, one of which had disorder present. In all of the structures which featured a layered packing arrangement, the co-former molecule forms interactions with the PX molecule through a carboxylic acid group, enabling the formation of two hydrogen bonds and encouraging the formation of a layered architecture. Through the study a series of solvates of a co-crystal

with layered structures were identified which showed interesting structural and thermal properties. Upon desolvation the PX molecule undergoes a tautomeric transition in the solid state which produces a colour change from yellow to white of which was found to be reversible through exposure to solvent vapour. Thermal, structural and spectroscopic analysis enabled the transition to be studied in detail. Through the rearrangement of the molecules in the crystal structure upon desolvation, the layered architecture is not retained in the structure of the desolvated form.

Another structural attribute that may affect the properties of a substance is the presence of molecular disorder. Chapter 8 describes an investigation into orientational disorder in 5CL whereby different levels of disorder could be refined from different crystals. The initial aims of the study were to investigate the effect of the crystallisation conditions on the level of disorder, with a view to exerting control over this effect. However, the level of disorder was not found to be uniform across crystals selected from the same experiment, which resulted in challenges in attributing the crystallisation conditions to the level of disorder in the crystals. A lack of reliability in the refined level of disorder was also evident due to the inherent difficulty in assignment of the space group. In several cases reasonable structural refinements could be achieved in either $P2_1/n$ or $P2_1/m$.

9.2 Future work

Looking to the future a number of themes arise. The effect of the PP123 polymer additive on the crystal morphology of SA was studied in detail, however a number of other parameters could be investigated. A more detailed investigation into the effect of different cooling rates on the morphology of SA in the presence of polymer additives as well as the effect of the stirring speed would enhance the understanding of the additive effect under different conditions. Detection of the nucleation temperature in such experiments would provide further understanding of the effect of the supersaturation on the crystal morphology. A Design of Experiments approach would be advantageous, enabling the conditions required to produce the most optimised morphology to be identified. It was also shown in this work that the polymer additive used could be applied to modify the morphology of another dicarboxylic acid. Developments would further target crystallisation of other dicarboxylic acids, allowing for comparisons to be made between the morphologies produced in the presence of the polymer additive. Another area of future significance to the work presented is the measurement and comparison of the particle properties of the different morphologies of SA identified.

Significant future work remains in terms of transfer of the SA system to the continuous environment. In order to make the production of the block-like crystals of SA in the presence of the polymer additives in the COBC sustainable, optimisation of the mixing conditions within the platform is required to prevent the severity of back-mixing and sedimentation. The implementation of seeding within the COBC would also be advantageous in prevention of nucleation on the walls of the crystalliser. This may enable access to improved particle size distributions and operation for prolonged periods. In terms of crystallisation in segmented flow, it is clear that the solid recovery requires optimisation for both experiments with and without additives present. Although the presence of the PP123 polymer was incompatible with the liquid segmented flow set-up, the use of the PPG4000 additive proved to be promising in the initial experiment. In future experiments, increasing the concentration of the PPG4000 additive may enable more effective production of the desired block-like crystals of SA. Crystallisations of SA in the presence of polymer additives could also be carried out in other continuous crystallisation platforms such as an MSMPR set-up.

In the study of the effect of the PP123 additive on the crystal morphology of SA, the most desirable morphology was tuned by altering the concentrations of the two components. A more detailed investigation into the effect of the structurally similar additives shown to impact the morphology of IZN may identify conditions required to access improved morphology for the API material. For example, the presence of the 44BP additive produced elongated crystals of IZN in the concentration tested; use of the additive in slightly lower concentrations may induce a less extreme effect and less elongated crystals. Furthermore, the knowledge gained from indexing the crystal faces may help to design future additives to induce an effect on the crystal morphology. Additional studies involving face indexing of other systems where reproducible morphology changes were observed, such as the use of urea as an additive, would therefore be beneficial.

A series of molecular complexes of PX were identified in this work, some of which were produced in larger quantities through crystallisation techniques other than evaporation. Production of the other complexes of interest through these methods may enable production of enough substance to measure and compare their physical properties and make correlations with the structural attributes observed.

To date, a method of characterising the occupancy of disorder without the requirement for single crystals has not yet been determined. This is significant in terms of scale-up since the product of is often a crystalline powder. Since studies of 5CL showed that the level of

disorder is inconsistent in crystals selected from the same experiment, a method of probing the disorder in the bulk is necessary in order to exploit this structural attribute for physical property optimisation in the future.

References

1. X.-W. Ni, *The Chemical Engineer*, 2008, **800**, 36-38.
2. R. J. Davey and J. Garside, *From Molecules to Crystallizers An Introduction to Crystallization*, Oxford University Press Inc., New York, United States, 2000.
3. W. Beckmann, Mechanisms of Crystallization, *Crystallization Basic Concepts and Industrial Applications*, ed. W. Beckmann, Wiley-VCH, Weinheim, Germany, 2013, pp. 7-34.
4. A. S. Myerson and R. Ginde, Crystals, crystal growth and nucleation, *Handbook of Industrial Crystallization*, Second edn., ed. A. S. Myerson, Butterworth-Heinemann, 2002, pp. 33-65.
5. S. Lawton, G. Steele, P. Shering, L. Zhao, I. Laird and X.-W. Ni, *Org. Process Res. Dev.*, 2009, **13**, 1357-1363.
6. S. Lee and C. Hoff, Large-Scale Aspects of Salt Formation: Processing of Intermediates and Final Products, *Handbook of Pharmaceutical Salts: Properties Selection and Use*, eds. P. Heinrich Stahl and C. G. Wermuth, VHCA, Zurich, Switzerland, 2008, pp. 192-220.
7. J. W. Mullin, *Crystallization*, 4th edn., Butterworth-Heinmann, Oxford, 2001.
8. D. Erdemir, A. Y. Lee and A. S. Myerson, *Acc. Chem. Res.*, 2009, **42**, 621-629.
9. A. D. Randolph and M. A. Larson, *Theory of Particulate Processes: Analysis and Techniques of Continuous Crystallisation*, Academic Press, New York, 1971.
10. R. J. Davey, S. L. Schroeder and J. H. ter Horst, *Angew. Chem. Int. Ed.*, 2013, **52**, 2166–2179.
11. H.-H. Tung, E. L. Paul, M. Midler and J. A. McCauley, *Crystallization of Organic Compounds An Industrial Perspective*, John Wiley & Sons, Inc., Hoboken, New Jersey, 2009.
12. P. G. Vekilov, *Cryst. Growth Des.*, 2010, **10**, 5007-5019.
13. D. Gebauer and H. Cölfen, *Nano Today*, 2011, **6**, 564-584.
14. S. Lohani and D. J. W. Grant, Thermodynamics of Polymorphs, *Polymorphism in the Pharmaceutical Industry*, ed. R. Hilfiker, Wiley-VCH Verlag GmbH & Co. KGaA, Weinheim, Germany, 2006, pp. 21-42.
15. L. Cronin, P. J. Kitson and C. C. Wilson, Process Understanding - Crystallization *Process understanding for scale-up and manufacture of active ingredients*, ed. I. N. Houson, Wiley-VCH, Weinheim, Germany, 2011, pp. 199-225.
16. P. Hartman and W. G. Perdok, *Acta Cryst.*, 1955, **8**, 49-52.
17. P. Hartman and W. G. Perdok, *Acta Cryst.*, 1955, **8**, 521-524.
18. P. Hartman and W. G. Perdok, *Acta Cryst.*, 1955, **8**, 525-529.

19. M. A. Lovette, A. R. Browning, D. W. Griffin, J. P. Sizemore, R. C. Snyder and M. F. Doherty, *Ind. Eng. Chem. Res.*, 2008, **47**, 9812-9833.
20. L. A. M. J. Jetten, H. J. Human, P. Bennema and J. P. Van Der Eerden, *J. Cryst. Growth*, 1984, **68**, 503-516.
21. H. J. Human, J. P. Van Der Eerden, L. A. M. J. Jetten and J. G. M. Odekerken, *J. Cryst. Growth*, 1980, **51**, 589-600.
22. D. M. Camacho, K. J. Roberts, K. Lewtas and I. More, *J. Cryst. Growth*, 2015, **416**, 47-56.
23. L. A. Smith, A. Duncan, G. B. Thomson, K. J. Roberts, D. Machin and G. McLeod, *J. Cryst. Growth*, 2004, **263**, 480-490.
24. W. M. L. Wood, *Powder Technol.*, 2001, **121**, 53-59.
25. P. Dandekar, Z. B. Kuvadia and M. F. Doherty, *Annu. Rev. Mater. Res.*, 2013, **43**, 359-386.
26. J. D. H. Donnay and D. Harker, *Am. Mineral.*, 1937, **22**, 446-467.
27. V. Bisker-Leib and M. F. Doherty, *Cryst. Growth Des.*, 2001, **1**, 455-461.
28. P. Hartman and P. Bennema, *J. Cryst. Growth*, 1980, **49**, 145-156.
29. C. Schmidt and J. Ulrich, *J. Cryst. Growth*, 2012, **353**, 168-173.
30. C. J. Tilbury, D. A. Green, W. J. Marshall and M. F. Doherty, *Cryst. Growth Des.*, 2016, **16**, 2590−2604.
31. A. L. Rohl, *Curr. Opin. Solid State Mater. Sci.*, 2003, **7**, 21-26.
32. R. J. Davey, J. W. Mullin and M. J. L. Whiting, *J. Cryst. Growth*, 1982, **58**, 304-312.
33. M. D. Eddleston, K. E. Hejczyk, A. M. C. Cassidy, H. P. G. Thompson, G. M. Day and W. Jones, *Cryst. Growth Des.*, 2015, **15**, 2514-2523.
34. N. Blagden, R. J. Davey, H. F. Lieberman, L. Williams, R. Payne, R. Roberts, R. Rowe and R. Docherty, *J. Chem. Soc., Faraday Trans.*, 1998, **94**, 1035-1044.
35. R. J. Davey, N. Blagden, S. Righini, H. Alison, M. J. Quayle and S. Fuller, *Cryst. Growth Des.*, 2001, **1**, 59-65.
36. R. A. Sullivan and R. J. Davey, *CrystEngComm*, 2015, **17**, 1015-1023.
37. C. Scott and S. Black, *Org. Process Res. Dev.*, 2005, **9**, 890-893.
38. R. Davey, W. Fila and J. Garside, *J. Cryst. Growth*, 1986, **79**, 607-613.
39. M. Salvalaglio, T. Vetter, F. Giberti, M. Mazzotti and M. Parrinello, *J. Am. Chem. Soc.*, 2012, **134**, 17221-17233.
40. I. Weissbuch, M. Lahav and L. Leiserowitz, Crystal Morphology Control with Tailor-Made Additives; A Stereochemical Approach, *Advances in Crystal Growth Research*, eds. K. Sato, Y. Furukawa and K. Nakajima, Elsevier B. V., 2001, pp. 381-400.

41. L. Addadi, Z. Berkovitch-Yellin, I. Weissbuch, M. Lahav and L. Leiserowitz, A Link Between Macroscopic Phenomena and Molecular Chirality: Crystals as Probes for the Direct Assignment of Absolute Configuration of Chiral Molecules, *Topics in Stereochemistry*, eds. E. L. Eliel, S. H. Wilen and N. L. Allinger, Wiley & Sons Ltd., New York, 1986, vol. 16, pp. 1-85.
42. A. Saleemi, I. I. Onyemelukwe and Z. Nagy, *Front. Chem. Sci. Eng.*, 2013, **7**, 79-87.
43. N. M. Reis, Z. K. Liu, C. M. Reis and M. R. Mackley, *Cryst. Growth Des.*, 2014, **14**, 3191-3198.
44. B. A. Hendriksen and D. J. W. Grant, *J. Cryst. Growth*, 1995, **156**, 252-260.
45. T. Vetter, M. Mazzotti and J. Brozio, *Cryst. Growth Des.*, 2011, **11**, 3813-3821.
46. L. R. Agnew, D. L. Cruickshank, T. McGlone and C. C. Wilson, *Chem. Commun.*, 2016, **52**, 7368-7371.
47. L. H. Thomas, C. Wales, L. Zhao and C. C. Wilson, *Cryst. Growth Des.*, 2011, **11**, 1450-1452.
48. L. H. Thomas, C. Wales and C. C. Wilson, *Chem. Commun.*, 2016, **52**, 7372-7375.
49. E. H. Lee, S. R. Byrn and M. T. Carvajal, *Pharmaceut. Res.*, 2006, **23**, 2375-2380.
50. C. H. Gu, K. Chatterjee, V. Young and D. J. W. Grant, *J. Cryst. Growth*, 2002, **235**, 471-481.
51. Z. Berkovitch-Yellin, *J. Am. Chem. Soc.*, 1985, **107**, 8239-8253.
52. R. J. Davey, S. N. Black, D. Logan, S. J. Maginn, J. E. Fairbrother and D. J. W. Grant, *J. Chem. Soc., Faraday Trans.*, 1992, **88**, 3461-3466.
53. S. Mirza, I. Miroshnyk, J. Heinämäki, J. Rantanen, O. Antikainen, P. Vuorela, H. Vuorela and J. Yliruusi, *Cryst. Growth Des.*, 2008, **8**, 3526-3531.
54. E. Simone, G. Steele and Z. K. Nagy, *CrystEngComm*, 2015, **17**, 9370-9379.
55. S. Garnier, S. Petit and G. Coquerel, *J. Cryst. Growth*, 2002, **234**, 207-219.
56. X. He, J. G. Stowell, K. R. Morris, R. R. Pfeiffer, H. Li, G. P. Stahly and S. R. Byrn, *Cryst. Growth Des.*, 2001, **1**, 305-312.
57. T. Mukuta, A. Y. Lee, T. Kawakami and A. S. Myerson, *Cryst. Growth Des.*, 2005, **5**, 1429-1436.
58. *Generally Recognized as Safe (GRAS)*, US Food and Drug Administration http://www.fda.gov/Food/IngredientsPackagingLabeling/GRAS/, Accessed 29th August, 2016.
59. S. Xie, S. K. Poornachary, P. S. Chow and R. B. H. Tan, *Cryst. Growth Des.*, 2010, **10**, 3363-3371.

60. S. L. Raghavan, A. Trividic, A. F. Davis and J. Hadgraft, *Int. J. Pharm.*, 2001, **212**, 213-221.
61. G. A. Ilevbare, H. Liu, K. J. Edgar and L. S. Taylor, *Cryst. Growth Des.*, 2012, **12**, 6050-6060.
62. N. S. Trasi and L. S. Taylor, *Cryst. Growth Des.*, 2012, **12**, 3221-3230.
63. K. Abbou Oucherif, S. Raina, L. S. Taylor and J. D. Litster, *CrystEngComm*, 2013, **15**, 2197-2205.
64. D. E. Alonzo, S. Raina, D. Zhou, Y. Gao, G. G. Z. Zhang and L. S. Taylor, *Cryst. Growth Des.*, 2012, **12**, 1538-1547.
65. G. A. Ilevbare, H. Liu, K. J. Edgar and L. S. Taylor, *Cryst. Growth Des.*, 2012, **12**, 3133-3143.
66. D. Wieckhusen, Development of Batch Crystallizations, *Crystallization Basic Concepts and Industrial Applications*, ed. W. Beckmann, Wiley-VCH, Weinheim, Germany, 2013, pp. 187-202.
67. D. Braga and F. Grepioni, *Angew. Chem. Int. Ed.*, 2004, **43**, 4002-4011.
68. T. Friščić and W. Jones, *Cryst. Growth Des.*, 2009, **9**, 1621-1637.
69. S. A. Ross, D. A. Lamprou and D. Douroumis, *Chem. Commun.*, 2016, **52**, 8772-8786.
70. C. Medina, D. Daurio, K. Nagapudi and F. Alvarez-Nunez, *J. Pharm. Sci.*, 2010, **99**, 1693-1696.
71. A. J. Smith, P. Kavuru, L. Wojtas, M. J. Zaworotko and R. D. Shytle, *Mol. Pharmaceutics*, 2011, **8**, 1867-1876.
72. M. Sowa, K. Slepokura and E. Matczak-Jon, *CrystEngComm*, 2014, **16**, 10592-10601.
73. G. G. Z. Zhang, R. F. Henry, T. B. Borchardt and X. Lou, *J. Pharm. Sci.*, 2007, **96**, 990-995.
74. W. Beckmann, Crystallization: Introduction, *Crystallization Basic Concepts and Industrial Applications*, ed. W. Beckmann, Wiley-VCH, Weinheim, Germany, 2013, pp. 1-6.
75. J. Chen, B. Sarma, J. M. B. Evans and A. S. Myerson, *Cryst. Growth Des.*, 2011, **11**, 887-895.
76. A. J. Alvarez and A. S. Myerson, *Cryst. Growth Des.*, 2010, **10**, 2219-2228.
77. A. J. Rogers, C. Inamdar and M. G. Ierapetritou, *Ind. Eng. Chem. Res.*, 2013, **53**, 5128–5147.
78. K. A. Powell, G. Bartolini, K. E. Wittering, A. N. Saleemi, C. C. Wilson, C. D. Rielly and Z. K. Nagy, *Cryst. Growth Des.*, 2015, **15**, 4821-4836.

79. K. A. Powell, A. N. Saleemi, C. D. Rielly and Z. K. Nagy, *Chem. Eng. Process.*, 2015, **97**, 195-212.
80. *NiTech Solutions*, http://www.nitechsolutions.co.uk/, Accessed 4th August, 2016.
81. X.-W. Ni, *Plug flow: fact and myth*, Manufacturing Chemist Pharma, http://www.manufacturingchemist.com/technical/article_page/Plug_flow_fact_and_myth/37442, Accessed 31st August, 2016.
82. M. Sultana and K. F. Jensen, *Cryst. Growth Des.*, 2012, **12**, 6260-6266.
83. J. Evans, *The Chemical Engineer*, 2013, **860**, 32-34.
84. T. Vetter, C. L. Burcham and M. F. Doherty, *Chem. Eng. Sci.*, 2014, **106**, 167-180.
85. S. P. F. Miller, A. S. Raw and L. X. Yu, Scientific Considerations of Pharmaceutical Solid Polymorphism in Regulatory Applications, *Polymorphism in the Pharmaceutical Industry*, ed. R. Hilfiker, Wiley-VCH Verlag GmbH & Co. KGaA, Weinheim, Germany, 2006, pp. 385-403.
86. G. R. Desiraju, *Crystal engineering: The design of organic solids*, Elsevier, Amsterdam, The Netherlands, 1989.
87. G. A. Jeffrey, *An introduction to hydrogen bonding*, Oxford Univeristy Press, New York, 1997.
88. M. C. Etter, *Acc. Chem. Res.*, 1990, **23**, 120-126.
89. G. R. Desiraju, *Angew. Chem. Int. Ed. Eng.*, 1995, **34**, 2311-2327.
90. G. R. Desiraju, *J. Mol. Struct.*, 2003, **656**, 5-15.
91. T. Steiner, *Angew. Chem. Int. Ed.*, 2002, **41**, 48-76.
92. L. Pauling, *The Nature of the Chemical Bond*, Cornell University Press, New York, 1939.
93. G. R. Desiraju and T. Steiner, *The Weak Hydrogen Bond*, Oxford University Press, New York, 1999.
94. G. C. Pimentel and A. L. McClellan, *The hydrogen bond*, W. H. Freeman & Co Ltd., London, 1960.
95. E. Arunan, G. R. Desiraju, R. A. Klein, J. Sadlej, S. Scheiner, I. Alkorta, D. C. Clary, R. H. Crabtree, J. J. Dannenberg, P. Hobza, H. G. Kjaergaard, A. C. Legon, B. Mennucci and D. J. Nesbitt, *Pure. Appl. Chem.*, 2011, **83**, 1619-1636.
96. L.-l. Ooi, *Principles of X-ray Crystallography*, Oxford University Press Inc., New York, United States, 2010.
97. P. Atkins and J. de Paula, *Atkins' Physical Chemistry*, Seventh edn., Oxford University Press, New York, United States, 2002.
98. C. A. Hunter and J. K. M. Sanders, *J. Am. Chem. Soc.*, 1990, **112**, 5525-5534.

99. A. D. McNaught and A. Wilskinson, *IUPAC. Compendium of Chemical Terminology - Gold Book XML on-line corrected version 2.3.2*, Blackwell Scientific Publications, http://goldbook.iupac.org/.
100. G. Gilli, Molecules and molecular crystals, *Fundamentals of Crystallography*, Second edn., ed. C. Giacovazzo, Oxford University Press, New York, United States, 2002, p. 589.
101. W. C. McCrone, *Physics and Chemistry of the Organic Solid State*, eds. D. Fox, M. M. Labes and A. Weissberger, Interscience Publishers, London, 1965, vol. 2, pp. 725-767.
102. J. D. Dunitz and J. Bernstein, *Acc. Chem. Res.*, 1995, **28**, 193-200.
103. P. Di Martino, A. M. Guyot-Hermann, P. Conflant, M. Drache and J. C. Guyot, *Int. J. Pharm.*, 1996, **128**, 1-8.
104. J. Bauer, S. Spanton, R. Henry, J. Quick, W. Dziki, W. Porter and J. Morris, *Pharmaceut. Res.*, 2001, **18**, 859-866.
105. V. López-Mejías, J. W. Kampf and A. J. Matzger, *J. Am. Chem. Soc.*, 2009, **131**, 4554-4555.
106. V. López-Mejías, J. W. Kampf and A. J. Matzger, *J. Am. Chem. Soc.*, 2012, **134**, 9872-9875.
107. S. SeethaLekshmi and T. N. Guru Row, *Cryst. Growth Des.*, 2012, **12**, 4283-4289.
108. J. Bernstein, *Polymorphism in Molecular Crystals*, Oxford University Press, Oxford, 2002.
109. R. Hilfiker, Polymorphism in Crystalline Systems, *Crystallization Basic Concepts and Industrial Applications*, ed. W. Beckmann, Wiley-VCH, Weinheim, Germany, 2013, pp. 85-103.
110. G. R. Desiraju, *J Chem Sci*, 2010, **122**, 667-675.
111. N. Blagden, M. de Matas, P. T. Gavan and P. York, *Advanced Drug Delivery Reviews*, 2007, **59**, 617-630.
112. N. Schultheiss and A. Newman, *Cryst. Growth Des.*, 2009, **9**, 2950-2967.
113. S. L. Childs, G. P. Stahly and A. Park, *Mol. Pharmaceutics*, 2007, **4**, 323-338.
114. P. Heinrich Stahl and B. Sutter, Salt Selection, *Polymorphism in the Pharmaceutical Industry*, ed. R. Hilfiker, Wiley-VCH Verlag GmbH & Co. KGaA, Weinheim, Germany, 2006, pp. 309-332.
115. J. Mahieux, M. Sanselme and G. Coquerel, *Cryst. Growth Des.*, 2015, **16**, 396−405.
116. V. S. Minkov, A. A. Beloborodova, V. A. Drebushchak and E. V. Boldyreva, *Cryst. Growth Des.*, 2014, **14**, 513-522.

117. W. Clegg, *Crystal Structure Determination*, Oxford University Press Inc., New York, United States, 1998.
118. S. R. Byrn, R. R. Pfeiffer, G. Stephenson, D. J. W. Grant and W. B. Gleason, *Chem. Mater.*, 1994, **6**, 1148-1158.
119. P. J. Cox, G. I. Gilmour and S. M. MacManus, *Int. J. Pharm.*, 2000, **204**, 133-136.
120. R. C. B. Copley, S. A. Barnett, P. G. Karamertzanis, K. D. M. Harris, B. M. Kariuki, M. Xu, E. A. Nickels, R. W. Lancaster and S. L. Price, *Cryst. Growth Des.*, 2008, **8**, 3474-3481.
121. J. S. Clawson, S. Kennedy-Gabb, A. Y. Lee and R. C. Copley, *J Pharm Sci*, 2011.
122. A. D. Bond, *CrystEngComm*, 2012, **14**, 2363.
123. JEOL, *The Theory of the Scanning Electron Microscope*.
124. M. Mahon, Advanced Structural Methods Lecture Notes, University of Bath, 2013.
125. W. Massa, *Crystal Structure Determination*, 2nd edn., Springer-Verlag, 2004.
126. M. T. Weller, *Inorganic Materials Chemistry*, Oxford University Press Inc., New York, United States, 1994.
127. S. C. Wallwork, *Introduction to the Calculation of Structure Factors*, University College Cardiff Press for the International Union of Crystallography, http://www.iucr.org/__data/assets/pdf_file/0015/13083/3.pdf, 2014.
128. D. Giron and D. J. W. Grant, Evaluation of Solid-State Properties of Salts, *Handbook of Pharmaceutical Salts Properties, Selection and Use*, eds. P. H. Stahl and C. G. Wermuth, VHCA and WILEY-VCH, Zurich and Weinheim, 2008, p. 67.
129. D. Q. M. Craig, Characterization of Polymorphic Systems Using Thermal Analysis, *Polymorphism in the Pharmaceutical Industry*, ed. R. Hilfiker, Wiley-VCH Verlag GmbH & Co. KGaA, Weinheim, Germany, 2006, pp. 43-79.
130. R. Hilfiker, Characterisation of Crystalline Products, *Crystallization Basic Concepts and Industrial Applications*, ed. W. Beckmann, Wiley-VCH, Weinheim, Germany, 2013, pp. 149-171.
131. E. J. W. Wynn, *Powder Technol.*, 2003, **133**, 125-133.
132. *FBRM Method of Measurement*, Mettler Toledo, http://www.mt.com/us/en/home/supportive_content/specials/Lasentec-FBRM-Method-of-Measurement.html, Accessed 1st August, 2016.
133. *CrystalClear, version 1.01.614*, 2007, Technobis Crystallization Systems, Alkmaar, The Netherlands.
134. *CrysAlisPro, version 1.171.38.43*, Rigaku Oxford Diffraction, Oxford, UK.
135. *CrystalClear, version 2.0*, Rigaku Corporation, Tokyo, Japan.
136. *XPREP,* Bruker AXS Inc., Madison, Wisconsin, USA.
137. G. Sheldrick, *Acta Cryst.*, 2008, **A64**, 112-122.

138. G. Sheldrick, *Acta Cryst.*, 2015, **C71**, 3-8.
139. L. J. Farrugia, *J. Appl. Cryst.*, 1999, **32**, 837-838.
140. L. J. Farrugia, *J. Appl. Cryst.*, 2012, **45**, 849-854.
141. C. F. Macrae, I. J. Bruno, J. A. Chisholm, P. R. Edgington, P. McCabe, E. Pidcock, L. Rodriguez-Monge, R. Taylor, J. Van De Streek and P. A. Wood, *J. Appl. Cryst.*, 2008, **41**, 466-470.
142. *APEX2,* Bruker AXS Inc., Madison, Wisconsin, USA.
143. *SADABS,* Bruker AXS Inc., Madison, Wisconsin, USA.
144. *US Food and Drug Administration SCOGS*, http://www.fda.gov/Food/IngredientsPackagingLabeling/GRAS/SCOGS/ucm261458.htm.
145. S. Aitipamula, A. B. H. Wong, P. S. Chow and R. B. H. Tan, *CrystEngComm*, 2013, **15**, 5877-5887.
146. M. L. Cheney, D. R. Weyna, N. Shan, M. Hanna, L. Wojtas and M. J. Zaworotko, *Cryst. Growth Des.*, 2010, **10**, 4401-4413.
147. E. van der Voort, *J. Cryst. Growth*, 1991, **110**, 662-668.
148. G. D. Rieck, *Recueil des Travaux Chimiques des Pays-Bas*, 1944, **63**, 170-180.
149. V. Chikhalia, R. T. Forbes, R. A. Storey and M. Ticehurst, *Eur. J. Pharm. Sci.*, 2006, **27**, 19-26.
150. K. M. Carver and R. C. Snyder, *Ind. Eng. Chem. Res.*, 2012, **51**, 15720-15728.
151. Q. Yu, L. Dang, S. Black and H. Wei, *J. Cryst. Growth*, 2012, **340**, 209-215.
152. A. V. Trask, N. Shan, W. D. S. Motherwell, W. Jones, S. Feng, R. B. H. Tan and K. J. Carpenter, *Chem. Commun.*, 2005, 880-882.
153. R. C. Snyder, S. Veesler and M. F. Doherty, *Cryst. Growth Des.*, 2008, **8**, 1100-1101.
154. C. Acquah, M. Cagnetta, L. E. K. Achenie, S. L. Suib and A. Karunanithi, *Ind. Eng. Chem. Res.*, 2015, **54**, 12108−12113.
155. E. Batrakova, S. Lee, S. Li, A. Venne, V. Alakhov and A. Kabanov, *Pharmaceut. Res.*, 1999, **16**, 1373-1379.
156. C. J. Brown, Y. C. Lee, Z. K. Nagy and X. Ni, *CrystEngComm*, 2014, **16**, 8008-8014.
157. B. A. Hendriksen, D. J. W. Grant, P. Meenan and D. A. Green, *J. Cryst. Growth*, 1998, **183**, 629-640.
158. K. V. R. Prasad, R. I. Ristic, D. B. Sheen and J. N. Sherwood, *Int. J. Pharm.*, 2001, **215**, 29-44.
159. S. S. Kadam, H. J. M. Kramer and J. H. ter Horst, *Cryst. Growth Des.*, 2011, **11**, 1271-1277.

160. R. J. Davey, N. Blagden, S. Righini, H. Alison and E. S. Ferrari, *The Journal of Physical Chemistry B*, 2002, **106**, 1954-1959.
161. Y. Zhang and M. F. Doherty, *AIChE J.*, 2004, **50**, 2101-2112.
162. H. Lorenz and W. Beckmann, Purification by Crystallization, *Crystallization Basic Concepts and Industrial Applications*, ed. W. Beckmann, Wiley-VCH, Weinheim, Germany, 2013, pp. 129-148.
163. E. Simone, W. Zhang and Z. K. Nagy, *Cryst. Growth Des.*, 2015, **15**, 2908-2919.
164. A. N. Saleemi, G. Steele, N. I. Pedge, A. Freeman and Z. K. Nagy, *Int. J. Pharm.*, 2012, **430**, 56-64.
165. M. R. Abu Bakar, Z. K. Nagy, A. N. Saleemi and C. D. Rielly, *Cryst. Growth Des.*, 2009, **9**, 1378-1384.
166. E. Simone, A. R. Klapwijk, C. C. Wilson and Z. K. Nagy, *Cryst. Growth Des.*, 2017, **17**, 1695-1706.
167. Z. Wu, S. Yang and W. Wu, *CrystEngComm*, 2016, **18**, 2222-2238.
168. K. S. Elvira, X. C. i Solvas, R. C. R. Wootton and A. J. deMello, *Nat. Chem.*, 2013, **5**, 905-915.
169. C.-X. Zhao, L. He, S. Z. Qiao and A. P. J. Middelberg, *Chem. Eng. Sci.*, 2011, **66**, 1463-1479.
170. R. Vacassy, J. Lemaître, H. Hofmann and J. H. Gerlings, *AIChE J.*, 2000, **46**, 1241-1252.
171. M. Jiang, Z. Zhu, E. Jimenez, C. D. Papageorgiou, J. Waetzig, A. Hardy, M. Langston and R. D. Braatz, *Cryst. Growth Des.*, 2014, **14**, 851-860.
172. B. Ahmed, D. Barrow and T. Wirth, *Adv. Synth. Catal.*, 2006, **348**, 1043-1048.
173. M. N. Kashid, I. Gerlach, S. Goetz, J. Franzke, J. F. Acker, F. Platte, D. W. Agar and S. Turek, *Ind. Eng. Chem. Res.*, 2005, **44**, 5003-5010.
174. J. Lu, J. D. Litster and Z. K. Nagy, *Cryst. Growth Des.*, 2015, **15**, 3645-3651.
175. R. D. Dombrowski, J. D. Litster, N. J. Wagner and Y. He, *Chem. Eng. Sci.*, 2007, **62**, 4802-4810.
176. K. Robertson, P.-B. Flandrin, A. R. Klapwijk and C. C. Wilson, *Cryst. Growth Des.*, 2016, **16**, 4759-4764.
177. Asynt, http://www.asynt.com/.
178. L. Zhao, V. Raval, N. E. B. Briggs, R. M. Bhardwaj, T. McGlone, I. D. H. Oswald and A. J. Florence, *CrystEngComm*, 2014, **16**, 5769–5780.
179. T. McGlone, N. E. B. Briggs, C. A. Clark, C. J. Brown, J. Sefcik and A. J. Florence, *Org. Process Res. Dev.*, 2015, **19**, 1186-1202.
180. P. Stonestreet and A. P. Harvey, *Chem. Eng. Res. Des.*, 2002, **80**, 31-44.

181. N. E. B. Briggs, U. Schacht, V. Raval, T. McGlone, J. Sefcik and A. J. Florence, *Org. Process Res. Dev.*, 2015, **19**, 1903−1911.
182. G. Rajalakshmi, V. R. Hathwar and P. Kumaradhas, *Acta Cryst.*, 2014, **B70**, 331-341.
183. A. Lemmerer, *CrystEngComm*, 2012, **14**, 2465-2478.
184. A. Lemmerer, J. Bernstein and V. Kahlenberg, *J. Chem. Crystallogr.*, 2011, **41**, 991-997.
185. S. M. A. Mashhadi, U. Yunus, M. H. Bhatti and M. N. Tahir, *J. Mol. Struct.*, 2014, **1076**, 446-452.
186. B. Swapna, D. Maddileti and A. Nangia, *Cryst. Growth Des.*, 2014, **14**, 5991-6005.
187. P. Grobelny, A. Mukherjee and G. R. Desiraju, *CrystEngComm*, 2011, **13**, 4358-4364.
188. W. M. Haynes, Section 3 Physical constants of organic compounds, *CRC Handbook of Chemistry and Physics*, 96th edn., Taylor and Francis Group, LLC, 2016.
189. L. Lyn, H. Sze, A. Rajendran, G. Adinarayana, K. Dua and S. Garg, *Acta Pharm.*, 2011, **61**, 391-402.
190. L. H. Thomas, A. R. Klapwijk, C. Wales and C. C. Wilson, *CrystEngComm*, 2014, **16**, 5924-5932.
191. S. L. Childs and K. I. Hardcastle, *Cryst. Growth Des.*, 2007, **7**, 1291-1304.
192. K. Naelapää, J. van de Streek, J. Rantanen and A. D. Bond, *J. Pharm. Sci.*, 2012, **101**, 4214-4219.
193. M. Nyström, J. Roine, M. Murtomaa, R. Mohan Sankaran, H. A. Santos and J. Salonen, *Eur. J. Pharm. Biopharm.*, 2015, **89**, 182-189.
194. Z. Lavrič, J. Pirnat, J. Lužnik, U. Puc, Z. Trontelj and S. Srčič, *J. Pharm. Sci.*, 2015, **104**, 1909-1918.
195. J. Bordner, J. A. Richards, P. Weeks and E. B. Whipple, *Acta Cryst.*, 1984, **C40**, 989-990.
196. E. M. Horstman, J. A. Bertke, E. H. Kim, L. C. Gonzalez, G. G. Z. Zhang, Y. Gong and P. J. A. Kenis, *CrystEngComm*, 2015, **17**, 5299-5306.
197. C. Wales, L. H. Thomas and C. C. Wilson, *CrystEngComm*, 2012, **14**, 7264.
198. K. Fucke, S. A. Myz, T. P. Shakhtshneider, E. V. Boldyreva and U. J. Griesser, *New J. Chem.*, 2012, **36**, 1969.
199. A. Mishnev and G. Kiselovs, *Z. Naturforsch.*, 2013, **68**, 168-174.
200. G. Bolla, P. Sanphui and A. Nangia, *Cryst. Growth Des.*, 2013, **13**, 1988-2003.

201. U. J. Griesser, The Importance of Solvates, *Polymorphism in the Pharmaceutical Industry*, ed. R. Hilfiker, Wiley-VCH Verlag GmbH & Co. KGaA, Weinheim, Germany, 2006, pp. 211-233.
202. A. Bertoluzza, M. Rossi, P. Taddei, E. Redenti, M. Zanol and P. Ventura, *J. Mol. Struct.*, 1999, **480–481**, 535-539.
203. E. Redenti, M. Zanol, P. Ventura, G. Fronza, A. Comotti, P. Taddei and A. Bertoluzza, *Biospectroscopy*, 1999, **5**, 243-251.
204. P. Taddei, A. Torreggiani and R. Simoni, *Biopolymers*, 2001, **62**, 68-78.
205. *ACD/I-Lab, National Chemical Database Service*, http://ilab.cds.rsc.org/.
206. M. Shalaeva, J. Kenseth, F. Lombardo and A. Bastin, *J. Pharm. Sci.*, 2008, **97**, 2581-2606.
207. G. Kortüm, W. Vogel and K. Andeussow, *Dissociation Constants of Organic Acids in Aqueous Solution*, Butterworths, London, 1961.
208. W. M. Haynes, Section 5 Thermochemistry, Electrochemistry, and Solution Chemistry: Dissociation constants of organic acids and bases, *CRC Handbook of Chemistry and Physics*, 96th edn., Taylor and Francis Group, LLC, 2016.
209. L. G. Bray, J. F. J. Dippy, S. R. C. Hughes and L. W. Laxton, *J. Chem. Soc.*, 1957, 2405-2408.
210. S. A. Barnett, A. T. Hulme, N. Issa, T. C. Lewis, L. S. Price, D. A. Tocher and S. L. Price, *New J. Chem.*, 2008, **32**, 1761.
211. H. Sternglanz and C. E. Bugg, *Biochim. Biophys. Acta*, 1975, **378**, 1-11.
212. D. E. Braun, T. Gelbrich, K. Wurst and U. J. Griesser, *Cryst. Growth Des.*, 2016, **16**, 3480-3496.

Appendices

List of publications

The following papers have been published from work presented in this thesis or from related work carried out during these studies:

A. R. Klapwijk, E. Simone, Z. K. Nagy and C. C. Wilson, Tuning Crystal Morphology of Succinic Acid Using a Polymer Additive. *Cryst. Growth Des.*, 2016, 16 (8), 4349-4359 [DOI: 10.1021/acs.cgd.6b00465].

M. Sowa, A. R. Klapwijk, M. Ostendorf and W. Beckmann, Particle Engineering of an Active Pharmaceutical Ingredient for Improved Micromeritic Properties. *Chem. Eng. Technol.,* 2017, *in press* [DOI: 10.1002/ceat.201600663].

E. Simone, A. R. Klapwijk, C. C. Wilson and Z. K. Nagy, Investigation of the Evolution of Crystal Size and Shape during Temperature Cycling and in the Presence of a Polymeric Additive Using Combined Process Analytical Technologies. *Cryst. Growth Des.*, 2017, 17, 1695-1706 [DOI: 10.1021/acs.cgd.6b01683].

K. Robertson, P.-B. Flandrin, A. R. Klapwijk and C. C. Wilson, Design and Evaluation of a Meso-scale Segmented Flow Reactor (KRAIC). *Cryst. Growth Des.*, 2016, 16 (8), 4759-4764 [DOI: 10.1021/acs.cgd.6b00885].

K. E. Wittering, L. A. Agnew, A. R. Klapwijk, K. Robertson, A. J. P. Cousen, C. C. Wilson and D. L. Cruickshank, Crystallisation and physicochemical property characterisation of conformationally-locked co-crystals of fenamic acid derivatives. *CrystEngComm*, 2015, 17 (19), 3610-3618 [DOI: 10.1039/C5CE00297D].

L. H. Thomas, A. R. Klapwijk, C. Wales and C. C. Wilson, Intermolecular hydrogen transfer and solubility tuning in multi-component molecular crystals of the API piroxicam. *CrystEngComm*, 2014, 16 (26), 5924 - 5932 [DOI: 10.1039/C4CE00246F].

Appendix A4 (Chapter 4)

A4.1 ^{1}H NMR analysis

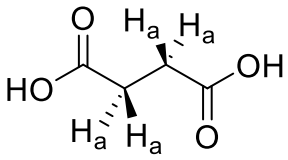

Figure A4.1 – The structure of succinic acid with the hydrogen atoms labelled.

SA sample crystallised with PP123 additive: ^{1}H NMR (500MHz, D_2O) δ ppm 2.64 (4H, s, H_a), 4.75 (s, H_2O).

SA sample crystallised without PP123 additive: ^{1}H NMR (500MHz, D_2O) δ ppm 2.64 (4H, s, H_a), 4.75 (s, H_2O).

A4.2 MALDI-TOF MS

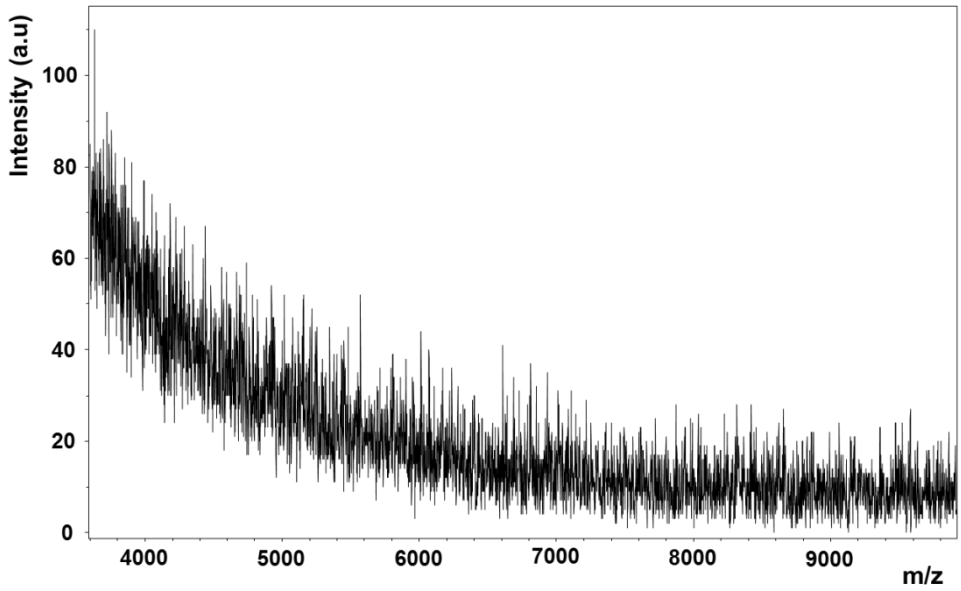

Figure A4.2 - MALDI-TOF MS analysis of SA sample crystallised in the presence of 0.5% PP123 additive showing that PP123 was not detected.

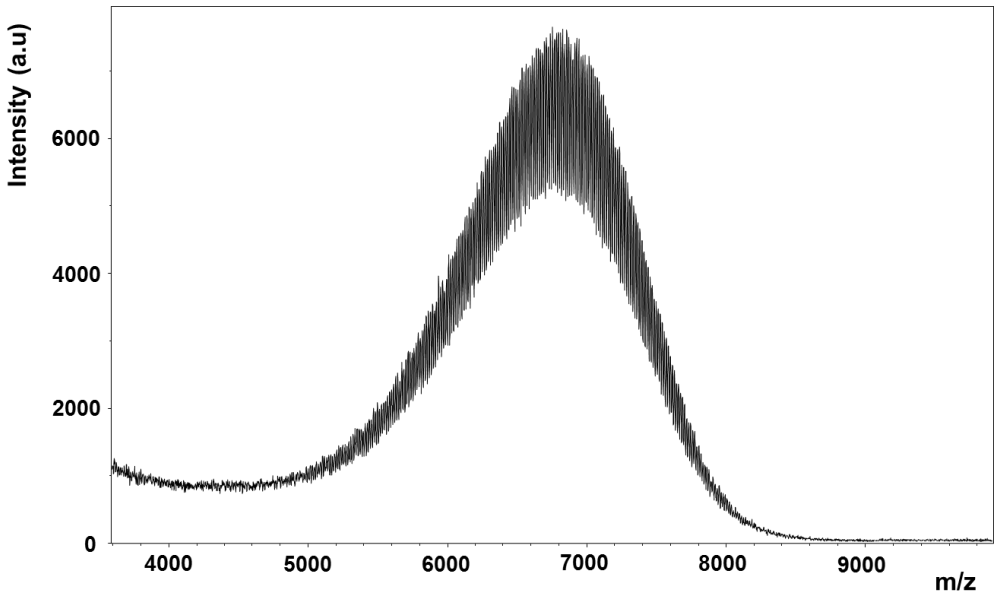

Figure A4.3 - MALDI-TOF MS analysis of PP123 polymer (5 mg ml^{-1}).

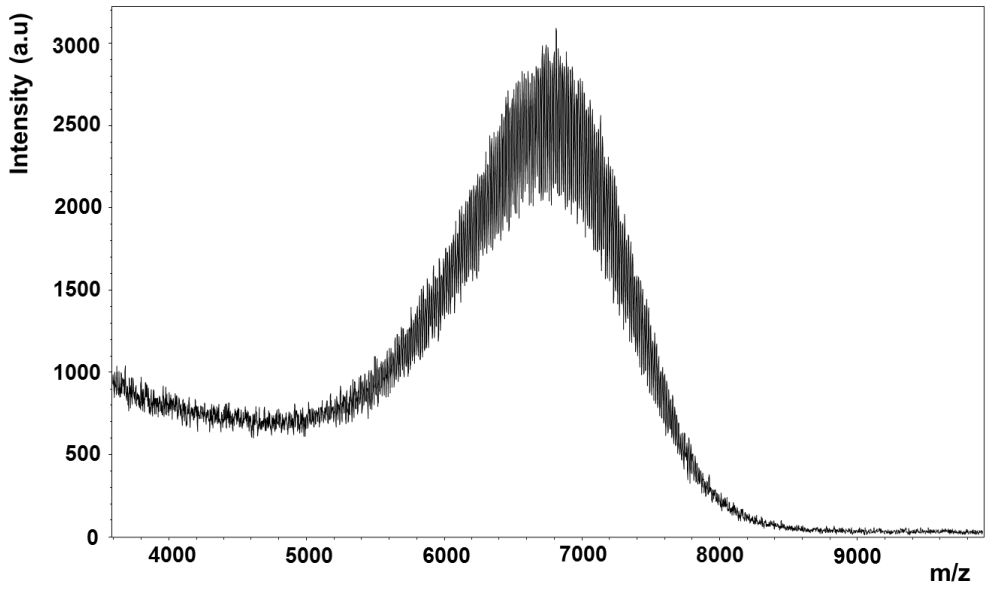

Figure A4.4 - MALDI-TOF MS analysis of PP123 polymer (0.5 mg ml^{-1}).

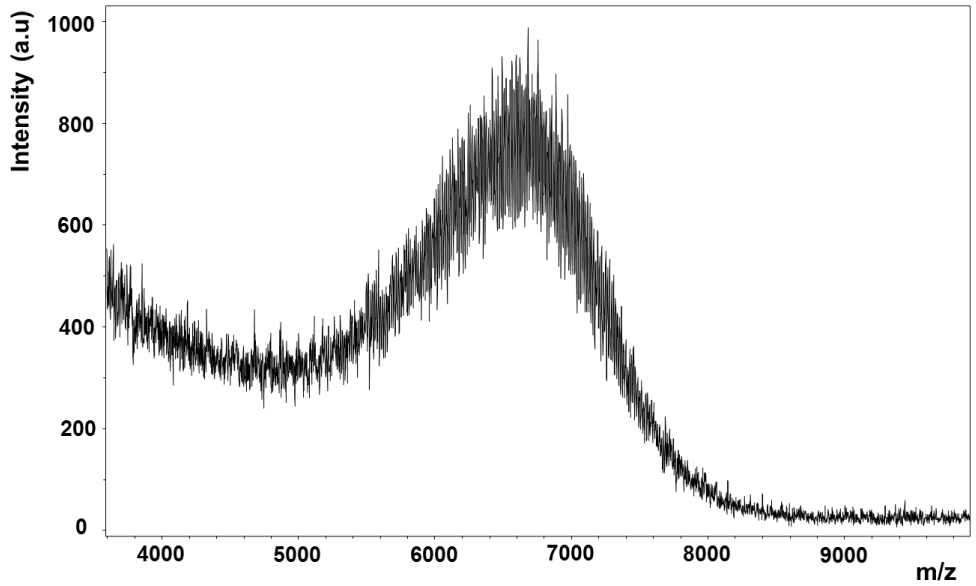

Figure A4.5 - MALDI-TOF MS analysis of PP123 polymer (0.05 mg ml^{-1}).

Appendix A6 (Chapter 6)

A6.1 Tables of experiments carried out

Table A6.1 - Crystallisations of IZN carried out from ethanol.

Additive	Ratio used				
	Evaporative	Cooling (150 rpm)	Cooling (200 rpm)	Cooling (400 rpm)	Cooling (overhead stirring)
Nicotinic acid	100:1, 1:1	10:1	10:1	10:1	N/A
Isonicotinic acid	100:1, 1:1	10:1	10:1	10:1	10:1
Nicotinamide	100:1, 1:1	10:1	10:1	10:1	N/A
Isonicotinamide	100:1, 1:1	10:1	10:1	10:1	N/A
2-picolinic acid	100:1, 1:1	10:1	10:1	10:1	10:1
Pyrazine carboxamide	100:1, 1:1	10:1	10:1	10:1	N/A
PEG	100:1, 1:1	10:1	10:1	10:1	N/A
PPG	100:1, 1:1	10:1	10:1	10:1	N/A
PP123	100:1, 1:1	10:1	10:1	10:1	N/A
PF127	100:1, 1:1	10:1	10:1	10:1	N/A
Biuret	10:1, 1:1	10:1	10:1	10:1	10:1
Urea	10:1, 1:1	10:1	10:1	10:1	N/A
Resorcinol	10:1, 1:1	10:1	10:1	10:1	N/A
Imidazole	10:1, 1:1	10:1	10:1	10:1	N/A
Benzoic acid	10:1, 1:1	10:1	10:1	10:1	N/A
Oxalic acid	10:1, 1:1	10:1	10:1	10:1	N/A
Malic acid	10:1, 1:1	10:1	10:1	10:1	N/A
2,4-dinitrobenzoic acid	10:1, 1:1	10:1	10:1	10:1	10:1
3-methylbenzoic acid	10:1, 1:1	10:1	10:1	10:1	N/A
4-fluorobenzoic acid	10:1, 1:1	10:1	10:1	10:1	N/A
4-hydroxybenzoic acid	10:1	10:1	10:1	10:1	N/A
2,2'-bipyridyl	10:1, 1:1	10:1	10:1	10:1	N/A
4,4'-bipyridyl	10:1, 1:1	10:1	10:1	10:1	10:1
2-aminopyridine	10:1, 1:1	10:1	10:1	10:1	N/A

Table A6.2 - Crystallisations of IZN carried out from water.

Additive	Ratio used	
	Evaporative	Cooling (400 rpm)
Nicotinic acid	100:1, 1:1	10:1
Isonicotinic acid	100:1, 1:1	10:1
Nicotinamide	100:1, 1:1	10:1
Isonicotinamide	100:1, 1:1	10:1
2-picolinic acid	100:1, 1:1	10:1
Pyrazine carboxamide	100:1, 1:1	10:1
PEG	100:1, 1:1	10:1
PPG	100:1, 1:1	10:1
PP123	100:1, 1:1	10:1
PF127	100:1, 1:1	10:1
Biuret	10:1, 1:1	10:1
Urea	10:1, 1:1	10:1
Resorcinol	10:1, 1:1	10:1
Imidazole	10:1, 1:1	10:1
Oxalic acid	10:1, 1:1	10:1
Malic acid	10:1, 1:1	10:1
2,4-dinitrobenzoic acid	10:1, 1:1	10:1
4-hydroxybenzoic acid	10:1, 1:1	10:1
2,2'-bipyridyl	10:1, 1:1	10:1
4,4'-bipyridyl	10:1, 1:1	10:1
2-aminopyridine	10:1, 1:1	10:1

Table A6.3 - Evaporative crystallisations of IZN carried out in other solvents.

Additive	Solvent		
	IPA:H_2O (1:1)	MeOH	ACN
	Ratio used		
Nicotinic acid	100:1, 1:1	100:1, 1:1	100:1, 1:1
Isonicotinic acid	100:1, 1:1	100:1, 1:1	100:1, 1:1
Nicotinamide	100:1, 1:1	100:1, 1:1	100:1, 1:1
Isonicotinamide	100:1, 1:1	100:1, 1:1	100:1, 1:1
2-picolinic acid	100:1, 1:1	100:1, 1:1	100:1, 1:1
Pyrazine carboxamide	100:1, 1:1	100:1, 1:1	100:1, 1:1
PEG	100:1, 1:1	100:1, 1:1	100:1, 1:1
PPG	100:1, 1:1	100:1, 1:1	100:1, 1:1
PP123	100:1, 1:1	100:1, 1:1	100:1, 1:1
PF127	100:1, 1:1	100:1, 1:1	100:1, 1:1

A6.2 ^{1}H NMR analysis

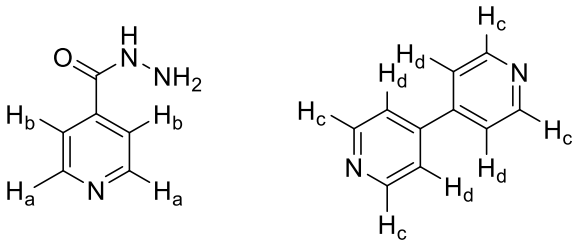

Figure A6.1 – The structures of (left) isoniazid and (right) 4,4'-bipyridyl with the hydrogen atoms labelled.

IZN: ^{1}H NMR (500MHz, D_2O) δ ppm 4.75 (s, H_2O), 7.64 (1H, d, Hb), 8.63 (1H, d, Ha).

44BP: ^{1}H NMR (500MHz, $CDCl_3$) δ ppm 1.63 (s, H_2O), 7.27 (s, $CHCl_3$), 7.55 (1H, d of d, Hd), 8.76 (1H, d of d, Hc).

IZN crystallised from ethanol by evaporative crystallisation: ^{1}H NMR (500MHz, D_2O) δ ppm 4.75 (s, H_2O), 7.67(1H, d, Hb), 8.65 (1H, d, Ha).

IZN crystallised from ethanol in the presence of 44BP via evaporative crystallisation: ^{1}H NMR (500MHz, $CDCl_3$) δ ppm 4.75 (s, H_2O), 7.67 (m, 1, Hb), 8.65 (m, 1, Ha).

A6.3 Powder X-ray diffraction

Evaporative crystallisation of IZN from ethanol

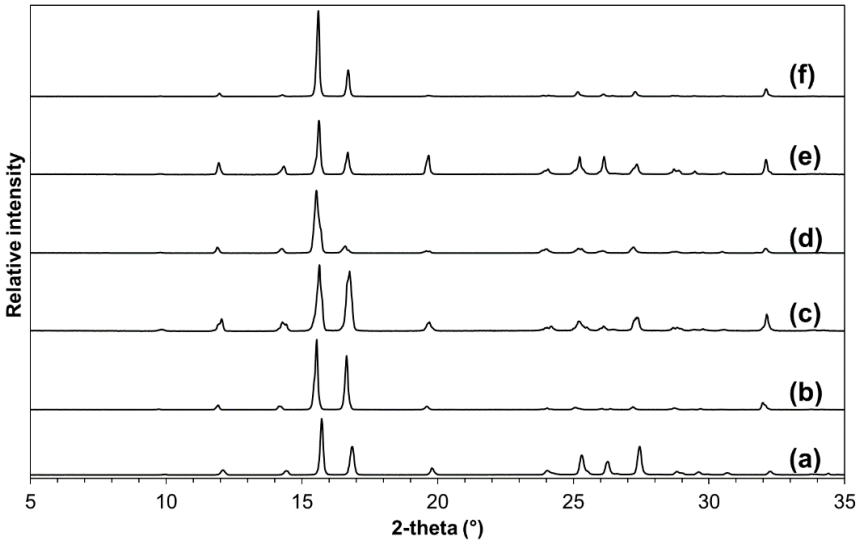

Figure A6.2 - PXRD patterns of isoniazid crystallised evaporatively from ethanol in the presence of (a) no additive, (b) 4-fluorobenzoic acid, (c) 4-hydroxybenzoic acid, (d) imidazole, (e) benzoic acid and (f) resorcinol, all in a 10:1 molar ratio.

Cooling crystallisation of IZN from ethanol

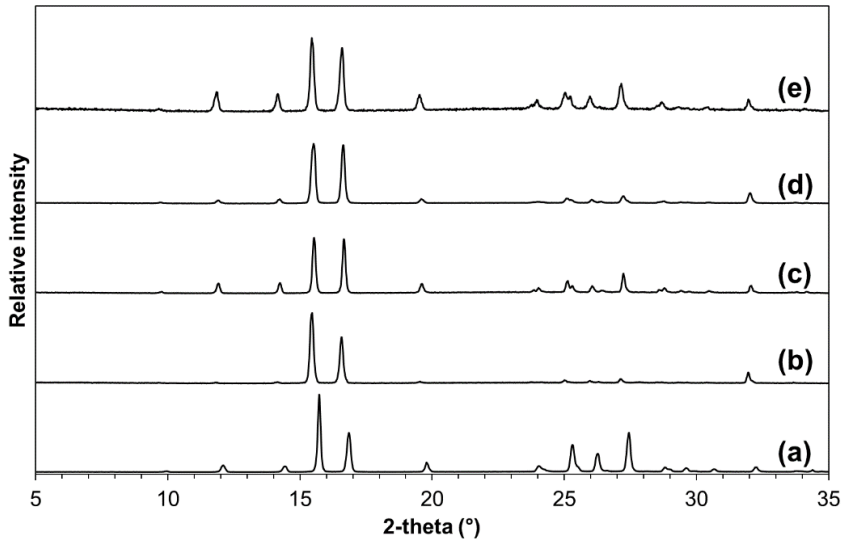

Figure A6.3 - PXRD patterns of isoniazid crystallised in a cooling environment from ethanol in the presence of (a) no additive, (b) isonicotinic acid, (c) nicotinic acid, (d) 2-picolinic acid and (e) biuret, all in a 10:1 molar ratio at 1 ml scale with magnetic bottom stirring.

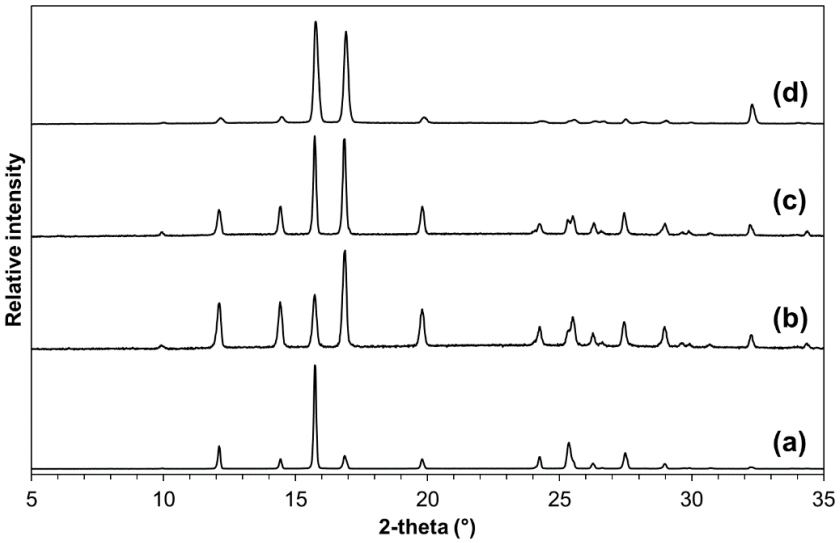

Figure A6.4 – PXRD patterns of isoniazid crystallised in a cooling environment from ethanol in the presence of (a) no additive, (b) biuret, (c) 2-picolinic acid and (d) isonicotinic acid, all in a 10:1 molar ratio at 10 ml scale with overhead stirring.

Evaporative crystallisation of IZN from water

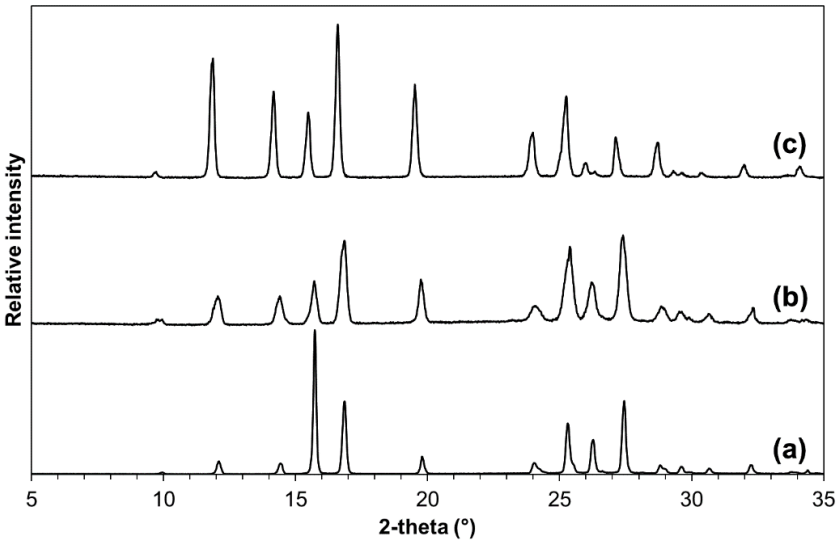

Figure A6.5 - PXRD patterns of isoniazid crystallised evaporatively from water in the presence of (a) no additive, (b) 2-picolinic acid and (c) isonicotinic acid, both in a 100:1 molar ratio.

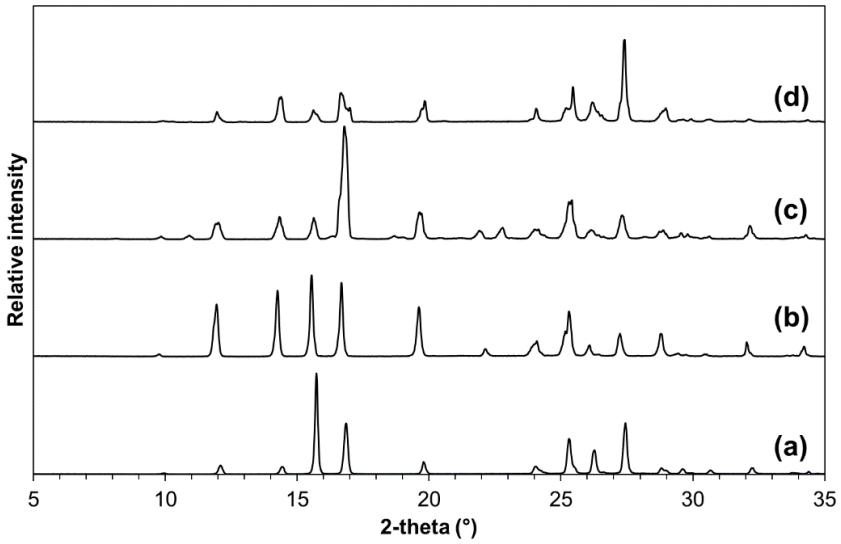

Figure A6.6 - PXRD patterns of isoniazid crystallised evaporatively from water in the presence of (a) no additive, (b) urea, (c) resorcinol and (d) 4-hydroxybenzoic acid, all in a 10:1 molar ratio.

Cooling crystallisation of IZN from water

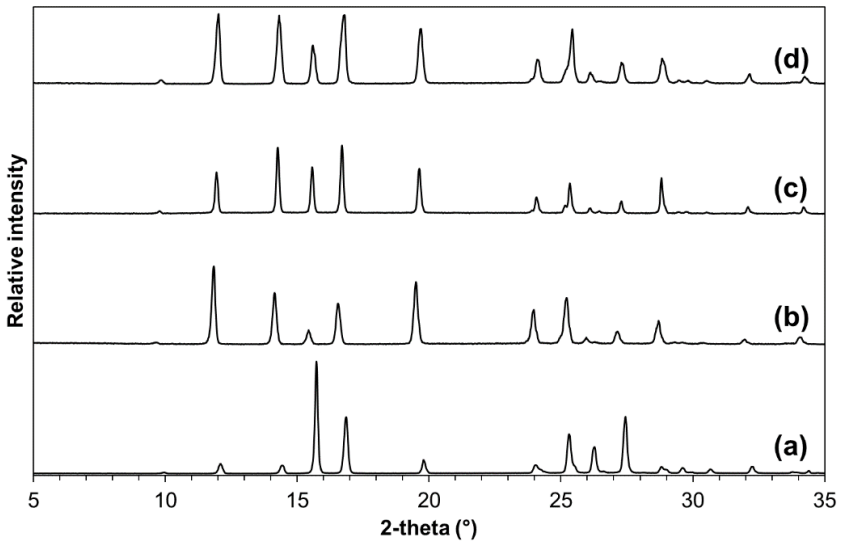

Figure A6.7 - PXRD patterns of isoniazid crystallised in a cooling environment from water in the presence of (a) no additive, (b) imidazole, (c) urea and (d) 2,2-bipyridyl, all in a 10:1 ratio at 1 ml scale.